STARS

University of Central Florida
STARS

Electronic Theses and Dissertations, 2004-2019

2014

An uncooled mid-wave infrared detector based on optical response of laser-doped silicon carbide.

Geunsik Lim
University of Central Florida

Part of the Materials Science and Engineering Commons
Find similar works at: https://stars.library.ucf.edu/etd
University of Central Florida Libraries http://library.ucf.edu

This Doctoral Dissertation (Open Access) is brought to you for free and open access by STARS. It has been accepted for inclusion in Electronic Theses and Dissertations, 2004-2019 by an authorized administrator of STARS. For more information, please contact STARS@ucf.edu.

STARS Citation
Lim, Geunsik, "An uncooled mid-wave infrared detector based on optical response of laser-doped silicon carbide." (2014). *Electronic Theses and Dissertations, 2004-2019*. 4593.
https://stars.library.ucf.edu/etd/4593

University of Central Florida
STARS
Showcase of Text, Archives, Research & Scholarship

AN UNCOOLED MID-WAVE INFRARED DETECTOR BASED ON OPTICAL RESONSE OF LASER-DOPED SILICON CARBIDE

by

GEUNSIK LIM
B.S. Sunchon National University, 2000
M.S. Korea University, 2003

A dissertation submitted in partial fulfillment of the requirements
for the degree of Doctor of Philosophy
in the Department of Materials Science and Engineering
in the College of Engineering and Computer Science
at the University of Central Florida
Orlando, Florida

Fall Term
2014

Major Professor: Aravinda Kar

© 2014 Geunsik Lim

ABSTRACT

This dissertation focuses on an uncooled Mid-Wave Infra-Red (MWIR) detector was developed by doping an n-type 4H-SiC with Ga using the laser doping technique. 4H-SiC is one of the polytypes of crystalline silicon carbide, a wide bandgap semiconductor. The dopant creates an energy level of 0.30 eV, which was confirmed by optical spectroscopy of the doped sample. This energy level corresponds to the MWIR wavelength of 4.21 μm. The detection mechanism is based on the photoexcitation of electrons by the photons of this wavelength absorbed in the semiconductor.

This process modifies the electron density, which changes the refraction index and, therefore, the reflectance of the semiconductor is also changed. The change in the reflectance, which is the optical response of the detector, can be measured remotely with a laser beam such as a He-Ne laser. This capability of measuring the detector response remotely makes it a wireless optical detector. The variation of refraction index was calculated as a function of absorbed irradiance based on the reflectance data for the as-received and doped samples. A distinct change was observed for the refraction index of the doped sample, indicating that the detector is suitable for applications at 4.21 μm wavelength. The Ga dopant energy level in the substrate was confirmed by optical absorption spectroscopy. Secondary ion mass spectroscopy (SIMS) of the doped samples revealed an enhancement in the solid solubility of Ga in the substrate when doping is carried out by increasing the number of laser scans. Higher dopant concentration increases the

number of holes in the dopant energy level, enabling photoexcitation of more electrons from the valence band by the incident MWIR photons.

The detector performance improves as the dopant concentration increases from 1.15×10^{19} to 6.25×10^{20} cm^{-3}. The detectivity of the optical photodetector is found to be 1.07×10^{10} $cm\cdot Hz^{1/2}/W$ for the case of doping with 4 laser passes. The noise mechanisms in the probe laser, silicon carbide MWIR detector and laser power meter affect the performance of the detector such as the responsivity, noise equivalent temperature difference (NETD) and detectivity. For the MWIR wavelength 4.21 and 4.63 μm, the experimental detectivity of the optical photodetector of this study is found to be 1.07×10^{10} $cm\cdot Hz^{1/2}/W$, while the theoretical value is 2.39×10^{10} $cm\cdot Hz^{1/2}/W$. The values of NETD are found to be 404.03 and 15.48 mK based on experimental data for an MWIR radiation source of temperature 25°C and theoretical calculation respectively.

The doped SiC also has a capability of gas detection since gas emission spectra are in infrared range. Similarly, the sensor is based on the semiconductor optics principle, i.e., an energy gap is created in a semiconductor by doping it with an appropriate dopant to ensure that the energy gap matches with an emission spectral line of the gas of interest. Specifically four sensors have been fabricated by laser doping four quadrants of a 6H-SiC substrate with Ga, Al, Sc and P atoms to detect CO_2, NO, CO and NO_2 gases respectively. The photons, which are emitted by the gas, excite the electrons in the doped sample and consequently change the electron density in various energy states. This phenomenon affects the refraction index of the semiconductor and, therefore, the reflectivity of the semiconductor is altered by the gas. The optical response of this semiconductor sensor is the reflected power of a probe beam, which is a He-Ne laser beam in

this study. The CO_2, NO, CO and NO_2 gases change the refraction indices of Ga-, Al-, Sc- and Al-doped 6H-SiC, respectively, more prominently than the other gases tested in this study. Hence these doped 6H-SiC samples can be used as CO_2, NO, CO and NO_2 gas sensors respectively.

ACKNOWLEDGMENTS

I would like to thank all the people who have contributed and supported to finish the research at College of Optics and Photonics/CREOL and Department of Materials Science and Engineering, University of Central Florida. First of all my heartfelt appreciation goes to my advisor, Prof. Aravinda Kar, for his guidance, encouragements, and support throughout my doctoral studies. His helpful suggestion s and countless discussions have made this work possible. I am also grateful to Dr. Sachin Bet, Dr. Chong Zhang and Dr. Nathaniel Quick for their support, contribution and encouragement to the success of this research work.

I would like to thank my committee members, Prof. Kevin Coffey, Prof. Neelkanth Dhere, Prof. Patrick LiKamWa and Prof. Raj Vaidyanathan for their time and helpful comments on my dissertation. Appreciation also goes to all LAMP group members for their assistance, discussions and inspirations. Finally, I would like to express my gratitude to my family and friends for their love, understanding and support.

TABLE OF CONTENTS

LIST OF FIGURES xi
LIST OF TABLES xvi
LIST OF ACRONYMS/ABBREVIATIONS xvii
CHAPTER 1: INTRODUCTION 1
1.1 Motivation 1
1.2 Outline 5
1.3 Literature Reviews 8
1.3.1 Infrared Detector 8
1.3.2 Laser Applications 14
1.3.3 Laser Doping 18
1.3.4 Silicon Carbide 21
1.4 Objectives 28
CHAPTER 2: LASER DOPING 30
2.1 Introduction 30
2.2 Experimental Procedure 33
2.3 Mathematical Models 36
2.3.1 Thermal Model for Temperature Distribution 36
2.3.2 Diffusion Model with Temperature-Dependent Diffusion Coefficient 40
2.4 Results and Discussion 44
2.4.1 Temperature Distribution in SiC during Laser Doping 44
2.4.2 Current-Voltage (I-V) Characteristics of the Doped Sample 46
2.4.3 Dopant Profiles in SiC 48
2.5 Conclusions 58
CHAPTER 3: MODELING OF REFLECTANCE AS A FUNCTION OF DOPANT CONCENTRATION 60
3.1 Introduction 60

3.2 Infrared Radiometry 61
3.3 Infrared Optics 68
3.4 Optical Property of the Detector 73
3.4.1 Absorption Mechanism 73
3.4.2 Reflectance of the SiC Detector at He-Ne Laser Wavelength 76
3.5 Effect of Dopant Concentration on the Low Signal Detectibility of the Doped Samples...83
CHAPTER 4: THEORETICAL APPROACH OF FIGURES OF MERIT 92
4.1 Introduction.....92
4.2 Theoretical Detectivity 92
4.3 Theoretical NETD 94
4.4 Effect of Photogenerated Electrons on the Reflectance of the Doped Region 95
CHAPTER 5: THEORETICAL NETD AND DETECTIVITY FROM NOISE SOURCES 99
5.1 Introduction.....99
5.2 Noises in the SiC Detector.....99
5.3 Noises in He-Ne Laser Probe Beam.....100
5.4 Interferometric Noise due to Interaction between the He-Ne Laser and the SiC Detector 103
5.5 Noise due to He-Ne Laser Detector (Si-based Photodetector) 105
5.6 Noise Equivalent Temperature Difference (NETD) due to Various Noise Mechanisms .107
5.7 Effect of NETD on Detectivity (D^*).....110
CHAPTER 6: CHARACTERIZATION OF INFRARED DETECTOR.....114
6.1 Introduction.....114
6.2 Spectroscopic Analysis of the Dopant Energy Level.....117
6.3 Measurement of the Optical Response 121
6.3.1 Optical Setup for Irradiance on the Ga-doped SiC sample 123
6.3.2 Measurement of Optical Signal for Testing the Response of the Ga-doped Sample .125
6.3.3 Multiple Reflections of the He-Ne beam 127
6.3.4 Analysis of the Reflected Power to Determine the Detectivity and the NETD for the Ga-doped Sample 128

6.4 Results and Discussion 134
6.4.1 Changes in the Reflectance and Refraction Index of the SiC Detector as a Function of the Absorbed MWIR Irradiance 134
6.4.2 Effect of Radiation Collection Lenses and the Power Resolution of the Si He-Ne Beam Detector 140
6.4.3 NETD and Detectivity 142
6.4.4 Comparison of Theoretical and Experimental value of NETD and Detectivity 149
6.4.5 Measurement of Sensor Response at Different Temperatures of the Sensor 151
6.4.6 Effect of Sensor Temperature on Its Performance 154
6.5 Conclusions 156
CHAPTER 7: GAS SENSING APPLICATION 158
7.1 Introduction 159
7.2 Gas Sensing Mechanism 162
7.2.1 Operating Principle of the Gas Sensor 162
7.2.2 Dopant Selection Procedure for Sensor Fabrication 165
7.3 Experimental Procedure 167
7.3.1 Laser Doping of Silicon Carbide for Sensor Fabrication 167
7.3.2 Interferometeic Measurement for Testing the Sensor 168
7.4 Results and Discussion 170
7.4.1 Absorption Peaks of the Ga- and Al-doped 6H-SiC Sensors 171
7.4.2 Determination of Refraction Index for As-received 6H-SiC Sample, Ga-doped and Al-doped Sensors 174
7.4.3 Analysis of the Sensor Response 184
7.5 Conclusions 191
CHAPTER 8: SUMMARY 193
8.1 Conclusions 193
8.2 Future Work 196
APPENDIX A: DOPANT CONCENTRATION DISTRIBUTION 199
APPENDIX B: PHOTOEXCITED FREE ELECTRON DENSITY 202
APPENDIX C: NETD AND DETECTIVITY 204

APPENDIX D: LIST OF PUBLICATIONS 219
REFERENCES 223

LIST OF FIGURES

Figure 1-1: Construction of gas sensors with receptor and transducer. 3

Figure 1-2: Comparison of the detectivity (D^*) of various available detectors when operated at the indicated temperature [16]. PC – photoconductive detector, PV – photovoltaic detector, PEM – photoelectromagnetic detector, and HEB – hot electron bolometer. 10

Figure 2-1: Experimental setup for laser doping of n-type 4H-SiC with Ga.....34

Figure 2-2: Doped quadrants of dimensions 3 mm × 3 mm each for different number of laser scans. 35

Figure 2-3: Temperature distribution along the depth of the substrate during laser doping for 4 laser passes.....45

Figure 2-4: Current-voltage plots for as-received n-type 4H-SiC sample and after the sample was doped with Ga (p-type dopant) under different numbers of laser passes: (a) measured on the same surface of the sample and (b) measured across the thickness of the sample with one probe on the p-doped side and the other probe on the parent n-type side.....47

Figure 2-5: Ga dopant concentration obtained by converting the original SIMS data from the arbitrary unit to cm^{-3} using an ion-implanted n-type 4H-SiC standard.....49

Figure 2-6: Maximum error for different number of laser passes; (a) one-pass, (b) two-pass, (c) three-pass and (d) four-pass, showing ε_m for determing the values of Q and D_0.....51

Figure 2-7: Diffusion coefficients as a function of temperature for different number of laser passes.....55

Figure 2-8: Comparison of experimental (SIMS data) and calculated Ga concentration profiles for different number of laser passes. 56

Figure 3-1: View factor associated with radiation exchange between differential surfaces of area dA_i and dA_j [70].....62

Figure 3-2: Spectral radiance of blackbody as a function of wavelength at different temperatures.....64

Figure 3-3: View factor for three-dimensional geometry of coaxial parallel disks [71].....68

Figure 3-4: Ray geometry of the irradiance to the detector with one focusing lens. 69

Figure 3-5: Multiple reflection in (a) as-received and (b) as-received and Ga-doped 4H-SiC layers.....77

Figure 3-6: Spectroscopic data showing the optical properties of as-received n-type 4H-SiC and Ga-doped samples with different numbers of laser scans: (a) absorbance, (b) reflectance, and (c) transmittance in the wavelength range 4-5 μm. 86

Figure 3-7: Experimental setup for testing the optical response of the as-received and Ga-doped samples at the MWIR wavelengths 4.21 and 4.63 μm.....88

Figure 3-8: Effects of the source temperature and the dopant concentration on the MWIR detectibility with the SiC detector being at room temperature (25°C): (a) total radiance in the wavelength bands ranging from 4.2 to 4.29 μm around the peak wavelength 4.21 μm and from 4.54 to 4.66 μm around the peak wavelength 4.63 μm in the MWIR emission spectrum of the source, and absorbed irradiance in the doped samples with two CaF_2 lenses, (b) effects of the dopant concentration on the change in the reflected power of the He-Ne laser, showing that high dopant concentration (as in the case of four-pass sample) is more sensitive for detecting MWIR photons emitted by a source maintained at room temperature, and (c) comparison of the theoretical and experimental reflectances at the He-Ne laser wavelength in the presence of the MWIR irradiance.....89

Figure 6-1: Spectroscopic data showing the optical properties of Ga-doped, laser heat treated and as-received 4H-SiC (a) absorbance, (b) reflectance, and (c) transmittance in the wavelength range 4-5 μm. 118

Figure 6-2: Optical arrangement to examine the detector response and ray geometry to calculate the irradiance on the SiC MWIR detector due to the radiance of a stainless steel source.....122

Figure 6-3: Reflected powers of the He-Ne beam at room and higher temperatures of the source to determine NETD. T_{BG} is the background temperature of other materials surrounding the source. It is 25°C in this study and the reflected power is lower than that of the source due to the difference in emissivity. 134

Figure 6-4: Effects of the radiance of the source and the number of lenses on the optical response of the detector (Ga-doped sample) compared to the as-received (undoped) sample, showing that the doped sample produces a significant optical signal at the He-Ne laser wavelength of 632.8 nm: (a) effect of the source temperature on its radiance at two wavelengths, (b) reflected powers, (c) reflectances and (d) changes

in the reflectance of the as-received and Ga-doped samples. The resolution of the Si He-Ne beam detector was 0.63 nW. 136

Figure 6-5: Effects of the radiance of the source and the number of lenses on the refraction index of the detector compared to the as-received sample, showing a significant effect on the refraction index of the detector at the He-Ne laser wavelength of 632.8 nm: (a) refraction indices and (b) changes in the refraction index of the as-received and Ga-doped samples. The resolution of the Si He-Ne beam detector was 0.63 nW. 139

Figure 6-6: Effects of the source temperature, the number of lenses and the resolution of the Si He-Ne beam detector on the MWIR detectibility of the SiC detector: (a) threshold source temperature for MWIR detection with just the source lens and without any lens, (b) MWIR detection at room temperature (25°C) with two lenses and 0.63 nW resolution of the Si detector, and (c) effects of the resolution of Si detector on MWIR detection by the SiC detector, showing that low resolution and two lenses enable MWIR detection at room temperature of the source. 141

Figure 6-7: Effects of signal-to-noise ratio on the detectivity and NETD of just the SiC optical photodetector for three different time constants (10, 100 and 1000 ns) of the detector. 148

Figure 6-8: Effects of dopant concentration on the MWIR detectibility of the SiC detector and comparison between theoretical and experimental results: (a) theoretical $NETD_{Th}$ for each noise source and (b) total theoretical and experimental ($NETD_{Exp}$). $NETD_{Exp}$ was obtained by keeping the detector at 25°C and the radiation source at 35°C and 45°C. 150

Figure 6-9: Effects of dopant concentration on the MWIR detectibility of the SiC detector and comparison between theoretical and experimental results: (a) theoretical detectivity for each noise source and (b) total theoretical and experimental detectivity. The detectivity was determined by keeping the detector and radiation source at 25°C each. 151

Figure 6-10: Measurement of the optical signal at different temperatures of the sensor. (a) Liquid nitrogen flows through a channel to cool the sensor and (b) the sensor is heated to about 550°C on a hot plate before placing it on a ceramic seat in an aluminum sample holder. 153

Figure 6-11: Reflected power of the He-Ne laser at different temperatures of the four-pass Ga-doped 4H-SiC sensor. 155

Figure 7-1: (a) Photoexcitation of LOGS by the gas of interest. (b) Interrogation of the sensor with a He-Ne beam, showing the working principle of LOGS. 163

Figure 7-2: Experimental setup for testing the optical response of LOGS.....169

Figure 7-3: Optical properties of (a) as-received, (b) Ga-doped, and (c) Al-doped 6H-SiC in the wavelength range 0.2 – 25 μm at room temperature.....173

Figure 7-4: The reflected power of a He-Ne laser due to an as-received 6H-SiC sample for different gases (a) air, (b) carbon monoxide, (c) carbon dioxide, (d) nitrogen monoxide, and (e) nitrogen dioxide at various temperatures.....176

Figure 7-5: The reflected power of a He-Ne laser beam due to a Ga-doped 6H-SiC sample for different gases (a) air, (b) carbon monoxide, (c) carbon dioxide, (d) nitrogen monoxide, and (e) nitrogen dioxide at various temperatures.....178

Figure 7-6: The reflected power of a He-Ne laser due to an Al-doped 6H-SiC sample for different gases (a) air, (b) carbon monoxide, (c) carbon dioxide, (d) nitrogen monoxide, and (e) nitrogen dioxide at various temperatures.....180

Figure 7-7: A typical multi-beam interference pattern for the reflected power.....183

Figure 7-8: Comparison of the optical properties of Ga-doped 6H-SiC sensor in the presence of different gases, indicating the selectivity for sensing the CO_2 gas: (a) refraction indices and (b) change in the refraction indices.....185

Figure 7-9: Comparison of the optical properties of Al-doped 6H-SiC sensor in the presence of different gases, indicating the selectivity for sensing the NO gas: (a) refraction indices and (b) change in the refraction indices.....186

Figure 7-10: Comparison of (a) difference of refraction indices ($\Delta n = n(\lambda, T, c, gas) - n(\lambda, T, c, air)$) and (b) difference of reflectances ($\Delta\rho = \rho(\lambda, T, c, gas) - \rho(\lambda, T, c, air)$) for Sc-doped 6H-SiC in combustion gases. 188

Figure 7-11: Comparison of (a) difference of refraction indices ($\Delta n = n(\lambda, T, c, gas) - n(\lambda, T, c, air)$) and (b) difference of reflectances ($\Delta\rho = \rho(\lambda, T, c, gas) - \rho(\lambda, T, c, air)$) for P-doped 6H-SiC in combustion gases. 189

Figure 7-12: Variation of reflectivity as a function of electron density in a typical crystalline SiC semiconductor material, showing that the reflectivity changes fairly rapidly for $n_e = 10^{19} - 5\times10^{19}$ cm^{-3} and, therefore, the detector is expected to be sensitive in this range of n_e. 190

Figure 8-1: Optical setup for detector performance with LED as a probe beam. 196

Figure 8-2: Focal plane array can be built on a single SiC chip which has less loss of signal due to the diffusion of electrons to the neighboring pixels than other semiconductor materials.....198

LIST OF TABLES

Table 1-1: Comparison of the optical infrared detector with a conventional infrared detector. .5

Table 1-2: Properties of silicon carbide [27, 28]. 22

Table 1-3: Crystallographic properties of silicon carbide [27, 28]. 24

Table 2-1: Properties of n-type 4H-SiC substrate with the optical properties at the wavelength of 1064 nm. 44

Table 2-2: Diffusion parameters of Ga in n-type 4H-SiC during laser doping. 52

Table 2-3: Surface concentration and diffusion lengths of Ga in n-type 4H-SiC substrate. 57

Table 3-1: Optical properties of as-received n-type 4H-SiC and Ga-doped samples with different numbers of laser scans at the MWIR wavelength 4.21 μm. 84

Table 5-1: Theoretical values of $NETD_{Th}$ and detectivity of Ga-doped 4H-SiC IR detector in 4.21 μm. 113

Table 6-1: Optical properties for as-received and doped 4H-SiC.....120

Table 6-2: Performances of various infrared detectors at 4.21 μm wavelength. 145

Table 7-1: Classification of SiC-based gas sensors. 161

Table 8-1: Comparison of the optical infrared detector with a conventional infrared detector. 197

LIST OF ACRONYMS/ABBREVIATIONS

Acronyms

A_d	SiC detector area
Bi	Biot number
c	Speed of light
C	Center of the lens surface curvature
C_0	Dopant concentration at the substrate surface
C_{Ex}	Experimental dopant concentration
C_i	Initial dopant concentration distribution
C_p	Specific heat capacity
C_{Th}	Theoretical dopant concentration
d	Substrate thickness
D	Diffusion coefficient
D^*	Detectivity
D^*_{Exp}	Experimental detectivity
D^*_{Th}	Theoretical detectivity
D_0	Pre-exponential factor
dA_s	Differential surface area of the source
dA_S	Differential surface area of the source lens

Δf_d	Noise bandwidth of SiC detector
E_b	Binding energy
E_F	Fermi energy level
E_g	Bandgap energy
F	f-number of lens
Fo	Fourier number
h_H	Heat transfer coefficient
h	Planck constant
hh	Heavy hole band
I_0	Laser irradiance
I_a	Absorbed irradiance
I_p	Incident photon flux
k	Thermal conductivity
K	Proportionality constant
k_B	Boltzmann constant
l_c	Characteristic diffusion length of electron
lh	Light hole band
m_e	mass of an electron
M_R	Refraction matrix
M_S	System matrix
N_a	Acceptor concentration

n_d	Refraction index of detector
N_d	Donor concentration
Nd: YAG	Neodynium-doped Yttrium Aluminium Garnet; $Nd:Y_3Al_5O_{12}$
N_e	Free electron density
$NETD_{Exp}$	Experimental noise equivalent temperature difference
$NETD_{Th}$	Theoretical noise equivalent temperature difference
n_{i1}	Refraction index of the first incident medium
n_{i2}	Refraction index of the second incident medium
n_{t1}	Refraction index of the first transmitted medium
n_{t2}	Refraction index of the second transmitted medium
p_1	Maximum point of the ray on the first medium
p_2	Maximum point of the ray on the second medium
P_i	Incident laser power
p_I	Maximum point of the image
p_O	Maximum point of the object
P_r	Reflected laser power
P_t	Transmitted laser power
Q	Activation energy
Q	Electron charge
$\Re$	Responsivity
R	Reflectance

r	Radius vector joining the differential areas dA_s and dA_S
R_1	Radius of the lens sphere
SiC	Silicon carbide
SO	Split-off band
SS	Stainless steel radiation source
t_e	Equilibrium electron population time
T_i	Initial temperature
T_L	Laser temperature
T_s	Source temperature
T_{SiC}	SiC detector temperature
V	Volume
y_1	Height of an incident point on the first interface from the optical axis
y_2	Height of a transmitted point on the second interface from the optical axis
y_I	Height of the image (detector) from the optical axis
y_O	Height of the object (radiation source) from the optical axis
Z	Diffusion length

Abbreviations

CVD	Chemical vapor deposition
CW	Continuous wave

DPB	Double position boundary
FPA	Focal plane array
GILD	Gas immersed laser doping
HAZ	Heat affected zone
HEB	Hot electron bolometer
IR	Infrared
I-V	Current-voltage
LCP	Liquid chemical processing
LDSE	Laser doped selective emitter
LIMPID	Laser induced melting of pre-deposited impurity doping
LPE	Liquid phase epitaxy
LWIR	Long wave infrared
MEMS	Micro-electro-mechanical system
MOSFET	Metal-oxide-semiconductor field-effect-transistor
MWIR	Mid-wave infrared
NETD	Noise equivalent temperature difference
PC	Photoconductive detector
PEM	Photoelectromagnetic detector
PV	Photovoltaic detector
RIN	Relative intensity noise
SIMS	Secondary ion mass spectroscopy

VPE	Vapor phase epitaxy

Greek Symbols

α	Thermal conductivity
ε_0	Permittivity of free space
ε_M	Maximum error
ε_s	Emissivity of radiation source
η_e	External quantum efficiency
η_i	Internal quantum efficiency
κ_d	Absorption index
λ	Wavelength
λ_0	Central wavelength of the detector response
μ	Absorption coefficient
ν_M	Frequency of MWIR radiation
ρ_D	Density
ρ	Reflectance
σ	Standard deviation of noise distribution
σ^2	Noise variance
τ_t	laser-substrate interaction time
τ	Transmittance

τ_0	Transmissivity of lens
τ_c	Recombination time
τ_d	Characteristic diffusion time
ω_0	Resonant frequency of electron
$\Delta\lambda_0$	Full width at half maximum around λ_0
θ_1	Supplement of apex angle of the beam with θ_{i1}
θ_{t1}	Angle on the interface of an incident beam with the optical axis
θ_s	Angle subtended by r with the normal to the area dA_s
θ_S	Angle subtended by r with the normal to the area dA_S
θ_{t1}	Angle on the interface of a transmitted beam with the optical axis

CHAPTER 1: INTRODUCTION

1.1 Motivation

The jewel beetles are able to detect flames of a forest fire with supersensitive receptors approximately 50 miles away. The sensory organs located on their underside are pits containing a large number of receptors (sensilla) that are extremely responsive precisely to the infrared radiation that comes from a forest fire [1-3]. With this ability, jewel beetles are the first creatures to move into such an inhospitable environment. This insect needs burnt wood from a blazing forest fire to lay eggs to the still smoldering bark of a tree. As is known, this beetle, bed bugs, vampire bats and some snakes are the only creatures with this ability [4-6]. This capability to detect infrared radiation which is either from a fire or heat produced by an animal can be mounted around forests and ready to register and alert foresters of a fire. The military is also trying to mimic the features of the infrared detector on some applications which include thermal imaging, guidance, reconnaissance, surveillance, ranging and communication systems [7-9].

Infrared detectors are generally classified into photon detectors and thermal detectors. In the former detectors, the radiation is absorbed within the material by interaction with electrons, either bound to lattice atoms, or to impurity atoms or with free electrons. Photons are directly converted into free electrons by photoexcitation across the energy bandgap of the semiconductor. The output signal which results from the changed electronic energy distribution produces a current, voltage, resistance or refraction index change of the detectors as schematically shown in

Figure 1-1(a). Therefore, the photon detectors show a selective wavelength dependence of the response per unit incident radiation power. They have high sensitivity and fast response when compared to thermal detectors. However, the temperature of the detectors must be low enough to less significant of the photoexcited electrons across the bandgap (band-to-band transitions). That is particularly true of the extrinsic photodetectors such as doped germanium and silicon. To achieve this, the photon detectors require cryogenic cooling below 77 K for accurate measurements to eliminate thermally generated carriers [10]. The need for cooling is a considerable problem which inhibits the more widespread use of IR systems. The cooling requirements add considerably to the cost, bulk, weight, power consumption and inconvenience of infrared systems and it is highly desirable that they be eliminated or reduced. Therefore one of the main research goals is increase in working temperature of photodetectors. The need for cooling is a major limitation of IR photon detectors and a number of concepts to improve performance of the near room temperature IR photodetectors have been proposed. Silicon-based devices are limited to an operation temperature below 250°C because silicon does not keep its nature as a semiconductor in the region where a lot of electron-hole pairs are thermally generated, while silicon carbide-based infrared detectors can operate at high temperatures up to 800°C [11].

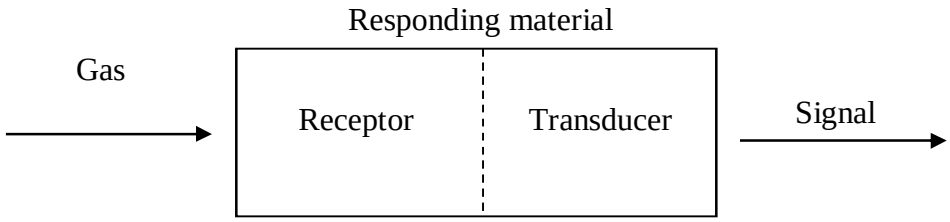

(a)

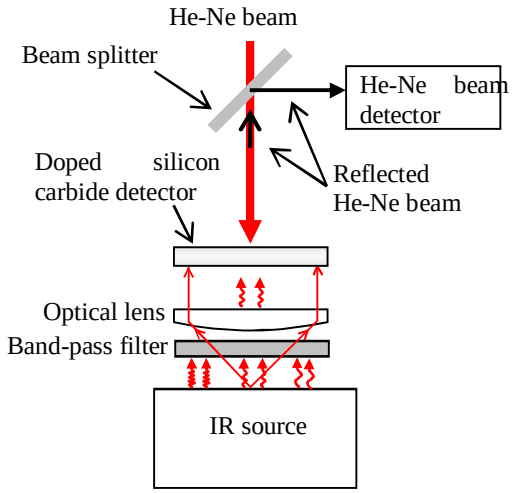

(b)

Figure 1-1: Construction of gas sensors with receptor and transducer.

A new approach is investigated in this study to fabricate MWIR detectors that can operate at room temperature. The detector operates on the principle of semiconductor optics involving both the semiconductor and optical properties. Crystalline silicon carbide, which is a wide bandgap (3.23 eV for 4H-SiC and 3.0 eV for 6H-SiC) semiconductor, offers a unique advantage for

tuning its photon detectibility to a desired wavelength by doping it with appropriate dopants. Specifically an n-type 4H-SiC substrate is doped with Ga to fabricate a MWIR detector for the wavelength 4.21 μm. The selection of the dopant is based on the energy level of 0.30 eV created by Ga in this substrate [12, 13], which corresponds to a quantum of energy at the wavelength 4.21 μm. Due to this photon energy-matched dopant energy level, the electron density in the impurity energy level of the 4H-SiC semiconductor can be altered by photoexcitation of electrons from the valence band to the dopant energy level. This change in the electron density modifies the refraction index of the semiconductor and therefore its reflectance changes, which represents the detector response. This response is probed with a He-Ne laser of wavelength 632.8 nm as schematically shown in Figure 1-1(b). The SiC-based infrared detector can be described as a device, which upon exposure to infrared radiations, alters one or more of its physical properties, e.g., optical property and electrical conductivity, in a way that can be measured and quantified directly or indirectly. The characteristics of the SiC-based infrared detector are compared in Table 1-1 with the classes of conventional infrared detector used to detect the changes of physical properties.

Table 1-1: Comparison of the optical infrared detector with a conventional infrared detector.

Parameters	Electrical photodetector	Wireless optical photodetector
Responsivity ($\Re$)	Voltage (or current) produced by the detector per incident power [V/W].	Change in the reflectance of detector per incident power [W^{-1}].
Detectivity (D^*)	Responsivity of an active area of 1 cm^2 at 1 Hz noise-equivalent bandwidth.	Responsivity of an active area of 1 cm^2 at 1 Hz noise-equivalent bandwidth.
Response mechanism	Physical mobility (transport) of photo-generated electrons through an electrical circuits.	Quantum mobility (transition) of photo-generated electrons between two energy levels.

1.2 Outline

This dissertation is composed of 10 chapters, including this chapter.

Chapter 1 introduces the backgrounds of infrared detector, laser applications, laser doping and silicon carbide material. It also includes the research motivation of optical infrared detector and its objectives.

Chapter 2 explores the laser doping technique which was used for fabrication of doped silicon carbide as an infrared detector. A continuous wave laser heating model is examined to determine

the temperature distribution in the silicon carbide substrate during the laser doping process and the diffusion model based on spatially-varied diffusion coefficient is presented. Through the diffusion model, the pre-exponential factor and activation energy for the diffusion of Gallium dopant are determined. The SIMS data and the prediction model are compared as well. The substrate was scanned with different number of laser passes to control the dopant concentration profile in order to study the effect of laser passes on the diffusion coefficient.

Chapter 3 deals with the modeling of reflectance of the doped silicon carbide at He-Ne laser wavelength as a function of dopant concentration. Since the photons from the radiation source excite electrons from the valence band to the dopant energy level in the doped SiC, infrared radiometry about irradiance and infrared optics about absorbed irradiance in the detector material are introduced. Consequently the electron densities are modified in these two energy levels, which affect the refraction index of the semiconductor and, therefore, the reflectance of the doped region changes. Therefore optical property of the detector, absorption mechanism and reflectance, is characterized. The theoretical and experimental data of reflectance as a function of dopant concentration which was obtained with different laser scan are shown.

Chapter 4 examines the theoretical approach of figure of merit, detectivity and NETD. The theoretical detectivity is obtained with four-pass sample due to the highest internal quantum efficiency and compared the detectivities of other samples with different dopant concentration. Similarly, the theoretical NETD is obtained with the improved radiation collection capability and the optimized dopant concentration.

Chapter 5 investigates the theoretical NETD and detectivity from the noise sources which includes noise mechanisms in doped SiC detector, inherent in the He-Ne laser, the interaction between the detector and He-Ne laser, and the noise of the He-Ne laser detector. From the noise sources within the SiC-Si optical photodetector system, the detector performances such as NETD and detectivity are evaluated. The detectivity equation which is effected by NETD is derived through this chapter. The NETD and detectivity data from each noise source are compared and the total theoretical data are obtained.

Chapter 6 characterizes the infrared detector through experimental setup to measure the optical response. The spectroscopic data of the opant energy level are analyzed and verified by comparing the as-received to doped SiC sample. Measurement of optical signal for testing the response of the Ga-doped sample was conducted. Finally it was analyzed the reflected power to determine the detectivity and the NETD of the doped sample. It concludes that significant changes in the reflectance and refraction index of the Ga-doped sample confirm that such samples can be used as MWIR detectors.

Chapter 7 demonstrates the capability of doped SiC detector as a gas sensor. Specifically four sensors have been fabricated by laser doping four quadrants of a 6H-SiC substrate with Ga, Al, Sc and P atoms to detect CO_2, NO, CO and NO_2 gases respectively. The optical response of this semiconductor sensor is the reflected power of a probe beam, which is a He-Ne laser beam. The CO_2, NO, CO and NO_2 gases change the refraction indices of Ga-, Al-, Sc- and Al-doped 6H-SiC, respectively, more prominently than the other gases tested. So these doped 6H-SiC samples can be used as CO_2, NO, CO and NO_2 gas sensors respectively.

Finally, the conclusion of this dissertation is presented and the future work is proposed in Chapter 8.

1.3 Literature Reviews

1.3.1 Infrared Detector

In 1800, Herschel studied the spectrum of sunlight with a prism by measuring temperature of each color [14-16]. He built a crude monochromator which consisted of liquid in a glass thermometer with a specially blackened bulb to absorb radiation and he discovered of the existence of thermal radiation in the invisible beyond the red, which is from the Latin 'infra' means below. After the most import steps in the development of infrared (IR) detectors by Seebeck (thermoelectric effect and the first thermocouple in 1821), Nobili (construction thermocouple series in 1829) and Melloni (modified thermocouple by using bismuth and antimony in 1833) in 19th century [14-16], the IR imaging systems had progressed steadily over 20th century. Until now, there has been considerable progress towards the development of optoelectronics related materials and device design innovations. Currently, third-generation IR systems are being developed which provide enhanced capabilities such as larger numbers of pixels, higher frame rates, better thermal resolution, multicolor functionality, and other on-chip signal processing functions after first-generation (linear arrays for scanning systems) and second-generation (2-dimensional arrays for staring systems which scanning electronically).

Based on limits of spectral bands of commonly used IR detectors, the infrared spectrum is segmented into near infrared (NIR, 0.8-1.1 μm), short wave infrared (SWIR, 0.9-2.5 μm), mid wave infrared (MWIR, 3-5 μm), long wave infrared (LWIR, 8-14 μm), very long wave infrared (VLWIR, 12- 25 μm) and far infrared (FIR, > 25 μm) [17]. Especially radiation is either scattered or absorbed as it propagates through the atmosphere since there are three good infrared transmission windows at 1-3 μm, 3-5 μm and 8-12 μm. These IR wavelength windows dictate the choice of wavelengths used in infrared sensor design. Wavelength 1 μm is a sensitivity limit of popular Si detectors. Similarly wavelength of 3 μm is a long-wave sensitivity limit of PbS and InGaAs detectors; wavelength 6 μm is a sensitivity limit of InSb, PbSe, PtSi detectors and HgCdTe detectors optimized for 3-5 μm atmospheric window; and finally wavelength 15 μm is a long-wave sensitivity limit of HgCdTe detectors optimized for 8-12 μm atmospheric window. It is well shown in Figure 1-2 which is compared of the spectral detectivity of various available detectors when operated at the indicated temperature [16]. In this figure, theoretical curves for the back-ground-limited detectivity with dashed lines for ideal photovoltaic and photoconductive detectors and thermal detectors are also shown.

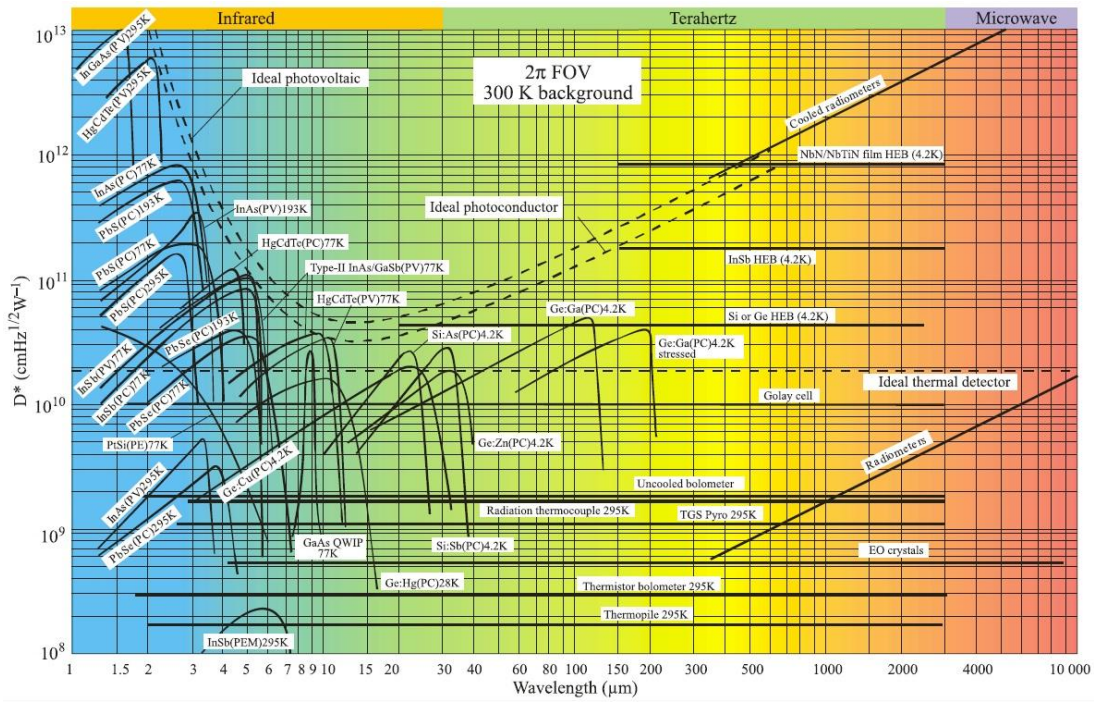

Figure 1-2: Comparison of the detectivity (D^*) of various available detectors when operated at the indicated temperature [16]. PC – photoconductive detector, PV – photovoltaic detector, PEM – photoelectromagnetic detector, and HEB – hot electron bolometer.

Moreover, the hotter object emits more of their energy at shorter wavelengths according to Wien's law. A blackbody source at 300 K has a peak irradiance at a wavelength of about 9.7 μm, otherwise for a source at 1000 K the maximum irradiance occurs at 2.9 μm. Therefore, detectors operating in the LWIR band are well suited to image room temperature objects (people or buildings), while MWIR band imagers are sensitive for viewing objects at higher temperatures such as hot engines and exhaust gases. Even the LWIR band imagery may exhibit a higher sensitivity for room temperature objects, the MWIR band imagery presents a better resolution.

The primary spectral bands for infrared imaging are 3 to 5 and 8 to 12 μm because atmospheric transmission is highest in these bands.

The majority of IR detectors can be classified in two categories: photon detectors (quantum detectors) and thermal detectors. The IR radiation is absorbed with the material by interaction with electrons either bound to lattice atoms or to impurity atoms or with free electrons in photon detectors. There are two types of photon detectors: 1) photoconductive (PC) where the electrical conductivity of the semiconductor changes as a function of the photon intensity; 2) photovoltaic (PV) where a voltage is generated across a PN junction as photons impinge the semiconductor. The PC detectors again divided by intrinsic and extrinsic.

The most popular PC detector is doped extrinsic silicon such as Si:*x*; where *x* is Ga, As, In and Germanium such as Ge:Hg. Among these Si:As and Si:Ga are the advanced detector due to the higher dopant levels which reduce recombination noise and have longer spectral response than standard extrinsic devices. Silicon has several advantages over Germanium such as a lower dielectric constant giving shorter dielectric relaxation time and lower capacitance, higher dopant soluility and larger photoionization cross section for higher quantum efficiency and lower refraction index for lower reflectance. However, these were not sufficient to warrant the necessary development efforts needed to bring it to the level of the highly developed Germanium detectors [14-16].

At an earlier date, the first high performance extrinsic detectors were based on germanium which based on the techniques for controlled impurity introduction in it. Its response from copper, zinc and gold impurity levels in germanium gave rise to devices using in the 8-14 μm long

wavelength IR spectral window and further beyond to the 14-30 μm very long wavelength range. These detectors were widely used at wavelengths beyond 10 μm prior to the development of the intrinsic detectors and they must be operated at lower temperatures to achieve performance similar to that of intrinsic detectors.

On the other hand, the most popular intrinsic PC is HgCdTe due to its producibility, cost and low detector impedance. And also these narrow bandgap semiconductors have extended wavelength capabilities and improved sensitivity. An intrinsic PC detector includes InSb, InGaAs/InP and Ge. These alloys have advantages of customized detection response and bandgap engineering for specific applications. HgCdTe is also used as an intrinsic photovoltaic (PV) detector like as InSb and PbSnTe materials. Although these narrow bandgap semiconductors have higher capabilities such as high optical absorption coefficient, high electron mobility and low thermal generation rate, the difficulties in growing HgCdTe material due to the high vapor pressure of Hg encouraged the development of alternative detector technologies. PbSnTe was an alternative candidate [14-16]. However, its drawbacks, i.e., high dielectric constant and large temperature coefficient of expansion mismatch with silicon that cause smearing image and failure of the indium bonds in hybrid structure between silicon readout and the detector array, make it hard to use as a IR detector. PtSi material uses an internal photoemission mechanism which is included in PV detector.

HgCdTe is the most widely used for IR photodectors over the past years and at present. And extrinsic silicon and PbSnTe have been developed as alternative IR detectors. At the same time, Schottky barriers on silicon, SiGe heterojunctions, AlGaAs multiple quantum wells, GaInSb

strain layer superlattices, high temperature superconductors become competitors [14-16]. A considerable progress towards the detector materials and designs used to fabricate focal plane arrays (FPAs) improve the detectivity and enable to have infrared products. In particular, the band-gap engineering of various compound semiconductors has led to new and emerging detector architectures. Advances in optoelectronics related materials science such as meta-materials and nanostructures enhanced performance and low cost products in a wide range of applications. Even photon detector exhibits both a good signal-to-noise performance and a very fast response, it needs cryogenic cooling to prevent the thermal generation of charge carriers because the thermal transitions compete with the optical ones and making non-cooled devices very noisy.

Moreover, two types of thermal detectors such as pyroelectric detectors and silicon bolometers show interesting capabilities as a IR detector [14-16]. The incident radiation is absorbed to change the material temperature and the resultant change in some physical property is used to generate an electrical output in thermal detectors which include electrical resistance in a bolometer, thermal gas expansion of Golay cell and polarization in pyroelectric materials. Photon detectors convert photons directly into charge carriers and no intermediate process is involved such as the heating in a thermal detector to produce a change of a measurable electrical property. Thus, thermal effects on the detector material are not depending on wavelength but on radiation power. Although a response time of thermal detector is slower than photon detector, it has been shown that extremely good imagery can be obtained from large thermal detector arrays operating uncooled condition. The response speed and the moderate sensitivity can be compensated by a large number of elements in 2-dimensional electronically scanned arrays which shows the best

values of noise-equivalent-temperature-difference (NETD) below 0.05 K due to achievement of less effective noise bandwidths as 100 Hz.

1.3.2 Laser Applications

After inventing of the Nd:YAG and CO_2 lasers, these were applied in materials processing in manufacturing environments. Currently all kind of lasers are used to process of variety of materials in many interesting ways. Since the electro-magnetic energy is absorbed in materials, most laser material processing has been concerned with the interactions of laser and materials. When laser beam irradiates on material surface, absorption of electromagnetic energy occurs by photon-electron interactions in solids. The laser induced material is heated by this laser energy that results in phase transition which may be hardening or annealing, melting or rapid solidification to form new phases and vaporization to remove material.

When laser induced excitation rates are slow compared to the thermalization time, then the absorbed laser energy is directly transformed into heat. Otherwise, if the excitation time is shorter than the thermalization time in the material, non-thermal and ablation mechanisms can occur. For more details, the laser-material interaction can be simplified by three steps: the initial generation of a free electron plasma followed by energy relaxation and modification of the material. The laser-excited electrons transfer their energy to the lattice, leading to a permanent material modification. In the thermal regime, melting and ablation occur after the excited

electrons redistribute energy to the lattice and the electrons and the lattice remain in equilibrium within the duration of the laser pulse. The time scale for the material to reach a common temperature is determined by the electron-phonon coupling constant. Heat diffusion from the electrons to the lattice (electon-phonon-relaxation-time) is a material property that has a typical value on the order of 1 to 10 picoseconds [18].

Depending on the laser fluence, the resulting temperature of the material may exceed the melting point and melting begins at the surface and then move inward within approximately the same timescale. At a higher fluence as energy densities around 1 J/cm^2 with pico- and femtosecond pulses, these lasers are called ultrafast lasers, the boiling point is exceeded and the gas phase will nucleate homogeneously in the superheated liquid [19]. If the rate of gas bubble formation is high in comparison to the cooling rate of the liquid, material will be explosively ejected from the surface resulting in a phase explosion, i.e., ablation. With the conventional lasers (nanosecond pulse duration), material is removed by thermal ablation wherein the material is locally heated to near the boiling temperature.

However, with ultrafast pulses, the pulse is short enough that very little energy from laser couples into the material as heat (the electron-lattice coupling can be neglected). The short pulse energy goes into exciting electrons which then causes a small section of the material to ablate, and leaves behind a very limited heat-affected zone (HAZ) typically much less than a micron, i.e., low thermal penetration depth. The material disorders non-thermally before the lattice has equilibrated with the carriers for pulses of sub-picosecond duration even below the damage threshold. The energy from laser can be deposited in a localized region through non-linear

absorption such as multiple-photon processes in the form of multi-photon ionization and avalanche ionization that lead to the formation of a plasma which is a quasi-free charge carriers in the material consisting of a mixture of electrons and ions [20].

Therefore, it will be removed resulting in extremely fine control of the position of material removal throughout the laser beam profile. And since the plasma formation rate above a threshold that depends on the material and laser parameters increases extremely strong, optical breakdown occurs in this parameter range. A high degree of precision during machining material by non-linear absorption requires that spatially localized reproducible small amounts of energy which can be introduced into the thin material. This cold ablation avoids unwanted heat transfer almost completely, thus making the ultrafast laser an extremely promising tool especially for high-precision procedures that require machining accuracy down to a few micro- and nano-meter regimes.

In recent years, precision micromachining and its improvement of process development meet customer demand to reduce the size, weight and material cost of leading-edge devices. Fast pace high-tech industries in flat panel displays for touch screens, tablets, smartphones and TVs has led to ultrafast industrial lasers that are becoming important tools for applications requiring high precision. Ultrafast lasers can achieve very high peak power usually a several giga-watt that is powerful enough for full ionization of almost any materials for high precision micro-machining. This non-linear effect of ionization including multiphoton and tunnel ionizations induces cold ablation of materials, not limited of deep UV wavelength range. It avoids unwanted heat transfer

almost completely which allows micromaching of several materials of thin, fragile and wide bandgap semiconductor.

Many industries currently use lasers for cutting fragile materials. There are various known ways to cut these materials. In conventional cutting process by lasers the separation of fragile materials relies on laser scribing and separation by mechanical force or thermal stress induced crack propagation. Nearly all current laser cutting techniques exhibit one or more shortcomings: (1) they are limited in their ability to perform a cutting of thin materials due to a large heat-affected zone associated with long pulse laser (nanosecond scale), (2) they produce a thermal stress often results in cracking of the surface near the laser illuminated region due to a shock wave and uncontrolled material removal and finally (3) they can easily cause damage to the other layer of materials by undesired laser interaction.

Even ultrafast lasers have a low throughput and unreliability in industrial environment, it has a lot of benefits which include no crack creation near ablation region, reduce process step by single-step direct-write method, high quality of cut, micro-machining of any type of material and capability of machining of hard materials. It is critical that edge cracking and residual edge stress are avoided in thin fragile substrates that is almost always break from the edge, even when stress is applied to the center. Moreover, the lack of available precision laser cutting methods has been particularly troublesome in thin materials process since unwanted direction cracking can occur. Thin layer materials cutting by ultrafast lasers produces essentially no residual stress in the material resulting in higher edge strength as well as high-quality processing in micro-machining. Ultrafast lasers also provide greater control of depth and selectivity with respect to the bottom

layer because more materials are removed as vapor which there is less thermal diffusion in the vertical direction.

1.3.3 Laser Doping

The use of laser to dope silicon semiconductor began during the 1960s. A high-efficiency solar cell through which single-junction photovoltaic cells have theoretical efficiency limits greater than 50% by laser photochemical doping [21]. To dope semiconductor, many possible methods are available. It includes ingot doping, ion implantation, alloying using impurity metals, dopant diffusion (liquid or solid phase) using gases or doped materials deposited by epitaxy. However, for building up pn-junctions is challenging on development of highly effective and robust low-cost doping techniques. Epitaxial dopant diffusion requires high temperatures and ion implantation needs a heating step to heal substrate damage and to activate the implanted dopants. Moreover, oxygen contamination in these techniques also is carefully considered [22]. Therefore, there is great interest in the further development of laser doping of semiconductor materials.

Since high temperatures are necessary for diffusion, strong optical absorption is required in a substrate. The laser energy is absorbed in semiconductor materials on a timescale of the electron-phonon scattering events which is about 10^{-13} second, starts to be redistributed into vibrational modes of the atomic system. Therefore, heating rates approaching 10^{15} K/s are achievable with femto- and pico-second pulses in the heated zone. For nano-second pulses regime, thermal energy delivered during the initial portion of the pulse can diffuse a distance during the

remainder of the pulse. Thus, the temperature profile induced is influenced by heat diffusion during in this time regime.

By using laser doping technique, concentrations orders of magnitude beyond the equilibrium solubility limit which results in a drastic increase in both the visible and infrared absorptance of silicon, increased gain and extended photoresponse in silicon-based photodetectors can be obtained. Defects such as vacancies, dislocations and micro-cracks can be generated by laser-induced heating, stresses and shock waves that may significantly enhance diffusion due to thermal diffusion and stress effects. The real concentration of vacancies can be much higher than their equilibrium concentration. Also laser-induced heating can significantly reduce the heating up and cooling down times by providing fast heating and cooling rates associated with traditional furnace processing.

Laser doping for solar cells was developed at the University of New South Wales as laser-doped selective emitter (LDSE) for improvement of cell efficiency [23]. Through laser doping, openings in the dielectric layer are created and heavily doped simultaneously as the laser beam passes in a single process step can be obtained. Therefore, it imposes localized heating on the wafer to form heavily doped selective emitters, while sparing the remaining area from high temperature processes. Local confinement of chemical and physical reactions up to several nanometer ranges can be obtained through laser doping technique. The precise depth of diffusion as well as the shape of the dopant profile can be accurately controlled by adjusting the amount of laser radiation entering the sample. This ability to fabricate ultra-shallow source and drain

junctions is critically important to the continued scaling of deep submicron in semiconductor industry.

Laser doping can be achieved by introducing the dopants as a gas, a liquid, a thin film, or by ion. Laser doping techniques can be categorized into three processing types: 1) gas immersed laser doping (GILD), 2) wet laser doping with liquids and 3) dry laser doping with solid films which is also known as laser induced melting of pre-deposited impurity doping (LIMPID). GILD technique by using a XeCl laser to simultaneously dissociate adsorbed species and drive them into the n- and p-type silicon developed for As^+ doping for a depth of 600 Å by Carey et al. [24]. In gas phase precursors, the atomic species for doping by absorption, and dissociation of, can be liberated by direct photon absorption or by vibrational energy transfer of laser radiation. The precursors can decompose upon random collision with the laser excited surface. Furthermore, annealing by laser involves heating the substrate sufficiently to re-distribute and activate the atoms, while simultaneously recrystallizing the damaged semiconductor surface. Landi et al. [25] modeled one-dimensional laser doping of silicon with arsenic by GILD technique. Their model showed that the role of multiple pulses in producing an abrupt box-like doping profile.

In gaseous dopant precursor, the effectively infinite dopant source present in the ambient atmosphere during doping enables the formation of a continuous doped surface layer in parallel with surface texturing. The vast majority of precursors used for laser doping have been specifically designed for more established thin film technologies such as vapor- and liquid-phase epitaxy (VPE and LPE) or chemical vapor deposition (CVD).

Another laser process pioneered by the Fraunhofer, liquid chemical processing (LCP) creates a selective emitter in a manner similar to that of LDSE, in that it uses a laser to simultaneously pattern the SiNx layer while inducing localized dopant diffusion with different delivery mechanism for the phosphorous-containing liquid rather than being applied to the entire wafer surface. The liquid is directed at the wafer in the form of a jet that also serves as a light guide to deliver the laser beam. They presented a theoretical consideration to be able to simulate laser heating, phase changes, evaporation and dopant diffusion for pulse lengths down to a few nanoseconds. Comprehensive modeling of laser doping has been performed in case of liquid-phase diffusion by Fogarassy et al. [26]. The model shows that the agreement for gradual increase in doped depth with the higher laser flunces as expected by the increased melting depth. Good agreed models and experimental results obtained for a ruby laser irradiation of thin films of various dopants such as Sb, Ga, Bi and In which are deposited on silicon substrates.

Since GILD and wet laser doping tend to impose challenges associated with complexity of the laser system, costs and throughput in a production environment, the dry laser processing (LIMPID) is currently seen as the most viable option for laser doping. This enhances the cell's response to solar energy and can significantly increase overall performance.

1.3.4 Silicon Carbide

Silicon carbide (SiC) is an attractive wide bandgap semiconductor material for gas sensor applications in harsh environments due to high melting temperature, high thermal conductivity,

high breakdown field, and good oxidation-resistant properties at elevated temperatures. The properties of SiC are summarized in Table 1-1. Since SiC is a semiconductor material, integration of microsensors, microactuators, and integrated circuits on a common substrate using microfabrication techniques are possible.

Table 1-2: Properties of silicon carbide [27, 28].

	3C	4H	6H
Thermal conductivity (W/cm·°C)	3.6	3.7	4.9
Thermal diffusivity (cm^2/s)	1.6	1.7	2.2
Bulk modulus (GPa)	250	220	97
Dielectric constant (static)	9.72	9.66 (⊥c axis) 10.03 (//c axis)	9.66 (⊥c axis) 10.03 (//c axis)
Energy gap (eV)	2.36	3.23	3.0
Effective electron mass (in units of m_0) longitudinal m_l/m_0 transverse m_t/m_0	 0.68 0.25	 0.29 0.42	 2.0 0.42
Effective hole masses (in units of m_0)	0.6	~1	~1
Breakdown field (V/cm)	$\sim 10^6$	$3\text{-}5\times 10^6$	$3\text{-}5\times 10^6$
Mobility ($cm^2/V\cdot s$) Electrons Holes	 ≤800 ≤320	 ≤900 ≤120	 ≤400 ≤90
Diffusion coefficient (cm^2/s) Electrons Holes	 ≤20 ≤8	 ≤22 ≤3	 ≤10 ≤2
Refraction index (Infrared)	2.55	2.55 (⊥c axis) 2.59 (//c axis)	2.55 (⊥c axis) 2.59 (//c axis)

In fact, SiC showing polytypes of various stacking sequences with the same Si-C sub-unit. There are more than 170 of these polytypes known, but technologically important ones are 3C-, 4H-, and 6H-SiC (Ramsdell notation). In all main polytypes of SiC, some atoms have been observed in association with cubic (symbol C) and with hexagonal (symbol H) lattice sites. SiC is composed of carbon and silicon in a stoichiometric ratio of 1:1 in the diamond unit cell. Each atom is bonded to four atoms of the respective other element in tetrahedral configuration. The stacking sequence is shown for the three most common polytypes, 3C, 4H and 6H in Table 1-2. The basic building block of SiC is a hexagonal bilayer with alternating site occupation in which each element is exclusively positioned in one of the two upper or lower sublayers. Imagine a layer of Si atoms stacked hexagonal patterns as A position on the first layer and the next layer that can placed according to a closed packed structure will be placed on the B position or the C position. The different polytypes will be constructed by permutations of these three positions. For instance will the 6H-SiC polytype have a stacking sequence ABCACB… The number thus denotes the periodicity and the letter the resulting structure which in this case is hexagonal. The 3C-SiC polytype is the only cubic polytype and it has a stacking sequence ABCABC… or ACBACB… A common crystalline defect is the so called double positioning boundary (DPB), which is a commonly seen possible stacking sequence ABCABC and ACBACB meet. The growth of 3C-SiC on on-axis 6H-SiC substrates and the consequent evolution and control of the DPB defect has been studied in detail by Powell et al. [29].

Table 1-3: Crystallographic properties of silicon carbide [27, 28].

	3C	4H	6H
Stacking sequence viewed in the $[11\bar{2}0]$ plane	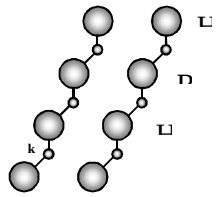	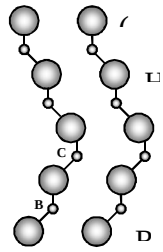	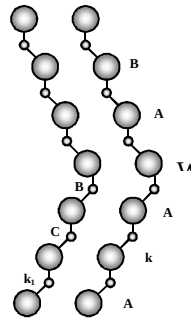
Crystal structure	Zinc blende	Hexagonal	Hexagonal
Stacking sequence	ABC	ABAC	ABCACB
Space group	F-43m	$P6_3mc$	$P6_3mc$
Atomic base	Si 0, 0, 0 C 1/4, 1/4, 1/4	Si 0, 0, 0 Si 2/3, 1/3, 1/2 C 0, 0, 3/16 C 2/3, 1/3, 11/16	Si 0, 0, 0 Si 2/3, 1/3, 1/6 Si 1/3, 2/3, 1/3 C 0, 0, 1/8 C 2/3, 1/3, 7/24 C 1/3, 2/3, 11/24
Lattice parameter (nm)	a = 0.43596 $\approx a_{hex}$ = 0.30828	a = 0.308051 c = 1.008481	a = 0.308129 c = 1.51198
Stacking fault energy	0.1 mJ/m^2	14.7 mJ/m^2	2.5-2.9 mJ/m^2
Hexagonality	0%	33%	50%

Due to the stacking sequence, it is likely that the surface energy of different sites differs. This energy would be a superposition of energies ranging far down in the crystal, which would be acting as a sort of memory. In the sequence, the A position has a different surrounding lattice than the B and C positions. We call this position the hexagonal site, *h*. It is simply characterized as the turning point of the zig zag pattern. The other two positions (B and C) are called cubic, k_1 and k_2. An impurity replacing a host atom at one of the three sites will obtain a different binding

energy depending on the site it replaces. Thus, 4H-SiC has two binding energies for the nitrogen donor, which has consequences when designing devices. 6H-SiC has three energy levels for nitrogen and 3C-SiC has only one [30].

With similar crystallographic characteristics, the structures fall into two categories referred to as alpha (α) and beta (β) silicon carbide (Thibault notation). The α category contains primarily hexagonal, rhombohedral and trigonal structures while the β category contains one cubic or zinc blende structure. The cubic or zinc blende structure, referred to as β-SiC, 3C-SiC, is expected to have the high electron mobility ($\leq$800 $cm^2/V{\cdot}s$). The beta form is also a potential substrate for important cubic structured materials such as α-GaN and diamond. The beta polytype, although having the most favorable electrical characteristics, is difficult to grow in a monocrystalline form due to its apparent metastability resulting in a solid state transformation into an alpha structure [30]. Due to the difficulty in the growth of β-SiC, most commercial efforts for producing bulk monocrystalline growth have concentrated on the more easily prepared α polytype, referred to as 4H- and 6H-SiC. In the area of epitaxial growth of thin films, though, both 3C and 6H-SiC are of considerable commercial interest with both n- and p-type conductivity possible with the addition of the appropriate impurities. Early experiments were often made on 3C-SiC, which had been grown on Si wafers, but this material is not as good as the bulk crystal growth using a seeded sublimation method now available [30].

The electronic bandgap of different polytypes varies from 2.4 to 3.3 eV. With these different bandgaps of different polytypes and their lattice parameters parallel to the hexagonal bilayers being practically equal, the development of strain free heterostructures composed from different

polytypes appears feasible. A different, yet similarly important aspect for the successful use of SiC in device production is the generation of oxide films. In particular, for metal-oxide-semiconductor field-effect-transistor (MOSFET) devices and passivation layers a low defect density is essential both in the oxide layer itself and at the SiC/SiO_2 interface [31].

Due to reduction of the number of electron-hole pairs formed from thermal activation across the bandgap, the 4H polytype is the most common for electronic devices at high temperature operation. The 3C-SiC polytype is more common for MEMS-based sensors due to its high electron mobility and ability to be epitaxially grown on Si (thus greatly decreasing the cost of wafers) [27, 28].

However, SiC has several advantages over other wide-bandgap semiconductors at the present time including commercial availability of substrates, known device processing techniques, and the ability to grow a thermal oxide for use as masks in processing, device passivation layers, and gate dielectrics. SiC device crystals have traditionally had orders of magnitude fewer crystal dislocation defects than GaN [31]. Thus, it is not surprising that more wide bandgap research aimed at high ambient temperature devices has been carried out on SiC than GaN. As a result, SiC is more advanced in some important technology areas than the III-Ns, such as better control of crystal impurities needed to realize electronic devices. Dopant impurity diffusion is practically nonexistent in the wide bandgaps for envisioned operating temperatures (< 600°C), but elements that interfere with electrical properties (such as hydrogen) can undesirably be activated at this temperature in the III-N crystals. Crystal dislocation defects present in both SiC and GaN adversely affect the I-V properties of p-n junctions, causing leakage currents larger than those

predicted [31]. Therefore, commercialization of these devices cannot be expected until the technology has matured somewhat. The high quality of the SiC material available today and the maturity of the processing technology has allowed commercialization of SiC devices to begin.

Difficult crystal growth and material quality challenges remain to be surmounted in these materials. Mass-produced single-crystal SiC wafers have been commercially available for more than a decade, while III-nitride (III-N) device crystals have mostly been grown by heteroepitaxy on foreign substrates like sapphire and SiC. Therefore, more wide bandgap research at high temperature devices focused on SiC. This includes Schottky diodes and UV photo-detectors [32, 33]. It has also permitted the demonstration of high quality prototypes of other devices, such as large-area (>1 mm^2) SiC X-ray detectors based on Schottky diodes which function in a wide range of operating temperature up to 150°C [34]. Therefore, if commercialization is to be realized in the near future, SiC is the preferred material for the development of gas sensors that can function in extreme environments.

In this study, the infrared optical photon detector based on SiC is described with uncooled condition. The detection principle and infrared response is explained, and the various devices that have been developed are described together with a number of applications in which they have been tested.

1.4 Objectives

The purpose of this research was to characterize the optical infrared detector which was fabricated in silicon carbide using laser doping technique. This dissertation consists of largely two parts. The first part is for laser doing and the second part is for characterizing performances of the doped infrared detector. The infrared detector is based on the semiconductor optics principle, i.e., an energy gap is created in a semiconductor by doping it with an appropriate dopant to ensure that the energy gap matches an emission spectral line for infrared wavelength of interest. The application of this infrared detection was applied for gas detection as well. Modeling work and experimental work for each part are included in this research. To achieve this objective following research accomplishments were attained:

Laser doping in silicon carbide

a) Development of thermal and diffusion model in order to obtain the dopant concentration profile by considering spatially-varying temperature-dependent diffusion coefficient in a diffusion model.
b) Experimental work of laser doping with the process parameters which was optimized in the model.
c) Analyze the doped sample to verify whether the incorporation of dopant into silicon carbide modifies the absorption characteristics of the as-received sample by examining the optical properties of the doped sample.

Characterization of performance as optical infrared detector

a) Modeling of optical property for doped silicon carbide which was tested of optical response with the probe beam.
b) Development of theoretical values of noise equivalent temperature difference (NETD) and detectivity.
c) Experimental test of optical response on the doped sample.
d) Obtaining experimental values of NETD and detectivity.

Gas sensor application

a) Experimental work of laser doping in silicon carbide with dopants.
b) Optical response test of the doped samples to verify the capability of gas detection.

CHAPTER 2: LASER DOPING

2.1 Introduction

Silicon carbide (SiC) has numerous polytypes and the most commonly available phases are the cubic (3C-SiC) and hexagonal (6H-SiC and 4H-SiC) crystal structures. Crystalline SiC is an attractive material for modern electronics involving high temperature, high frequency, and high power device applications due to its high thermal conductivity (4.9 W/cm·K), high melting temperature (3100 K peritectic temperature), high breakdown field (3-5 MV/cm), and very good radiation- and oxidation-resistant properties [35, 36]. However some of the thermochemical properties of SiC, such as high melting point, very good thermal and chemical stability and very low diffusion coefficient of impurities, cause the incorporation and activation of dopants in SiC by the conventional thermal diffusion process extremely difficult. Many dopant atoms occupy the interstitial positions in the lattice during the diffusion process and they must be transferred to the substitutional sites to create electrically active doped sites. The conventional solid state diffusion process, which occurs under an isothermal condition in a furnace to form diffused layers of impurities, is inappropriate for diffusion at high activation energies (1.29-2.69 eV) in SiC [36]. The laser doping technique is a nonisothermal solid state diffusion process in which the substrate is not melted and the diffusion can be carried out at much higher temperatures than in the conventional diffusion process. This nonisothermal, high temperature diffusion mechanism enhances the dopant diffusion coefficient.

Usually the dopant diffusion coefficients are very low in ion-implanted substrates. The diffusion coefficient of B in SiC was found to be 4.38×10^{-14} cm^2/s for which transient and field-enhanced diffusion of implanted B was proposed for the migration of B within 4H-SiC [37-39]. A lower limit was determined to be 7.0×10^{-12} cm^2/s for the effective diffusion coefficient of B at 1600°C. Usov et al. [40] reported very low diffusion coefficient of Al in SiC as 2.0×10^{-15} cm^2/s at 1700°C, pointed out that the structure of the implanted layer may have a strong effect on the redistribution of Al and proposed a dissociative diffusion mechanism during the high-temperature implantation. The ion implantation process causes significant lattice damage. In spite of annealing the implanted samples at extremely high temperatures (1400-1700°C) for redistributing and activating the dopants, a large fraction of the implanted ions remains at the interstitial sites, resulting in poor electrical activity. Laser doping was examined as a promising alternative technique because of its several advantages [41-46]. It can be carried out at room temperature ambient, unlike the large volume heating in furnace-based doping, by heating only the doped region to a high temperature with a laser beam. This localized heating was utilized to demonstrate doping from gas or solid precursor [47-49] and annealing of ion-implanted SiC [50].

Forming shallow junctions, particularly p+ shallow junctions, is difficult by the conventional ion implantation technique due to the lack of controlling low energy ion beams precisely. Doping techniques were developed using excimer lasers to form very shallow junctions in silicon wafers [51-53]. Silicon absorbs excimer lasers strongly in the near-surface region due to its large absorption coefficient. So the pulsed laser can heat up a very thin surface layer to high temperatures and produce a shallow doped region with solid phase dopant solubility much higher than those obtained by the conventional isothermal diffusion process.

Polytype phase transitions were observed in ion-implanted SiC crystals annealed at high temperatures [54-56]. Such phase transitions are not desirable for electronic devices. At high temperatures, most common metals or metal silicides used in modern device fabrication melt and the properties of most common dielectrics such as SiO_2 change. Laser annealing is considered to prevent the polytype phase transition since the implanted layer is heated to the annealing temperature within a very short (50 – 150 ns) laser pulse, inducing rapid heating and cooling of the layer [55].

Tian et al. [57, 58] studied the diffusion of nitrogen and aluminum in SiC using pulsed excimer and Nd:YAG lasers. They presented a diffusion model based on temperature-averaged diffusion coefficient by dividing the dopant concentration profile into two distinct regions, near-surface and far-surface regions. For these two regions, they determined the effective diffusion coefficients as 2.4×10^{-5} and 9.2×10^{-6} cm^2/s for nitrogen and 1.2×10^{-5} and 1.3×10^{-6} cm^2/s for aluminum, respectively, which are six orders of magnitude higher than the typical values for these two dopants in SiC. Bet et al. [59] examined the effects of the laser electromagnetic field and thermal stresses on the dopant diffusion during laser doping. They doped SiC with Cr and reported its effective diffusion coefficients as 4.61×10^{-10} cm^2/s at 2898 K and 6.92×10^{-12} cm^2/s at 3046 K for 6H-SiC and 4H-SiC, respectively, and demonstrated that almost all of the Cr atoms were in their electrically activated state. They also analyzed the surface roughness and crystalline quality of the laser-doped sample by atomic force microscopy and high resolution transmission electron microscopy, respectively, and demonstrated that the laser-doping process did not damage the substrate surface and crystalline order of the sample.

In this study, Ga atoms are incorporated into n-type 4H-SiC using a continuous wave (CW) Nd:YAG laser of wavelength 1064 nm and the dopant concentration profiles were measured using secondary ion mass spectrometry (SIMS). A CW laser heating model is presented to determine the temperature distribution in the SiC substrate during the laser doping process, whereas the previous studies [57-61] considered pulsed laser heating. The dopant concentration profile is determined theoretically by considering spatially-varying temperature-dependent diffusion coefficient in a diffusion model, which differs from the previous models [57-61] where the dopant profiles were divided into two regions and the temperature was considered constant in each region. Therefore the present model enables fitting the experimental dopant profile with a single theoretical curve. Comparing the SIMS data to the model predictions, the pre-exponential factor and activation energy for the diffusion of Ga are determined. The substrate was scanned with different number of laser passes to control the dopant concentration profile in order to study the effect of laser passes on the diffusion coefficient, which was not investigated in previous studies.

2.2 Experimental Procedure

An n-type 4H-SiC substrate of length, width and thickness 10, 10 and 0.375 mm, respectively, was cleaned by soaking it in H_2O_2:H_2SO_4 (1:1 by volume) solution for 15 minutes. It was then rinsed with de-ionized water and dipped into buffered oxide etchant. The clean substrate was

placed in a chamber of 1 mTorr vacuum. The experimental laser doping setup is shown in Figure 2-1.

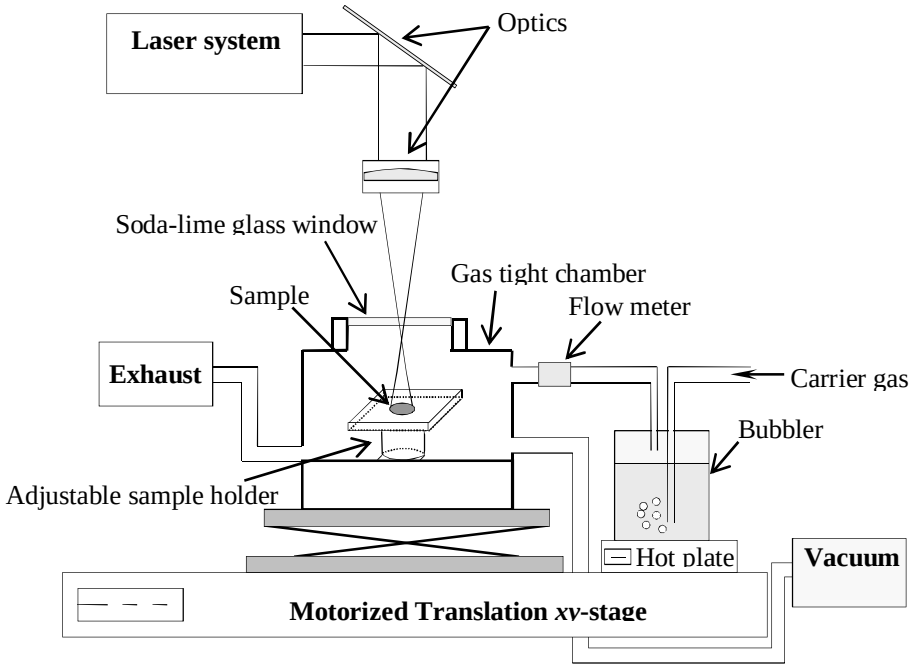

Figure 2-1: Experimental setup for laser doping of n-type 4H-SiC with Ga.

A bubbler containing triethylgallium ($(C_2H_5)_3Ga$) was used to dope the substrate. The precursor vapor was produced by placing the bubbler in a water bath of temperature 100°C and the vapor was carried to the vacuum chamber with a carrier gas Ar. The substrate was simultaneously heated with a CW Nd:YAG laser to produce Ga atoms by thermal decomposition of the precursor vapor at the laser-heated spot and to induce the diffusion of Ga atoms into the substrate. A laser beam of power 10.5 W was delivered to the substrate with a lens of focal length 150 mm

to create a laser spot of diameter 200 μm on the substrate surface. The laser beam scanning was achieved by moving the substrate at the speed of 0.8 mm/s in the *x* direction with an *x*-*y* translation stage (Figure 2-2).

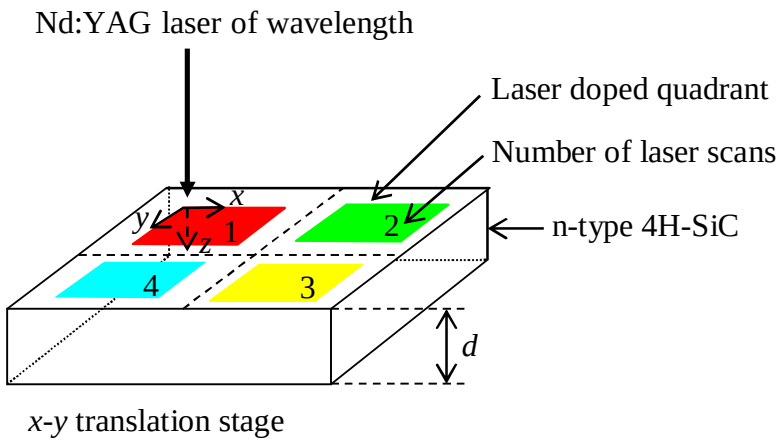

Figure 2-2: Doped quadrants of dimensions 3 mm × 3 mm each for different number of laser scans.

After scanning a distance of 3 mm, the substrate was moved in the *y* direction and the scanning was repeated in the *x* direction. This cycle was continued to produce a doped region of length 3 mm and width 3 mm in one quadrant at the top surface of the substrate. Similarly the other three quadrants were doped by varying the number of laser passes. The substrate was at room temperature at the starting moment of each scan in the *x* direction.

After the doping experiment, the sample was cleaned with a KOH (45 wt. %) solution and then rinsed with acetone, methanol and de-ionized water to carry out SIMS studies. The dopant depth and concentration distribution were measured using a PHI Adept 1010 Dynamic SIMS system with O_2^+ sources forming the primary ion beam of current 200 nA and voltage 5 kV. All measurements were performed under the following conditions, raster size 200 μm, depth resolution 1 nm, mass resolution 100 amu, mass range 0 - 340 amu, quadrupole mass analyzer, and the detection area was 5% of the raster area. With these conditions, the analyzed area is estimated to be 200 μm × 200 μm.

2.3 Mathematical Models

2.3.1 Thermal Model for Temperature Distribution

The density of phonons, i.e., the random vibrational motions of the Si, C and Ga atoms, depends on the temperature of the substrate. Thus the temperature affects the diffusion of dopant atoms in the substrate. The laser-induced temperature distribution can be estimated by solving the heat conduction equation for a given doping condition. In the present case, the optical properties of the n-type SiC substrate at the wavelength of the laser are such that the substrate reflects the incident laser beam partially and absorbs it partially as the laser beam propagates through the substrate. The absorption occurs due to the interaction between the laser beam and the free carriers of the n-type substrate, resulting in a volumetric source of thermal energy for heating the

substrate. Since the laser beam moves relative to the substrate, the heating process involves three-dimensional, transient heat conduction with advection. To simplify the thermal analysis in this study, the following one-dimensional, transient heat conduction equation is considered because most of the heat conducts in one direction along the thickness of the substrate:

$$k\frac{\partial^2 T(z,t)}{\partial z^2} + S(z) = \rho_D C_P \frac{\partial T(z,t)}{\partial t}, \tag{2-1}$$

where k, ρ_D and C_P are the thermal conductivity, density and specific heat capacity at constant pressure of the 4H-SiC substrate, respectively, and $T(z,t)$ represents the temperature of the substrate at any depth z (Figure 2-2) and time t. $S(z)$ is the volumetric heat source given by [62, 63] $S(z) = I_0\mu(1-R)e^{-\mu z}$ for a laser beam propagating in the z direction, where I_0 is the laser irradiance at the substrate surface, μ is the absorption coefficient of the substrate and R is its reflectivity. The boundary and initial conditions for Equation (2-1) are given by

$$\frac{\partial T}{\partial z} = 0 \quad \text{at } z = 0, \tag{2-2}$$

$$-k\frac{\partial T}{\partial z} = h_H(T - T_\infty) \quad \text{at } z = d, \tag{2-3}$$

$$T(z,0) = T_i \quad \text{at } t = 0, \tag{2-4}$$

where h_H is the heat transfer coefficient, T_∞ is the ambient temperature inside the vacuum chamber far away from the bottom surface of the substrate, d is the substrate thickness and T_i is its initial temperature. Defining a set of dimensionless variables as $T_1(z_1,t_1) = \dfrac{T(z,t)-T_\infty}{\left[(1-R)I_0\mu d^2\right]\dfrac{1}{k}}$, $z_1 = \dfrac{z}{d}$ and $t_1 = \dfrac{t}{\tau_t}$, where τ_t is the laser-substrate interaction time given by the ratio of the laser beam diameter to the laser scanning speed relative to the substrate, and letting $T_1(z_1,t_1) = \theta(z_1,t_1) + \dfrac{1}{(\mu_1)^2}e^{-\mu_1 z_1} - \dfrac{z_1}{\mu_1} + \dfrac{1}{\mu_1}\{1+Bi\} - \dfrac{e^{-\mu_1}}{\mu_1}\left\{\dfrac{1}{\mu_1} - Bi\right\}$ where $\mu_1 = \mu d$ and Bi is the Biot number given by $Bi = \dfrac{hd}{k}$. Equation (2-1) and the boundary and initial conditions (Equations. (2-2)-(2-4)) can be written as follows

$$\frac{\partial^2\theta(z_1,t_1)}{\partial z_1^{\,2}} = \frac{1}{Fo}\frac{\partial\theta(z_1,t_1)}{\partial t_1}, \tag{2-5}$$

where Fo is the Fourier number, $Fo = \dfrac{\alpha\tau}{d^2}$, and α is the thermal conductivity, $\alpha = \dfrac{k}{\rho_D C_P}$,

$$\frac{\partial\theta(z_1,t_1)}{\partial z_1} = 0 \quad \text{at } z_1 = 0, \tag{2-6}$$

$$-\frac{\partial\theta(z_1,t_1)}{\partial z_1} = (Bi)\theta(z_1,t_1) \quad \text{at } z_1 = 1, \tag{2-7}$$

and

$$\theta(z_1,0) = \frac{T_i - T_\infty}{I_0 \mu d^2 (1-R)\frac{1}{k}} - \frac{1}{(\mu_1)^2} e^{-\mu_1 z_1} + \frac{z_1}{\mu_1} - \frac{1}{\mu_1}\{1+Bi\} + \frac{e^{-\mu_1}}{\mu_1}\left\{\frac{1}{\mu_1} - Bi\right\}. \tag{2-8}$$

Equation (2-3) can be solved by the method of separation of variables to obtain the temperature distribution as

$$T(z,t) = T_\infty + \frac{1}{k}\{(1-R)I_0 \mu d^2\}\left[\sum_{n=1}^{\infty}\left[\frac{(T^* - A_2) f_2 - A_1 f_3 - \frac{1}{(\mu_1)^2} f_4}{f_1}\right]\cos(\lambda_n z_1) B_3 e^{-\lambda_n^2 Fot_1}\right. \\ \left. + \frac{1}{(\mu_1)^2} e^{-\mu_1 z_1} - \frac{z_1}{\mu_1} + \frac{1}{\mu_1}\{1+Bi\} - \frac{e^{-\mu_1}}{\mu_1}\left\{\frac{1}{\mu_1} - Bi\right\}\right], \tag{2-9}$$

where the eigenvalues, λ_n, are obtained by solving the transcendental equation $\lambda_n \tan(\lambda_n) = Bi$, and f_1, f_2, f_3 and f_4 are given by $f_1 = \frac{Bi + \lambda_m^2 + Bi^2}{2(\lambda_m^2 + Bi^2)}$, $f_2 = \frac{\sin(\lambda_m)}{\lambda_m}$, $f_3 = -\frac{1}{\lambda_m^2} + \frac{\cos(\lambda_m)}{\lambda_m^2}(1+Bi)$ and $f_4 = \frac{\mu_1 + e^{-\mu_1 z_1}\cos(\lambda_m z_1)(Bi - \mu_1)}{(\mu_1)^2 - \lambda_m^2}$. The temperature distribution, $T(z,t)$, is obtained from

Equation (2-9) and used in the following diffusion model to determine the temperature-dependent diffusion coefficient of Ga in SiC during laser doping.

2.3.2 Diffusion Model with Temperature-Dependent Diffusion Coefficient

Due to the localized heating capability of lasers with precise control on energy delivery, the substrate can be heated to very high temperatures for doping different regions selectively without any melting. The temperature varies along the depth of the substrate, providing a nonisothermal mechanism for the diffusion of dopant atoms. Also high temperatures represent high energy states for the random vibrational motions of the atoms, which can facilitate the migration of dopants. The dopant concentration distribution is modeled using the following one-dimensional, transient diffusion equation [64]:

$$\frac{\partial}{\partial z}\left[\left(D_0 e^{\left(\frac{Q}{k_B T(z,\tau)}\right)}\right)\frac{\partial C(z,t)}{\partial z}\right]=\frac{\partial C(z,t)}{\partial t}, \tag{2-10}$$

where D_0, Q and k_B are the pre-exponential factor, activation energy per atom and the Boltzmann constant, respectively. $D_0 e^{\left(\frac{Q}{k_B T(z,\tau)}\right)}$ is the temperature-dependent diffusion coefficient of Ga in 4H-SiC, where $T(z,\tau)$ is used instead of $T(z,t)$ because the substrate is expected to attain a quasi-steady state temperature distribution within the laser-substrate interaction time τ_t as the laser beam passes over the substrate. The boundary and initial conditions for Equation (2-10) are

$$C(0,t) = C_0 \quad \text{at } z = 0, \tag{2-11}$$

$$C(\infty,t) = 0 \quad \text{as } z \rightarrow \infty, \tag{2-12}$$

and

$$C(z,0) = C_i(z), \tag{2-13}$$

where C_0 and $C_i(z)$ are the dopant concentration at the substrate surface and the initial dopant concentration distribution in the substrate, respectively, which are obtained from the SIMS data for the doped samples. For different number of laser passes, $C_i(z)$ is given by

$$C_i(z) = 0 \quad \text{for the first pass,} \tag{2-14}$$

$$C_i(z) = C_1(z,0) \quad \text{for the second pass,} \tag{2-15}$$

$$C_i(z) = C_2(z,0) \quad \text{for the third pass,} \tag{2-16}$$

and

$$C_i(z) = C_3(z,0) \qquad \text{for the fourth pass.} \tag{2-17}$$

The Laplace transform of Equation (2-10) yields

$$D_T\big(T(z,\tau)\big)\frac{d^2\overline{C}(z,s)}{dz^2} + D_T{}'\big(T(z,\tau)\big)\frac{d\overline{C}(z,s)}{dz} - \frac{s}{D_0}\overline{C}(z,s) = \frac{-C_i(z)}{D_0}, \tag{2-18}$$

where $D_T\big(T(z,\tau)\big) = e^{\left(-\frac{Q}{k_B T(z,\tau)}\right)}$ and $D_T'\big(T(z,\tau)\big) = \frac{dD_T\big(T(z,\tau)\big)}{dz}$. Equation (2-18) can be simplified (see Appendix A) to obtain the following expression for the dopant concentration distribution.

$$C(z,t) = \frac{1}{\big(D_T\big(T(z,\tau)\big)\big)^{1/4}}\left[C_0\big(D_T\big(T(0,\tau)\big)\big)^{1/4} erfc\left(\frac{L(z)}{2\sqrt{D_0 t}}\right) + \int_0^{L(\infty)} F_1(z')\left\{\frac{\exp\left(-\frac{\big(L(z')+L(z)\big)^2}{4D_0 t}\right) - \exp\left(-\frac{\big(L(z)-L(z')\big)^2}{4D_0 t}\right)}{\sqrt{\pi t}}\right\}dz', \right.$$
$$\left. + \int_0^{L(\infty)} F_2(z') I_{G1} dz' - \int_0^{L(\infty)} F_2(z') I_{G2} dz'\right] \tag{2-19}$$

where

$$I_{G1} = \frac{2}{\sqrt{\pi}}\left(C_i(z') + \frac{C(z',\tau) - C_i(z')}{\tau}(t)\right)\left[\sqrt{t}\exp\left\{-\frac{(L(z')+L(z))^2}{4D_0 t}\right\} - \sqrt{\pi\frac{(L(z')+L(z))^2}{4D_0 t}}\,erfc\left(\sqrt{\frac{(L(z')+L(z))^2}{4D_0 t}}\right)\right]$$
$$-\frac{2}{\sqrt{\pi}}\left(\frac{C(z',\tau) - C_i(z')}{\tau}\right)\left[\frac{2\sqrt{\pi}}{3}\left\{\frac{(L(z')+L(z))^2}{4D_0}\right\}^{3/2} erfc\left(\sqrt{\frac{(L(z')+L(z))^2}{4D_0 t}}\right) + \frac{1}{2}\frac{\exp\left\{-\frac{(L(z')+L(z))^2}{4D_0 t}\right\}}{t^{3/2}}\left\{\frac{2}{3} - \frac{4}{3}\frac{(L(z')+L(z))^2}{4D_0 t}\right\}\right] \tag{2-20}$$

and

$$I_{G2} = \frac{2}{\sqrt{\pi}}\left(C_i(z') + \frac{C(z',\tau) - C_i(z')}{\tau}(t)\right)\left[\sqrt{t}\exp\left\{-\frac{(L(z')-L(z))^2}{4D_0 t}\right\} - \sqrt{\pi\frac{(L(z')-L(z))^2}{4D_0 t}}\,erfc\left(\sqrt{\frac{(L(z')-L(z))^2}{4D_0 t}}\right)\right]$$
$$-\frac{2}{\sqrt{\pi}}\left(\frac{C(z',\tau) - C_i(z')}{\tau}\right)\left[\frac{2\sqrt{\pi}}{3}\left\{\frac{(L(z')-L(z))^2}{4D_0}\right\}^{3/2} erfc\left(\sqrt{\frac{(L(z')-L(z))^2}{4D_0 t}}\right) + \frac{1}{2}\frac{\exp\left\{-\frac{(L(z')-L(z))^2}{4D_0 t}\right\}}{t^{3/2}}\left\{\frac{2}{3} - \frac{4}{3}\frac{(L(z')-L(z))^2}{4D_0 t}\right\}\right]. \tag{2-21}$$

Equation (2-19) is used to calculate the dopant concentrations at various depths by varying the values of D_0 and Q, and these two parameters are determined by reducing the error between the theoretical results and the SIMS data.

2.4 Results and Discussion

2.4.1 Temperature Distribution in SiC during Laser Doping

The temperature distribution in the substrate is calculated using Equation (2-9) for various thermophysical properties listed in Table 2-1.

Table 2-1: Properties of n-type 4H-SiC substrate with the optical properties at the wavelength of 1064 nm.

Absorption coefficient, μ (cm^{-1})	45.73
Absorptance of SiC substrate, A	0.67
Reflectance of SiC substrate, R	0.15
Heat transfer coefficient, h_H (W/cm^2·K)	5
Thermal conductivity, k (W/cm·K)	3.7
Thermal diffusivity, α (cm^2/s)	1.7
Thickness of substrate, d (μm)	375

The laser irradiance was varied to calculate the optimum temperature for laser doping by maintaining the substrate temperature below its melting temperature, which is the peritectic temperature of 3100 K for SiC, in this study. These calculations enable selecting the laser doping

parameters to prevent any thermal damage and crystalline phase transformation of the substrate. Figure 2-3 shows the temperature distribution at time $t = \tau = 0.25$ s over the entire thickness (375 μm) of the substrate.

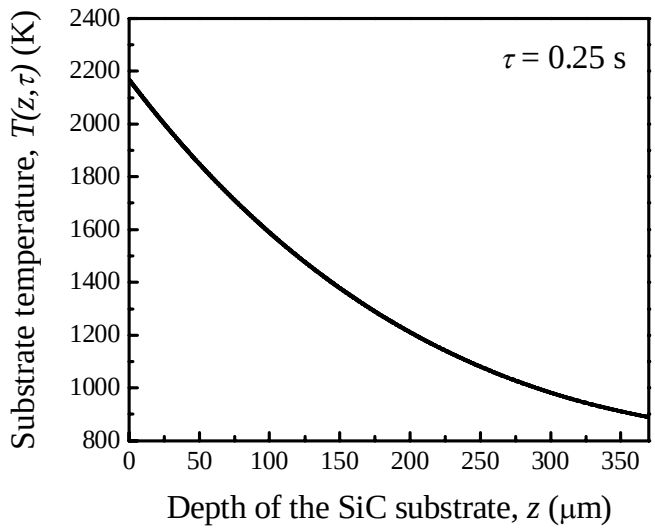

Figure 2-3: Temperature distribution along the depth of the substrate during laser doping for 4 laser passes.

The maximum temperature is 2172 K at the surface for the case of doping with 4 laser passes and it gradually decreases due to cooling through heat dissipation along the thickness. Based on these calculations, the laser parameters were selected for carrying out the doping experiments as discussed in section 2.2. The laser irradiance at the substrate surface was 334.23 kW/cm^2.

2.4.2 Current-Voltage (I-V) Characteristics of the Doped Sample

The current-voltage characteristics of the sample were measured with a Tektronix 577 *I-V* curve tracer equipped with tungsten probes. Since the parent as-received sample was an n-type 4H-SiC substrate, which was doped with a p-type dopant Ga, a p-n junction is expected to form in the sample. The *I-V* characteristics of both the sample surface and p-n junction are presented in Figures 2-4(a) and (b) respectively. The surface *I-V* characteristics are symmetric for the forward and reverse biases, indicating no p-n junction formed at the sample surface. Figure 2-4(b), on the other hand, shows the typical p-n diode characteristics with large breakdown voltage in the reverse bias, while rapid increase in current for the forward bias.

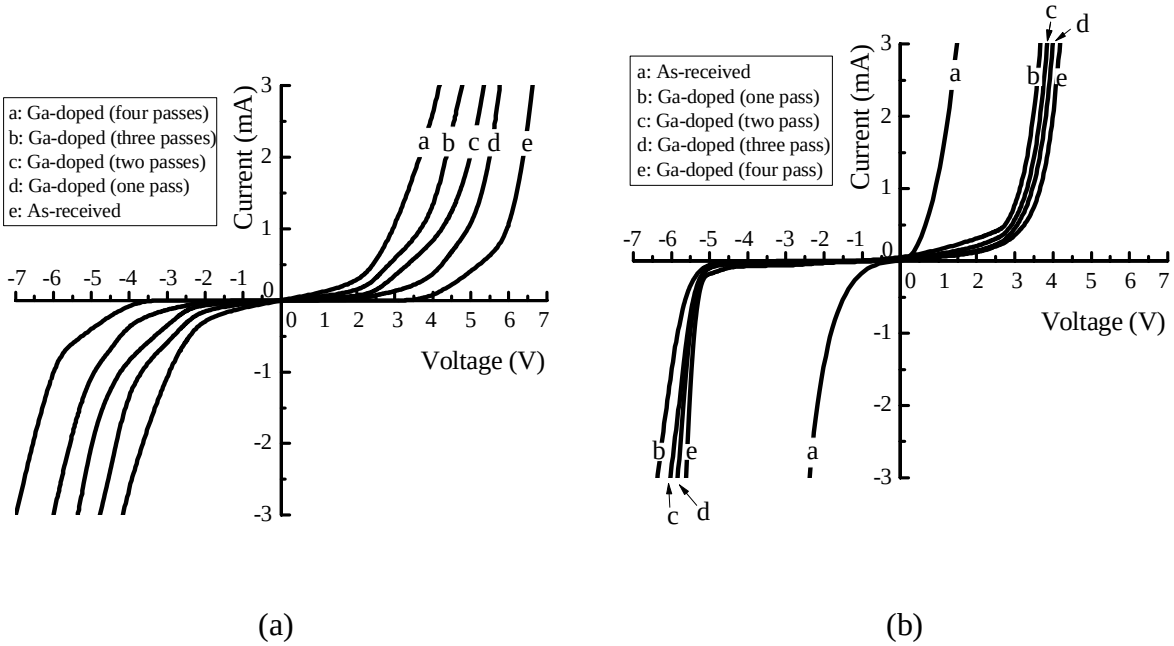

Figure 2-4: Current-voltage plots for as-received n-type 4H-SiC sample and after the sample was doped with Ga (p-type dopant) under different numbers of laser passes: (a) measured on the same surface of the sample and (b) measured across the thickness of the sample with one probe on the p-doped side and the other probe on the parent n-type side.

The surface *I-V* characteristics were measured with the probes placed 1 mm apart on the silver contacts at the surface of each sample. While the symmetric *I-V* curves are due to the measurements of the surface characteristics, the nonlinear current responses could be due to Schottky contacts between the probes and sample. In the nonlinear regime where diffusion current dominates, the curves are parallel within the scope of experimental error, indicating that all of the samples have the same resistance. In the linear regime, however, the resistances for the as-received, one-pass, two-pass, three-pass, and four-pass samples are found to be 282, 31.3, 20.8, 8.33 and 4.55 kΩ, respectively, indicating that higher dopant concentration reduces the

surface resistance. This trend could be due to the effect of the p-n junction beneath the surface with higher built-in potential at higher dopant concentrations, which may affect the flow of electrons from one probe to the other probe. Also higher dopant concentrations may affect the work function at the surface of the doped region, which can reduce the contact resistance between the sample surface and metal contact. For Figure 2-4(b), the I-V characteristics were measured across the sample thickness with one probe in contact to the p-doped side and the other probe contacting the as-received n-type side. The results in this figure indicate that the laser-doped Ga atoms were effective in forming p-n diodes of different *I-V* characteristics corresponding to different dopant concentrations. The *I-V* trend of the parent as-received sample indicates that the probes might form Schottky contacts with the sample.

2.4.3 Dopant Profiles in SiC

Typical values of the Ga dopant concentration, which are obtained from the SIMS analysis, are presented in Figure 2-5 for 4 laser passes. The original SIMS data of arbitrary units are converted to cm^{-3} using an ion-implanted n-type 4H-SiC standard, which was prepared by implanting Ga ions into the substrate with a dose of 10^{16} cm^{-2} at 150 keV.

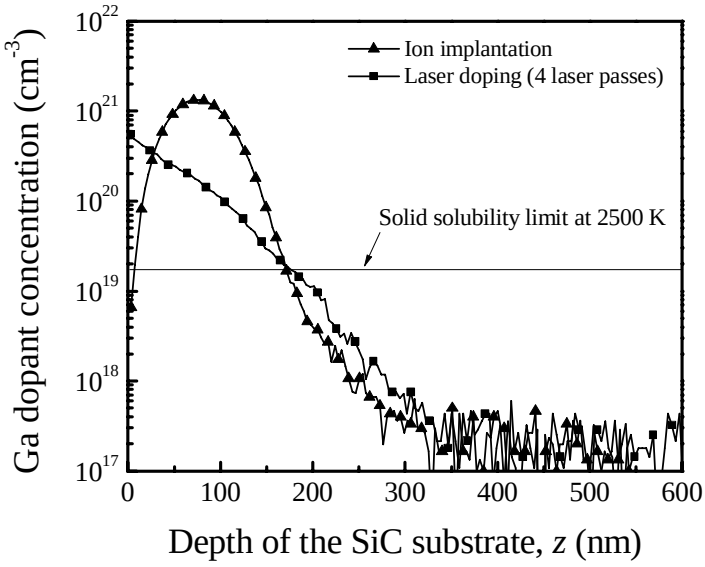

Figure 2-5: Ga dopant concentration obtained by converting the original SIMS data from the arbitrary unit to cm^{-3} using an ion-implanted n-type 4H-SiC standard.

The concentration profile of the ion-implanted sample exhibits an increasing and then decreasing trends in the near- and far-surface regions, respectively, which differ from the monotonically decreasing trend of the profile obtained by laser doping. The concentration of Ga is found to be 6.25×10^{20} cm^{-3} at the substrate surface, which exceeds its solid solubility limit (1.8×10^{19} cm^{-3}) in SiC [65].

The ability to predict and control the dopant concentration profiles is important for the design and development of semiconductor and optoelectronic devices. Equation (2-19) can be used to calculate the dopant profiles provided the temperature-dependent diffusion coefficient, particularly the values of Q and D_0, are known. These two diffusion parameters are determined

in this study by comparing the experimental dopant profiles, i.e., the SIMS data, to the theoretical profiles obtained from Equation (2-19) for different values of Q and D_0. The experimental dopant concentrations, $C_{ex}(z_i,\tau)$ for i = 1, 2, 3, ·····, N, are obtained from the SIMS data at N different points along the depth of the substrate. The theoretical dopant concentrations, $C_{th}(z_i,\tau)$ for i = 1, 2, 3, ·····, N, are calculated from Equation (2-18) by substituting the temperature, $T(z_i,\tau)$, obtained from the thermal model of Equation (2-9) and by selecting certain representative values of Q and D_0. The absolute percentage error between the experimental and theoretical results are calculated as $\varepsilon_i(Q,D_0)=\left|\frac{C_{ex}(z_i,\tau)-C_{th}(z_i,\tau)}{C_{ex}(z_i,\tau)}\right|\times 100$ for each selected depth z_i and for different values of N such as N = 10, 15, 20. From these values of $\varepsilon_i(Q,D_0)$, the largest value is selected as the maximum percentage error $\varepsilon_m(Q,D_0)$ for a given set of Q and D_0 used for calculating $\varepsilon_i(Q,D_0)$. Then another set of Q and D_0 is selected to determine $\varepsilon_m(Q,D_0)$. The maximum percentage errors are plotted in Figures 2-6(a-d) as a function of Q with D_0 as the parameter for each doped quadrant corresponding to a specific number of laser pass.

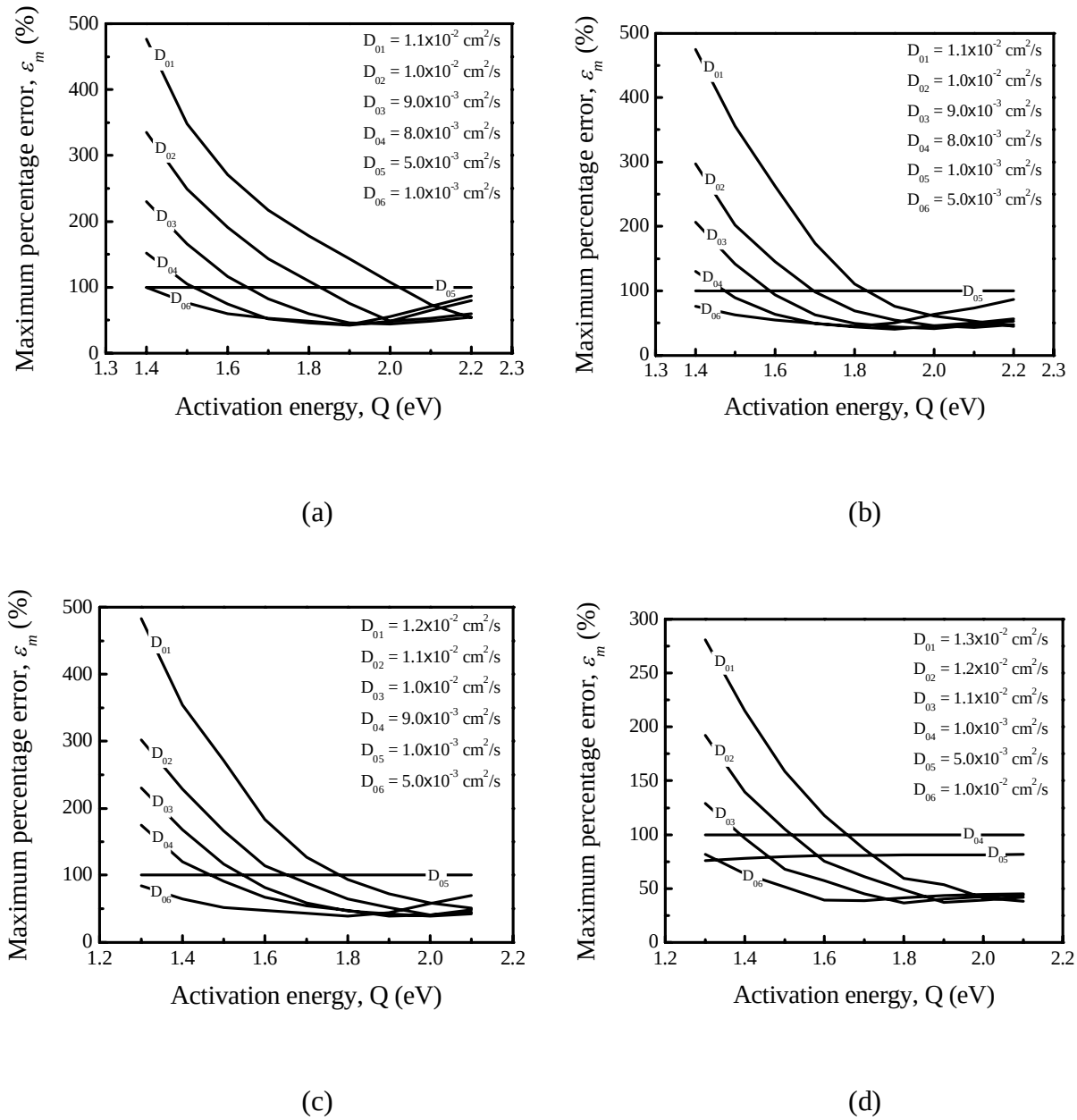

Figure 2-6: Maximum error for different number of laser passes; (a) one-pass, (b) two-pass, (c) three-pass and (d) four-pass, showing ε_m for determing the values of Q and D_0.

Good fitting can be obtained between the theoretical curves and the experimental dopant profiles by changing these two parameters. For D_0 = 7.8×10^{-3} cm^2/s, the least value of the maximum error, ε_m, is found to be 50.73% for the one-pass doped quadrant with corresponding Q = 1.9 eV as shown in Figure 2-6(a) and listed in Table 2-2.

Table 2-2: Diffusion parameters of Ga in n-type 4H-SiC during laser doping.

Number of laser passes	Activation energy Q (eV)	Pre-exponential factor D_0 (cm^2/s)	Maximum error ε_m (%)	Surface temperature $T(0,\tau)$ (K)	Diffusion coefficient D (cm^2/s)
1	1.9	7.8×10^{-3}	50.73	2168	2.99×10^{-7}
	1.91	7.83×10^{-3}	42.9	2168	2.87×10^{-7}
2	1.9	8.4×10^{-3}	48.35	2169	3.63×10^{-7}
	1.89	8.41×10^{-3}	40.65	2169	3.3×10^{-7}
3	1.9	9.4×10^{-3}	44.25	2171	3.23×10^{-7}
	1.88	9.43×10^{-3}	38.99	2171	4.25×10^{-7}
4	1.8	1.1×10^{-2}	46.98	2172	7.32×10^{-7}
	1.84	1.05×10^{-2}	36.81	2172	5.53×10^{-7}

It can be seen in Table 2-2 that the values of Q and D_0 vary in the second decimal point onwards for reducing the value of ε_m from 50.73% to 42.9%, which do not affect the value of the diffusion coefficient significantly. For the cases of two-, three- and four-pass, the diffusion parameters Q and D_0 are obtained by determining the least value of the maximum error, ε_m, from Figures 2-6(b-d), respectively, and listed in Table 2-2 with the corresponding diffusion coefficients. The surface temperature, $T(0,\tau)$, which is calculated from Equation (2-9), is slightly higher for the case of four-pass than for one-pass. The temperature depends on two optical properties of the substrate, absorption coefficient and reflectance, which are affected by the dopant concentration in the substrate. To determine the optical properties such as the reflectance, transmittance, absorbance and absorption coefficient of the doped samples at the wavelength 1064 nm, a Nd:YAG laser of this wavelength was incident on the sample at a small incident angle. The incident, reflected and transmitted powers of the laser beam were measured with a power meter, which are denoted by P_i, P_r and P_t respectively. The reflectance, transmittance and absorbance are given by P_r / P_i, P_t / P_i and $(P_i - P_r - P_t)/P_i$ respectively. The absorption coefficient (μ_a) was calculated using the relation $\mu_a = \frac{1}{d}\ln\left(\frac{P_i - P_r}{P_t}\right)$ based on the Beer-Lambert law.

Since the dopant concentration increases as the number of laser passes increases, these two properties are different for the four samples. The absorption coefficients are 45.73, 52.74, 53.01 and 53.2 cm^{-1} for the as-received, one-, two- and three-pass samples, respectively, and the corresponding reflectances are 0.15, 0.14, 0.14 and 0.13 at 1064 nm wavelength. $T(0,\tau)$ is

calculated using these optical properties assuming that the thermophysical properties of the substrate are not affected by the dopant concentration. The surface temperature and, consequently, the diffusion coefficient, increase due to the decrease in reflectance as the number of laser passes increases.

The values of Q and D_0 are listed in Table 2-2 for the maximum errors, i.e., $\varepsilon_m(Q, D_0)$ = 42.9%, 40.65%, 38.99% and 36.81% for one-, two-, three- and four-pass cases respectively. The maximum error is less for the case of four-pass than for one-pass. The activation energy, pre-exponential factor and diffusion coefficient are 1.84 eV, 1.05×10^{-2} cm^2/s and 5.53×10^{-7} cm^2/s at the substrate surface, respectively, for four-pass and the corresponding values are 1.91 eV, 7.83×10^{-3} cm^2/s and 2.87×10^{-7} cm^2/s for one-pass. The variation of diffusion coefficients is shown in Figure 2-7 as a function of the substrate temperature for different laser passes.

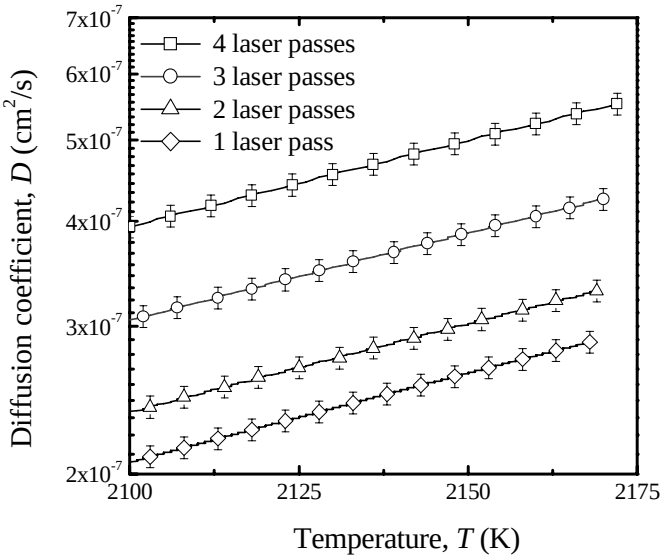

Figure 2-7: Diffusion coefficients as a function of temperature for different number of laser passes.

The diffusion coefficient has the highest value at the substrate surface and then it decreases linearly along the depth as the substrate temperature decreases, which may be due to more random vibrational motions of the Si, C and Ga atoms at high temperatures than at low temperatures. Another reason could be that the dopant atoms can diffuse by occupying the vacancies and interstitial sites created by laser irradiation and that the vacancy density decreases as the distance from the hottest point increases. It should be noted that the diffusion coefficient is higher for 4 laser passes than for 1 pass. This result may be explained by considering that a certain number of vacant and interstitial sites are created in each laser pass and a fraction of these sites is occupied by the dopant atoms during the pass. In the subsequent pass, the left-over sites from the previous pass and the newly created sites during the current pass contribute to the

migration of the dopant atoms, causing enhanced diffusion coefficient as the number of laser passes increases.

Based on the values of Q and D_0 obtained above, the theoretical Ga concentration distributions are calculated using Equation (2-18) for different laser passes and compared to the experimental concentrations in Figure 2-8.

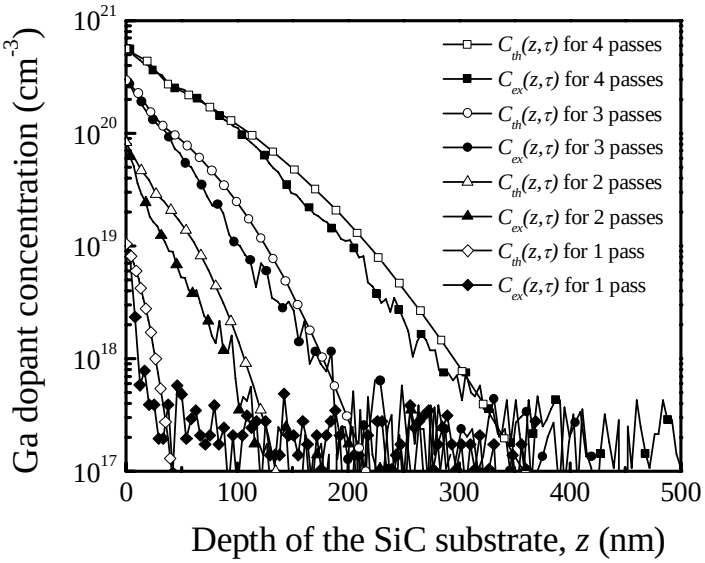

Figure 2-8: Comparison of experimental (SIMS data) and calculated Ga concentration profiles for different number of laser passes.

Although the theoretical results predict the same trend as the experimental data, the difference between the theory and experiment is small in the case of doping with 4 laser scans for which the maximum error, $\varepsilon_m(z_i,\tau)$, has the least value as indicated in Table 2.2. The surface concentrations

and the diffusion lengths of Ga are listed in Table 2.3 for four different laser passes showing that the concentrations and the lengths increase as the number of passes increases.

Table 2-3: Surface concentration and diffusion lengths of Ga in n-type 4H-SiC substrate.

Number of laser passes	Surface concentration $C(z,t)$ (cm^{-3})	Diffusion length z (nm)
1	1.15×10^{19}	42
2	1.19×10^{20}	128
3	3.22×10^{20}	210
4	6.25×10^{20}	360

The concentration of Ga is about 1000 times higher at the substrate surface than at the end of the diffusion length inside the substrate, which may be due to the following effects. The presence of a surface partially relieves the stress caused by the mismatch in the atomic size of the dopant and matrix atoms, since the atoms are surrounded by certain types of atoms (Si, C and Ga) on one side of the surface and are exposed to different atoms of the ambient medium on the other side of the surface. Also there is a stress field near the surface due to atomic reconstruction and rapid cooling inherent in laser processing. These effects enhance the impurity solubility and diffusion causing high dopant concentrations near the surface [66].

The dopant atoms dissolve substitutionally in the SiC lattice by interacting with native point defects of interstitials or vacancies [67]. The vacancy concentration can be much higher during laser heating than when the substrate is at room temperature because of thermal diffusion in the steep temperature gradient (Soret effect) at the laser-heated surface, thermal stresses due to nonisothermal heating, laser-induced shock waves, electronic excitations and random vibrational motions of the atoms. Therefore the dopant concentration is generally high in the near-surface region. The enhanced diffusion coefficient and the increase in the surface concentration of Ga indicate that excess point defects of vacancies and interstitials are produced during laser doping.

2.5 Conclusions

Gallium was incorporated into n-type 4H-SiC substrate using a CW Nd:YAG laser for different number of laser scans. The laser parameters were selected using a thermal model to incorporate dopants without melting the substrate. Particularly solid-phase diffusion of Ga was achieved below the peritectic temperature of SiC. The surface *I-V* curves show that higher dopant concentrations reduce the resistance at the sample surface, while the bulk *I-V* characteristics across the sample thickness indicate the doped samples as p-n diodes. The surface concentration and the diffusion length of Ga are 6.25×10^{20} cm^{-3} and 360 nm respectively for the case of four laser passes, which are higher than the cases of fewer laser passes. Using the experimental Ga concentration, the activation energy, pre-exponential factor and diffusion coefficient were calculated by a method of parameter fitting based on a diffusion model involving temperature-

dependent diffusion coefficient. The values of these diffusion parameters are 1.84 eV, 1.05×10^{-2} cm^2/s and 5.53×10^{-7} cm^2/s, respectively, for the case of four laser passes. The diffusion coefficient is five orders of magnitude higher than the typical diffusion coefficient of Ga in SiC, which indicates that the laser doping process enhances the dopant diffusion coefficient significantly. Comparison of experimental and calculated dopant concentration profiles shows that they exhibit similar trends along the depth of the substrate.

CHAPTER 3: MODELING OF REFLECTANCE AS A FUNCTION OF DOPANT CONCENTRATION

3.1 Introduction

The operating principle of the SiC optical photodetector is that the photons of this wavelength excite electrons from the valence band to the dopant energy level. Consequently the electron densities are modified in these two energy levels, which affect the refraction index of the semiconductor and, therefore, the reflectance of the doped region changes. Since the Ga atoms form a deep energy level in 4H-SiC, the electron density in this acceptor level is expected to be small at room temperature in the absence of MWIR irradiance. In the presence of MWIR irradiance, however, this acceptor level will be populated by electrons. Considering the electron densities in these three levels, the refraction index of the doped sample at the He-Ne laser wavelength in the presence of MWIR irradiance can be obtained by the classical multi-oscillator Lorentz model for non-absorbing dense media. This change in the reflectance, which constitutes the optical response of the detector, is probed with a helium-neon (He-Ne) laser. Both the He-Ne laser beam and the MWIR waves can undergo multiple reflections in the 4H-SiC sample, increasing the absorption of photons in the detector.

The dopant concentration is one of the most important parameters for controlling the performance of detectors because it affects the density of states and, therefore, the population of photoexcited carriers. However, it affects the dark current as well, increasing the detector noise at high dopant concentrations. The dopant concentration also affects the photon absorption

quantum efficiency, detectivity and the background-limited infrared performance temperature [68]. It has been shown that high absorption quantum efficiency corresponds to high absorption coefficient as a function of dopant concentration but such detectors also exhibit substantially high dark current. Yang et al. [69] investigated the optimal dopant concentration (10^{18} cm^{-3}) to increase the quantum efficiency and decrease the dark current of a quantum-well infrared photodetector.

3.2 Infrared Radiometry

Radiometry concerns collection of electromagnetic energy from an arbitrary extended source. In general, it is necessary to take into account the geometry of the source-detector system to calculate the signal incident on the detector. The detector intercepts a small fraction of the radiated signal among all of the emitted radiations. To compute radiation exchange between any two surfaces, it is needed to calculate the view factor which is defined as the fraction of the radiation leaving the surface of a radiation source that is intercepted by surface of the detector as shown in Figure 3-1.

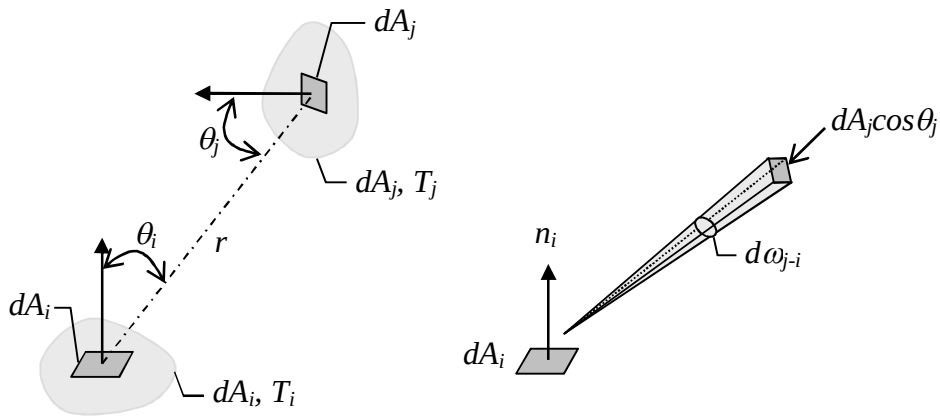

Figure 3-1: View factor associated with radiation exchange between differential surfaces of area dA_i and dA_j [70].

The subscripts i and j are substituted by s and S for the source and lens, respectively, in the analysis below.

Infrared radiations are electromagnetic waves in the wavelength range longer than the visible wavelengths, lying from 0.75 μm (1.65 eV) to 1000 μm (1.2 meV). A typical infrared radiation source is a blackbody, which is an idealized cavity with emissivity approaching unity. The radiant energy it emits at a particular wavelength is a function of the wavelength and its temperature. Planck's blackbody radiation theory provides the following formula for the spectral radiance of a blackbody at any temperature T [71]:

$$L_{\lambda,b}(\lambda,T) = \frac{C_1}{\lambda^5\left[\exp\left(\frac{C_2}{\lambda T}\right)-1\right]}, \tag{3-1}$$

which represents the amount of energy emitted per unit time per unit area of a blackbody surface per unit solid angle per unit wavelength interval $\Delta\lambda$ about the wavelength λ, i.e., $L_{\lambda,b}(\lambda, \mathrm{T})$ is in units of W/m^2·sr·μm, where the wavelength λ is in units of micrometer (μm). Here the first and second radiation constants are $C_1 = 2hc^2 = 1.191\times10^8$ W·μm^4/m^2·sr and $C_2 = hc/k_B = 1.439\times10^4$ μm·K, where h, c and k_B are the Planck constant, speed of light in vacuum and Boltzmann constant respectively. To obtain the spectral radiance in terms of photon, Equation (3-1) can be divided by hc/λ (energy per photon) $L_{q,\lambda} = L_{\lambda,b}(\lambda,T)\lambda / hc$.

Equation (3-1) can be used to determine the spectral radiance of a real body such as a stainless steel (S. S.) surface, which is given by $L_{\lambda.,s}(\lambda,T) = \varepsilon_{\lambda,s}(\lambda,T)\times L_{\lambda,b}(\lambda,T)$, where $L_{\lambda,s}(\lambda,T)$ and $\varepsilon_{\lambda,s}(\lambda,T)$ are the spectral radiance and spectral emissivity of the S. S. surface, respectively, at any temperature T. The emissivity of heavily oxidized S. S. has been reported to be 0.7 at the wavelengths 4.21 and 4.63 μm [70]. The reason for considering the MWIR wavelength 4.63 μm at this point will become clear when the optical properties of the detector are discussed in the section on results and discussion. $L_{\lambda,b}(\lambda,T)$ is plotted in Figure 3-2 as a function of wavelength to show the changes in the radiance and the dominant spectral range as the temperature increases.

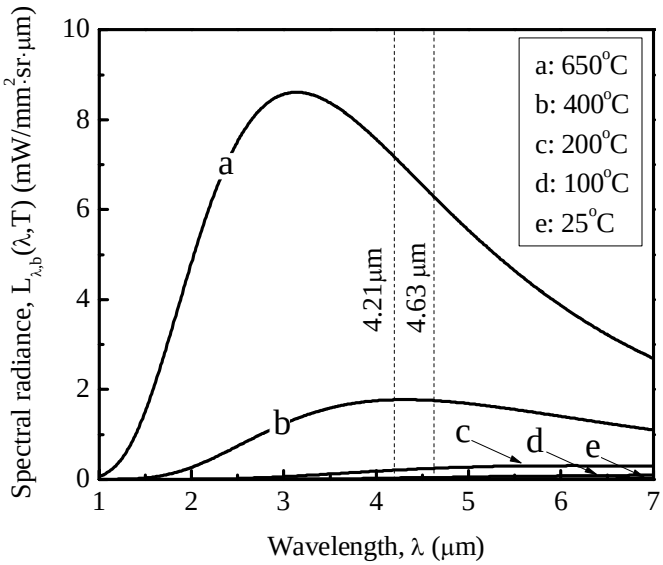

Figure 3-2: Spectral radiance of blackbody as a function of wavelength at different temperatures.

At 100°C, the spectral radiances of the S. S. surface are 6.61 and 9.43 μW/mm^2·sr·μm at 4.21 and 4.63 μm respectively. At 200°C, the spectral radiances of the S. S. surface are 45.87 and 54.96 μW/mm^2·sr·μm at 4.21 and 4.63 μm respectively. Since the results in Figure 3-2 show that the radiances of a blackbody are negligibly small at lower temperatures for these two wavelengths, the detector response has been examined in this study at higher temperatures starting at 200°C. From spectral radiance vs. wavelength plot, we see that the blackbody spectral distribution has a maximum and that the corresponding wavelength λ_{max} depends on temperature. The plot of λ_{max} versus source temperature is a hyperbola. The analytic relationship can be derived from the condition for the peak of Equation (3-1) by setting the partial derivative with respect to λ equal

to zero. In so doing, we obtain $\lambda_{max}T = C_3$, where the third radiation constant is C_3 = 2897.8 μm·K. It is known as Wien's displacement law, which the decrease in the wavelength of peak radiance as the temperature increases is quantified by the law. For example, a blackbody source at T = 120, 200 and 400°C have its maximum spectral radiance at approximately 7.37, 6.13 and 4.31 μm, respectively. According to this result, the maximum spectral radiance is displaced to shorter wavelengths with increasing temperature. The temperature of λ_{max} in MWIR ranges from 89.25-693°C. With second partial derivative of the Wien's displacement law in terms of temperature we can consider of how much the radiance changes with temperature, which is also important to the sensitivity of an infrared system. At a source temperature of T = 200 and 400°C, we have maximum contrast $\partial L_{\lambda,b}(\lambda,T)/\partial T$ occurring at wavelength of about 6.13, 5.09 and 3.58 μm from Equation (3-2), which is not the wavelength for maximum radiance.

$$\lambda_{\max} = \frac{2410\mu mK}{T} \tag{3-2}$$

At the wavelength of 4.21 μm, the maximum contrast occurring at a source temperature of 572.447 K.

The amount of energy that reaches the lens of area A_S from the source of area A_s per unit time is given by

$$q_{s\to S} = \int_{\lambda_0-\Delta\lambda_0/2}^{\lambda_0+\Delta\lambda_0/2} \int_{A_s}\int_{A_S} \varepsilon_{\lambda,s}(\lambda,T) L_{\lambda,b}(\lambda,T) \cos\theta_s \cos\theta_S dA_s \frac{dA_S}{r^2} d\lambda\,, \tag{3-3}$$

where

dA_s = Differential surface area of the source.

dA_S = Differential surface area of the source lens.

r = Radius vector joining the differential areas dA_s and dA_S.

θ_s = Angle subtended by r with the normal to the area dA_s.

θ_S = Angle subtended by r with the normal to the area dA_S.

λ_0 = Central wavelength of the detector response.

$\Delta\lambda_0$ = Full width at half maximum around λ_0.

Generally, the emissivity, $\varepsilon_{\lambda,s}(\lambda,T)$, and the blackbody radiance, $L_{\lambda,b}(\lambda,T)$, depend on the direction in which the radiation is emitted. It is assumed that the stainless steel surface is a diffuse emitter and, therefore, $\varepsilon_{\lambda,s}(\lambda,T)$ and $L_{\lambda,b}(\lambda,T)$ will be independent of direction. So the irradiance on the lens, ($I_S(T)$), can be written as follows using Equation (3-4):

$$\begin{aligned} I_S(T) &= \frac{q_{s\to S}}{A_S} \\ &= \pi\left[\frac{1}{A_S}\int_{A_s}\int_{A_S}\frac{\cos\theta_s\cos\theta_S}{\pi r^2}dA_s dA_S\right]\int_{\lambda_0-\Delta\lambda_0/2}^{\lambda_0+\Delta\lambda_0/2}\varepsilon_{\lambda,s}(\lambda,T)L_{\lambda,b}(\lambda,T)d\lambda \\ &= \pi F_{Ss}\int_{\lambda_0-\Delta\lambda_0/2}^{\lambda_0+\Delta\lambda_0/2}\varepsilon_{\lambda,s}(\lambda,T)L_{\lambda,b}(\lambda,T)d\lambda \end{aligned} \tag{3-4}$$

where F_{Ss} is the view factor as the source is viewed by the source lens and it is given by

$$F_{Ss} = \frac{1}{A_S} \int_{A_s} \int_{A_S} \frac{\cos\theta_s \cos\theta_S}{\pi r^2} dA_s dA_S \,. \tag{3-5}$$

By the reciprocity relation,

$$A_S F_{Ss} = A_s F_{sS} \,. \tag{3-6}$$

Applying Equation (3-6) into Equation (3-5), the irradiance on the source lens is given by

$$I_S(T) = \pi \frac{A_s}{A_S} F_{sS} \int_{\lambda_0 - \Delta\lambda_0/2}^{\lambda_0 + \Delta\lambda_0/2} \varepsilon_{\lambda,s}(\lambda,T) L_{\lambda,b}(\lambda,T) d\lambda \tag{3-7}$$

The absorbed irradiance on the detector (Ga-doped 4H-SiC) is given by $I_a(T) = \alpha_d \times I_S(T)$, where α_d is the absorptivity of the detector.

The view factors are tabulated in Ref. [71] for different geometries and arrangements of the source and viewing surfaces. For this study, which involves the geometry of coaxial parallel disks (radii of the disks are $\tilde{r}_i$ and $\tilde{r}_j$), the view factor is calculated using the equation shown in Figure 3-3.

Coaxial parallel disks

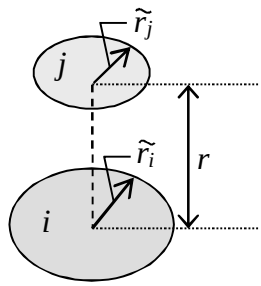

$$R_i = \tilde{r}_i / r, \quad R_j = \tilde{r}_j / r$$

$$S = 1 + \frac{1 + R_j^2}{R_i^2}$$

$$F_{ij} = \frac{1}{2}\left[S - \left\{S^2 - 4(r_j / r_i)^2\right\}^{1/2}\right]$$

Figure 3-3: View factor for three-dimensional geometry of coaxial parallel disks [71].

3.3 Infrared Optics

Optical design in the infrared is similar in principle to its in the visible range. Thus many of the design principles of visible optics are directly applicable to the infrared. However, there are some differences; for example, ordinary glass is opaque to IR beyond 3 μm, whereas germanium, which is opaque in the visible range, is transparent from 1.8 μm to 25 μm. In the infrared range a convenient way to visualize the radiant flux from the radiation source is as a series of wave front that passes through an optical system.

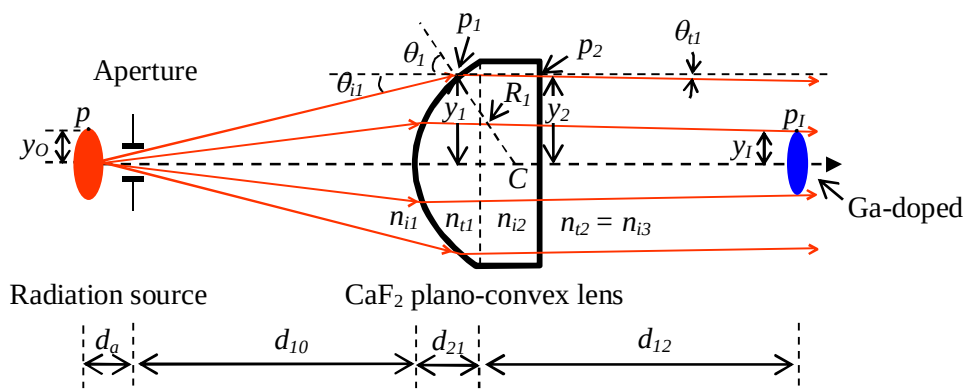

Figure 3-4: Ray geometry of the irradiance to the detector with one focusing lens.

The symbols of geometrical optics in Figure 3-4 are,

θ_{i1} = Angle on the interface of an incident beam with the optical axis.

θ_{t1} = Angle on the interface of a transmitted beam with the optical axis.

θ_1 = Supplement of apex angle of the beam with θ_{i1}.

C = Center of the lens surface curvature.

n_{i1} = Refraction index of the first incident medium.

n_{i2} = Refraction index of the second incident medium.

n_{i3} = Refraction index of the third incident medium.

n_{t1} = Refraction index of the first transmitted medium.

n_{t2} = Refraction index of the second transmitted medium.

p_1 = Maximum point of the ray on the first medium.

p_2 = Maximum point of the ray on the second medium.

p_O = Maximum point of the object.

p_I = Maximum point of the image.

R_1 = Radius of the lens sphere.

y_1 = Height of an incident point on the first interface from the optical axis.

y_2 = Height of a transmitted point on the second interface from the optical axis.

y_O = Height of the object (radiation source) from the optical axis.

y_I = Height of the image (detector) from the optical axis.

Applying Snell's law in Figure 3-4 at point p_1 yields $n_{i1}sin(\theta_{i1} + \theta_1) = n_{t1}sin(\theta_{t1} + \theta_1)$. For small $(\theta_{i1} + \theta_1)$, $sin(\theta_{i1} + \theta_1) = (\theta_{i1} + \theta_1)$. It becomes $n_{i1}(\theta_{i1} + y_1/R_1) = n_{t1}(\theta_{t1} + y_1/R_1)$ because $\theta_1 = y_1/R_1$. This expression can be rewritten as $n_{t1}\theta_{t1} = n_{i1}\theta_{i1} - ((n_{t1} - n_{i1})/R_1)y_1$ by rearranging the terms. The power of a single refracting surface is $P_1 = (n_{t1} - n_{i1})/R_1$. Therefore, the refraction equation for the first interface is [72]

$$n_{t1}\theta_{t1} = n_{i1}\theta_{i1} - P_1 y_1 . \tag{3-8}$$

The ray advances through the source lens and the height of the transmitted beam at p_2, y_{t1}, can be related to the height of the incident beam, y_{i1}, as $y_{t1} = y_{i1} + d_{21}\theta_{t1}$ on the basis that $tan(\theta_{t1}) \approx \theta_{t1}$. This is known as the transfer equation. Assuming θ_{t1} to be negligible, y_{t1} can be expressed as

$$y_{t1} = 0 + y_{i1}. \tag{3-9}$$

Equations. (3-8) and (3-9) can be rewritten in the following matrix form:

$$\begin{bmatrix} n_{t1}\theta_{t1} \\ y_{t1} \end{bmatrix} = \begin{bmatrix} 1 & -P_1 \\ 0 & 1 \end{bmatrix} \begin{bmatrix} n_{i1}\theta_{i1} \\ y_{i1} \end{bmatrix}. \tag{3-10}$$

Equation (3-10) is the refraction matrix. Similarly, we have $n_{i2}\theta_{i2} = n_{t1}\theta_t$ and $y_{i2} = d_{21}\theta_{t1} + y_{t1}$. This could be written as

$$\begin{bmatrix} n_{i2}\theta_{i2} \\ y_{i2} \end{bmatrix} = \begin{bmatrix} 1 & 0 \\ d_{21}/n_{t1} & 1 \end{bmatrix} \begin{bmatrix} n_{t1}\theta_{t1} \\ y_{t1} \end{bmatrix}. \tag{3-11}$$

Equation (3-11) is the transfer matrix. Equations. (3-10) and (3-11) yield the following refraction and transfer matrices, respectively.

$$M_R = \begin{bmatrix} 1 & -P_1 \\ 0 & 1 \end{bmatrix}, \tag{3-12}$$

$$M_T = \begin{bmatrix} 1 & 0 \\ d_{21}/n_{t1} & 1 \end{bmatrix}. \tag{3-13}$$

The optical system matrix is then defined by the product of the refraction and transfer matrices:

$$M_S = M_{R,2} M_{T,21} M_{R,1}, \tag{3-14}$$

where $M_{R,2}$ is the refraction matrix of the second interface and it can be expressed as $M_{R,2} = \begin{bmatrix} 1 & -P_2 \\ 0 & 1 \end{bmatrix}$ and $M_{T,21} = \begin{bmatrix} 1 & 0 \\ d_{21}/n_{t1} & 1 \end{bmatrix}$, $M_{R,1} = \begin{bmatrix} 1 & -P_1 \\ 0 & 1 \end{bmatrix}$. Therefore, the system matrix is written as

$$M_S = \begin{bmatrix} 1 - \dfrac{P_2 d_{21}}{n_{t1}} & -P_1 - P_2 + \dfrac{P_2 P_1 d_{21}}{n_{t1}} \\ \dfrac{d_{21}}{n_{t1}} & 1 - \dfrac{P_1 d_{21}}{n_{t1}} \end{bmatrix}. \tag{3-15}$$

The concept of image formation enters directly from the object (radiation source) to the image planes (detector area). Consequently, the first operator $M_{T,1O}$ transfers the reference point from the object. The next operator M_S then carries the ray through the source lens, and a final transfer $M_{T,12}$ bring it to the image plane. Thus the ray at the image point (p_I) is given by

$$\begin{bmatrix} n_I\theta_I \\ y_I \end{bmatrix} = \begin{bmatrix} 1 & 0 \\ d_{12}/n_I & 1 \end{bmatrix} \begin{bmatrix} 1-\dfrac{P_2 d_{21}}{n_{t1}} & -P_1 - P_2 + \dfrac{P_2 P_1 d_{21}}{n_{t1}} \\ \dfrac{d_{21}}{n_{t1}} & 1-\dfrac{P_1 d_{21}}{n_{t1}} \end{bmatrix} \begin{bmatrix} 1 & 0 \\ d_{1O}/n_O & 1 \end{bmatrix} \begin{bmatrix} n_O\theta_O \\ y_O \end{bmatrix}. \tag{3-16}$$

Equation (3-16) was derived for height of the object (y_O) which is the radius of the radiation source. y_I is height of the detector and it is 4.2 μm in the experimental setup.

3.4 Optical Property of the Detector

3.4.1 Absorption Mechanism

Three absorption mechanisms are of interest for infrared detector applications of photodetector devices: (1) bandgap or intrinsic absorption where the photon energy must be higher than the bandgap, (2) impurity level-to-band absorption, used in extrinsic infrared photodetectors, and (3) free carrier absorption, in which the photon energy is absorbed by free carriers in either conduction or valence band.

The intrinsic semiconductors have a fundamental absorption edge, which is caused by the onset of optical transitions across the fundamental bandgap of the material. This is the physical processes that occur when electrons are excited between the bands of a solid by making optical transitions. This process is called interband absorption and it gives rise to sharp lines in the

absorption and emission spectra. During the transition an electron jumps from the band at lower energy to the one above it by absorbing a photon. The Pauli exclusion principle demands that there is an electron in the initial state in the lower band and the final state in the upper band must be empty, equivalent to the creation of an electron-hole pair. It is apparent that the minimum energy is bandgap of the material (E_g) and interband transitions will not be possible unless $h\nu > E_g$. The mutual Coulomb attraction between an electron in the conduction band a hole in the valence band, which is called exicitons, is negligibly small in this direct semiconductors (e.g., free excitons in silicon and germanium have 14 meV and 4 meV respectively).

Extrinsic semiconductor of infrared detector is the controlled doping of semiconductors with impurities such as donors and acceptors. Impurities added to a semiconductor can usually be categorized as “donors” or “acceptors”. Donors are atoms that have one extra valence electron compared to the atoms in the surrounding lattice. The extra electron does not participate in bonding orbitals and hence is only weakly bound to the impurity by the Coulomb force. At low temperature, the electron orbits around the impurity in a way that can be modeled by the Bohr model of the atom.

The binding energy (E_b) is typically of the order of kT at room temperature so at room temperature the electron is ionized into the conduction band and is free to move around as a conduction electron. Acceptors have one valence electron less than the host material such as a group III element in Si or Ge. In this case, the acceptor provides an empty state or a “hole” where a valence electron could sit. If this hole moves away from the acceptor (i.e. if a neighboring valence electron occupies this available state), the acceptor becomes negatively

charged and the positive hole may end up being bound by Coulomb interactions, just like the donor electrons. Again, though, the binding energy is small and at room temperature, the holes may move freely around as positive charge-carriers. Because these are so weakly bound, the valence-band-acceptor and donor-conduction-band transitions are not seen at room temperature. They can, however, be observed at low temperatures, such as the example of vanence-band-to-acceptor absorption in Boron-doped Si at low temperature. These absorption resonances occur in the far infrared (here at least ~30 meV).

The impurity levels give rise to two new absorption mechanisms, in addition to any of the free carrier effects when the acceptor states are occupied. If the acceptor states are empty, then it will be possible to absorb light by exciting electrons from the valence band to the acceptor states as discussed before. The other absorption mechanism is free carrier absorption which results from the excitation of a free carrier into an available state higher in its respective band. The carrier density is the density of free electrons or holes generated by the doping process. The only difference between electrons and holes in free carriers is in the effective mass that is used. The presence of free carriers leads to the absorption of light which is called free carrier absorption and can be observed below the fundamental absorption edge at the bandgap where the semiconductor would normally be transparent.

Optical transitions can take place in which an electron is promoted from an occupied state below the Fermi energy level (E_F) in the light hole (lh) band to an empty one in the heavy hole (hh) band above E_F. It is known as intervalence band absorption in p-type semiconductors. Other intervalence band transitions are possible in which an electron is promoted from the split-off (SO)

band to either the lh or hh band, which is denoted as the energy *E* of the holes in the different bands against the hole wave vector *k*.

3.4.2 Reflectance of the SiC Detector at He-Ne Laser Wavelength

Both the He-Ne laser beam and the MWIR waves can undergo multiple reflections in the 4H-SiC sample, increasing the absorption of photons in the detector. This will improve the quantum efficiency and, therefore, the detector response. The undoped as-received sample offers two air–SiC interfaces at the top and bottom surfaces of the sample as shown in Figure 3-5(a). On the other hand, the Ga-doped sample has three interfaces between the air and doped region, doped region and silicon carbide, and silicon carbide and air as shown in Figure 3-5(b).

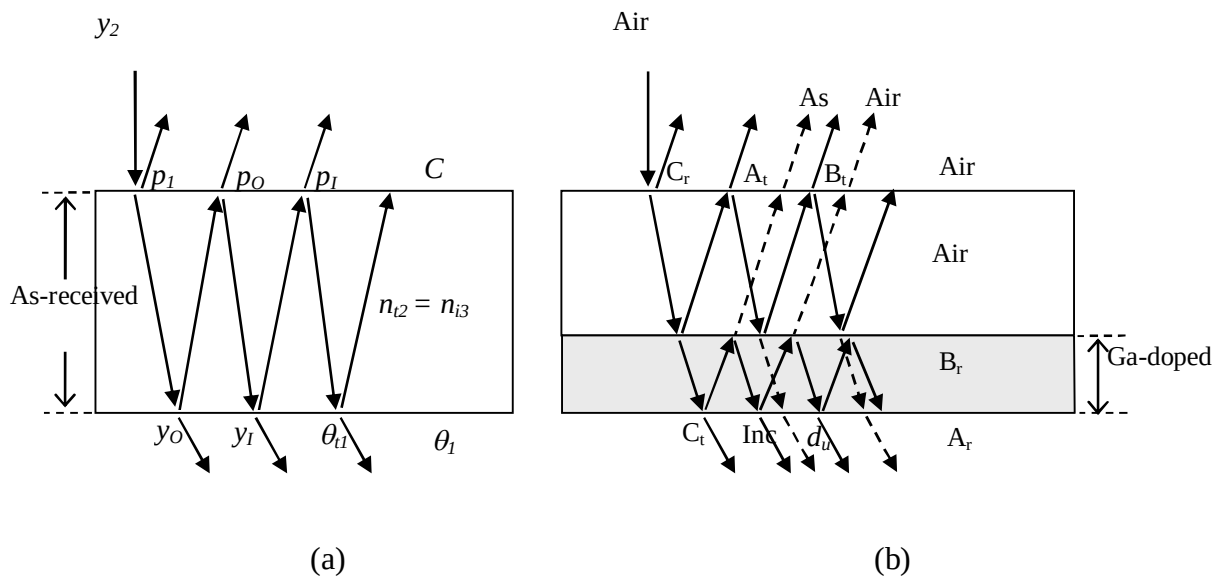

Figure 3-5: Multiple reflection in (a) as-received and (b) as-received and Ga-doped 4H-SiC layers.

When the He-Ne beam is incident on the top surface of the as-received 4H-SiC sample, a fraction of this beam is reflected, absorbed and transmitted in the sample. These fragmented beams undergo further reflection and transmission at the bottom surface of the sample. Summing powers of all the rays at various points on the top (reflectance) surface such as A_r, B_r and C_r and on the bottom (transmittance) surface such as A_t, B_t and C_t in Figure 3-5(a), the reflectance ($\rho_{u,j}$) and transmittance ($\tau_{u,j}$) of the undoped sample can be written as follows for j-th wavelength [73]:

$$\rho_{u,j} = R_{as,j} + \frac{R_{as,j}(1-R_{as,j})^2 e^{-2\mu_{u,j}d_u}}{1-R_{as,j}{}^2 e^{-2\mu_{u,j}d_u}}, \tag{3-17}$$

$$\tau_{u,j} = \frac{(1-R_{as,j})^2 e^{-\mu_{u,j} d_u}}{1-R_{as,j}{}^2 e^{-2\mu_{u,j} d_u}}, \tag{3-18}$$

where the subscripts $j = l$ and $j = \lambda$ represent the optical properties for the He-Ne laser and MWIR wavelengths respectively. For example, $\rho_{as,l}$ and $\tau_{as,l}$ would be the reflectivity and transmissivity at the interface of air and silicon carbide based on Fresnel formula, respectively, and $\mu_{u,l}$ is the absorption coefficient of the undoped sample for the He-Ne laser wavelength. d_u is the thickness of the as-received undoped sample and it is d_u = 0.375 mm.

In the case of the doped sample, the interface between the doped region and silicon carbide, which is embedded in the sample as shown in Figure 3-5(b), will cause additional reflection and transmission of the beam. Summing the powers of the first reflected and transmitted beams at A_r, B_r and C_r and at A_t, B_t, C_t, and the second reflected and transmitted beams at $A_r^{'}$, $B_r^{'}$ and $C_r^{'}$ and at $A_t^{'}$, $B_t^{'}$ and $C_t^{'}$, respectively, the reflectance ($\rho_{d,j}$) and transmittance ($\tau_{d,j}$) of the doped sample can be written as follows for j-th wavelength [73]:

$$\begin{aligned}\rho_d &= R_{au} + R_{du}(1-R_{au})^2 e^{-2\mu_u d_u} + \frac{R_{du}^2 R_{au}(1-R_{au})^2 e^{-4\mu_u d_u}}{1-R_{du}R_{au}e^{-2\mu_u d_u}} \\ &\quad + (1-R_{au})^2(1-R_{du})^2 R_{du} e^{-2\mu_u d_u} e^{-2\mu_d d_d} + \frac{(1-R_{au})^2(1-R_{du})^2 R_{au} R_{ad} R_{du} e^{-4\mu_u d_u} e^{-2\mu_d d_d}}{1-R_{au}R_{du}e^{-2\mu_u d_u}}\end{aligned} \tag{3-19}$$

$$\tau_d = (1-R_{au})(1-R_{ad})(1-R_{du})^3 R_{au} R_{ad} e^{-3\mu_u d_u} e^{-3\mu_d d_d} + \frac{(1-R_{au})(1-R_{ad})(1-R_{ad}) e^{-\mu_u d_u} e^{-\mu_d d_d}}{1-R_{ad} R_{du} e^{-2\mu_d d_d}}$$
$$+ \frac{(1-R_{au})(1-R_{ad})(1-R_{du})^3 R_{au} R_{ad} R_{du} e^{-3\mu_u d_u} e^{-5\mu_d d_d}}{1-R_{ad}{}^2 R_{du} e^{-2\mu_d d_d}} \tag{3-20}$$

where ρ_d is the reflectance of the doped sample at the He-Ne laser wavelength in the presence of MWIR irradiance on the sample. The subscript *ad* in the reflectivity term represents the interface between the air and doped region, and *du* the interface between the doped region and undoped silicon carbide. R_{au}, R_{du} and R_{ad} are the reflectivities at the interfaces between the air and undoped region, the doped and undoped regions, and the air and doped region, respectively. The absorption coefficients and thicknesses of the doped and undoped regions are denoted by μ_d and μ_u, and d_d and d_u, respectively.

Equation (3-19) is used to calculate the reflectance of the SiC detector at the He-Ne laser wavelength in the presence of MWIR irradiance. It is also used to determine the refraction and absorption indices of the Ga-doped region at the MWIR wavelength. The thickness of the doped region was taken to be the depth up to which the Ga atoms diffuse in the 4H-SiC substrate during the doping experiment, which was found to be 360 nm from the SIMS data for the sample doped with 4 laser-passes. The reflectivities R_{ad} and R_{du} can be determined from the Fresnel equation for normal incidence as follows:

$$R_{ad} = \frac{(n_d - 1)^2 + (\kappa_d)^2}{(n_d + 1)^2 + (\kappa_d)^2} \tag{3-21}$$

$$R_{du} = \frac{(n_d - n_u)^2 + (\kappa_d - \kappa_u)^2}{(n_d + n_u)^2 + (\kappa_d + \kappa_u)^2}, \tag{3-22}$$

where n_d and κ_d are the refraction and absorption indices of the doped sample at the He-Ne laser wavelength in the presence of MWIR irradiance on the sample respectively. Similarly n_u and κ_u are the refraction and absorption indices of the undoped sample at the He-Ne laser wavelength in the presence of MWIR irradiance respectively. Since the absorption indices of the doped and undoped samples are negligibly small at the He-Ne laser wavelength and the changes in the refraction index of the undoped sample in the presence of MWIR irradiance are also negligibly small [31], only the refraction index of the doped sample will be considered to examine the reflectance change of the detector at the probe beam wavelength.

The electron densities in the conduction and valence bands and in the dopant energy level affect the refraction index. Since the Ga atoms form a deep energy level in 4H-SiC, the electron density in this acceptor level is expected to be small at room temperature in the absence of MWIR irradiance. In the presence of MWIR irradiance, however, this acceptor level will be populated by electrons. Considering the electron densities in these three levels, the refraction index of the doped sample at the He-Ne laser wavelength in the presence of MWIR irradiance (n_d) can be obtained by the classical multi-oscillator Lorentz model for non-absorbing dense media, which yields the following dispersion equation [72]:

$$\frac{n_d^{\,2}(\omega)-1}{n_d^{\,2}(\omega)+2}=\frac{e^2}{3\varepsilon_0 m_e}\sum_{i=1}^{3}\frac{N_{e,i}}{\omega_{0i}^{\,2}-\omega^2}, \tag{3-23}$$

where ε_0 is the permittivity of free space and m_e is the mass of an electron. ω_{0i} is the resonant frequency of the electrons in the i-th energy level in the presence of MWIR irradiance and ω is the angular frequency of the He-Ne laser. $N_{e,i}$ is the electron density corresponding to the resonant frequency ω_{0i} [74], which represents the contributing number of electrons per unit volume in the conduction and valence bands and in the Ga dopant energy levels for i = 1, 2 and 3, respectively, in the presence of MWIR irradiance. So $N_{e,2}$ can be expressed as $N_{e,2}=N_{e,V}-N_{e,3}$, where $N_{e,V}$ is the initial free electron density in the valence band. $N_{e,V}$ is given by [75] $N_{e,V}=\frac{N_d-N_a}{2}+\sqrt{\left(\frac{N_d-N_a}{2}\right)^2+n_i^{\,2}}$, where N_d and N_a are the donor and acceptor concentrations, respectively, and n_i is the intrinsic electron concentration in a p-type semiconductor. This expression yields the free electron density for compensated semiconductor assuming that all donors and acceptors are ionized. $N_{e,1}$, which is the free electron density in the conduction band, can be written as [75] $N_{e,1}=\left(\frac{N_d-N_a}{2N_a}\right)N_C\exp\left(-\frac{E_g}{k_BT}\right)$, where N_C is the effective density of states in the conduction band, which is written as $N_C=2\left(\frac{2\pi m_e k_B T}{h^2}\right)^{3/2}$, and E_g, k_B and h are the energy bandgap of the semiconductor, and the Boltzmann and Planck constants respectively.

In the presence of MWIR irradiance, some of the electrons will jump from the valence band to the dopant level, which will change the electron densities in these two levels. The electron density, $N_{e,3}$, in the dopant energy level due to the MWIR irradiance can be obtained by noting that $N_{e,3} = \tilde{N}_e / A_d d_d$, where the number of photoexcited electrons is $\tilde{N}_e = \eta_e \tilde{N}_p$ based on the definition of external quantum efficiency, and $\tilde{N}_p = I_p A_d t_e$. Here $\tilde{N}_p$ is the number of MWIR photons incident on the SiC detector, η_e is the external quantum efficiency, $A_d d_d$ is the volume of the He-Ne probe beam inside the SiC detector, I_p is the photon flux incident on the detector surface from the MWIR source and t_e is taken as the time to reach the equilibrium population of electrons in the dopant energy level during the MWIR irradiance. I_p is related to the absorbed irradiance $I_a(T)$ at a given radiation source temperature T by the expression $I_p = \frac{\lambda}{hc}\frac{I_a(T)}{\alpha}$, where c is the speed of light in vacuum and α is the absorbance of the doped sample based on multiple reflections at the MWIR wavelength (λ). Therefore, $N_{e,3}$ can be expressed as

$$N_{e,3} = \frac{\eta_e}{d_d}\frac{\lambda}{hc}\frac{I_a(T)}{\alpha} t_e . \tag{3-24}$$

The equilibrium electron population time, t_e, can be related to the acceptor concentration, N_a, by noting that more holes are produced in the acceptor level as the acceptor concentration increases and that longer time would be required for a given absorbed photon flux to fill up the holes as the

number of holes increases. So $t_e \propto N_a$, i.e., $t_e = KN_a$, where K is the proportionality constant. Now Equation (3-24) can be written as

$$N_{e,3} = \frac{\eta_e}{d_d} \frac{\lambda}{hc} \frac{I_a(T)}{\alpha} KN_a, \tag{3-25}$$

In Equation (3-25), $\eta_e K / d_d$ can be identified as the Einstein transition probability for the transition of electrons from a lower energy level to a higher energy level [76]. Substituting Equations (3-22), (3-23) and (3-25) into Equation (3-19), the reflectance can be shown to vary with the dopant concentration.

3.5 Effect of Dopant Concentration on the Low Signal Detectibility of the Doped Samples

Usually the overall quantum efficiency determines the maximum achievable device sensitivity. Large absorption coefficient enables high quantum efficiency and the control of dopant concentration improves the quantum efficiency. The internal quantum efficiency (ratio of the number of photoexcited electrons to the number of MWIR photons entering into the detector) and the external quantum efficiency (ratio of the number of photoexcited electrons to the number of MWIR photons incident on the detector), which depend on the optical properties of the detector, are found to increase with increasing dopant concentration as listed in Table 3-1.

Table 3-1: Optical properties of as-received n-type 4H-SiC and Ga-doped samples with different numbers of laser scans at the MWIR wavelength 4.21 μm.

Number of laser passes	Doped layer thickness, d (nm)	Average dopant concentration (atoms/cm^3)	Absor-bance	Reflec-tance	Transmi-ttance	Absorption index, κ	Absorption coefficient, μ (mm^{-1})	Quantum efficiency (%)	
								η_e	η_i
As-received	-	-	0.12	0.41	0.47	1.21×10^{-4}	0.36	-	-
1	42	3.97×10^{17}	0.25	0.33	0.42	4.17×10^{-4}	1.24	17.3	17.5
2	128	4.97×10^{18}	0.32	0.32	0.36	5.36×10^{-4}	1.6	17.8	18.0
3	210	3.03×10^{19}	0.39	0.30	0.31	7.24×10^{-4}	2.16	18.5	18.9
4	360	5.25×10^{19}	0.45	0.28	0.28	8.59×10^{-4}	2.56	19.9	20.4

To determine the internal quantum efficiency in the Ga doped regions, the expression given by Dhar [77], which is applicable to multiple reflections in a single medium, is modified in this study to include multiple reflections of the MWIR radiations in the doped and undoped regions. The resulting expression is

$$\eta_i = \left\{ \left(1 + R_{ad} R_{du} e^{-2\mu_d d_d}\right)\left(1 + R_{du} e^{-\mu_d d_d}\right)\left(\frac{1 - e^{-\mu_d d_d}}{1 - R_{ad} R_{du} e^{-2\mu_d d_d}}\right)\right\} . \\ \times \left[\left(1 - R_{ad}\right) + \left\{R_{au}\left(1 - R_{ad}\right)\left(1 - R_{du}\right)^2 e^{-\mu_u d_u} e^{-2\mu_d d_d}\right\}\right] \tag{3-26}$$

The first and second terms within the square brackets in Equation (3-26) are due to the multiple reflections at MWIR radiation in the doped and undoped regions, respectively. The reflectance and transmittance data, which are obtained from the spectroscopic results in Figure 3-6, are substituted into Equation (3-21) and Equations (3-22) and (3-23) are applied to Equation (3-19) for determining the refraction and absorption indices as listed in Table 3-1.

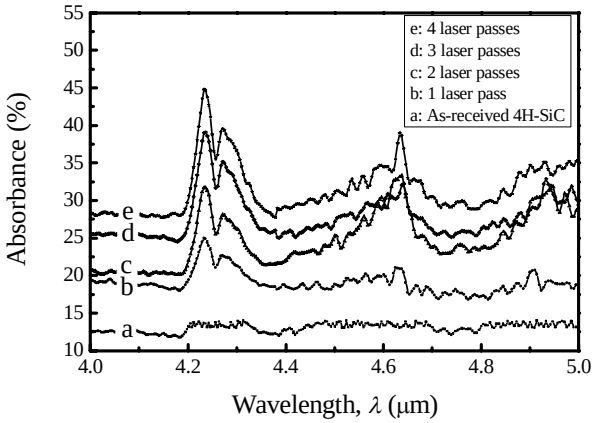

(a)

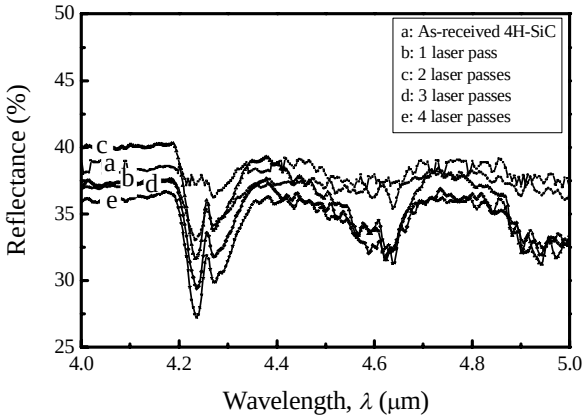

(b)

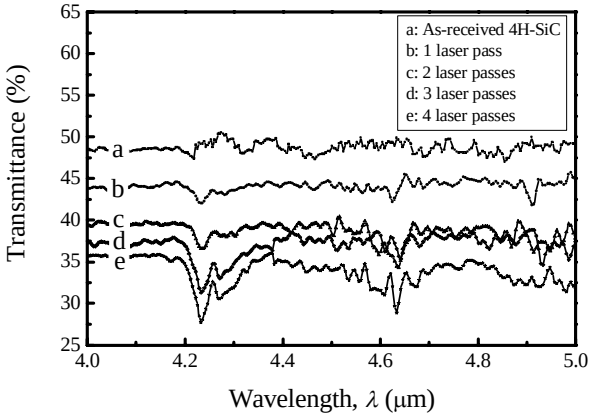

(c)

Figure 3-6: Spectroscopic data showing the optical properties of as-received n-type 4H-SiC and Ga-doped samples with different numbers of laser scans: (a) absorbance, (b) reflectance, and (c) transmittance in the wavelength range 4-5 μm.

This table also lists other parameters required in Equation (3-26) to determine η_i. The four-pass Ga-doped sample exhibits the highest internal quantum efficiency of 20.4% among the samples considered in this study, while without consideration of the right term the η_i is 16.8%. Several imaging device parameters can be optimized for high sensitivity. These include quantum efficiency, charge-transfer efficiency (moving the charge from the pixel to the output port without loss or added spurious charge), and the noise to read out this charge. The purpose is to convert all or most of the photons, which incident on the device, to photoexcited electrons and then to read out these photoelectrons without losing any and without adding any read-out noise [78].

For infrared imaging systems, which detect the thermal radiation from objects in the field of view, an important measure of performance is its ability to detect small changes in the temperature of the radiation source. To determine the minimum temperature of the radiation source for which the SiC detector (doped sample) produces a detectable optical signal, the resolution of measuring the reflected He-Ne laser power by a silicon-based power meter was examined for a given set of radiation collection optics. Two plano-convex lenses were placed between the source and the SiC detector as shown in Figure 3-7 and the power meter was operated in the sub-nanowatt (0.63 nW) resolution scale.

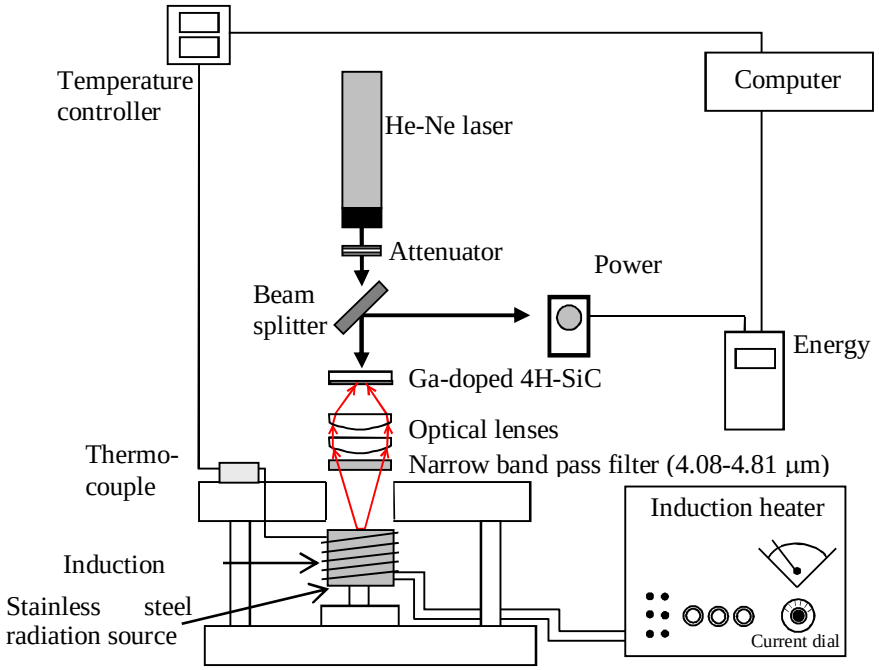

Figure 3-7: Experimental setup for testing the optical response of the as-received and Ga-doped samples at the MWIR wavelengths 4.21 and 4.63 μm.

Figures 3-8(a) and (b) show the total radiance of the source in 4.21 and 4.63 μm bands and the absorbed irradiance (I_a) in the SiC detector for detectable response with one-, two-, three- and four-pass samples as a function of the source temperature. At low powers of the reflected He-Ne beam, the power meter exhibited an error of 0.3% as shown in Figure 3-8(b).

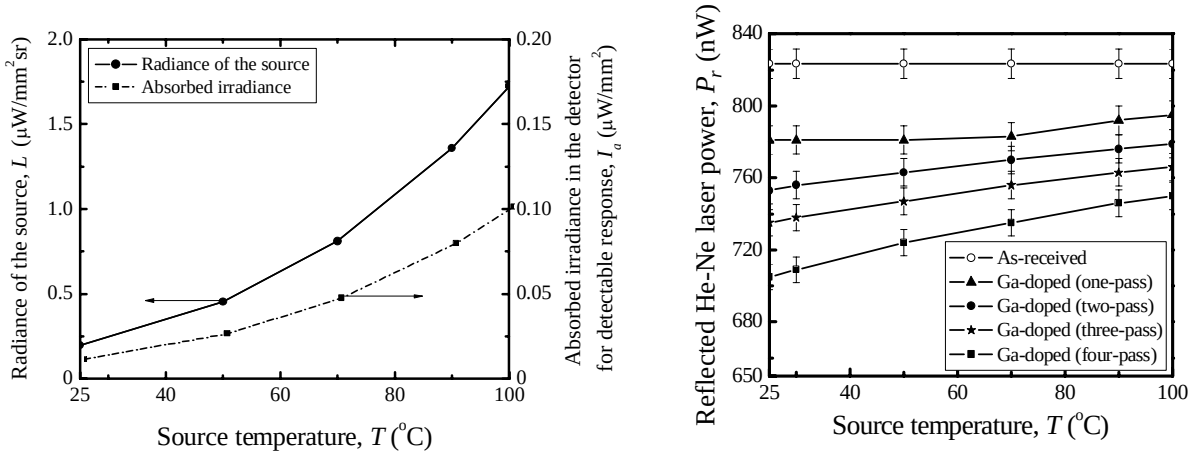

(a) (b)

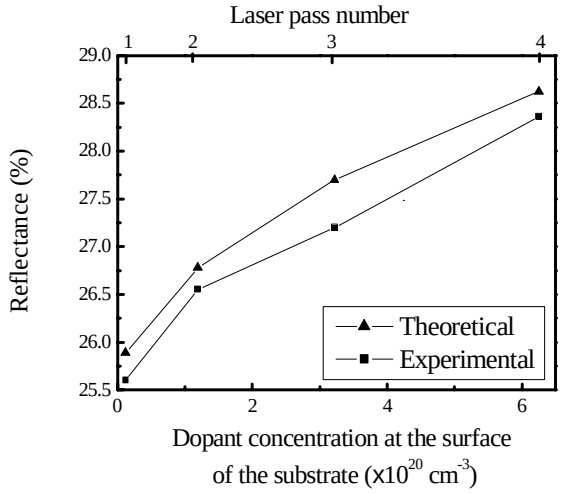

(c)

Figure 3-8: Effects of the source temperature and the dopant concentration on the MWIR detectibility with the SiC detector being at room temperature (25°C): (a) total radiance in the wavelength bands ranging from 4.2 to 4.29 μm around the peak wavelength 4.21 μm and from 4.54 to 4.66 μm around the peak wavelength 4.63 μm in the MWIR emission spectrum of the source, and absorbed irradiance in the doped samples with two CaF_2 lenses, (b) effects of the dopant concentration on the change in the reflected power of the He-Ne laser, showing that high dopant concentration (as in the case of four-pass sample) is more sensitive for detecting

MWIR photons emitted by a source maintained at room temperature, and (c) comparison of the theoretical and experimental reflectances at the He-Ne laser wavelength in the presence of the MWIR irradiance.

The dopant concentration also affects the capability of the SiC detector to detect radiations from a source that is at room temperature (25°C). It can be seen in Figure 3-8(b) that the detector response begins at the source temperature 70°C for the one-pass sample with dopant concentration 1.15×10^{19} cm^{-3}, while a detectable signal is obtained when the source is at room temperature for the two-pass sample with dopant concentration 1.19×10^{20} cm^{-3}. The change in the reflected power of the He-Ne beam increases further as the dopant concentration increases in the three- and four-pass samples. These results indicate that although the SiC MWIR detector can operate at room temperature, the dopant concentration is important in detecting objects that are at room temperature. Its overall detection capability depends on the characteristics of various subsystems such as the radiation collection optics, resolution of the He-Ne laser power meter, stability of the He-Ne laser output power and dopant concentration.

The effect of the dopant concentration on the reflectance of the SiC detector at the He-Ne laser wavelength was investigated theoretically using Equations. (3-19) and (3-25). Considering multiple reflections of the MWIR radiation in the doped region of thickness d_d = 360 nm for the four-pass sample, its external quantum efficiency (η_e) and absorbance at the MWIR wavelength are found to be 19.9% and 45% respectively. For this sample, the dopant concentration N_a = 6.25×10^{20} cm^{-3} and the absorbed irradiance is I_a = 1.1 nW/mm^2 when the radiation source is at room temperature (25°C). Considering ω_{0i} = 5.09×10^{13}, 2.9×10^{13}, 4.47×10^{14} Hz for i = 1, 2 and 3

and t_e = 0.6 μs since strong absorption occurs at the resonance frequency [79, 80], the theoretical reflectances are determined as 25.9%, 26.8%, 27.7%, and 28.7% for the one-, two-, three- and four-pass samples respectively. These results are compared with experimental data in Figure 3-8(c), showing good agreement in the trends between theory and experiment.

CHAPTER 4: THEORETICAL APPROACH OF FIGURES OF MERIT

4.1 Introduction

It is essential to characterize and compare performance of different types of IR detectors. Figures of merit are used to compare the measured performance of one detector against the measured performance of other detectors to perform a given task. Basic parameters on figure of merit when evaluating the performance of various IR detectors are 1) response time, 2) responsivity, 3) noise equivalent power (*NEP*), 4) normalized detectivity, D^*, 5) noise equivalent temperature difference (*NETD*), and 6) minimum resolvable temperature difference (*MRTD*). The definitions of these parameters are their fundamental limits in the uncooled thermal IR detectors. Moreover, these parameters can be predicted with theoretical calculation. In this chapter, the theoretical figures of merit are discussed and the parameters will be compared with the experimental results in the next two chapters as well.

4.2 Theoretical Detectivity

The specific detectivity of the system has been determined using the data (manufacturer's specifications) for the Si detector and theoretical result for SiC as discussed in this chapter since

experimental data are not available for SiC. The specific detectivity of the system (D^*_{Th}) can be related to the specific detectivities of the component detector of the system by noting that [81]

$$D^*_{Th} = \frac{\sqrt{A_d}}{NEP_{System}}, \tag{4-1}$$

where the noise equivalent power of the system (NEP_{System}) is given by [82, 83]

$NEP_{System} = \sqrt{(NEP_{Si})^2 + (NEP_{SiC})^2}$ which can be substituted into Equation (4-1) to write

$$\frac{1}{D^*_{Th}} = \sqrt{\left(\frac{1}{D^*_{Si}}\right)^2 + \left(\frac{1}{D^*_{SiC}}\right)^2}, \tag{4-2}$$

where the relation $NEP_i = \sqrt{A_d} / D^*_i$ is used for i = Si and SiC and the detector area A_d is considered to be the same for both the Si and SiC detectors since the He-Ne laser beam diameter defines the effective area for the optical response measurement. The value of NEP_{Si} for Si detector is 0.2 pW/Hz$^{1/2}$. From this value, the specific detectivity of Si detector (D^*_{Si}) is calculated as 1.33×10^{12} cm·Hz$^{1/2}$/W based on A_d = 1.13 mm^2. The detectivity of the SiC detector can be obtained from the following expression [75]

$$D^*_{SiC} = \frac{c\sqrt{\eta_i}\,\exp\left(\frac{hc}{2\lambda k_B T}\right)}{\sqrt{4\pi hc^4 k_B T/\lambda^4}\left[1+\frac{2\lambda k_B T}{hc}+2\left(\frac{\lambda k_B T}{hc}\right)^2\right]^{1/2}}, \tag{4-3}$$

where, η_i is the internal quantum efficiency of the SiC detector. The detectivity value from Equation (4-3) is 1.29×10^{11} cm·Hz$^{1/2}$/W with four-pass sample due to the highest internal quantum efficiency and the detectivities of other doped samples.

4.3 Theoretical NETD

The theoretical value of $NETD_{Th}$ can be obtained using the relationship between *NETD* and detectivity as [84], $NETD_{Th} = \frac{4F^2}{D^*_{Th}\tau_0\left(\frac{dI_a}{dT}\right)}\sqrt{\frac{\Delta f}{A_d}}$, where the *f*-number of the detector lens is F = 0.866 and the transmissivity of the lens and filter is τ_0 = 0.93. The theoretical and experimental values of *NETD* are plotted in Figure 8(b), showing that the theoretical $NETD_{Th}$ is 11 mK based on the two MWIR emission bands of the source and it does not vary with the dopant concentration. The experimental $NETD_{Exp}$, however, varies from 2.818 K to 404 mK as the dopant concentration increases from 1.15×10^{19} to 6.25×10^{20} cm^{-3} respectively. This discrepancy between the theoretical and experimental results might be due to the quality of the as-received

sample that was an n-type 4H-SiC substrate, the diffusive loss of photoexcited electrons from the Ga-doped region, and the imperfection and misalignment of the radiation collection optics. As-received epitaxial SiC sample with low diffusivity of electrons, improved radiation collection capability and optimized dopant concentration are expected to lower the $NETD_{Exp}$ of Ga-doped SiC detectors.

4.4 Effect of Photogenerated Electrons on the Reflectance of the Doped Region

Absorption of the incident photon energy by the doped sample causes photoexcited electrons due to the jumping of electrons from the valence band to the Ga dopant energy level. The change in the number density of electrons due to photoexcited electrons can be obtained from the following equation (see Appendix B):

$$\frac{d(\Delta N_e)}{dt} = \frac{I_a \eta_{i,SiC}}{h\nu_M V} - \left(\frac{\Delta N_e}{\tau_c} - \frac{\Delta N_e A_d}{V} \sqrt{\frac{D}{2\tau_d}} \right), \tag{4-4}$$

where the first term on the right hand side is the rate of photogeneration of electrons per unit volume, V, of the doped region, and the second and third terms are the rates of electron density loss due to recombination and diffusion of electrons from the photoexcited region, respectively. Here ΔN_e is the rate of change in the number of electrons in the photoexcited state per unit

volume of the doped region. $\eta_{i,SiC}$ and h are the internal quantum efficiency of the SiC detector and Planck's constant, respectively, and ν_M is the frequency of the MWIR radiation. τ_c is the recombination time, i.e., the lifetime of the electrons in the photoexcited state, and A_d is the surface area of the SiC detector region. D is the diffusivity of the photoexcited electrons and τ_d is the characteristic diffusion time. I_a is the absorbed irradiance of the MWIR radiation, which can be expressed as [75], $I_a = \alpha_d \varepsilon_s \tau_0 \frac{A_d}{4F^2} T_s \left(\frac{dI_a}{dT_s} \right)_{\lambda_{12}}$, where α_d is the absorbance of the doped sample for the MWIR wavelength λ. The absorbance is determined by considering multiple reflections inside the sample. ε_s and τ_0 are the emissivity of the radiation source and the transmissivity of the radiation collection optics (e.g., lens and filter), respectively. F is the f-number of the detector lens, respectively. $\left(\frac{dI_a}{dT_s} \right)_{\lambda_{12}} = \left(\frac{dI_a}{dT_s} \right)_{\lambda_1} + \left(\frac{dI_a}{dT_s} \right)_{\lambda_2}$, where $\left(\frac{dI_a}{dT_s} \right)_{\lambda_1}$ and $\left(\frac{dI_a}{dT_s} \right)_{\lambda_2}$ are the changes in absorbed irradiance with respect to the source temperature (T_s) due to the emission bands centered around two MWIR wavelengths λ_1 = 4.21 μm and λ_2 = 4.63 μm, respectively. These two wavelengths are considered because they represent two absorbance peaks of the detector (Figure (2a)) and the filter of this study transmits them from the radiation source to the detector.

Equation (4-3) yields the following expression for the change in the photoexcited electron density at steady state:

$$\Delta N_e = \frac{I_a \eta_{i,SiC} \tau_c \sqrt{2\tau_d}}{(V\sqrt{2\tau_d} + A_d \tau_c \sqrt{D})h\nu_M}, \tag{4-5}$$

Another optical effect is the interference due to multiple reflections of the MWIR radiation in the doped and undoped regions of the detector. The Ga-doped sample has three interfaces between the air and doped region, the doped region and undoped silicon carbide, and the undoped silicon carbide and air. The reflectance due to multiple reflections at these interfaces can be expressed in Equations (3-18)-(3-20). The reflectance is a function of the reflectivity, R, and the absorption coefficient, μ. Noting that R depends on the free electron density, N_e, through the refraction and absorption indices, $n(N_e)$ and $\kappa(N_e)$, and the absorption coefficient depends on the absorption index, $\mu(\kappa(N_e))$, the functional dependence of reflectance on these variables can be expressed as $\rho_d = f\left[R\{n(N_e),\kappa(N_e)\},\mu(\kappa(N_e))\right]$, which yields the following expression for changes in the reflectance:

$$\Delta\rho_d = \Delta N_e \left[\frac{\partial \rho_d}{\partial R}\left(\frac{\partial R}{\partial n_d}\frac{dn_d}{dN_e} + \frac{\partial R}{\partial \kappa}\frac{d\kappa}{dN_e} \right) + \frac{\partial \rho_d}{\partial \mu_d}\left(\frac{\partial \mu_d}{\partial \kappa}\frac{d\kappa}{dN_e} \right) \right], \tag{4-6}$$

where R refers to the reflectivities of the doped region in SiC at two interfaces, i.e., R_{ad} and R_{du}. Since the absorption indices are found to be 1.42×10^{-4} and 1.53×10^{-4} for the undoped and doped samples, respectively, at the He-Ne laser wavelength of 632.8 nm, the variation in κ is ignored in Equation (4-6), resulting in the following expression for $\Delta\rho_d$:

$$\Delta\rho_d = \Delta N_e \left[\frac{\partial \rho_d}{\partial R} \left(\frac{\partial R}{\partial n_d} \frac{dn_d}{dN_e} \right) \right], \tag{4-7}$$

The changes in the reflectance of the detector can be determined by Equation (4-7).

CHAPTER 5: THEORETICAL NETD AND DETECTIVITY FROM NOISE SOURCES

5.1 Introduction

The response of any detector system is severely affected by the noise of its different components. In the SiC optical photodetector, the noise may arise due to a variety of effects such as the interaction of the SiC detector with the incident photons from the source, noise mechanisms inherent in the He-Ne laser, the interaction between the detector and He-Ne laser, and the noise of the He-Ne laser detector.

5.2 Noises in the SiC Detector

The noises in the Ga-doped 4H-SiC detector are the photon shot noise, Johnson noise and the electron generation-recombination noise. When photons strike a detector, the photon-detector interactions immediately produce a signal variance or noise due to the fluctuations in the number of photons emitted by the source and due to the randomness in the production of photoexcited electrons. The mean square noise of the photoexcited electron density can be written as [85]

$$\left\langle \delta N_{e,Q}{}^{2} \right\rangle^{1/2} = \frac{l_c}{D\sqrt{A_d}} \left[\frac{2\varepsilon_s \alpha_d \eta_{i,SiC} \tau_0 T_s \Delta f_d}{4F^2 h\nu_M} \left(\frac{dI_a}{dT_s} \right)_{\lambda_{12}} \right]^{1/2}, \tag{5-1}$$

where l_c is the characteristic diffusion length of the electron in the detector and Δf_d is the noise bandwidth of the Ga-doped 4H-SiC detector.

The Johnson noise is the fluctuation of the photoexcited electrons due to their thermal motions, and the mean square of this noise can be written as [86]

$$\left\langle \delta N_{e,J}{}^{2} \right\rangle^{1/2} = \frac{l_c}{A_d D q} \sqrt{\frac{4 k_B T_d \Delta f_d}{R_{e,d}}} , \tag{5-2}$$

where k_B and T_d are the Boltzmann constant and the temperature of Ga-doped SiC detector. q is the charge of an electron and $R_{e,d}$ is the electrical resistivity of the detector.

The electron generation-recombination noise arises from the statistical fluctuation in the rate of photoexcitation of electrons from the valence band to the dopant energy level and the rate of relaxation of these photoexcited electrons from the dopant energy level to the valence band. The mean square of this noise can be written as [86]

$$\left\langle \delta N_{e,GR}{}^{2} \right\rangle^{1/2} = \frac{2 l_c{}^{3}}{\tau_c D^2 \sqrt{A_d}} \left[\frac{\varepsilon_s \alpha_d \eta_{i,SiC} \tau_0 T_s \Delta f_d}{4 F^2 h \nu_M} \left(\frac{dI_a}{dT_s} \right)_{\lambda_{12}} \right]^{1/2} , \tag{5-3}$$

5.3 Noises in He-Ne Laser Probe Beam

The phase noise fluctuations of a laser can produce intensity noise fluctuations [73]. The noises of a He-Ne laser are power noises due to the frequency and output fluctuations. Additionally the

interaction between the He-Ne laser and detector produces a noise in the reflected He-Ne laser power due to the fluctuations in the reflectance of the detector. The main noise mechanism for the laser is the spontaneous emission noise, yielding fluctuations in the emitted optical power and the emission frequency. Relative intensity noise (*RIN*) represents the amount of noise relative to the magnitude of signal, which is given by $\sigma^2/\langle P\rangle^2$, where σ is the standard deviation of the noise distribution, i.e., σ^2 is the noise variance and $\langle P\rangle$ is the average power of the signal. The total *RIN* is expressed in terms of power as [87]

$$RIN_{total} = \frac{\langle \delta P^2 \rangle}{\langle P \rangle^2}, \tag{5-4}$$

where δP is the power fluctuation of laser. Based on the spectral density of *RIN* in the optical frequency domain (ν_L), which is denoted by *RIN* (ν_L), the total *RIN* over all frequencies can also be written as [88]

$$RIN_{total} = \int_{-\infty}^{\infty} RIN(\nu_L) d\nu_L, \tag{5-5}$$

where ν_L is the frequency of the He-Ne laser. In terms of the reflected power fluctuations, $\delta P(t)$, in the oscillator cavity of the He-Ne laser, the Fourier transform of the autocorrelation function of $\delta P(t)$ leads to a spectral density of the square of the power fluctuations in units of W^2/Hz, which is denoted by $W_{\Delta P}(\nu_L)$. The corresponding spectral density of *RIN* is given by $RIN(\nu_L) = \frac{W_{\Delta P}(\nu_L)}{\langle P \rangle^2}$ with $W_{\Delta P}(\nu_L) = \left(\frac{1}{\pi}\right)\frac{\hbar\omega_m \eta_e P_L \Delta\rho_{d,L}}{t_p^{\,2}}\left(\frac{1}{\nu_L^{\,2} + \omega_1^{\,2}}\right)$, where $\hbar$ is the reduced

Planck constant, ω_m is the modulated angular frequency of the laser, i.e., the bandwidth of the He-Ne laser around its nominal angular frequency ω_1, η_e is the external quantum efficiency, P_L is the average power of the laser beam, $\Delta\rho_{d,L}$ is the reflectance change of the doped SiC detector at HeNe laser wavelength, and t_p is the pulse width at the half-intensity points of the laser [87, 88]. Similarly, in terms of frequency fluctuations, the spectral density of *RIN* is given by $RIN(\nu_L) = 4\pi^2\tau^2 W_{\Delta\omega}(\nu_L)$ corresponding to the spectral density of frequency noise $W_{\Delta\omega}(\nu_L) = \frac{\eta_e}{4\pi t_p^{\,2}}\left(\frac{\hbar\omega_m}{P_L\Delta\rho_{d,L}}\right)\left(\frac{\beta^2}{1+\left(\frac{\nu_L}{\omega_1}\right)^2}\right)$, where τ is the delay time for the arrival of the laser wavefronts to the interfaces of the SiC detector. β is the phase-amplitude coupling constant, i.e., the variation of the carrier density results in the random field amplitude fluctuation which involves an additional, delayed phase change, which enhances the laser linewidth [87]. Using these expressions and Equations (5-4) and (5-5), the reflected He-Ne laser power noises due to the power and frequency fluctuations, respectively, can be written as

$$\left\langle \delta P_{L,P}^{\;2} \right\rangle^{1/2} = \sqrt{\frac{\pi\eta_{e,L}P_L h\nu_L}{t_p^{\,2}\omega_1}}, \tag{5-6}$$

and

$$\left\langle \delta P_{L,F}^{\;2} \right\rangle^{1/2} = \sqrt{\frac{\pi\eta_{e,L}P_L h\nu_L \alpha_{SiC,L}^{\;2}\tau^2\omega_1}{2t_p^{\,2}}}, \tag{5-7}$$

where $\alpha_{SiC,L}$ is the absorbance of the SiC detector at He-Ne laser wavelength. Equations (5-6) and (5-7) are used in section 5.6 to calculate theoretical $NETD_{Th}$.

5.4 Interferometric Noise due to Interaction between the He-Ne Laser and the SiC Detector

Interference occurs due to multiple reflections of the He-Ne laser beam as it propagates inside the SiC detector. So the reflected power of the He-Ne laser can have interferometric noise, representing the phase of the laser varying randomly as a function of time. The laser has random phase fluctuations at the exit of the laser system. These phases are modified further as the laser beam travels through different optical paths inside the SiC detector, causing fluctuations in the power of the He-Ne laser reflected by the detector, i.e., a random signal is produced by the detector. The characteristics of the interferometer, which is the detector itself in the present case, are determined by the reflectivities at different interfaces inside the detector and the delay time τ. The spectral density of the interferometric noise due to multiple reflections can be expressed as [89]

$$RIN(\nu_L) = \frac{4r^2}{\pi}\left[\frac{\Delta\nu}{\nu_L{}^2 + (\Delta\nu)^2}\right]\left[sin^2(\omega_0\tau)\left\{1 + e^{-4\pi\Delta\nu\tau} - 2e^{-2\pi\Delta\nu\tau}\,cos(2\pi\nu_L\tau)\right\} + cos^2(\omega_0\tau)\left\{1 - e^{-4\pi\Delta\nu\tau} - 2e^{-2\pi\Delta\nu\tau}\frac{\Delta\nu}{\nu_L}sin(2\pi\nu_L\tau)\right\}\right], \quad (5\text{-}8)$$

where r is an effective reflection coefficient, which depends on the reflection coefficients of various interfaces of the detector. $\Delta\nu$ and ω_0 are the linewidth in frequency units and the center angular frequency of the He-Ne laser, respectively. It can be shown from Equation (5-8) that $RIN(\nu_L)$ is maximum, i.e., the conversion of the incident laser phase noise into the reflected laser intensity (signal) noise is maximum, when $\omega_0\tau = (n+1/2)\pi$ for n = 1, 2, 3, ... However, for the longer delay path and linewidth and in the limit of small phase fluctuations, i.e., $2\pi\tau\Delta\nu >> 1$, which holds good in the present case of the He-Ne laser for $\Delta\nu$ = 310 MHz and τ = 13.3 ns, Equation (5-8) simplifies to the following expression for $RIN(\nu_L)$:

$$RIN(\nu_L) = \frac{16}{\pi} r^2 \Delta\nu \tau^2 sinc^2(\nu_L \tau), \tag{5-9}$$

where the sinc function is defined by $sinc(x) = \frac{\sin x}{x}$. Small phase fluctuations occur in lasers with very narrow linewidth, resulting in less interferometric intensity noise. Based on the reflectivities R_{au}, R_{du} and R_{ad} and by considering that the polarizations the interfering fields are aligned, the effective reflection coefficient, r, is determined from the following expression [89]:

$$\begin{aligned} r(t,\tau) = {} & 2\left(1-\sqrt{R_{au}}\right)^4 R_{au} R_{du} \begin{cases} e^{-2\pi\Delta f|t|}\left[1+cos(2\omega_0\tau_1)e^{-4\pi\Delta f(\tau_1-|t|)}\right], |t| < \tau_1 \\ e^{-2\pi\Delta f\tau_1}\left[1+cos(2\omega_0\tau_1)\right], |t| > \tau_1 \end{cases} \\ & + 2\left(1-\sqrt{R_{au}}\right)^4\left(1-\sqrt{R_{du}}\right)^4 R_{au} R_{ad} \begin{cases} e^{-2\pi\Delta f|t|}\left[1+cos(2\omega_0\tau_2)e^{-4\pi\Delta f(\tau_2-|t|)}\right], |t| < \tau_2 \\ e^{-2\pi\Delta f\tau_2}\left[1+cos(2\omega_0\tau_2)\right], |t| > \tau_2 \end{cases} \end{aligned}, \tag{5-10}$$

where τ_1 and τ_2 are the delay times given by $\tau_1 = \frac{2d_u n_u}{c\cos(\theta_{t1})}$ and

$$\tau_2 = \frac{2d_d n_d}{c\cos(\theta_{t2})} + \frac{d_u n_u}{c\cos(\theta_{t1})}.$$

Using Equations (5-9), and (5-10), the reflected He-Ne laser power noise due to intensity fluctuations can be written as

$$\left\langle \delta P_{R,I}{}^2 \right\rangle^{1/2} = P_L \Delta\rho_{d,L} \sqrt{16\pi(1-\sqrt{R_{au}})^4 R_{au} \Delta\nu \left(R_{du}\tau_1 + (1-\sqrt{R_{du}})^4 R_{ad}\tau_2\right)}. \tag{5-11}$$

Equation (5-11) is used in section 5.6 to calculate $NETD_{Th}$.

5.5 Noise due to He-Ne Laser Detector (Si-based Photodetector)

The noise mechanisms in the Si detector are the photon shot noise caused by the He-Ne laser photons that are incident on the Si detector after being reflected by the SiC detector, and the Johnson, shot and generation-recombination noises due to the He-Ne laser photon-induced electrons in the Si detector. The photon shot noise due to the He-Ne laser is [85]

$$\left\langle \delta i_{Si,Q}{}^2 \right\rangle^{1/2} = q\sqrt{\frac{\eta_{e,Si} P_L \rho_{d,L} \Delta f_{Si}}{h\nu_L}}, \tag{5-12}$$

where $\eta_{e,Si}$ is the external quantum efficiency of the Si detector and Δf_{Si} is the noise bandwidth of the Si detector.

The Johnson or Nyquist noise describes the fluctuations in the voltage across a dissipative circuit element, caused by the thermal motion of the charge carriers. The charge neutrality is satisfied in

an electrical element (e.g., resistor) when considering the whole volume, but locally the random thermal motion of the carriers sets up fluctuating charge gradients and, therefore, a fluctuating voltage. The noise due to this thermal motion can be expressed as [85]

$$\left\langle \delta i_{Si,J}{}^{2} \right\rangle^{1/2} = \sqrt{\frac{4k_B T_{Si} \Delta f_{Si}}{R_{e,Si}}}\,, \tag{5-13}$$

where T_{Si} and $R_{e,Si}$ are the temperature and the electrical resistivity of the Si detector, respectively.

The current arising from random generation and flow of mobile charge carriers is identified with the shot noise. This shot noise is caused by the fluctuations in the current due to the discreteness of the charge carriers, and the random electronic emission for which the number of electrons emitted per unit time obey the Poisson statistics, yielding the following expression for the shot noise [85].

$$\left\langle \delta i_{Si,S}{}^{2} \right\rangle^{1/2} = \sqrt{2q\left\langle \delta i_{L,Q}{}^{2} \right\rangle^{1/2} \Delta f_{Si}}\,. \tag{5-14}$$

The generation-recombination noise, which addresses the population of charge carriers in an excited state and the transition of electrons from the excited state to their ground state, is given by [85]

$$\left\langle \delta i_{Si,GR}{}^{2} \right\rangle^{1/2} = 2qG\sqrt{\eta_{e,Si} \frac{P_L \rho_{d,L}}{h\nu_L} \Delta f_{Si} + g_{th} A_{Si} \Delta f_{Si} l_t}\,, \tag{5-15}$$

where G is the photoconductive gain. g_{th}, A_{Si} and l_t are the thermal generation of carriers, the area of Si detector, and the detector thickness, respectively.

5.6 Noise Equivalent Temperature Difference (NETD) due to Various Noise Mechanisms

From the above noise sources in the SiC optical photodetector, the detector performance can be evaluated. *NETD* is an important performance parameter of infrared imaging systems and it is defined as the temperature difference between two adjacent points on the target source for which the difference in the detector signals is equal to the noise of the detector. For the *NETD* calculation of SiC detector, the signal term is denoted by $\Delta N_e(T_s)$, which is the difference in the free electron density of the doped sample in the presence of the MWIR irradiation at a given temperature of the source T_s. When the source temperature varies from T_{s1} to T_{s2}, the detector signal is $\Delta N_e(T_s) = N_e(T_{s2}) - N_e(T_{s1})$). The noise equivalent power (*NEP*) is the incident infrared power on an infrared detector that generates a signal output that is equal to the root-mean-square (RMS) noise output (i.e., resulting in a signal to noise ratio, *S/N*, of 1). The signal-to-noise ratio can be calculated using the following expression

$$\frac{\Delta N_e}{\left\langle \delta N_e^{\,2} \right\rangle^{1/2}} = \frac{\Delta T_s \eta_{i,SiC} \tau_r \sqrt{4\tau_d} \left[\frac{\alpha_{SiC} \varepsilon_s \tau_0}{4F^2} \left(\frac{dL_B}{dT_s} \right)_{\lambda_{12}} \right]}{h\nu_M (d_d \sqrt{4\tau_d} + \tau_r \sqrt{D}) \left(\left\langle \delta N_{e,Q}^{\,2} \right\rangle^{1/2} + \left\langle \delta N_{e,J}^{\,2} \right\rangle^{1/2} + \left\langle \delta N_{e,GR}^{\,2} \right\rangle^{1/2} \right)}, \tag{5-16}$$

where $\left\langle \delta N_e^{\,2} \right\rangle^{1/2}$ represent the noise for a given noise mechanism which consists of photon shot noise from the radiation source, Johnson noise and generation-recombination noise. Since $\Delta T_{s\ at\ S/N\ =\ 1}$ = *NETD* by definition of *NETD* as the temperature of the target for which the signal to noise ratio equals unity, the generalized expression for *NETD* of the doped SiC detector is

$$NETD_{SiC} = \frac{4F^2 h\nu_M (d_d\sqrt{4\tau_d} + \tau_r\sqrt{D})\left(\left\langle \delta N_{e,Q}{}^2 \right\rangle^{1/2} + \left\langle \delta N_{e,J}{}^2 \right\rangle^{1/2} + \left\langle \delta N_{e,GR}{}^2 \right\rangle^{1/2}\right)}{\eta_{i,SiC}\alpha_{SiC}\varepsilon_s\tau_0\tau_r\sqrt{4\tau_d}\left(\frac{dL_B}{dT_s}\right)_{\lambda_{12}}}. \tag{5-17}$$

The signal-to-noise ratio for He-Ne laser beam and doped SiC detector due to interferometric noise cause by multiple reflection and interference can be calculated by $\frac{\Delta\rho_{SiC,L}}{\left\langle \delta\rho_{SiC,L}{}^2 \right\rangle^{1/2}} \equiv \frac{\Delta P_{r,L}}{\left\langle \delta P_{r,I}{}^2 \right\rangle^{1/2}}$. Since $\Delta T_{SiC\ at\ S/N\ =\ 1}$ = *NETD*, the generalized expression for *NETD* of the interaction between the He-Ne laser and SiC detector is [see Appendix C]

$$NETD_{L,SiC} = \left\langle \delta P_{r,I}{}^2 \right\rangle^{1/2} \Big/ \left(\frac{dP_{r,L}}{dT_{SiC}}\right), \tag{5-18}$$

where $P_{r,L}$ is the reflected power of He-Ne laser and T_{SiC} is the temperature of SiC detector.

The *NETD* for He-Ne laser and Si detector is determined from the power noise due to intensity and frequency fluctuation in the reflected He-Ne laser beam arriving at the Si detector $\left(\sqrt{\left\langle \delta P_{r,P}{}^2 \right\rangle + \left\langle \delta P_{r,F}{}^2 \right\rangle}\right)$. Since the He-Ne laser power noise can be measured as current in Si detector, the signal-to-noise ratio can be calculated by $\frac{\Delta i_{Si}}{\left\langle \delta i_{Si}{}^2 \right\rangle^{1/2}}$. Since $\Delta T_{L\ at\ S/N\ =\ 1}$ = *NETD*, the generalized expression for *NETD* of the fluctuation in the reflected power of the He-Ne beam arriving at the Si detector is

$$NETD_{L,Si} = \left(\left\langle \delta P_{r,P}{}^2 \right\rangle^{1/2} + \left\langle \delta P_{r,F}{}^2 \right\rangle^{1/2} \right) \Big/ \left(\frac{dP_L}{dT_L} \right), \tag{5-19}$$

where T_L is the temperature of the He-Ne laser.

The signal-to-noise ratio for He-Ne laser power meter (Si detector) can be calculated by $\frac{\Delta i_{Si}}{\left\langle \delta i_{Si}{}^2 \right\rangle^{1/2}}$.

The noise sources are photon shot noise from He-Ne laser, Johnson, shot and generation-recombination. Since $\Delta T_{SiC\ at\ S/N\ =\ 1} = NETD$, the generalized expression for *NETD* of Si detector itself is

$$NETD_{Si} = \frac{h\nu_L}{q\eta_{i,Si}\alpha_{Si}} \left\langle \delta i_{Si}{}^2 \right\rangle^{1/2} \Big/ \left(\frac{dP_{r,L}}{dT_{SiC}} \right), \tag{5-20}$$

where $\eta_{i,Si}$ and α_{Si} are the internal quantum efficiency and absorbance of Si detector at He-Ne laser wavelength. Therefore, taking into account all the fundamental noise sources described above, the total theoretical *NETD* can be obtained by [82] $NETD_{Th} = \sqrt{NETD_{SiC}{}^2 + NETD_{L,SiC}{}^2 + NETD_{L,Si}{}^2 + NETD_{Si}{}^2}$.

5.7 Effect of NETD on Detectivity (D^*)

*NETD*s are determined from the noise sources in the above section. The *NETD* affects the detectivity as given by $D^* = \frac{4F^2}{NETD \cdot \tau_0 \left(\frac{dL_B}{dT_s} \right)} \sqrt{\frac{\Delta f}{A_d}}$, where A_d is the detector area [85]. This expression of detectivity is applicable for radiations emitted by a blackbody (ε = 1) and for detectors of 100% absorbance. dL_B / dT_s is the derivative of the integrated blackbody radiance with respect to source temperature. The overall theoretical detectivity, D^*_{Th}, of the detector system of this study constitutes of four components: (i) the detectivity of SiC detector (D^*_{SiC}), (ii) the detectivity due to the interaction between the He-Ne laser and SiC detector ($D^*_{L,SiC}$), (iii) the detectivity due to the fluctuation in the reflected power of the He-Ne beam arriving at the Si detector ($D^*_{L,Si}$) and (iv) the detectivity due to the Si detector itself (D^*_{Si}).

The detectivity of SiC detector, D^*_{SiC}, can be obtained by modifying the above general detectivity expression to account for the absorbance of SiC detector (α_{SiC}) and the emissivity of stainless steel radiation source (ε_s):

$$D^*_{SiC} = \frac{4F^2}{NETD_{SiC} \alpha_{SiC} \varepsilon_s \tau_0 \left(\frac{dL_B}{dT_s} \right)_{\lambda_{12}}} \sqrt{\frac{\Delta f_{SiC}}{A_{SiC}}}, \tag{5-21}$$

The $NETD_{L,SiC}$ has been obtained in Equation (5-18) due to the noise from He-Ne laser and SiC detector. $NETD_{L,SiC}$ and detectivity, $D^*_{L,SiC}$, account for the noise mechanism arising due to changes in the temperature of SiC detector while the temperature of MWIR radiation source and He-Ne laser are kept constant. For this noise mechanism, section 5.2, the detectivity is given by (see Appendix C)

$$D^*_{L,SiC} = \frac{\sqrt{A_{Si}\Delta f_{Si}}}{NETD_{L,SiC}\alpha_{Si}\rho_{SiC,L}P_L \dfrac{d\rho_{SiC,L}}{dT_{SiC}}}, \tag{5-22}$$

The $NETD_{L,Si}$ has been obtained in Equation (5-19) due to the noise from fluctuation on the reflected power of the He-Ne laser beam arriving at the Si detector. $NETD_{L,Si}$ and detectivity, $D^*_{L,Si}$, account for the noise mechanism arising due to changes in the temperature of He-Ne laser while the temperature of MWIR radiation source and SiC detector are kept constant. For this noise mechanism, section 5.7, the detectivity is given by

$$D^*_{L,Si} = \frac{\sqrt{A_{Si}\Delta f_{Si}}}{NETD_{L,Si}\dfrac{dP_L}{dT_L}}. \tag{5-23}$$

The $NETD_{Si}$ has been obtained in Equation (5-20) due to the noise from the He-Ne laser power meter (Si detector). $NETD_{Si}$ and detectivity, D^*_{Si}, account for the noise mechanism arising due to changes in the temperature of SiC detector while the temperature of MWIR radiation source

and He-Ne laser are kept constant. For this noise mechanism, section 5.2, the detectivity is given by

$$D_{Si}^{*} = \frac{\sqrt{A_{Si}\Delta f_{Si}}}{NETD_{Si}\dfrac{dP_{r,L}}{dT_{SiC}}}. \tag{5-24}$$

Therefore, the total theoretical detectivity can be obtained by the following expression [82]:

$$\frac{1}{D_{Th}^{*}} = \sqrt{\left(\frac{1}{D_{d}^{*}}\right)^{2} + \left(\frac{1}{D_{R,PF}^{*}}\right)^{2} + \left(\frac{1}{D_{R,I}^{*}}\right)^{2} + \left(\frac{1}{D_{Si}^{*}}\right)^{2}}.$$

The theoretical detectivities and NETDs of the SiC-Si detector system were obtained using above Equations through (5-17) to (5-24) were calculated as listed in Table 5-1.

Table 5-1: Theoretical values of $NETD_{Th}$ and detectivity of Ga-doped 4H-SiC IR detector in 4.21 μm.

Detector components	Noise sources	Related equations	$NETD_{Th}$ (mK)	Detectivity, D_{Th}^* (cm·Hz$^{1/2}$/W)
Ga-doped 4H-SiC detector	1. photon shot noise from radiation source 2. Johnson noise 3. Generation-recombination	(5-1)-(5-3), (5-17), (5-21)	12.15	4.53×10^{10}
SiC detector + He-Ne laser probe beam	1. interferometric noise due to multiple reflection and interference of He-Ne beam in SiC	(5-4)-(5-7), (5-18), (5-22)	14.88	2.31×10^{10}
He-Ne laser probe beam + Si detector	1. power noise due to intensity fluctuation 2. power noise due to frequency fluctuation	(5-8)-(5-11), (5-19), (5-23)	16.72	2.05×10^{10}
He-Ne laser power meter (Si detector)	1. photon shot noise from He-Ne laser 2. Johnson noise 3. shot noise 4. Generation-recombination	(5-12)-(5-15), (5-20), (5-24)	19.84	1.73×10^{10}
Total			32.28	1.11×10^{10}

CHAPTER 6: CHARACTERIZATION OF INFRARED DETECTOR

6.1 Introduction

Although infrared (IR) focal-plane arrays (FPAs) have been widely used in many imaging systems, the demand for cameras and linear arrays sensitive to the MWIR (3-5 μm) and LWIR (8-12 μm) spectral bands is growing continually. These remote sensors are used in a variety of applications including the detection and monitoring of chemicals in atmospheric and other environments, telecommunications and semiconductor manufacturing systems [90-92]. These two wave bands exhibit excellent atmospheric transmission (>50%) compared to very low (<0.1%) transmission in the visible range. Also the wave band 5-8 μm is not very good for atmospheric transmission mostly due to water vapor in air. Therefore the MWIR and LWIR bands are suitable for detecting and monitoring pollution, relative humidity profiles and the distribution of different gases such as carbon monoxide, nitrous oxide in the atmosphere [93, 94]. This is because most of the principal absorption lines of gas molecules lie in the MWIR spectral range.

Infrared (IR) detectors are made of narrow bandgap semiconductors because of the low energy (0.05-1.3 eV) of infrared photons. Various materials are used for specific spectral ranges, which include indium gallium arsenide (InGaAs) for 0.7-2.6 μm range, indium arsenide (InAs) for 1-3.8 μm, indium antimonide (InSb) for 1-6.7 μm, lead sulfide (PbS) for 1-3.2 μm, lead selenide (PbSe) for 1.5-5.2 μm, mercury-cadmium-telluride ($Hg_{1-x}Cd_xTe$) for 0.8-25 μm, and vanadium

oxide (VO_x) for 2-16 μm. HgCdTe (MCT) is a variable-gap semiconductor depending on the composition of Hg and Cd, which is used as a crystalline intrinsic detector cell to produce IR detectors. The MCT detectors exhibit very high signal-to-noise ratio and very short response time [95-97]. To achieve this excellent performance, the MCT detectors require cryogenic cooling at 77 K, resulting in a costly and bulky detector system. The weak Hg-Te bond, which induces bulk, surface and interface instability, and the toxicity of Hg led to the development of detectors with other materials. Some of these detectors include Schottky barriers on silicon, SiGe heterojunctions, AlGaAs multiple quantum wells, GaInSb strain layer superlattices, high-temperature superconductors, pyroelectric and silicon bolometers [95]. In spite of considerable efforts, operating these devices at room temperature has been very difficult with the exception of thermal detectors.

Cooling is a major limitation of IR detectors and a number of devices has been investigated to overcome this problem. Photoconductors, photoelectromagnetic detectors, Dember effect detectors and MCT photodiodes [96] were some of the devices studied for room temperature operation. Different types of uncooled thermal IR detectors such as thermocouples, pyroelectric and ferroelectric detectors are currently available [98-100], which are based on different properties of materials. Microbolometer detectors are made of either vanadium oxide or amorphous silicon, while the ferroelectric detectors are made of barium strontium titanate. There are also bolometers that are optimized for broadband detection in the 3-5 μm and 8-12 μm wavelength regions simultaneously [101]. Much attention has been paid to uncooled IR detectors of other operating mechanism such as the optomechanical IR imaging system with bimaterial microcantilever array [102].

Recently crystalline silicon carbide, which is a wide bandgap (3.0-3.23 eV) semiconductor with excellent rad-hard property, high thermal conductivity (490 W/m·K) and high melting temperature (3100 K peritectic temperature), has been used to fabricate a variety of radiation detectors. High quality large-area X-ray detector based on SiC Schottky diodes, and high-energy particle (alpha and beta particles) detectors have been demonstrated. The particle detectors are based on the interaction between the charges of the incident particles and the orbital electrons of the absorber atoms (e.g., SiC) [103-105]. The operation of conventional radiation detectors, which are generally based on Ge or Si as the absorber atoms, is limited by the radiation damage threshold and thermal stability of the absorber material.

In this research, we have demonstrated a silicon carbide-based optical detector for the MWIR range, which produces optical signals. The simplicity of our detector is that a doped SiC can be used directly as the photon detector without any further microelectronics device fabrication steps and any electrical connection to the doped sample. Also the detector operates at room temperature. The wide bandgap of SiC offers a unique advantage for tuning its photon detectibility to a desired wavelength by doping it with an appropriate dopant. Ga has an acceptor energy level of 0.30 eV in 4H-SiC [12, 13] corresponding to 4.21 μm wavelength. The operating principle of the optical detector is that the electromagnetic (EM) waves of this wavelength excite electrons from the valence band to the dopant energy level. Consequently the electron density changes in these two energy levels, which affects the refraction index of the semiconductor and, therefore, modifies the reflectance of the doped region. This change in the reflectance represents the optical response of the detector, which is probed with a He-Ne laser.

6.2 Spectroscopic Analysis of the Dopant Energy Level

Two physical phenomena, laser heating of the substrate and diffusion of Ga atoms into the substrate, occur simultaneously during the above-mentioned laser doping process. To understand their effects, the optical properties of three types of samples, as-received 4H-SiC substrate, laser heat-treated sample prepared by heating an as-received substrate under the same laser processing conditions as in the doping process but without the Ga precursor inside the vacuum chamber, and Ga-doped sample, were measured using a Bruker Vertex 70 FTIR spectrometer equipped with a Helios infrared micro-sampling accessory. The Helios combines a rapid scan speed of 100 spectra per second with an infrared microscope of resolution 250 μm. The absorption spectra of the doped sample revealed a peak at 4.21 μm (0.30 eV) with 32% absorbance, which is higher than 16% and 12% absorbance of the laser heat-treated and as-received samples, respectively, as shown in Figure 6-1(a).

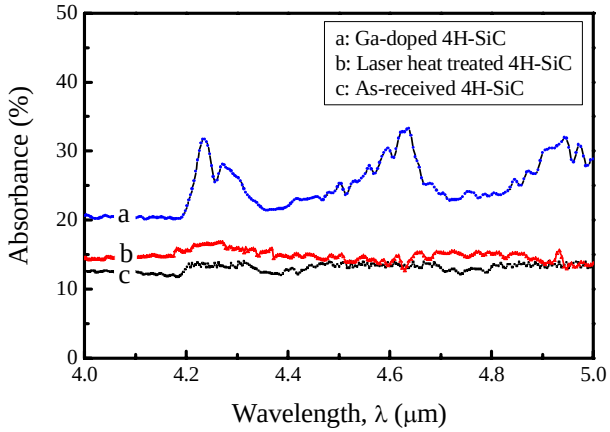

(a)

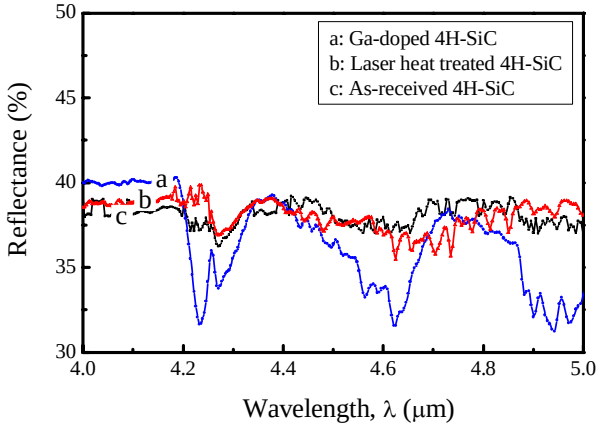

(b)

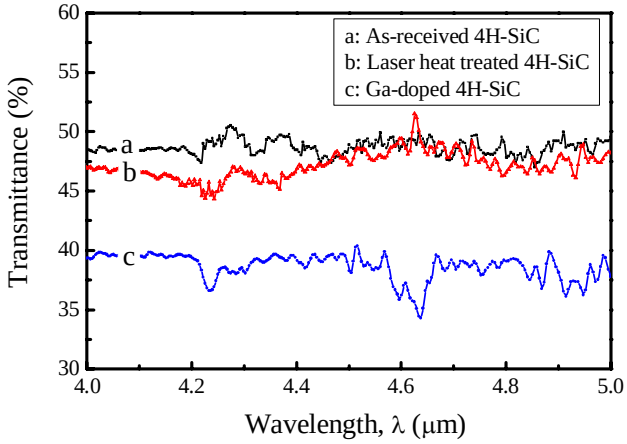

(c)

Figure 6-1: Spectroscopic data showing the optical properties of Ga-doped, laser heat treated and as-received 4H-SiC (a) absorbance, (b) reflectance, and (c) transmittance in the wavelength range 4-5 μm.

The optical properties of the laser heat- treated sample indicate that laser heating does not modify the substrate significantly compared to the as-received sample. However, the doped sample exhibits additional absorption peaks at the wavelengths 4.63 μm (0.27 eV) and 4.95 μm (0.25 eV) in Figure 6-1(a), which could be due to several reasons. Some of the Ga atoms might be at the interstitial sites of the silicon carbide lattice, which can modify the electronic structure and thereby affect the Ga acceptor energy level. Even when the Ga atoms are at the substitutional sites, they can occupy the Si or C lattice sites to form a p-type semiconductor with multiple acceptor levels. Also the Ga atoms can cause mechanical stresses in the lattice due to their atomic size being different from the sizes of the Si and C atoms, which can affect the acceptor energy levels.

Out of these two additional peaks, the peak at 4.63 μm will also contribute to the detector response since a narrow band pass filter of transmission range 4.08-4.81 μm is used in this study to extract the MWIR wavelengths from a broadband source of EM waves. The doped sample has higher absorption coefficient than the as-received sample as listed in Table 6-1, indicating that the Ga dopant has increased the absorption characteristics of the substrate. These spectroscopic data, therefore, show that the Ga dopant atoms have modified the optical properties of the as-received sample.

Table 6-1: Optical properties for as-received and doped 4H-SiC.

Wavelength, λ	At 0.6328 μm		At 4.21 μm		At 4.63 μm	
Sample	As-received	Ga-doped	As-received	Ga-doped	As-received	Ga-doped
Absorbance	0.51	0.54	0.12	0.32	0.12	0.30
Reflectance	0.30	0.28	0.41	0.32	0.39	0.33
Transmittance	0.19	0.18	0.47	0.36	0.49	0.37
Reflectivity	0.26	0.25	0.29	0.19	0.27	0.20
Absorption coefficient (mm^{-1})	2.823	3.038	0.360	1.601	0.358	1.461
Absorption index	1.421×10^{-4}	1.530×10^{-4}	1.205×10^{-4}	5.362×10^{-4}	1.319×10^{-4}	5.384×10^{-4}
Refraction index	3.442	3.217	3.333	2.545	3.163	2.618

The appearance of the additional absorption peak could be due to the presence of impurities or other defects in the n-type 4H-SiC substrate, which might have been activated during the laser doping process. Using SiC epilayer as the starting substrate can avoid the formation of such additional peaks because epilayers are much purer than the substrates obtained from bulk crystals. On the other hand, the detector response of this study can be considered to be due to two MWIR wavelengths 4.21 and 4.63 μm, which indicates the possibility of fabricating tunable detectors.

6.3 Measurement of the Optical Response

The detector (doped region) was tested to examine the effect of 4.21 μm wavelength on the optical response, i.e., the changes in the refraction index and reflectance, of the detector. It was placed above an infrared source and a set of optical elements consisting of two lenses and a filter as shown in Figure 6-2.

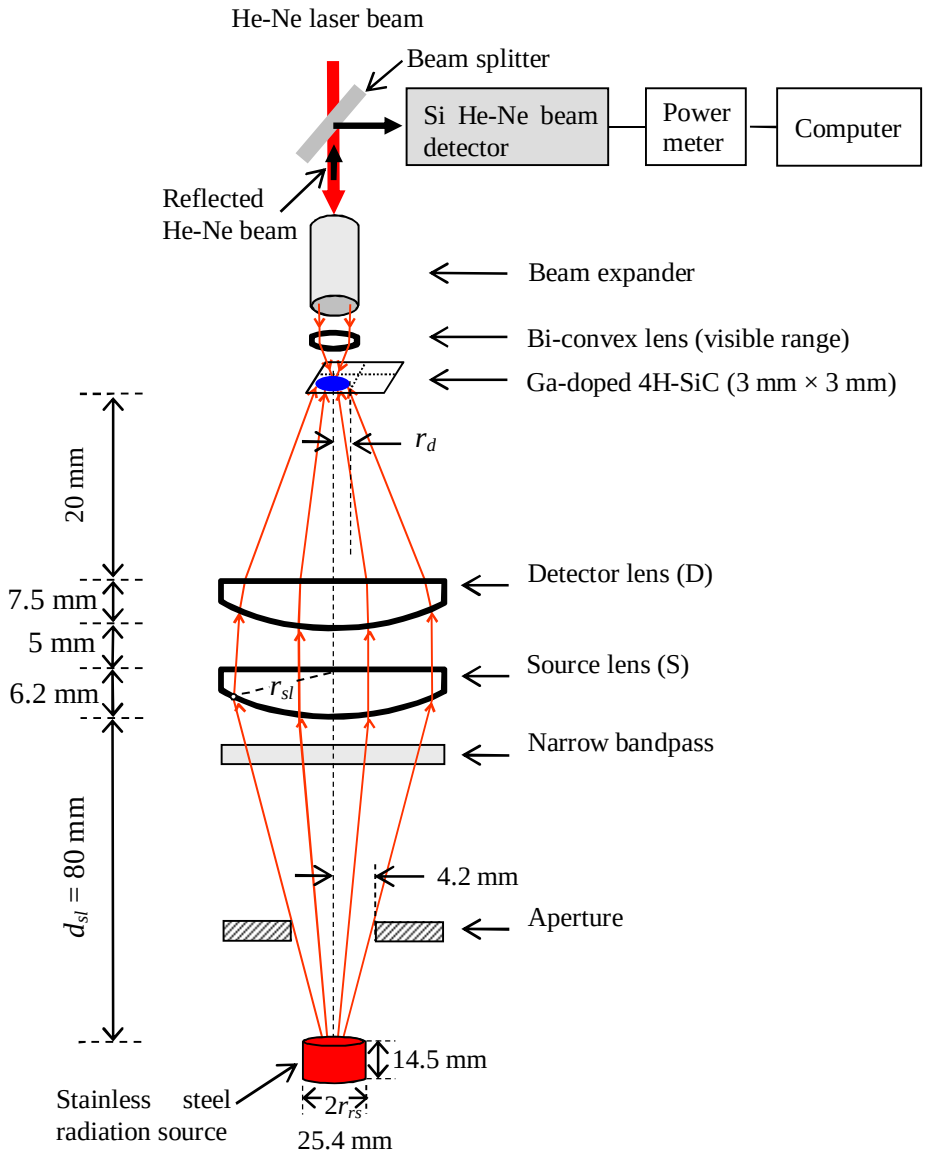

Figure 6-2: Optical arrangement to examine the detector response and ray geometry to calculate the irradiance on the SiC MWIR detector due to the radiance of a stainless steel source.

The purpose of the optics is to focus the waves of 4.21 μm to the detector. A He-Ne laser of wavelength 632.8 nm was used to measure the changes in the reflectance. A stainless steel solid cylinder of diameter 25.4 mm and height 14.5 mm was heated to a very high temperature to form a heavily oxidized surface, which was used as the MWIR radiation source. Siegel and Howell [70] reported that the emissivity of such a surface is 0.7 at 1200 K for the wavelengths 4.21 and 4.63 μm. At any wavelength (λ) and source temperature (T), the spectral radiance of the stainless steel surface, $L_{\lambda,s}(\lambda,T)$, can be determined based on the Planck blackbody radiation theory [71]. It is given by $L_{\lambda.,s}(\lambda,T) = \varepsilon_{\lambda,s}(\lambda,T)\times L_{\lambda,b}(\lambda,T)$, where $\varepsilon_{\lambda,s}(\lambda,T)$ and $L_{\lambda,b}(\lambda,T)$ are the spectral emissivity of the S. S. surface and the spectral radiance of blackbody, respectively. $L_{\lambda,s}(\lambda,T)$ is very small at room temperature for each of the wavelengths 4.21 and 4.63 μm. At 20°C, the spectral radiances of the stainless steel surface are 0.541 and 0.969 $\mu W/mm^2 \cdot sr \cdot \mu m$ at 4.21 and 4.63 μm respectively. At 25°C, the spectral radiances are 0.658 and 1.158 $\mu W/mm^2 \cdot sr \cdot \mu m$ at 4.21 and 4.63 μm respectively. So the detector needs to be very sensitive to detect any change in the source temperature. Also the EM wave collection optics needs to have very high quality to collect the maximum amount of waves from the source and focus them to a small spot on the detector.

6.3.1 Optical Setup for Irradiance on the Ga-doped SiC sample

The stainless steel source emits EM waves over a broad band from which a very small wavelength range around 4.21 μm was selected using a narrow band pass filter. The filter had a

high transmittance (~ 92.5%) in the range 4.08-4.81 μm and a sharp cut off outside this band. It is made of silicon monoxide and germanium thin films deposited on a silicon substrate and its safe operating temperature is below 200°C. Therefore it must be placed sufficiently away from the hot source to avoid any thermal damage to the filter.

To collect the EM waves from the source and direct them to the detector, two calcium fluoride (CaF_2) plano-convex lenses were used as shown in Figure 6-2. Due to high transmittance (~ 92%) in the range 1-8 μm and high optical damage threshold (~10 J/cm^2 at the CO_2 laser wavelength of 10.64 μm), CaF_2 lenses are commonly used in cryogenically cooled thermal imaging systems. Its refraction index and melting temperature are 1.418 at 4.21 μm and 1418°C respectively. The diameter, center thickness and effective focal length of the lens were 25.4, 6.2 and 50 mm for the source lens and 25.4, 7.5 and 40 mm for the detector lens respectively. The convex surfaces of both lenses were placed toward the incident waves (Figure 6-2) to reduce the spherical aberration [72]. To determine the field of view, i.e., the area of the source from where the lens collects the EM waves, a ray tracing method was used [72, 106]. Based on the dimensions of our experimental setup shown in Figure 2, the diameters of the field of view and irradiated spot are 25.4 and 3.8 mm respectively.

If there is no energy loss when the radiation propagates from the source lens to the detector lens, the absorbed irradiance in the detector (I_a) can be written as

$$I_a(T) = \alpha_{d,\lambda} \frac{A_{rs}}{r_d^2} F_{sl} \int_{\lambda_0 - \Delta\lambda_0/2}^{\lambda_0 + \Delta\lambda_0/2} L_{\lambda,s}(\lambda, T) d\lambda \ , \tag{6-1}$$

where $\alpha_{d,\lambda}$, A_{rs} and r_d are, respectively, the absorbance of the doped sample based on multiple reflections, surface area of the radiation source viewed by the source lens, and the radius of the irradiated spot on the detector for the MWIR wavelength λ. F_{sl} is the view factor as the radiation source is viewed by the source lens, which is given by

$$F_{sl} = \frac{1}{2}\left\{1 + \frac{d_{sl}^{\ 2} + r_{sl}^{\ 2}}{r_{rs}^{\ 2}} - \left[\left(1 + \frac{d_{sl}^{\ 2} + r_{sl}^{\ 2}}{r_{rs}^{\ 2}}\right)^2 - 4\left(\frac{r_{sl}}{r_{rs}}\right)^2\right]^{1/2}\right\}$$

for coaxial parallel disks [71], where r_{sl} and r_{rs} are the radii of the source lens and the radiation source, respectively, and d_{sl} is the distance from the radiation source to the source lens. λ_0 is the central wavelength to be detected by the detector and $\Delta\lambda_0$ is the spectral range, i.e., the full width at half maximum (FWHM) around λ_0. From the absorbance data of Ga-doped 4H-SiC in Figure 6-1(a), λ_0 would be 4.21 and 4.63 μm corresponding to the two absorption peaks and the values of $\Delta\lambda_0$ are 0.09 and 0.12 μm for these two wavelengths respectively.

6.3.2 Measurement of Optical Signal for Testing the Response of the Ga-doped Sample

The value of $I_a(T)$ needs to be maximized to optimize the change of the electron density in the valence band and the dopant energy level of the detector. This will cause a large change in the reflectivity of the detector per unit change in the source temperature for the He-Ne laser of wavelength 632.8 nm, improving the detector response. The optical signal is the reflected power of the He-Ne beam, which is measured to test the effect of the source temperature on the detector response. The stainless steel source was heated using an induction heater and the surface

temperature was measured with a thermocouple. The power input from the heater to the source was controlled to achieve stable source temperatures, which enabled carrying out detector response experiments at fixed temperatures.

To increase the irradiance at the detector surface, a ray tracing method was used for designing the MWIR radiation collection optics. The distances of the CaF_2 lenses were varied to obtain the largest source size (field of view) and the smallest irradiation spot on the detector (image size). The focal lengths of the source and detector lenses were 50 and 40 mm respectively. The source and image radii were 12.7 and 1.9 mm, respectively, when the source lens, detector lens and detector were at 80 mm from the source, 5 mm from the source lens and 20 mm from the detector lens, respectively, as shown in Figure 6-2. The narrow bandpass filter was placed right next to the convex surface of the source lens.

A He-Ne laser of wavelength 632.8 nm with an output power up to 15 mW was directed to the detector (doped region) at normal incidence. The incident power of the He-Ne laser was measured right below the beam splitter in Figure 6-2. The reflected laser beam was directed to a Si-based He-Ne detector as shown in Figure 6-2 to measure the reflected power that represents the optical signal of the SiC MWIR detector. The ratio of the reflected power to the incident power of the He-Ne beam yields the reflectance of the Ga-doped SiC sample. Experiments were conducted without any lens, with only the source lens and with both the source and detector lenses to examine the effect of irradiance, $I_a(T)$, on the optical response of the SiC detector.

6.3.3 Multiple Reflections of the He-Ne beam

Both the He-Ne laser beam and the MWIR waves can undergo multiple reflections in the 4H-SiC sample, increasing the absorption of photons in the detector. This will improve the quantum efficiency and, therefore, the detector response. The undoped as-received sample offers two air–SiC interfaces at the top and bottom surfaces of the sample. On the other hand, the Ga-doped sample has three interfaces between the air and doped region, doped region and undoped silicon carbide, and undoped silicon carbide and air. When the He-Ne beam is incident on the top surface of the undoped as-received 4H-SiC region, a fraction of this beam is reflected, absorbed and transmitted in the sample. These fragmented beams undergo further reflection and transmission at the bottom surface of the sample. Summing powers of all the rays at various points on the top (reflectance) surface and on the bottom (transmittance) surface [73], the reflectance (ρ_j) and transmittance (τ_j) of the undoped and doped samples are given by Equations (3-19) and (3-20), respectively.

The thickness of doped region was taken to be the depth up to which the Ga atoms diffuse in the 4H-SiC substrate during the doping experiment. This diffusion length is given by $d_d = 2\sqrt{D_{Ga} t_d}$, where D_{Ga} is the diffusion coefficient of Ga in the substrate and t_d is the diffusion time. Generally t_d is taken as the laser-substrate interaction time, which is the ratio of the laser beam diameter on the substrate surface to the speed of the laser beam relative to the substrate. The value of t_d is 0.25 s for the doping experiment in this study. It has been shown that the diffusion coefficient increases by 5 to 6 orders of magnitude in laser doping processes and that the

diffusion coefficient of aluminum (Al) atoms in silicon carbide is 1.2×10^{-5} cm^2/s [58]. Assuming similar trend for the diffusion of Ga, D_{Ga} was taken as 5.0×10^{-5} cm^2/s to estimate d_d as 500 nm.

It should be noted that Equations (6-2) and (6-3) involve reflectivity and absorption coefficient. While the reflectivity depends only on material properties itself, reflectance depends on the material dimensions also [107]. The absorption coefficient (μ) is related to the absorption index (κ) by the expression $\mu = 4\pi\kappa/\lambda$, where λ is the wavelength of interest in vacuum. If the refraction and absorption indices of each of the two media are, respectively, n_1 and κ_1, and n_2 and κ_2, the Fresnel reflectivity at the interface of these two media is given by $\rho = \frac{(n_2 - n_1)^2 + (\kappa_2 - \kappa_1)^2}{(n_2 + n_1)^2 + (\kappa_2 + \kappa_1)^2}$ for the wavelength λ. Utilizing these two expressions for absorption coefficient (μ) and reflectivity (ρ) in Equations (3-19) and (3-20), the refraction and absorption indices of the as-received and Ga-doped samples were calculated for the He-Ne laser and MWIR wavelengths for normal incidence on the samples at room temperature. These results are listed in Table 6-1. The reflectivity and absorption coefficient are two important parameters for determining the reflectance of the detector.

6.3.4 Analysis of the Reflected Power to Determine the Detectivity and the NETD for the Ga-doped Sample

Conventional photon detectors produce electrical signals. In such ***electrical photodetectors***, the photogenerated electrons migrate from the photon-detector interaction region to other parts of the detector and eventually flow through an electric circuit. An expression for the detectivity of this

type of detectors can be found in Ref. [28]. On the other hand, the ***optical photodetector*** of this study produces optical signals. In this optical photodetector, the photoexcited electrons populate a higher energy level depending on their lifetime and diffusive loss in the excited state. The detectivities of these two types of detectors, will therefore, involve different parameters.

The functionality of the optical photodetector of this study involves two devices. One of them is the Ga-doped 4H-SiC substrate, which acts as the MWIR detector and produces optical signals by reflecting a He-Ne beam. The second device is the Si detector coupled with a power meter, which detects the reflected He-Ne beam and measures its power. The detectivity, therefore, constitutes the performance of these two devices. The rms (root mean square) noise current is [108] $i_n = \sqrt{2e\bar{i}\Delta f}$ in the Si He-Ne beam detector, assuming that the shot noise in the detector is caused by the dc-photogenerated current $\bar{i}$ flowing across a potential barrier. Here e is the electron charge and Δf is the electrical bandwidth. The average output current, $\bar{i}$, is produced due to the incidence of background photons and the source photons on the SiC MWIR detector [108]. Since the photons are collected from the source using a lens and focused to a tiny spot on the detector, the irradiance on the detector would be much higher due to the source photons than the background photons.

In the presence of MWIR irradiance on the SiC detector, the average signal current, $\bar{i}_s$, can be expressed as $\bar{i}_s = \left(\eta_{e,Si} I^*_{r,l} \lambda_l A_{Si} \alpha_{Si} e\right)/(hc)$, where $\eta_{e,Si}$, A_{si} and α_{Si} are the external quantum efficiency, active area and absorbance of the Si He-Ne beam detector, respectively. $I^*_{r,l}$ is the irradiance on the Si detector due to the reflected He-Ne laser in the presence of MWIR irradiance

on the SiC detector and λ_l is the wavelength of the Ne-Ne laser. Therefore $I^*_{r,l}\lambda_l / hc$ is the number of He-Ne laser photons incident on the Si detector per unit area per unit time. The irradiance can be related to the reflectance of the SiC MWIR detector by the expression $I^*_{r,l} = \rho^*_{d,l} I^*_{i,l}$, where $I^*_{i,l}$ is the irradiance of the He-Ne laser incident on the SiC detector and $\rho^*_{d,l}$ is the reflectance of the SiC detector for the He-Ne laser wavelength in the presence of MWIR irradiance.

In the absence of any MWIR irradiance on the SiC detector, the average noise current, $\bar{i}_n$, can be expressed as $\bar{i}_n = \left(\eta_{e,Si} I_{r,l} \lambda_l A_{Si} \alpha_{Si} e\right)/\left(hc\right)$. Here $I_{r,l}$ is the irradiance on the Si He-Ne beam detector due to the reflected He-Ne laser in the absence of MWIR irradiance on the SiC MWIR detector. Identifying $\bar{i}_n$ as the average background current ($\bar{i}_{bg}$), i.e., $\bar{i}_n = \bar{i}_{bg} = \bar{i}$, and substituting it into i_n, the signal-to-noise ratio (S/N) can be written as $\bar{i}_s / i_n$, i.e.,

$$\frac{S}{N} = I^*_{r,l} \sqrt{\frac{\eta_{e,Si} A_{Si} \alpha_{Si}}{2 I_{r,l} \Delta f}} \sqrt{\frac{\lambda_l}{hc}} \,. \tag{6-2}$$

The minimum irradiance ($I^{*,m}_{r,l}$) for detectable signal is obtained by setting S/N = 1 in Equation (6-4), which yields $I^{*,m}_{r,l} = \left[\left(2 I_{r,l} \Delta f hc\right)/\left(\eta_{e,Si} A_{Si} \alpha_{Si} \lambda_l\right)\right]^{1/2}$. Therefore the noise-equivalent power (NEP), which is given by $I^{*,m}_{r,l} A_{Si}$, can be written as

$$NEP = \sqrt{\frac{2I_{r,l}A_{Si}\Delta f}{\eta_{e,Si}\alpha_{Si}}}\sqrt{\frac{hc}{\lambda_l}} \,. \tag{6-3}$$

The detectivity, which is defined as $D^* = \frac{\sqrt{A_{Si}\Delta f}}{NEP}$, can now be written as $D^* = \sqrt{\frac{\eta_{e,Si}\alpha_{Si}}{2I_{r,l}}}\sqrt{\frac{\lambda_l}{hc}}$.

This expression is modified using Equation (6-4) and the expression for $I^*_{r,l}$ to obtain D^* as

$$D^* = \frac{(S/N)}{\rho^*_{d,l}I^*_{i,l}}\sqrt{\frac{\Delta f}{A_{Si}}} \tag{6-4}$$

Equation (6-6) combines the effects of both the Si He-Ne beam detector and the SiC MWIR detector. It can be used to determine the noise equivalent temperature difference (NETD) based on the following equation [84]:

$$NETD = \frac{4F^2}{D^*\tau_0\left(\frac{dI_a}{dT}\right)_{\lambda_{1-}-\lambda_{2+}}}\sqrt{\frac{\Delta f}{A_d}} \,, \tag{6-5}$$

where F is the f-number of the detector lens, τ_0 is the product of the transmissivities of the lens and filter, and A_d is the active area of the detector. $\left(\frac{dI_a}{dT}\right)_{\lambda_{1-}-\lambda_{2+}}$, which is the change in absorbed

irradiance with respect to the source temperature in the emission band $\lambda_{1-} - \lambda_{2+}$, can be expressed as

$$\left(\frac{dI_a(T)}{dT}\right)_{\lambda_{1-}-\lambda_{2+}} = \left(\frac{\pi\varepsilon_{\lambda,s}A_s F_{sS}\alpha_{d,\lambda}}{A_d}\right)\left[\int_{\lambda_{1-}}^{\lambda_{1+}}\left\{\frac{C_1C_2\exp(C_2/\lambda T)}{T^2\lambda^6\left(\exp(C_2/\lambda T)-1\right)^2}\right\}d\lambda + \int_{\lambda_{2-}}^{\lambda_{2+}}\left\{\frac{C_1C_2\exp(C_2/\lambda T)}{T^2\lambda^6\left(\exp(C_2/\lambda T)-1\right)^2}\right\}d\lambda\right], \quad (6\text{-}6)$$

where C_1 and C_2 are two constants in Planck's blackbody radiation theory, which are given by $C_1 = 1.191\times10^8$ W·μm^4/m^2·sr and $C_2 = 1.439\times10^4$ μm·K. $\alpha_{d,\lambda}$ is the absorbance of the Ga-doped 4H-SiC sample, based on multiple reflections, for the MWIR wavelength λ and the two emission bands are from $\lambda_{1-} = 4.2$ to $\lambda_{1+} = 4.29$ μm and from $\lambda_{2-} = 4.54$ to $\lambda_{2+} = 4.66$ μm. $\varepsilon_{\lambda,s}$ is the emissivity of stainless steel radiation source, which is 0.7 for these emission bands. Noting that $\alpha_{d,\lambda} = 0.32$, Eq. (8) yields $\left(\frac{dI_a}{dT}\right)_{\lambda_{1-}-\lambda_{2+}} = 1.46\times10^{-3}$ μW/mm^{2}K. The transmissivities of the lens and filter are 1 and 0.925, respectively, at 4.21 μm, yielding $\tau_0 = 0.925$. $F = 1/(2\sin\theta)$ where $\sin\theta$ is 12.5/21.65 in this case (Figure 6-2) and, therefore $F = 0.866$. The spectral photon radiance (photons/s·cm^2·sr·μm) can be obtained by multiplying the absorbed irradiance by λ/hc. The detector absorbs a photon flux of 2.202×10^9 photons/s at 25°C in the present setup. The reflected power of the He-Ne beam does not change if the absorbed photon flux is less than this value.

NETD was also determined from experimental data using the relationship [109], $NETD = \sigma_n/SITF$, where σ_n and SITF are the standard deviation of the detector signal and the system intensity transfer function respectively. Based on Bessel's correction to the conventional

definition of the standard deviation, the expression for σ_n can be written as [32] $\sigma_n = \sqrt{\left[N\sum_{i=1}^{N}(P_i)^2 - \left(\sum_{i=1}^{N} P_i\right)^2 \right] / \left(N(N-1)\right)}$, where P_i, i = 1, 2, 3, ⋯⋯⋯ N, is the i-th value of the optical signal, i.e., the reflected power of He-Ne beam, measured at different times to obtain N signals for the same source temperature. The system intensity transfer function (SITF) [109] of the detector is given by $SITF = \left(\overline{P}_s - \overline{P}_{BG}\right) / \left(T_s - T_{BG}\right)$, where $\overline{P}_s$ and $\overline{P}_{BG}$ are the averages of N_s and N_{BG} values of the reflected He-Ne laser power for the source and background temperatures T_s and T_{BG}, respectively. Lloyd [84] pointed out how to select these two temperatures so that T_s - T_{BG} is not zero. Experiments were conducted to measure the variations in the reflected powers of He-Ne beam by keeping the stainless steel radiation source at room (ambient) and higher temperatures. The data were recorded in a computer using a data acquisition system for a period of 25 seconds at each temperature as presented in Figure 6-3. 100 values (N = 100) of the reflected He-Ne laser power were selected arbitrarily for each temperature to calculate NETD.

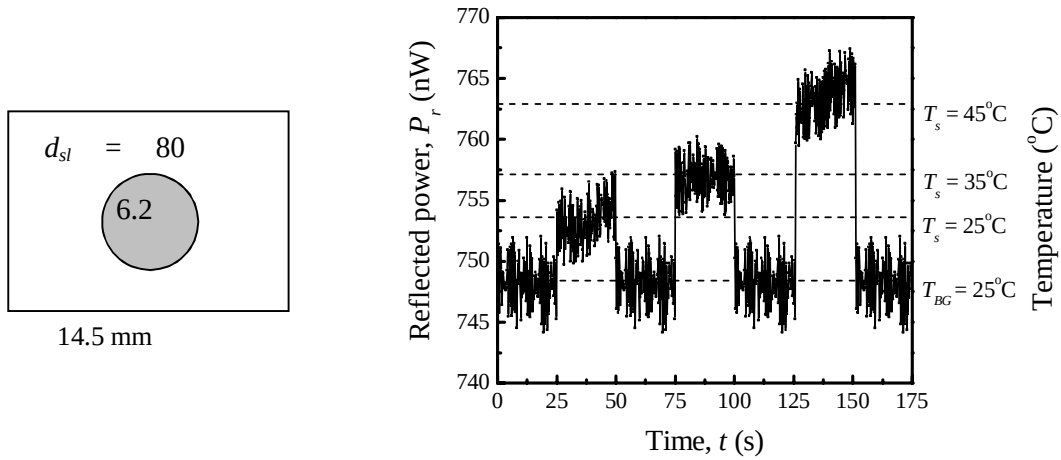

Figure 6-3: Reflected powers of the He-Ne beam at room and higher temperatures of the source to determine NETD. T_{BG} is the background temperature of other materials surrounding the source. It is 25°C in this study and the reflected power is lower than that of the source due to the difference in emissivity.

6.4 Results and Discussion

6.4.1 Changes in the Reflectance and Refraction Index of the SiC Detector as a Function of the Absorbed MWIR Irradiance

The SiC detector consists of two regions which are doped and undoped (as-received) regions. To calculate the optical properties of the detector, the properties of the doped region and the as-received sample were obtained. The powers (P_r) of a He-Ne beam reflected by the SiC detector were measured using a silicon He-Ne beam detector by varying the temperature of the stainless steel radiation source from room temperature (25°C) to 650°C. For a given temperature of the

source, its spectral radiance and its radiance within a finite spectral range are plotted as shown in Figure 6-4(a).

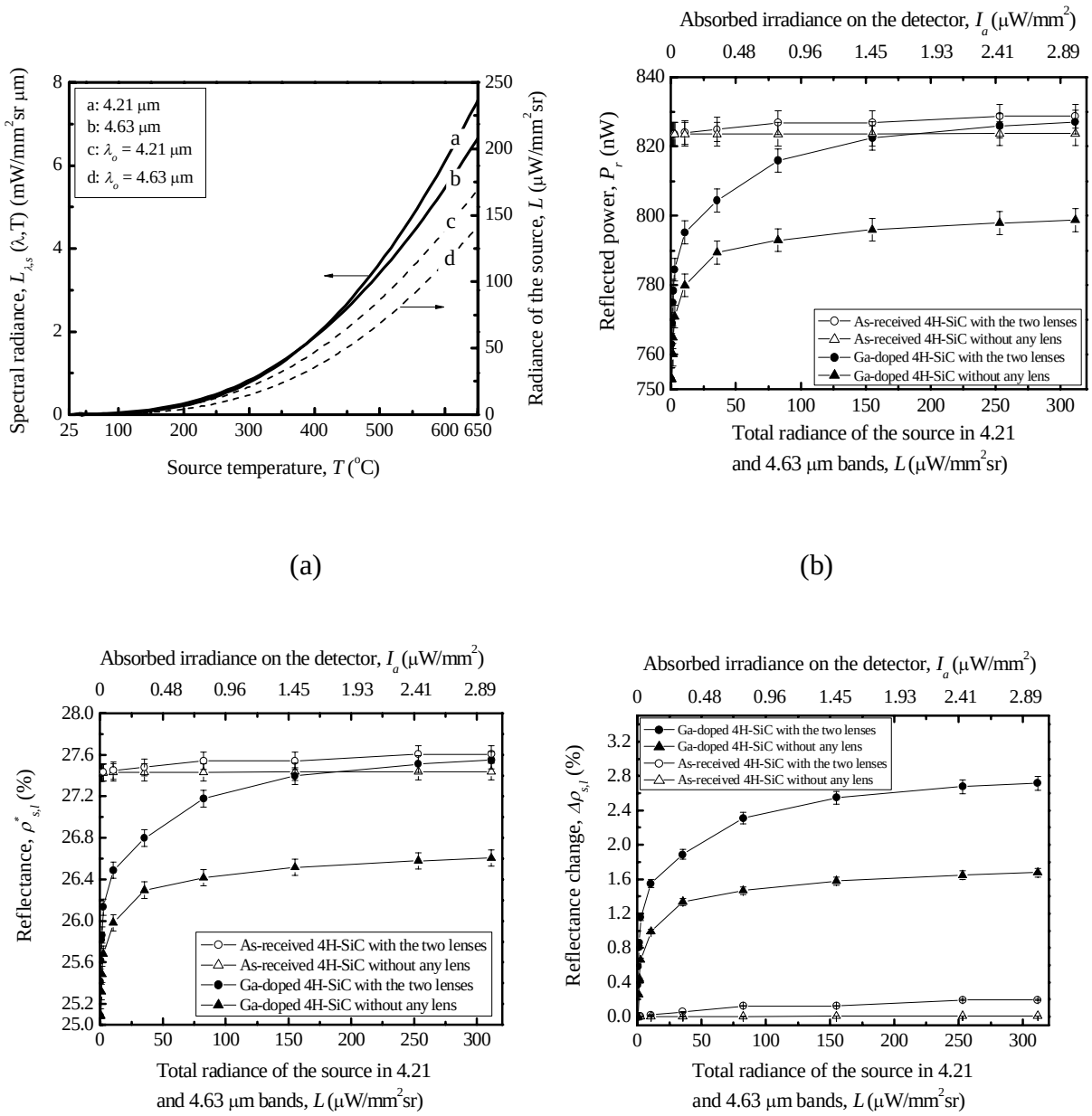

Figure 6-4: Effects of the radiance of the source and the number of lenses on the optical response of the detector (Ga-doped sample) compared to the as-received (undoped) sample, showing that the doped sample produces a significant optical signal at the He-Ne laser wavelength of 632.8 nm: (a) effect of the source temperature on its

radiance at two wavelengths, (b) reflected powers, (c) reflectances and (d) changes in the reflectance of the as-received and Ga-doped samples. The resolution of the Si He-Ne beam detector was 0.63 nW.

The source emits more radiation as its temperature increases and, consequently, the MWIR irradiance (W/cm^2) increases on the SiC detector. The reflectance is given by $\rho^*_{s,l} = P_r / P_i$, where $\rho^*_{s,l}$ represents the reflectance of the sample *s*, based on multiple reflections, for the He-Ne laser wavelength in the presence of MWIR irradiance on the sample. P_i is the power of the incident He-Ne beam on the sample, and $s = u$ and d for the undoped as-received and Ga-doped 4H-SiC samples respectively. For each type of sample, the reflected power was also measured by keeping the stainless steel radiation source at room temperature and the reflectance was calculated. This baseline reflectance is designated by $\rho_{s,l}$, which represents the reflectance of sample *s* for the He-Ne laser wavelength in the absence of any MWIR irradiance on the sample from a hot source. The values of $\rho_{s,l}$ are found to be 26.47% and 25.02% for the undoped and doped samples respectively. The change in the reflectance was obtained from $\Delta\rho_{s,l} = \rho_{s,l} - \rho^*_{s,l}$. These results are plotted in Figures 6-4(b-d), which show that the reflectance of the doped sample changes significantly due to the MWIR wavelengths 4.21 and 4.63 μm as the temperature of the radiation source increases, while the change is very small for undoped as-received sample. More photon flux from the source at elevated temperatures and the presence of Ga energy level corresponding to the photon energy in the doped sample are two important factors for better response of the doped sample than the undoped sample.

When the radiation source was at room temperature, the reflected and transmitted powers of the He-Ne beam were measured for both samples and the reflectance and transmittance were calculated. Using Equations (6-2) and (6-3), the baseline refraction ($n_{s,l}$) and absorption indices were calculated. $n_{s,l}$ represents the refraction index of sample *s* for the He-Ne laser wavelength in the absence of any MWIR irradiance on the sample from a hot source. The values of $n_{s,l}$ are found to be 3.442 and 3.217 for the undoped (as-received 4H-SiC) and Ga-doped samples respectively. The absorption indices are found to be 1.421×10^{-4} and 1.530×10^{-4} for the undoped and doped samples, respectively, at the He-Ne laser wavelength of 632.8 nm. Based on these values of the $n_{s,l}$, absorption indices and the reflectance data (Table 6-1) of the undoped and doped samples, the refraction index ($n^{*}_{s,l}$) of the SiC detector was calculated using Equations (6-2) and (6-3) for the He-Ne laser wavelength in the presence of MWIR irradiance on the sample. The change in the refraction index was obtained from $\Delta n_{s,l} = n_{s,l} - n^{*}_{s,l}$. These results are plotted in Figures 6-5(a) and (b), which show that the refraction index of the detector is distinctly different from the refraction index of the undoped sample in the presence of MWIR wavelengths 4.21 and 4.63 μm emitted by the radiation source.

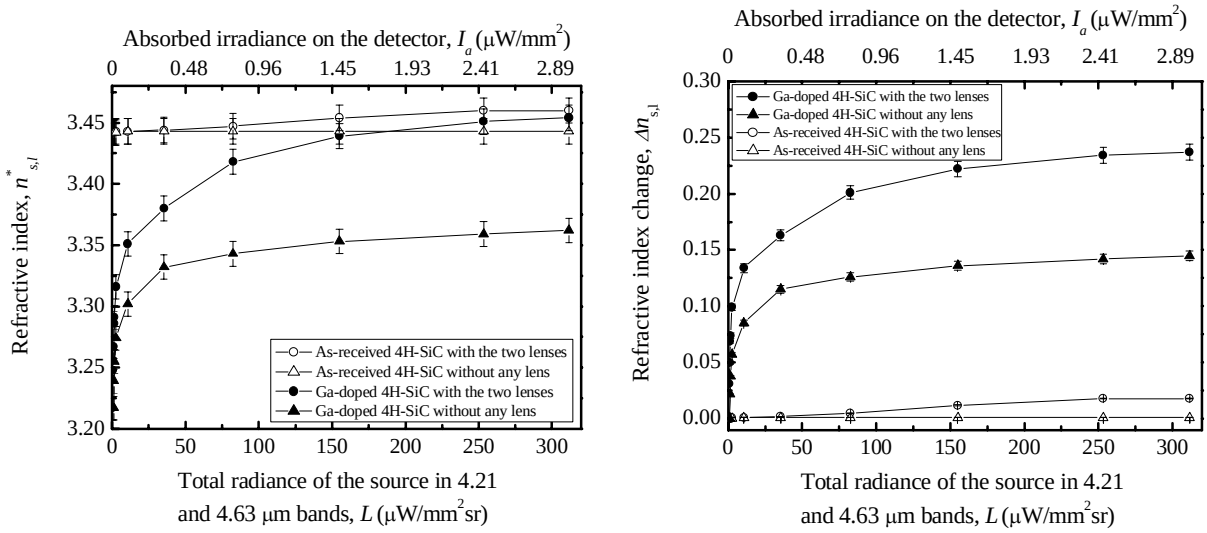

(a) (b)

Figure 6-5: Effects of the radiance of the source and the number of lenses on the refraction index of the detector compared to the as-received sample, showing a significant effect on the refraction index of the detector at the He-Ne laser wavelength of 632.8 nm: (a) refraction indices and (b) changes in the refraction index of the as-received and Ga-doped samples. The resolution of the Si He-Ne beam detector was 0.63 nW.

The doped sample has lower refraction index in the presence of the MWIR irradiance because of the lower refraction index of the doped sample at room temperature than the undoped sample. Figure 5(b) shows that a significant change in the refraction index of the doped sample, while the change is very small for the undoped sample. These significant changes in the reflectance and refraction index indicate that the Ga-doped sample can be used for fabricating MWIR detectors.

6.4.2 Effect of Radiation Collection Lenses and the Power Resolution of the Si He-Ne Beam Detector

To determine the minimum temperature of the radiation source for which the SiC detector produces a detectable optical signal, the radiation collection optics as well as the resolution of measuring the reflected He-Ne beam power by the Si detector were examined. Three optical arrangements were considered to collect the radiation, which are (i) no lenses, (ii) just one lens and (iii) two lenses between the source and SiC detector. The Si detector was operated in the nanowatt scale with resolutions of 0.631 nW and 48 nW. At this low power level of the reflected He-Ne beam, the Si He-Ne beam detector exhibited an error of 0.3%. These results are presented in Figure 6-6(c).

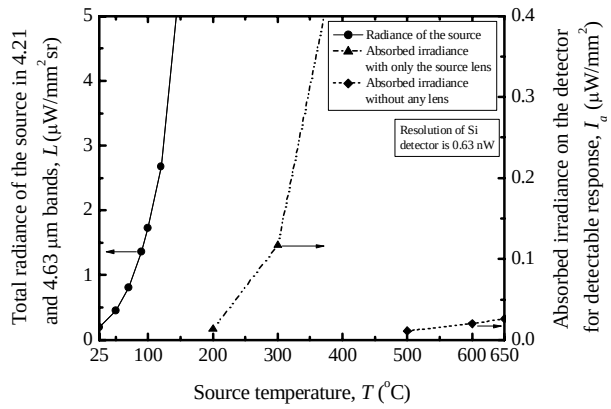

(a)

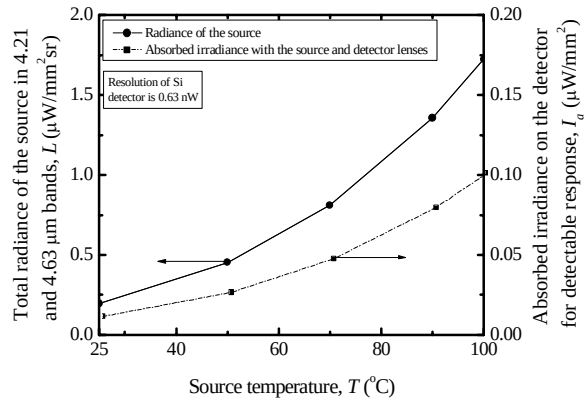

(b)

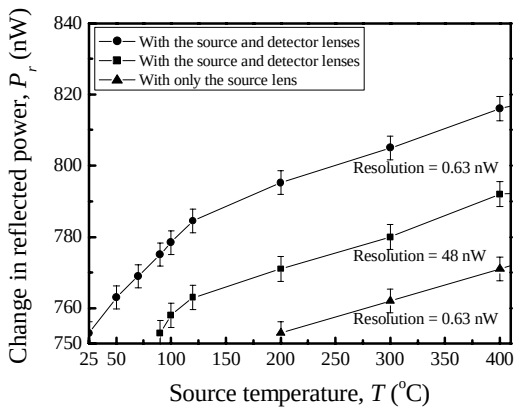

(c)

Figure 6-6: Effects of the source temperature, the number of lenses and the resolution of the Si He-Ne beam detector on the MWIR detectibility of the SiC detector: (a) threshold source temperature for MWIR detection with just the source lens and without any lens, (b) MWIR detection at room temperature (25°C) with two lenses and 0.63 nW resolution of the Si detector, and (c) effects of the resolution of Si detector on MWIR detection by the SiC detector, showing that low resolution and two lenses enable MWIR detection at room temperature of the source.

Figures 6(a) and (b) show the total radiance of the source in 4.21 and 4.63 μm bands and absorbed irradiance on the SiC detector for detectable response with no lenses, one lens and two lenses as a function of the source temperature. A detectable response is obtained at a lower temperature (25°C) with two lenses because two lenses collect more radiation from the source and produce higher irradiance on the SiC detector than the other two optical configurations. On the other hand, the He-Ne beam power measurement resolution of the Si detector also affects the radiation detection capability for a source of low temperature. It can be seen in Figure 6-6(c) that the detector response begins at the source temperature 90°C for 48 nW resolution, while a detectable signal is obtained for the source at room temperature with two lenses for 0.63 nW resolution. These results indicate that although the SiC MWIR detector can operate at room temperature, the optics and the resolution of the Si detector are important in detecting objects that are at room temperature.

6.4.3 NETD and Detectivity

Experimental NETD: As pointed out earlier, the MWIR detection in this study involves the response of the SiC MWIR detector, and the responses of the Si He-Ne beam detector and the associated power meter. The NETD of this SiC/Si detector system is calculated using the experimental values of the reflected He-Ne laser power (optical signal) as presented in Figure 3. The average values of the signals are $\overline{P}_{r,1}$ = 753 nW, $\overline{P}_{r,2}$ = 757 nW and $\overline{P}_{r,3}$ = 762 nW at 25°C, 35°C and 45°C, respectively, and the corresponding standard deviations are σ_1 = 9.342 nW, σ_2

= 6.257 nW and σ_3 = 9.877 nW. Applying SITF to two pairs of data at 25 and 35°C, and at 25 and 45°C, the system intensity transfer functions are obtained as $SITF_{12}$ = 0.5266 nW/K and $SITF_{13}$ = 0.7248 nW/K, respectively, and the corresponding values of NETD are $NETD_{12}$ = 1774 mK and $NETD_{13}$ = 863 mK.

These values of NETD are much higher than the required thermal resolution of 100 mK. Thermal resolution below 100 mK is achieved in staring thermal imagers using thermal detectors in focal plane arrays (FPAs) because NETD is influenced by the active area of the detector. For uncooled IR detector systems, Niklaus et al. [101] and Dong et al. [102] obtained an NETD of 7 K, while Picone [110] and Gupta and Ballato [111] reported NETD in the range of 50-100 mK. The SiC detector of this study can be configured as a focal plane array by laser doping selected regions of the substrate. To achieve low NETD, traditional infrared detectors also typically have integrated circuit amplifiers or gain elements on the same microchip as the detector to provide several orders of magnitude of amplification of the signal before being transmitted. These features are expected to lower the NETD of the uncooled SiC optical photodetector.

D^* based on experimental S/N: The detectivity of the SiC/Si detector system is determined from Equation (6-6) using the experimental result for the signal-to-noise ratio (*S/N*) and an appropriate value of Δf. Based on the data at room temperature (25°C) in Figure 3, $S/N = \overline{P}_{r,1}/\sigma_1 = 80.6$. The bandwidth is related to the time constant (t_c) of an instrument by the expression $\Delta f = 1/(2t_c)$. The results in Figure 3 were obtained using a Si He-Ne beam detector coupled with a power meter for which the time constant is t_c = 10 ms. The time constant of the SiC MWIR detector is expected to be much lower than 10 ms. For example, different polytypes of SiC, such as 3C-, 4H-, and

6H-SiC, have fast (< 20 ns) response time in photoconductive switches [112-116]. The response of a system, however, is governed by the component of longest time constant. Therefore the bandwidth of the SiC/Si detector system is taken as Δf = 50 Hz. Other parameters for the results in Figure 6-3 are the incident He-Ne laser irradiance on the SiC detector, $I^*_{i,l}$ = 26.786 nW/mm^2, the reflectance of the SiC detector, $\rho^*_{d,l}$ = 0.28 for the He-Ne laser wavelength and the Si detector area A_{Si} = 1.131 mm^2 for a He-Ne beam of diameter 1.2 mm. Substituting these values into Equation (6-6), the detectivity of the SiC/Si detector system is found to be 7.15×10^9 cm·Hz$^{1/2}$/W when both the detector and the radiation source are at 25°C.

The performances of various detectors at 4.21 μm wavelength are listed in Table 6-2 to compare the characteristics of the SiC/Si detector system with other IR detectors.

Table 6-2: Performances of various infrared detectors at 4.21 μm wavelength.

Detector	Operating Temp. (K) [Ref. 97]	Noise bandwidth, Δf (Hz) [Ref. 97]	Detectivity, D^* (cm·Hz$^{1/2}$/W) [Ref. 97]	NETD (mK)	$D^* / \sqrt{\Delta f}$
HgCdTe	77	1000	1.2×10^{11}	20 [Ref. 95]	3.8×10^{9}
InSb	77	1000	1.1×10^{11}	10 [Ref. 117]	3.5×10^{9}
PbSe	193	1000	3.3×10^{10}	200 [Ref. 110]	1.0×10^{9}
PtSi	300	30	3.0×10^{10}	100 [Ref. 14]	5.5×10^{9}
Au-doped Ge (Ge: Au)	77	1000	8.0×10^{9}	-	2.2×10^{8}
Thermocouple	300	10	1.8×10^{9}	100 [Ref. 110]	5.7×10^{8}
Pyroelectric	300	10	1.2×10^{9}	50 [Ref. 111]	3.8×10^{8}
Thermistor bolometer	300	10	1.9×10^{8}	50 [Ref. 101]	6.0×10^{7}
Thermopile	300	10	1.2×10^{8}	100 [Ref. 111]	3.8×10^{7}
SiC/Si detector system (this study)	298	50	7.15×10^{9}	1774	1.0×10^{9}

It should be noted that the optical configurations to collect infrared radiation from the field of view might not be the same for all the detectors listed in Table 6-2, and that the radiation collection optics affects the NETD significantly. Also the bandwidths are different for different detectors and that is why $D^* / \sqrt{\Delta f}$ is listed in Table 6-2 to compare this normalized detectivity of various detectors. This normalized detectivity of the SiC/Si detector system compares well

with other detectors. However, the NETD of the SiC/Si detector system is very large, which can be reduced by increasing the signal-to-noise ratio as discussed below.

Effect of Δf on D^*: Equation (6-6) shows that the detectivity can be increased by increasing the bandwidth of the detector. Newer models of Si He-Ne beam detector with associated power meter are available for which the time constant is t_c = 2 μs with corresponding bandwidth Δf = 2.5×10^5 Hz. With such fast Si detectors, the detectivity of the SiC/Si detector system would be 5.1×10^{11} cm·Hz$^{1/2}$/W. The detectivity of an ideal electrical photodetector [85] is 1.8×10^{11} cm·Hz$^{1/2}$/W for the MWIR wavelength 4.21 μm when the radiation source is at 27°C, and the detector temperature is sufficiently low so that the self-emission processes do not emit an appreciable number of photons. With lower time constant, the detectivity of the SiC/Si detector system would be higher than the ideal value because the SiC detector is based on the principle of generating optical signals with the photoexcited electrons remaining practically immobile inside the SiC detector. So the loss of photoexcited electrons occurs mainly due to their diffusion in this optical photodetector. In the conventional electrical photodetectors, on the other hand, electrical signals are produced due to mobile photogenerated electrons as they travel from the region of photon-detector interaction to other parts of the detector. So the loss of signal is due to both the scattering and diffusion of electrons in the electrical photodetectors.

Theoretical NETD: The detectivities and the corresponding values of Δf can be substituted into Equation (6-7) to determine the theoretical NETD of the SiC/Si detector system. Noting that the active area of the SiC detector is A_d = 1.131 mm^2 for a He-Ne beam of diameter 1.2 mm, and

using the values of F, τ_0 and $\left(\frac{dI_a}{dT}\right)_{\lambda_{1-}-\lambda_{2+}}$, which are discussed in section 6.3, the theoretical values of NETD are found to be 207 and 205 mK for the SiC/Si detector systems of detectivities 7.15×10^9 and 5.1×10^{11} cm·Hz$^{1/2}$/W respectively. Ideally these two values of NETD should be equal because it can be shown that NETD is independent of D^* and Δf by substituting D^* from Equation (6-6) into Equation (6-7). NETD is inversely proportional to S/N. The difference between the two values of NETD can be attributed to the computational rounding error. However, the theoretical NETD is much lower that the experimental NETD. This discrepancy between the theory and experiment might be due to the effect of $\left(\frac{dI_a}{dT}\right)_{\lambda_{1-}-\lambda_{2+}}$. All the photons of the absorbed irradiance, $I_a(T)$, might not contribute to the generation of optical signal and, consequently, the theoretical value of $\left(\frac{dI_a}{dT}\right)_{\lambda_{1-}-\lambda_{2+}}$ obtained from Equation (6-8) might be higher than the actual occurrence in the SiC detector.

Effects of S/N and time constant on the detectivity and NETD of just the SiC detector: Bai et al. [40] fabricated 4H-SiC PIN avalanche photodiodes (APDs) for ultraviolet (UV, 280 nm wavelength) photon detection and demonstrated a fairly large detectivity of 4.1×10^{14} cm·Hz$^{1/2}$/W. At the bias voltage of 144 V for this type of APDs, Bai et al. [118] reported the noise equivalent power (NEP) as 20 fW of incident light power and the highest incident light power as 4×10^3 fW, which leads to the signal-to-noise ratio of ~200. They [118] were able to reduce the NEP to ~4.4 fW using a lock-in amplifier, which significantly increases S/N to ~909. Qian et al. [119] fabricated a Si UV-sensitive photodetector and tested its response in the range of 300-650 nm at

different bias voltages. Their detector consisted of separate photoabsorption and charge multiplication regions, which were a shallow p-n junction for photoelectric conversion and a nearby n-p-n output transistor for signal amplification respectively. They were able to achieve S/N up to 7×10^6 with this particular amplification feature. The signal rise time of the photodetector was in the range of 2.16-750 ns for bias voltages varying from 1-20 V.

However, the operational mechanism of these electrical photodetector is different from the optical photodetector of this study. Equation (6-6) is used to determine the detectivity by replacing A_{si} with A_d and referring all other variables such as D^*, S/N and Δf to the characteristics of just the SiC detector, while NETD is calculated using Equation (6-7).

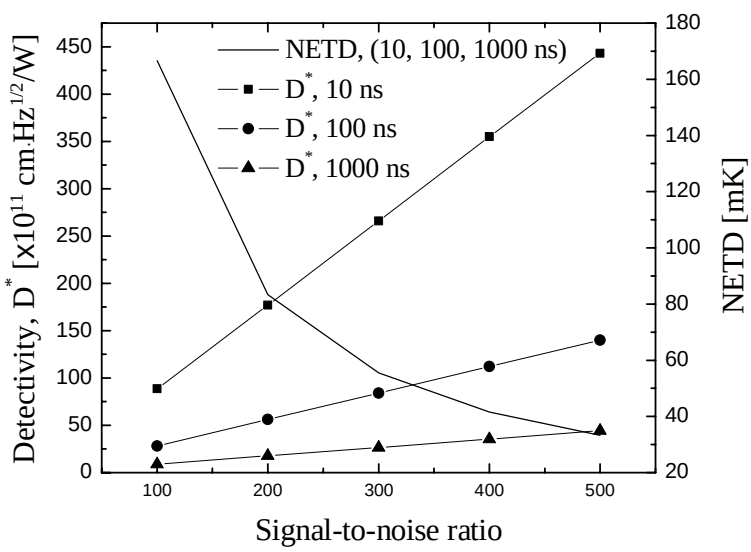

Figure 6-7: Effects of signal-to-noise ratio on the detectivity and NETD of just the SiC optical photodetector for three different time constants (10, 100 and 1000 ns) of the detector.

To examine the effects of S/N and Δf on D^* and NETD, S/N is varied from 100 to 500 for three different time constants 10, 100 and 1000 ns corresponding to $\Delta f = 5\times10^7$, 5×10^6 and 5×10^5 Hz respectively. The results are presented in Figure 6-7, showing that the detectivity is linearly proportional to S/N, while NETD is inversely proportional to S/N. Figure 6-7 also shows that the detectivity is affected by the time constant of the detector but the NETD is independent of the time constant for a given S/N. The NETD of the detector can be lowered by increasing its signal-to-noise ratio.

6.4.4 Comparison of Theoretical and Experimental value of NETD and Detectivity

The noise-equivalent temperature difference (*NETD*) is the one of the figure of merits defining the smallest temperature difference between two points of a source that a detector can image distinguishably. It represents the temperature of a source above the background (ambient) temperature that produces a signal in the detector equal to the RMS of the detector noise. $NETD_{Exp}$ can be determined as the ratio of the standard deviation of the detector signal (σ_n) to the System Intensity Transfer Function (SITF) as mentioned above section. These results are presented in Figures 6-8(a) and (b). Figure 6-8(a) shows the effect of different noise mechanisms on the theoretical $NETD_{Th}$ as a function of the dopant concentration in SiC. Figure 6-8(b), on the other hand, compares the experimental $NETD_{Exp}$ with the theoretical results. The difference between the theory and experiment may be due to the same reasons as in the case of detectivity.

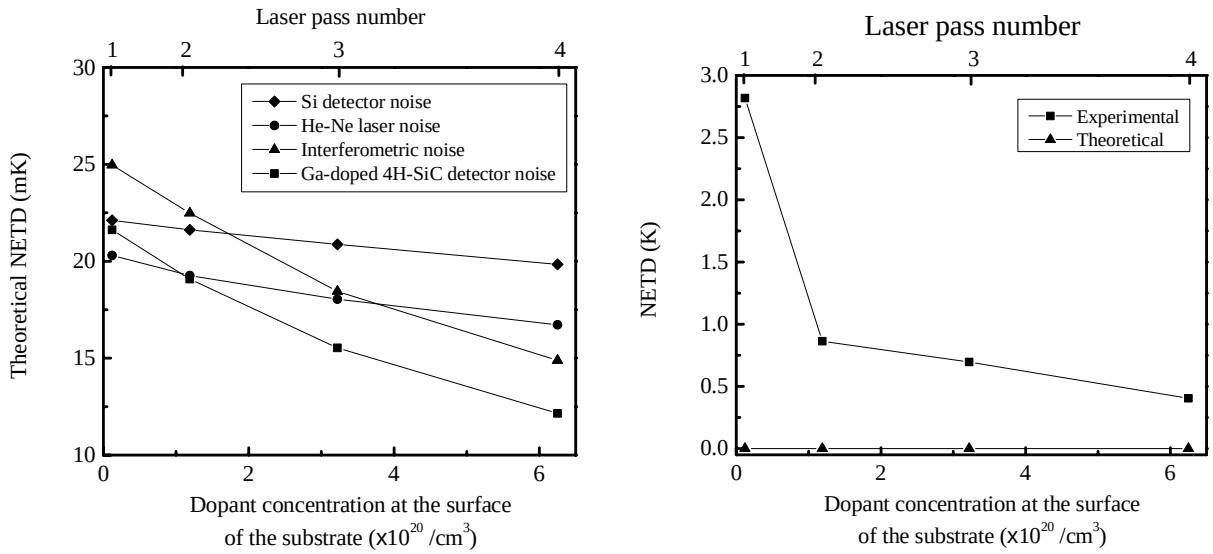

(a) (b)

Figure 6-8: Effects of dopant concentration on the MWIR detectibility of the SiC detector and comparison between theoretical and experimental results: (a) theoretical $NETD_{Th}$ for each noise source and (b) total theoretical and experimental ($NETD_{Exp}$). $NETD_{Exp}$ was obtained by keeping the detector at 25°C and the radiation source at 35°C and 45°C.

The theoretical detectivities of the SiC-Si detector system were obtained using Equations (5-21)-(5-24) for different dopant concentrations, and the corresponding theoretical detectivities were calculated as listed in Table 5-1. Figure 6-9(a) shows how the theoretical detectivity depends on different noise mechanisms as the dopant concentration is varied and the discrepancy between the theoretical and experimental results are presented in Fig. 6-9(b). This discrepancy may be due to several reasons such as the misalignment of different optical elements and loss of optical signal due to the scattering of the He-Ne beam in these elements including SiC. The loss of

photoexcited electrons due to diffusion, and absorption and scattering in various defect sites in the SiC substrate can also contribute to the discrepancy.

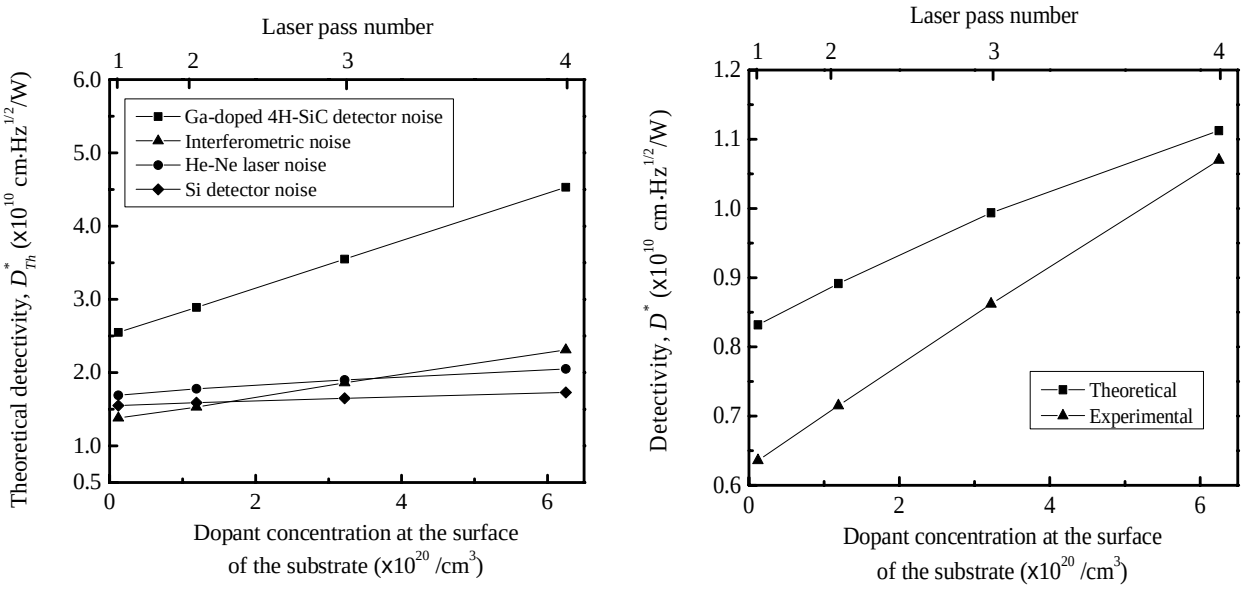

(a) (b)

Figure 6-9: Effects of dopant concentration on the MWIR detectibility of the SiC detector and comparison between theoretical and experimental results: (a) theoretical detectivity for each noise source and (b) total theoretical and experimental detectivity. The detectivity was determined by keeping the detector and radiation source at 25°C each.

6.4.5 Measurement of Sensor Response at Different Temperatures of the Sensor

The temperature affects the properties of semiconductors, such as the electron mobility, refraction index and vacant states in the acceptor level. Therefore the optical response of the sensor can vary with temperature. To determine the operating thermal range, the sensor

temperature was varied from -20°C to +500°C and its optical response was measured by the above-mentioned method in section 6.3. For measurements at low temperatures, a special copper box was fabricated to hold the sensor and a thermocouple as shown in Figure 6-8(a). The holder has a channel through which liquid nitrogen was circulated to maintain the sensor at low temperatures. For measurements at high temperatures, on the other hand, the sensor was placed in a ceramic insulating box having a thermocouple in contact the sensor as shown in Figure 9-1(b). The sensor was heated to about 550°C on a hot plate and then placed on the ceramic seat of the aluminum sample holder. These copper and aluminum sample holders were placed over the S. S. radiation source for measuring the optical response of the sensor.

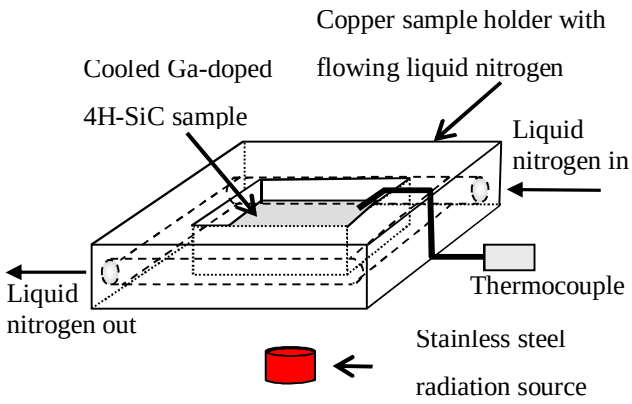

(a)

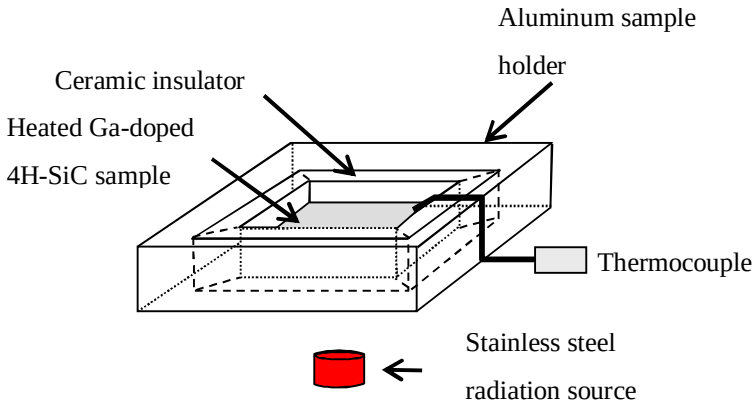

(b)

Figure 6-10: Measurement of the optical signal at different temperatures of the sensor. (a) Liquid nitrogen flows through a channel to cool the sensor and (b) the sensor is heated to about 550°C on a hot plate before placing it on a ceramic seat in an aluminum sample holder.

6.4.6 Effect of Sensor Temperature on Its Performance

The results in the previous sections were obtained by maintaining the sensor at room temperature (25°C). However, the temperature of the sensor plays an important role in affecting the electron density and mobility. The electron density in various energy states of a semiconductor can change with temperature, affecting the optical response of the sensor. Also the electron mobility, diffusion and leakage depend on temperature. Since these phenomena affect the noise and transfer function of sensors, special compensating features such as cooling system and high performance amplifiers are often attached either directly to the sensor or to the signal conditioning circuits for compensating temperature-induced errors [75, 89].

Figure 9-2 shows that the optical response of the 4H-SiC sensor varies with temperature. The sensor can differentiate the source temperatures 25°C and 30°C clearly when the sensor temperature is up to about 100°C.

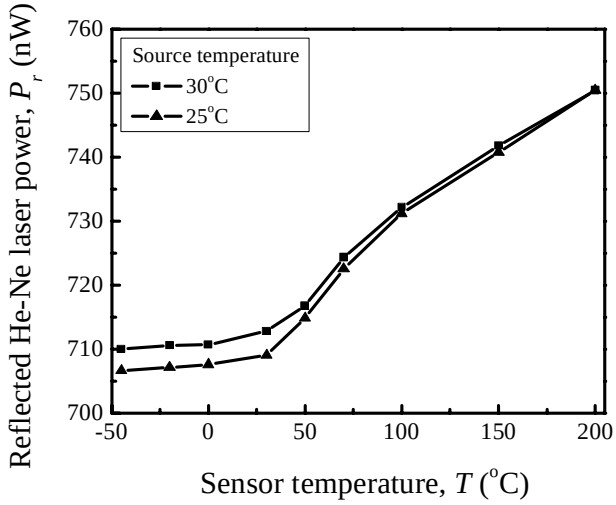

Figure 6-11: Reflected power of the He-Ne laser at different temperatures of the four-pass Ga-doped 4H-SiC sensor.

The thermal resolution of the sensor, i.e., the ability of the sensor to resolve the source temperature difference of 5°C, diminishes above the sensor temperature of 100°C. This reduction in thermal resolution could be due to increased noise at higher temperatures. The response of the sensor is fairly constant from about -50°C to slightly above the room temperature (25°C). Since the as-received sample was an n-type substrate containing a large amount (5×10^{18} cm^{-3}) of free carriers, the loss of photoexcited electrons due to collisions with the free carriers can reduce the thermal operating range of the sensor. Also the fluctuations in the thermal energy of these free carriers can contribute to the noise of the sensor. These phenomena can be reduced significantly by fabricating the sensor using SiC epilayer. Purer sensor materials are expected to widen the thermal operating range of the sensor.

6.5 Conclusions

We have fabricated an optical photodetector, which is an uncooled MWIR detector that produces optical signal. The detector response can be measured remotely using a He-Ne laser beam. Ga atoms were incorporated into a 4H-SiC substrate by a laser doping technique to fabricate the MWIR detector because Ga creates an impurity energy level corresponding to the wavelength 4.21 μm. Optical spectroscopy of the doped sample reveals additional absorption peaks at the MWIR wavelengths 4.63 μm and 4.95 μm. However, the presence of these absorption peaks in the doped sample demonstrates the possibility of fabricating tunable detectors.

Significant changes in the reflectance and refraction index of the Ga-doped sample confirm that such samples can be used as MWIR detectors. The detector produced optical signal due to radiations from a stainless steel surface, which was at room temperature (25°C), when two lenses were used as the MWIR radiation collection optics and the Si detector was operated at the sub-nanowatt resolution scale (0.631 nW) for measuring the change in the reflected He-Ne laser power. The detectivity of the SiC/Si detector system is 7.15×10^{9} cm·Hz$^{1/2}$/W for the MWIR wavelength 4.21 μm. It can be increased to 5.1×10^{11} cm·Hz$^{1/2}$/W with lower time constant, which is higher than the detectivity (1.8×10^{11} cm·Hz$^{1/2}$/W) of an ideal electrical photodetector. The increase in the detectivity might be due to the less loss of electrons in the optical photodetector than in the conventional electrical photodetectors. The NETD is found to be 1774 mK based on experimental data for the radiation source at 25°C, while it is 207 mK based on theoretical calculation.

Increasing the signal-to-noise ratio and optimizing the radiation collection optics and dopant concentration will lower the NETD of the detector. The optical response of the sensor is almost constant over the thermal operating range of about -50°C to 30ºC. This short range could be due to excessive free carriers in the as-received n-type 4H-SiC substrate. The free carriers degrade the sensor performance due to increased electronic noise with increasing temperature. High purity SiC such as epilayer is expected to widen the thermal operating range of the sensor.

CHAPTER 7: GAS SENSING APPLICATION

Laser optical gas sensors are fabricated using the crystalline silicon carbide polytype 6H-SiC, which is a wide bandgap semiconductor, and tested at high temperatures up to 650°C. The sensor operates on the principle of semiconductor optics involving both the semiconductor and optical properties of the material. It is fabricated by doping 6H-SiC with an appropriate dopant such that the dopant energy level matches with the quantum of energy of the characteristic radiation emitted by the combustion gas of interest. This radiation changes the electron density in the semiconductor by photoexcitation and, thereby, alters the refraction index of the sensor. The variation in the refraction index can be determined from an interference pattern. Such patterns are obtained for the reflected power of a Helium-Neon (He-Ne) laser of wavelength 632.8 nm as a function of temperature. SiC sensors have been fabricated by doping two quadrants of a 6H-SiC chip with gallium and aluminum of dopant energy levels E_V + 0.29 eV and E_V + 0.23 eV respectively. These doped regions exhibit distinct changes in the refraction index of SiC in the presence of carbon dioxide (CO_2) and nitrogen monoxide (NO) gases respectively. Therefore Ga- and Al-doped 6H-SiC can be used for sensing CO_2 and NO gases at high temperatures respectively.

7.1 Introduction

The monitoring and control of combustion-related emissions are a top priority in many industries. Advanced sensors are needed for harsh environments to optimize efficiency, minimize emissions and maintain stable operation, while following a varying load or adjusting to changes in the fuel composition. Emission-monitoring sensors for these applications include those for CO, NO_x, O_2, CO_2, hydrocarbons (HCs), and volatile organic compounds. Single crystal silicon carbide (SiC), which is a wide bandgap semiconductor (E_g = 2.36-3.23 eV), is an attractive sensor material for such harsh environments due to its high melting temperature (3100 K peritectic temperature), high thermal conductivity (490 W/m·K), high breakdown field (3-5 MV/cm) and chemical inertness, i.e., resistance to corrosion by acidic and basic species. Capacitors, Schottky diodes, p-n diodes, and field-effect transistors have been developed using SiC for a variety of applications [120-124]. Tobias et al. [125, 126] developed a hydrogen gas sensor based on Pt-gate metal-oxide-semiconductor (MOS) capacitor using silicon carbide (SiC) substrate for high temperature (550°C) applications, which operates in the constant capacitance mode and the slope of the current and voltage (C-V) curve changes with the gas exposure. Spetz et al. [127, 128] fabricated gas-sensitive metal insulator SiC field-effect transistors (MISiCFET), enabling more accurate control of the exhaust and flue gases up to 700°C.

However, such semiconductor device-based sensors have several drawbacks. Some of the drawbacks include cost owing to micro-fabrication of multilayers, lack of long-term reliability due to the diffusion of metal contact materials through the interface layer at high operating temperatures, lack of thermal stability of the insulating layer in the MOS capacitor at high (above

630°C) temperatures and the degradation of sensor performance due to the deposition of combustion products on catalytic metal [129]. Clean, efficient energy production requires chemical sensors with high sensitivity and rapid response time to monitor exhaust gases and to provide real-time feedback control for optimum combustion.

A SiC-based gas sensor can be described as a device, which upon exposure to a gaseous chemical compound or a mixture of chemical compounds, alters one or more of its physical properties, e.g., mass, electrical conductivity, or capacitance, in a way that can be measured and quantified directly or indirectly. The characteristics of the most common types of the SiC-based gas sensors are compared in Table 4 with the classes of sensor devices used to detect the changes of physical properties.

Table 7-1: Classification of SiC-based gas sensors.

Type	Conductivity sensors [130-134]	Semiconductor sensors				Optical sensors [153]
		Capacitor [135-141]	Diode		Transistor [150-152]	
			Schottky [142-147]	Junction [148, 149]		
Device structure	Resistor	MOSiC/ MISiC	MISiC	pn or hetero junction	MISiCFET	Doped SiC
Physical change	Resistance	Capacitance-Voltage	Current-Voltage	Current-Voltage	Current-Voltage	Optical properties (refraction index, transmittance)
Sensing materials	Metal oxide: In_2O_3, SnO_2, WO_3, TiO_2	Catalytic metal: Pd, Pt, Ir	Catalytic metal: Pd, Pt, Ir Metal oxide: SnO_2, WO_3, CeO_2, Ga_2O_3, TiO_2	Catalytic metal: Pd, Pt, Ir Metal oxide: SnO_2, WO_3	Catalytic gate metal: Pd, Pt, Ir Metal oxide: $InSnO_x$, n-ZnO, WO_3	Doped SiC
Operating temperature	650°C	640°C	600°C	500°C	600°C	650°C
Target gases and Sensitivity (ppm)	H_2, NO_2 (5 ppm)	CO (80-500 ppm), C_3H_8 (100-120 ppm), F_2 (0.03-100 ppm), H_2, NH_3 (20 ppm), NO (60-100 ppm), NO_2 (20 ppm)	CO (1000 ppm), NO (10 ppm), H_2, HC, O_2: 300 ppm	H_2, C_3H_6, NH_3, NO_x: 2-1000 ppm, NO (0.2-50 ppm), NO_2 (0.08-200 ppm)	CO (50-250 ppm), CO_2, H_2, HC (130-260 ppm), NH_3 (25-250 ppm), NO_x (200-1000 ppm), O_2 (80 ppm)	CO_2, NO
Response time (second)	~16-22 s	<20 ms	<5 ms	<1 s	<5 s	<1 ms

The silicon carbide based gas sensors for high temperature reviewed in this paper have been categorized into three general groups: (1) conductivity sensors; (2) semiconductor sensors; (3) optical sensors. The categorization of these gas sensors is based primarily on the principal physics and operating mechanisms of the sensor. Within each of these categories, some sensors may exhibit characteristics that overlap with other categories. For example, some semiconductor sensors may rely on electrical excitation or optical settings.

This chapter presents SiC-based laser optical gas sensors (LOGS), which were tested for carbon dioxide (CO_2) and nitrogen monoxide (NO) detection. The sensor operates on the principle of semiconductor optics, i.e., both the semiconductor and optical properties of SiC are utilized to achieve the sensor response. Since optical sensors are inherently wireless, they are advantageous for applications in harsh environments (high temperatures, soots and dusts) due to remote sensing capability. Optical interrogation of the sensor is superior to electrical interrogation because the former is wireless, while the latter requires physical electrical contacts. Also the amount of radiation emitted by different combustion gases increases with increasing temperature and therefore emission spectra-based optical sensors will provide fast response with high sensitivity at high temperatures. Dakshinamurthy et al. [154] reported that SiC can act as a Fabry-Pérot interferometer and demonstrated its applicability as a wireless optical sensor to detect combustion species at high temperatures and high pressures without requiring any external interferometer. This inherent interferometric capability has also been utilized to fabricate temperature and pressure sensors using SiC [155, 156].

7.2 Gas Sensing Mechanism

7.2.1 Operating Principle of the Gas Sensor

The principle of the sensor is explained in Figure 7-1(a), which shows the typical valance and conduction bands of a semiconductor and the dopant energy level.

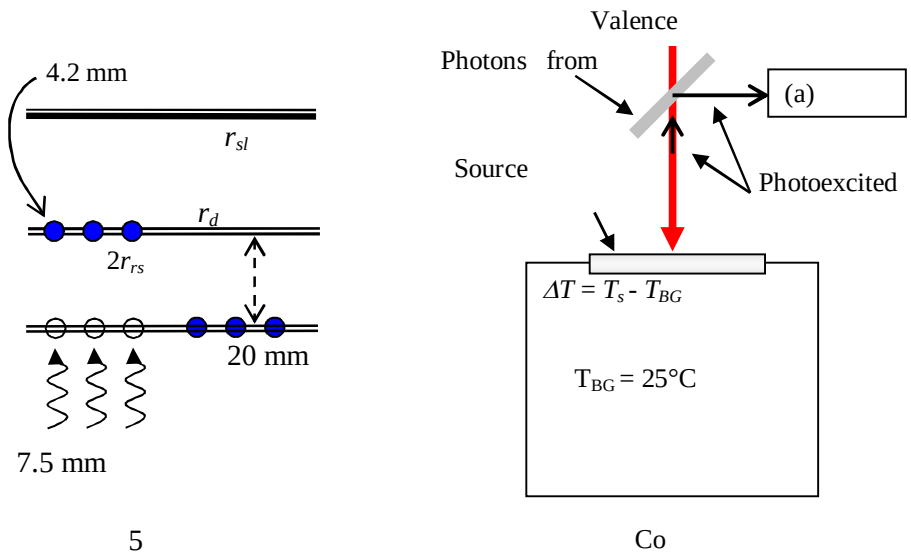

Figure 7-1: (a) Photoexcitation of LOGS by the gas of interest. (b) Interrogation of the sensor with a He-Ne beam, showing the working principle of LOGS.

The characteristic radiation from the gas interacts with the electrons in the valence band and raises the electrons to the dopant energy level. This process changes the electron density in these two (valence and dopant) energy states, which in turn, alters the reflectivity of the doped region. The dependence of reflectivity on the electron density can be explained by the Fresnel reflection mechanism and the Lorentz oscillator model.

The Fresnel reflection formula relates the reflectivity to the optical properties of materials by the following expression:

$$R_F(\omega) = \frac{[n(\omega)-1]^2 + \kappa^2(\omega)}{[n(\omega)+1]^2 + \kappa^2(\omega)}, \tag{7-1}$$

where $R_F(\omega)$ is the Fresnel reflectivity of the material at the material-air interface for an incident electromagnetic wave of angular frequency ω, and $n(\omega)$ and $\kappa(\omega)$ are the refraction and absorption indices, i.e., the real and imaginary parts of the complex refraction index respectively at the angular frequency ω. The refraction and absorption indices are related to the free electron density (N) by the classical multi-oscillator Lorentz model, which yields the following dispersion equation based on the bound and free electrons in semiconductors [72]:

$$n^2(\omega) = 1 + \frac{Ne^2}{\varepsilon_0 m} \sum_{\substack{j=1 \\ bound}}^{J} \frac{f_j\left(\omega_{0j}^2 - \omega^2\right)}{\left(\omega_{0j}^2 - \omega^2\right)^2 + (\gamma_j \omega)^2} \tag{7-2}$$

$$\kappa^2(\omega) = \frac{Ne^2}{\varepsilon_0 m} \sum_{\substack{j=1 \\ bound}}^{J} \frac{f_j(\gamma_j \omega)}{\left(\omega_{0j}^2 - \omega^2\right)^2 + (\gamma_j \omega)^2}, \tag{7-3}$$

where e is the electronic charge, ε_0 is the permittivity of free space and m is the mass of an electron. f_j, ω_{0j} and γ_j are the oscillator strength, resonant frequency and damping constant of the j-th oscillator respectively and J is the total number of oscillators.

The electron density changes in various energy levels when the doped semiconductor absorbs the energy of photons emitted by the gas of interest such as a combustion gas. Therefore the

refraction and absorption indices change as indicated by Eqations (7-2) and (7-3), which modifies the reflectivity as given by Equation (7-1). This change in the reflectivity affects the overall reflectivity of the sensor. The doped region of the semiconductor is interrogated with a He-Ne laser to measure the power of the reflected beam as shown in Figure 7-1(b). The overall reflectivity, which is the ratio of the reflected He-Ne laser power to the incident laser power, can be correlated to the concentration of the combustion species.

7.2.2 Dopant Selection Procedure for Sensor Fabrication

The spectroscopic data in the emission or absorption spectra can be used to determine the characteristic radiation of a given gas. CO_2 and NO, which are two combustion gases, have absorption lines at 4.32 and 5.26 μm corresponding to the photon energies 0.29 and 0.23 eV respectively [157-159]. These two lines are strong and fundamental peaks of CO_2 and NO in the range 1 to 7 μm. In addition to identifying strong spectral lines, another factor becomes important when the sensor is applied to detect a particular gas in a mixture of different gases. The absorption lines of all the species in the gas mixture needs to be analyzed to ensure that a spectral line is uniquely selected for the gas of interest in order to achieve gas-specific sensor response. For example, water vapor and NO are present in the combustion gases of typical power generation systems. Although both of them have spectral peaks at the same wavelength $\lambda = 5.26$ μm, H_2O has a distinct peak at $\lambda = 5.90$ μm [158]. Therefore, two sensors would be necessary corresponding to these two wavelengths so that H_2O can be detected based on the

optical response at $\lambda = 5.90\ \mu m$, while the response at the other wavelength will enable detecting NO with proper calibration of the sensor. However, the purpose of this paper is to show that the photons emitted by gases can be used to modify the refraction indices of SiC by doping it with appropriate dopants, which provides a photoexcitation mechanism for gas sensing applications.

The energy of a photon emitted by each of the CO_2 and NO gases at the above-mentioned spectral lines is 0.29 and 0.23 eV respectively. After determining the photon energy of a gas, an appropriate dopant element needs to be selected to create an energy level in the semiconductor corresponding to the photon energy. Lebedev [12, 13] presented the energy levels of several dopant elements in both 6H-SiC and 4H-SiC semiconductors, indicating that Ga and Al have acceptor energy levels 0.29 and 0.23 eV respectively in 6H-SiC. Therefore Ga and Al are selected as dopant elements to fabricate CO_2 and NO gas sensors, respectively, using 6H-SiC as the starting semiconductor. Generally intrinsic and extrinsic defect centers are present in SiC crystals giving rise to energetically deep levels in the forbidden gap. These deep levels may act either as trapping centers for electrons or holes or as recombination centers limiting the lifetime of free charge carriers. Troffer et al. [159] and Schöner et al. [160] employed the capacitance method to investigate the surface-barrier characteristics of deep centers in epitaxial n-type films of 6H-SiC compensated with each of Ga and Al dopants. They reported absorption edge transitions at 0.29 and 0.23 eV for Ga and Al acceptors respectively.

7.3 Experimental Procedure

7.3.1 Laser Doping of Silicon Carbide for Sensor Fabrication

An n-doped (5×10^{18} cm^{-3}) 6H-SiC wafer of length and width 1 cm each and thickness 279 μm was used to fabricate LOGS. The sample was cleaned by soaking in H_2O_2:H_2SO_4 (1:1 by volume) solution for 15 minutes, followed by de-ionized (DI) water rinsing and buffered oxide etch (BOE) dipping. The organic contaminants were removed from the sample surface by cleaning with acetone, methanol and de-ionized water. An experimental setup, which is the same as presented by Bet et al. [59], was used for doping the cleaned sample by placing it in a doping chamber that was pumped down to 1 mTorr vacuum. A metallorganic compound, triethylgallium ($(C_2H_5)_3Ga$), was used as a precursor to dope the sample. The precursor was heated in a bubbler immersed in a water bath maintained at 100°C. An inert gas Ar was used as the carrier gas to supply the evaporated precursor to the doping chamber, while the sample was heated with a continuous wave (CW) Nd:YAG laser of wavelength 1.06 μm. The precursor decomposes at the laser-heated SiC surface, producing Ga atoms that subsequently diffuse into the sample. Similarly another quadrant of the sample was doped with Al using trimethylaluminum ($(CH_3)_3Al$) as a precursor. The laser power, focal length, laser beam diameter and micro-stage speed were 10.5 W, 150 mm, 200 μm and 0.8 mm/sec respectively for both cases of doping. After the doping experiments, the sample was cleaned with a 45 wt.% KOH solution and then rinsed with acetone, methanol and DI water.

7.3.2 Interferometeic Measurement for Testing the Sensor

An experimental setup shown in Figure 7-2 was used to evaluate the performance of the LOGS fabricated by the above-mentioned doping method. The doped SiC sample was placed on a shallow groove of length, width and depth 10, 10 and 0.5 mm respectively, in a stainless steel cylindrical annular pedestal of outer and inner diameters 2.9 cm and 7.9 mm respectively.

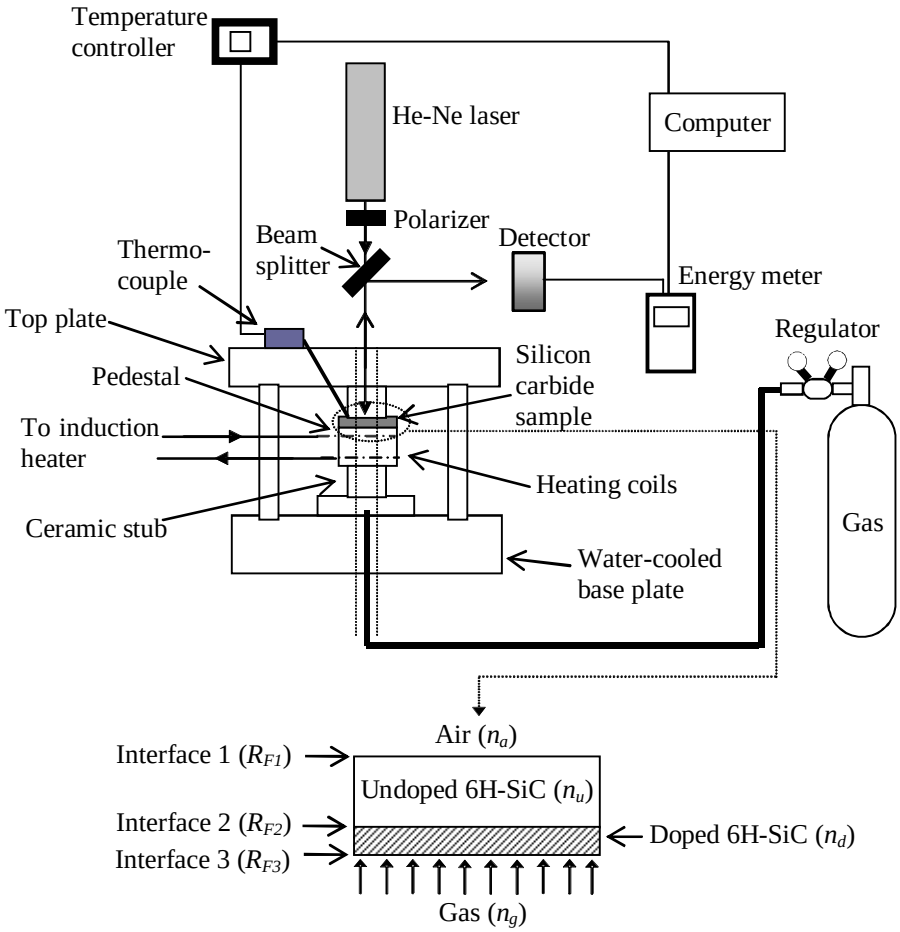

Figure 7-2: Experimental setup for testing the optical response of LOGS.

The pedestal was placed at the center of a water-cooled copper coil connected to an induction heater to heat the pedestal uniformly. This method allows fast heating of the sensor without excessively heating the surrounding mechanical components of the sensor holder and provides easy access to the sensor for reflectometry. The hot pedestal heats up the sensor and the gas for which the sensor needs to be tested. The gas was supplied to the bottom surface of the sensor

from a compressed gas cylinder as shown in Figure 7-2. The pressure of the gas was measured with a pressure gauge and the temperature of the sensor was measured with a thermocouple.

A CW He-Ne laser of wavelength 632.8 nm and output power up to 15 mW was directed to the sensor (doped region) at normal incidence. The laser beam transmits through a beam splitter and incidents on the sensor. The sensor reflects the beam toward the beam splitter, which, in turn, directs a fraction of the beam to a photodetector. One of the important properties of 6H-SiC is that it inherently acts as a Fabry-Pérot interferometer in which the laser beam reflects at both the top and bottom inner surfaces of the sensor multiple times. These multiple reflections produce a multibeam interference pattern, which is analyzed to determine the change in the refraction index of the sensor. Each doped region is designed to act as a sensor for a particular gas.

7.4 Results and Discussion

This study establishes a general principle for designing LOGS using the spectroscopic data. A semiconductor can be doped with an appropriate dopant, such as Ga and Al, to match the dopant energy level with the photon energy corresponding to a spectral line of the gas of interest. The photons of the gas change the electron density in the semiconductor by photoexcitation, which modifies the refraction index of the sensor. The reflectivity of the sensor, which depends on the refraction index, is measured with a laser beam and this optical response provides a gas sensing mechanism. The optical responses of the as-received sample and the Ga- and Al-doped sensors

were tested for different combustion gases such as CO, CO_2, NO, NO_2 as well as air to verify that the optical responses of the sensors (doped regions) are different from those of the as-received sample and that the sensors respond selectively to the gas for which they were designed. Additionally the optical responses of the as-received sample establish the initial (base line) properties of the sample, which allow determining the changes in the reflectivity or the refraction index of the sensor caused by the gas of interest.

7.4.1 Absorption Peaks of the Ga- and Al-doped 6H-SiC Sensors

To verify whether the incorporation of Ga and Al into 6H-SiC modifies the absorption characteristics of the as-received sample, the optical properties of the as-received sample and the Ga- and Al-doped samples were measured in the wavelength range 0.2 to 25 μm as shown in Figures 7-3(a)-(c).

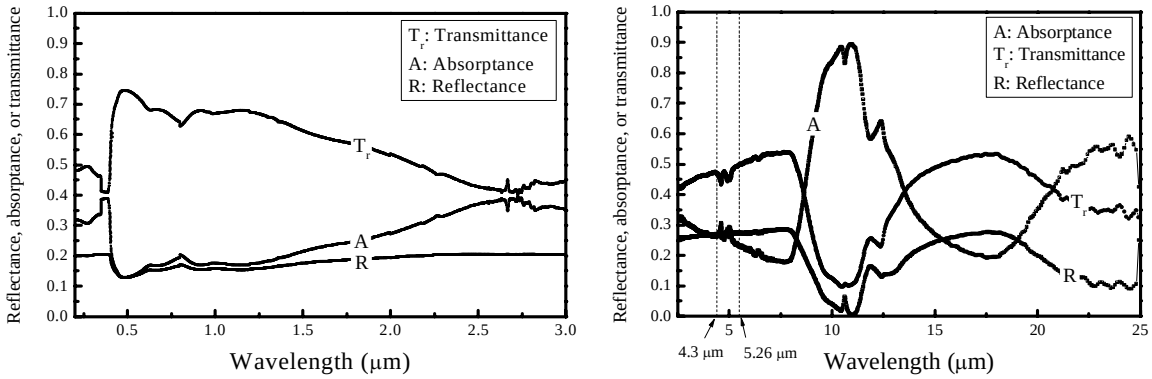
Reflectance, absorptance, or transmittance
Wavelength (μm)
T r: Transmittance
A: Absorptance
R: Reflectance
T r
A
R
4.3 μm
5.26 μm

(a)

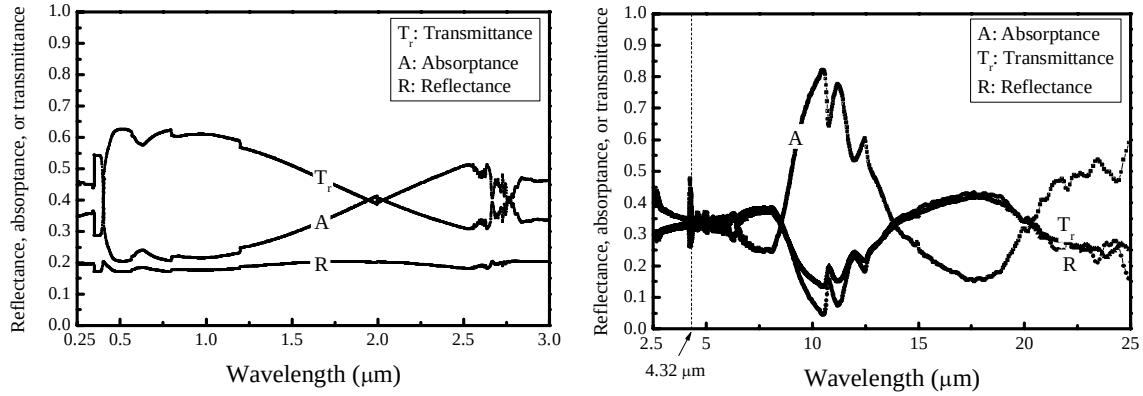
Reflectance, absorptance, or transmittance
Wavelength (μm)
T r: Transmittance
A: Absorptance
R: Reflectance
T r
A
R
4.32 μm

(b)

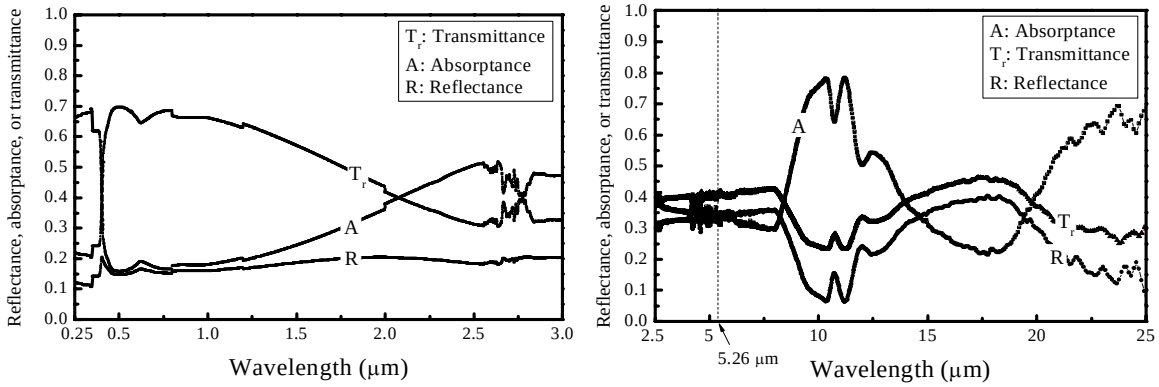
Reflectance, absorptance, or transmittance
Wavelength (μm)
T r: Transmittance
A: Absorptance
R: Reflectance
T r
A
R
5.26 μm

(c)

Figure 7-3: Optical properties of (a) as-received, (b) Ga-doped, and (c) Al-doped 6H-SiC in the wavelength range 0.2 – 25 μm at room temperature.

The Ga and Al dopant atoms are expected to increase the absorption peaks of 6H-SiC at the wavelengths 4.32 and 5.26 μm corresponding to the energy of a photon, 0.29 and 0.23 eV, emitted by the CO_2 and NO gases respectively. A Varian Cary 500 spectro-photometer was used for measuring the optical properties over the wavelength range 0.2 – 3 μm in 1 nm increments with the bandwidth of measurement set to less than 1 nm/point. A Bruker Vertex 70 FTIR spectrometer, which was equipped with a Helios infrared micro-sampling accessory, was used for the measurement in wavelength range 2.5 to 25 μm. The Helios combines a rapid scan speed of 100 spectra per second with a simple infrared microscope of resolution 250 μm.

Figure 3(a) shows that the absorptivities of the as-received sample are 26.8% and 24.5% at the wavelengths of 4.32 and 5.26 μm respectively. The Ga- and Al-doped samples exhibit relatively high absorptivities, i.e., 47.3% at 4.32 μm and 35.1% at 5.26 μm in Figures 3(b) and 3(c) respectively. Also the doped samples have higher absorption coefficients than the as-received sample. Based on the data in Figures 3(a)-(c) and the sample thickness, the values of the absorption coefficients are calculated as μ_{Ga} = 3.160 mm^{-1} and μ_a = 1.598 mm^{-1} at 4.32 μm and μ_{Al} = 2.107 mm^{-1} and μ_a = 1.309 mm^{-1} at 5.26 μm, where μ_{Ga}, μ_a and μ_{Al} are the absorption coefficients of the Ga-doped, as-received and Al-doped samples respectively. These

spectroscopic data, therefore, indicate that the Ga and Al dopant atoms have modified the optical properties of the as-received sample.

7.4.2 Determination of Refraction Index for As-received 6H-SiC Sample, Ga-doped and Al-doped Sensors

The effects of combustion gases and temperature are studied by examining the reflectivity of the as-received sample and the Ga- and Al-doped sensors. The measured reflected power exhibits an interference pattern with alternating maxima and minima as shown in Figures 7-4, 7-5 and 7-6. The constructive and destructive interferences among multiple beams, which are produced due to multiple reflections of the He-Ne beam between the top and bottom inner surfaces of the sensor, generate the observed cyclic pattern.

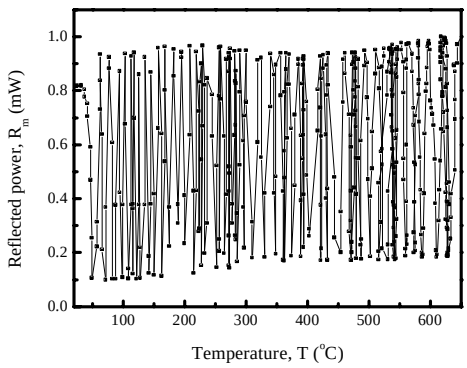
Reflected power, R_m (mW)
Temperature, T (°C)

(a)

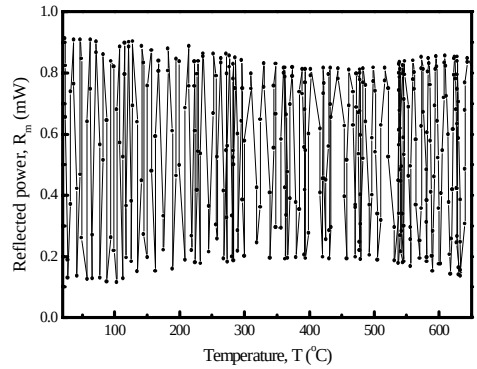
Reflected power, R_m (mW)
Temperature, T (°C)

(b)

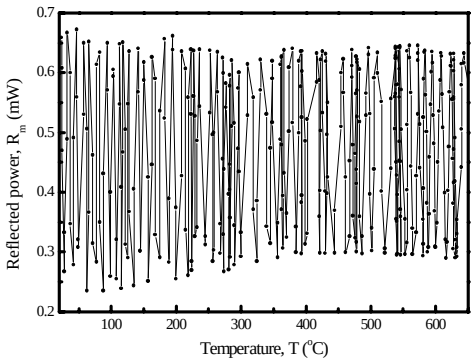
Reflected power, R_m (mW)
Temperature, T (°C)

(c)

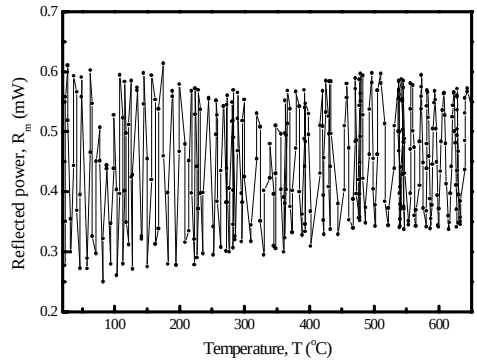
Reflected power, R_m (mW)
Temperature, T (°C)

(d)

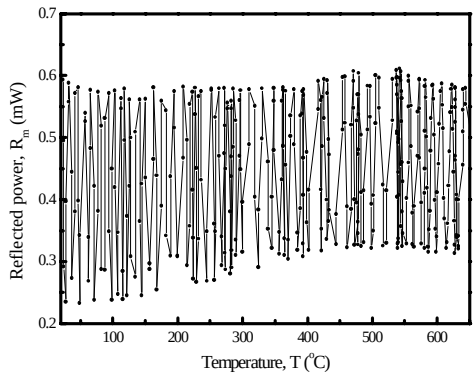
Reflected power, R_m (mW)
Temperature, T (°C)

(e)

Figure 7-4: The reflected power of a He-Ne laser due to an as-received 6H-SiC sample for different gases (a) air, (b) carbon monoxide, (c) carbon dioxide, (d) nitrogen monoxide, and (e) nitrogen dioxide at various temperatures.

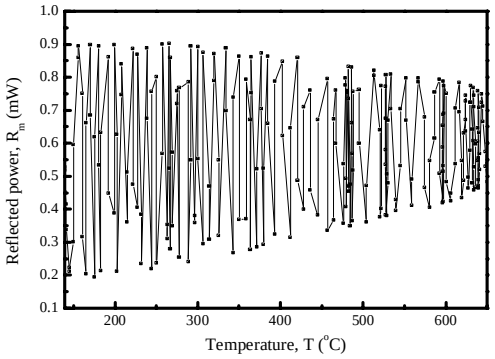
Reflected power, R_m (mW)
Temperature, T (°C)

(a)

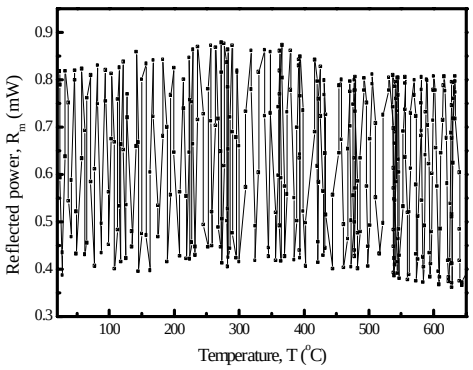
Reflected power, R_m (mW)
Temperature, T (°C)

(b)

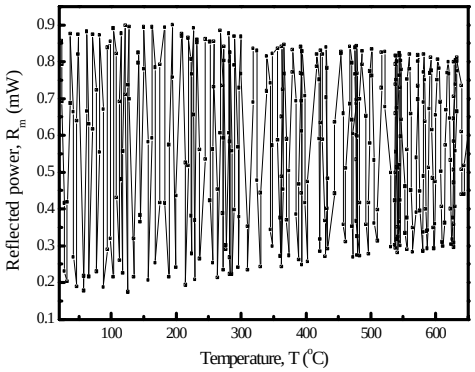
Reflected power, R_m (mW)
Temperature, T (°C)

(c)

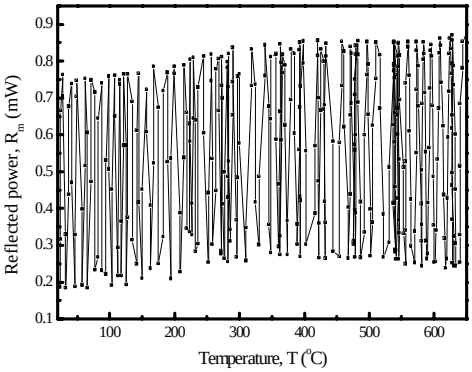
Reflected power, R_m (mW)
Temperature, T (°C)

(d)

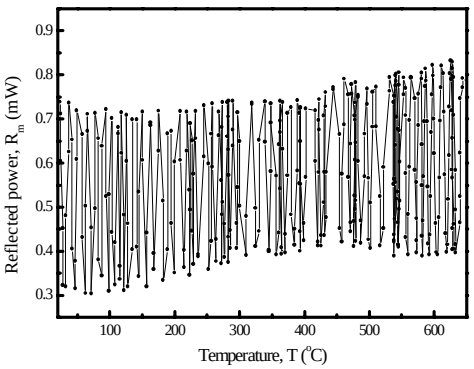
Reflected power, R_m (mW)
Temperature, T (°C)

(e)

Figure 7-5: The reflected power of a He-Ne laser beam due to a Ga-doped 6H-SiC sample for different gases (a) air, (b) carbon monoxide, (c) carbon dioxide, (d) nitrogen monoxide, and (e) nitrogen dioxide at various temperatures.

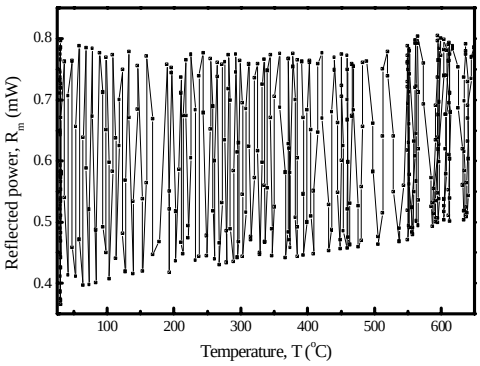
Reflected power, R_m (mW)
Temperature, T (°C)

(a)

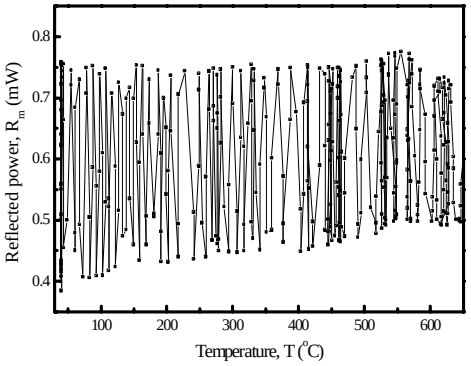
Reflected power, R_m (mW)
Temperature, T (°C)

(b)

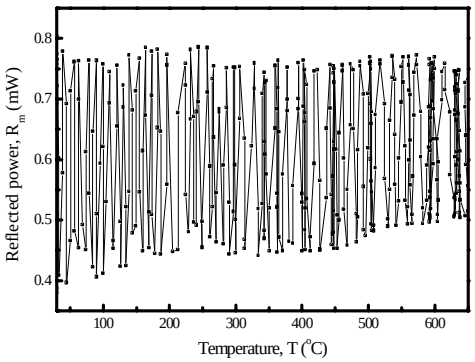
Reflected power, R_m (mW)
Temperature, T (°C)

(c)

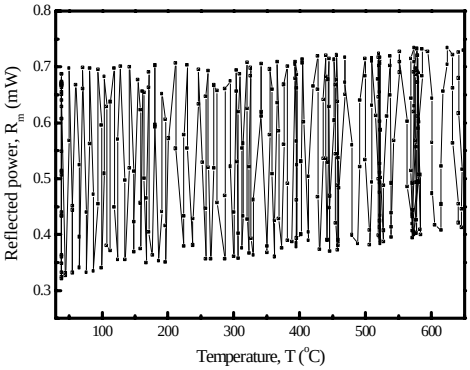
Reflected power, R_m (mW)
Temperature, T (°C)

(d)

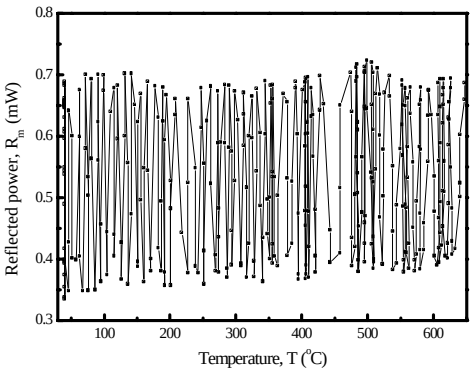
Reflected power, R_m (mW)
Temperature, T (°C)

(e)

Figure 7-6: The reflected power of a He-Ne laser due to an Al-doped 6H-SiC sample for different gases (a) air, (b) carbon monoxide, (c) carbon dioxide, (d) nitrogen monoxide, and (e) nitrogen dioxide at various temperatures.

The sensor response, i.e., the overall reflectivity (R_m), was calculated using the expression $R_m = P_r/P_i$, where P_r is the cyclic reflected power obtained as a function of the sensor temperature and P_i is the power of the incident He-Ne beam. The sensor is a non-absorbing medium at the He-Ne laser wavelength 632.8 nm since the He-Ne laser, which was used as a probe beam, is not absorbed by the 6H-SiC sample. To verify this, the refraction and absorption indices of the as-received, Ga- and Al-doped samples were calculated at the He-Ne laser wavelength for normal incidence at room temperature. The calculations were based on the Fresnel reflection formula and the Beer-Lambert law using the measured reflected and transmitted powers of the He-Ne laser beam. For the as-received, Ga- and Al-doped samples, the refraction indices were 2.576, 2.544 and 2.510, and the absorption indices were 9.192×10^{-5}, 1.611×10^{-4} and 1.541×10^{-4} respectively. The low values of the absorption indices indicate that the samples can be considered as non-absorbing media for the He-Ne laser.

For such non-absorbing media, the observed interference patterns can be analyzed using a multibeam interference model [72] involving reflections of the He-Ne beam at three interfaces. These three interfaces are the air-undoped SiC interface on top of the wafer (interface 1), undoped SiC-doped SiC interface inside the wafer (interface 2) and doped SiC-gas interface at the bottom of the wafer (interface 3) as shown in Figure 2. Since the undoped and doped 6H-SiC are nonabsorbing media, the Fresnel reflectivities are $R_{F1} = \frac{(n_u - n_a)^2}{(n_u + n_a)^2}$, $R_{F2} = \frac{(n_d - n_u)^2}{(n_d + n_u)^2}$ and

$R_{F3} = \frac{(n_g - n_d)^2}{(n_g + n_d)^2}$ at interfaces 1, 2 and 3 respectively for normal incident beams. Here n_a, n_u, n_d, and n_g are the refraction indices of air, undoped 6H-SiC, doped 6H-SiC, and gas respectively. Considering the refraction indices of air and gas to be unity, the values of these reflectivities are found to be R_{F1} = 19.42%, R_{F2} = 0.004%, and R_{F3} = 18.98 % for the Ga-doped 6H-SiC sample and R_{F1} = 19.42%, R_{F2} = 0.017% and R_{F3} = 18.51% for the Al-doped 6H-SiC sample. Since the values of R_{F2} are much smaller than the reflectivities at interfaces 1 and 3, the effect of interface 2 on the reflection of the He-Ne beam can be neglected. Therefore, the overall reflectivity (R_m) due to the multibeam interference caused by multiple reflections of the He-Ne beam at interfaces 1 and 3 can be used to analyze the observed sensor response. The multibeam interference pattern for such two-interface problems is given by the following expression [74]:

$$R_m = \frac{P_r}{P_i} = \frac{R_{F1} + R_{F3} + 2\sqrt{R_{F1}R_{F3}}\cos\phi}{1 + R_{F1}R_{F3} + 2\sqrt{R_{F1}R_{F3}}\cos\phi}, \tag{7-4}$$

where the phase angle (ϕ) is given by

$$\phi = \frac{2\pi}{\lambda_0}(n_u d_u + n_d d_d). \tag{7-5}$$

Here d_u and d_d are thicknesses of the undoped and doped 6H-SiC regions respectively and λ_0 is the wavelength of the He-Ne laser in vacuum. In this study, $d_u \approx 278.5$ μm and $d_d \approx 0.5$ μm,

resulting in $n_u d_u$ = 717.42 and $n_d d_d$ = 1.27 μm, which indicate that $n_d d_d$ can be neglected compared to $n_u d_u$ and therefore Equation (7-5) becomes $\phi = 2\pi n_u d_u / \lambda_0$. Since n_u and d_u depend on the temperature, the variation of phase angle (ϕ) with respect to temperature can be written as [154]

$$\frac{\partial \phi}{\partial T} = \frac{2\pi d_u}{\lambda_0}\frac{\partial n_u}{\partial T} + \frac{2\pi n_u}{\lambda_0}\frac{\partial d_u}{\partial T} = \frac{2\pi d_u}{\lambda_0}\left(\frac{\partial n_u}{\partial T} + \alpha n_u\right), \tag{7-6}$$

where $\alpha = (1/d_u)(\partial d_u / \partial T)$, which is the thermal expansion coefficient of the sensor. It is given by $\alpha = 3.19\times10^{-6} + 3.60\times10^{-9}T - 1.68\times10^{-12}T^2$ for 6H-SiC [161], where T is the absolute temperature. The phase angles of the reflected power in a typical interference pattern are represented in Figure 7-7, where the dashed box shows the adjacent reflected powers P_m and P_{m+1} corresponding to the temperatures T_m and T_{m+1} respectively.

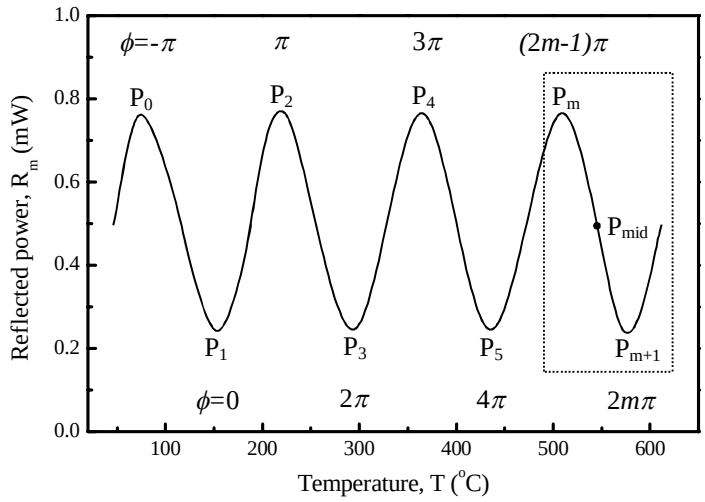

Figure 7-7: A typical multi-beam interference pattern for the reflected power.

The associated refraction indices are $n_{u,m}$ and $n_{u,m+1}$ at these two temperatures respectively. Assuming that the interference pattern is linear between two such consecutive points, the thermal expansion coefficient can be approximated between the temperatures T_m and T_{m+1} by the its value at the mid-point, P_{mid}, of the curve, i.e., $\alpha_{mid} = \alpha\left((T_m + T_{m+1})/2\right)$. Therefore the refraction index $n_{u,m+1}$ can be obtained at T_{m+1} from the following expression [154] by knowing the value of $n_{u,m}$ at T_m.

$$n_{u,m+1} = \frac{1}{1+\left(\alpha_{mid}\Delta T/2\right)}\left[\frac{\lambda_0}{2d_u} + \left(1 - \frac{\alpha_{mid}\Delta T}{2}\right)n_{u,m}\right], \tag{7-7}$$

where $\Delta T = T_{m+1} - T_m$.

Applying Equation (7-7) to the interference patterns of the as-received, Ga-doped and Al-doped samples in Figures 7-4, 7-5 and 7-6, respectively, the variations of the refraction index were calculated as a function of temperature for each gas.

7.4.3 Analysis of the Sensor Response

The refraction indices and the changes in the refraction index of the sensors are presented in Figures 7-8 and 7-9 for CO_2 and NO gas sensors respectively. It should be noted that the refraction indices of the as-received SiC, doped SiC and gas-excited doped SiC will be different since they have three different electronic states.

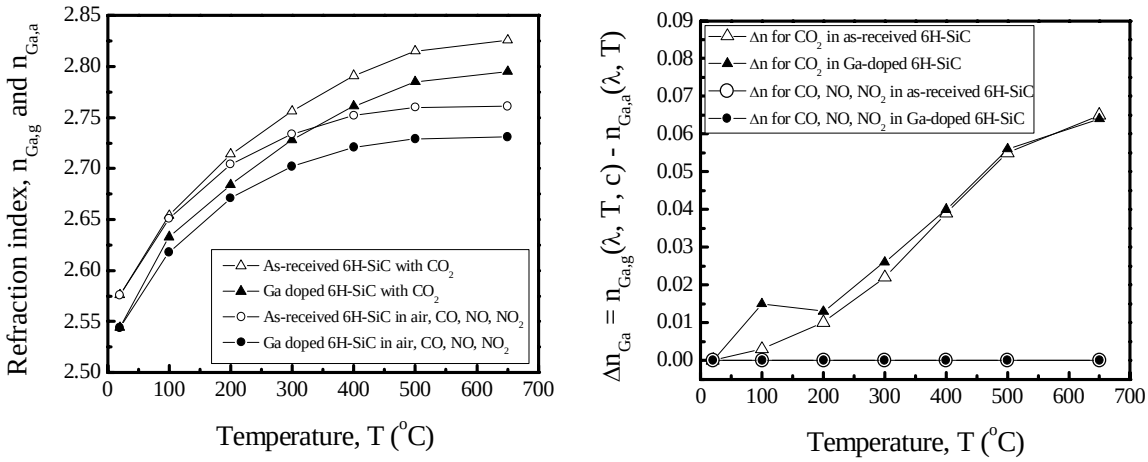

(a) (b)

Figure 7-8: Comparison of the optical properties of Ga-doped 6H-SiC sensor in the presence of different gases, indicating the selectivity for sensing the CO_2 gas: (a) refraction indices and (b) change in the refraction indices.

The refraction index of the gas-excited doped 6H-SiC, i.e., $n_{d,g} = n_{d,g}(\lambda,T,c)$, depends on the wavelength (λ) of the characteristic spectral line, temperature (T), and concentration (c) of the gas, where the subscript d = Ga and Al for Ga- and Al-doped samples respectively. The deviations of $n_{d,g}$ from the refraction index of doped 6H-SiC in air, i.e., $n_{d,a} = n_{d,a}(\lambda,T)$, are expressed as $\Delta n_d = n_{d,g}(\lambda,T,c) - n_{d,a}(\lambda,T)$, which are plotted in Figures 8 and 9 for the Ga- and Al-doped sensors respectively. Δn_d is an important parameter because it determines the gas-selectivity of the sensor.

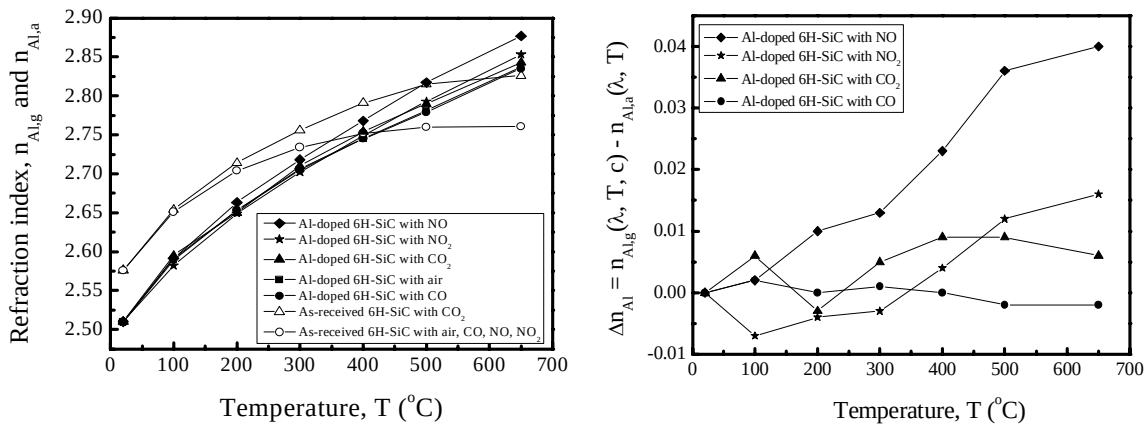

(a) (b)

Figure 7-9: Comparison of the optical properties of Al-doped 6H-SiC sensor in the presence of different gases, indicating the selectivity for sensing the NO gas: (a) refraction indices and (b) change in the refraction indices.

Figures 7-8(a) and (b) show the refraction indices and the changes in the refraction index (Δn_{Ga}) of the Ga-doped sensor for different gases. The refraction index curve due to the CO_2 gas is distinctly different from the refraction index data for the CO, NO and NO_2 gases. A single refraction index curve is obtained for the CO, NO and NO_2 gases, indicating that they do not interact with the Ga-doped sensor to affect its optical property. However, Figure 7-8(b) shows that the Δn_{Ga} curves of the as-received sample and the Ga-doped sensor coincide. This similarity in the optical response of the two samples can be explained by their optical properties as presented in Figure 7-3. It can be observed from Figures 3(a) and (b) that the as-received sample has an absorption peak at 0.29 eV similar to that of the Ga-doped sensor. The CO_2 gas sensor was designed by matching the Ga dopant energy level (E_V + 0.29 eV in 6H-SiC) with the photon

energy (0.29 eV corresponding to 4.32 μm wavelength) of the CO_2 gas. Therefore only the CO_2 gas causes photoexcitation to transfer the electrons from the lower to upper energy levels. Since Δn_{Ga} is unique for the CO_2 gas as indicated by Figure 7-8(b), the Ga-doped 6H-SiC can be used as a CO_2 gas sensor.

Figures 7-9(a) and (b) show the refraction indices and the changes in refraction index (Δn_{Al}) of the Al-doped sensor for different gases. Figure 7-9(b) shows that the NO gas changes the refraction index of the sensor more than the other gases. However, the refraction index of the sensor is lower for the NO gas than for the other gases at lower temperatures, which may be due to the presence of a stronger NO absorption line at 5.26 μm wavelength at higher temperatures. Figure 7-3(c), which shows the absorption spectrum of 6H-SiC obtained at room temperature, indicates that 6H-SiC does not have an absorption peak matching exactly with the photon energy (0.23 eV) of the NO gas. However, the NO gas might have an emission line matching exactly with the Al dopant energy level in 6H-SiC at high temperatures. Since the refraction index data show that the NO gas affects the refraction index of the doped sample differently compared to other gases at high temperatures, Al-doped 6H-SiC can be used as a NO gas sensor.

For Sc-doped 6H-SiC sensor, Δn and $\Delta\rho$ are presented in Figures 7-10(a) and (b), respectively. The sensor exhibits distinct selectivity for CO at temperatures higher than 400°C. And also the differences of refraction indices ($\Delta n = n(\lambda, T, c, gas) - n(\lambda, T, c, air)$) and reflectances ($\Delta\rho = \rho(\lambda, T, c, gas) - \rho(\lambda, T, c, air)$) for Al-doped 6H-SiC with CO has 0.05 and 8.1×10^{-3} at 650°C, respectively.

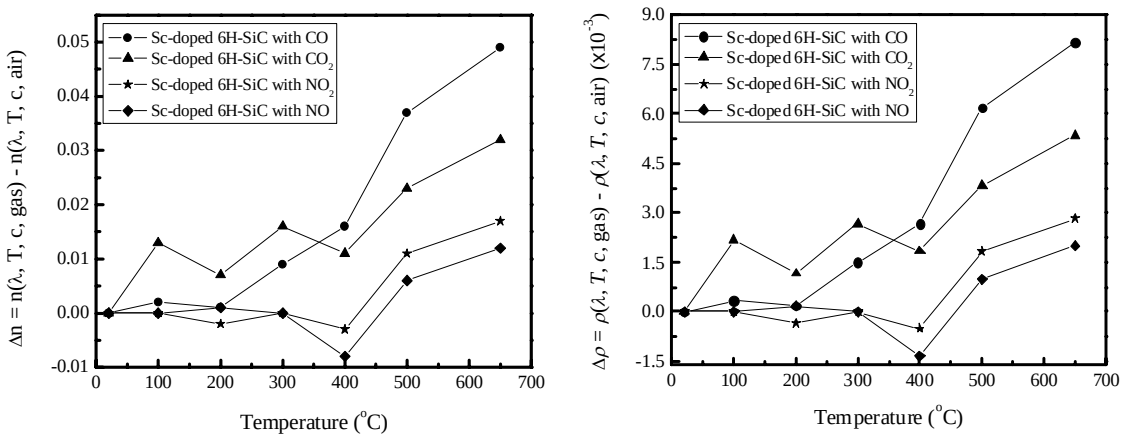

(a) (b)

Figure 7-10: Comparison of (a) difference of refraction indices ($\Delta n = n(\lambda, T, c, gas) - n(\lambda, T, c, air)$) and (b) difference of reflectances ($\Delta\rho = \rho(\lambda, T, c, gas) - \rho(\lambda, T, c, air)$) for Sc-doped 6H-SiC in combustion gases.

For P-doped 6H-SiC, Δn and $\Delta\rho$ are also presented in Figures 7-11(a) and (b), respectively. This sensor dominates selectivity for NO_2 gas after about 500°C with values of Δn = 0.055 and $\Delta\rho$ = 8.9×10^{-3} at 650°C. Since P is an n-type dopant in 6H-SiC, whereas Ga, Al and Sc are p-type dopants, photoexcitation occurs from the donor energy level to the conduction band in the P-doped sample. This effect may cause the P-doped sample to be less sensitive at low temperatures. Also the as-received sample was n-type, which may contain multiple donor energy levels, and this characteristic of the starting substrate may be attributed to the low selectivity of the P-doped sensor for NO_2 gas at low temperatures. An n-type 6H-SiC substrate has been laser-doped with

Ga, Al, Sc and P dopants to produce sensors for various combustion gases, particularly CO_2, NO, CO and NO_2 gases, respectively. The optical signal, refraction index and reflectance, changes significantly at high temperatures, indicating that the sensors can be used for detecting small concentrations of gases.

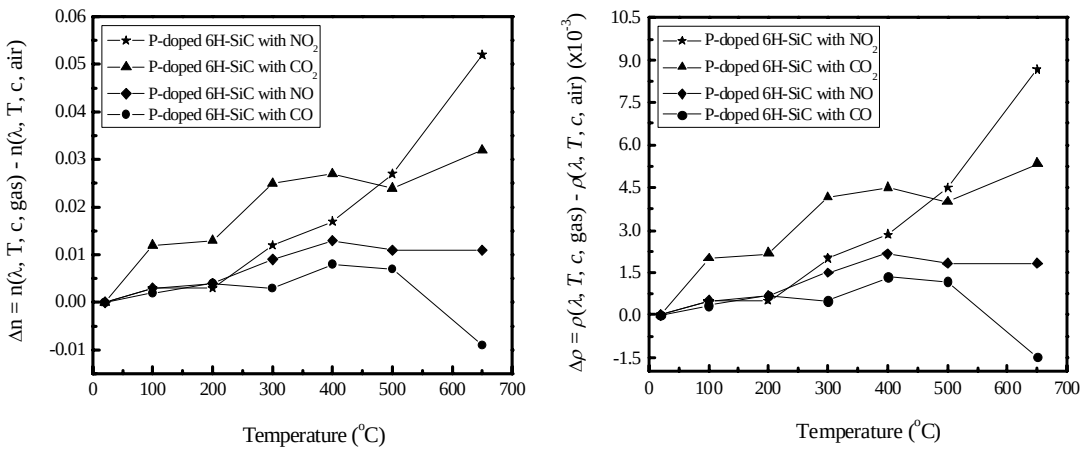

(a) (b)

Figure 7-11: Comparison of (a) difference of refraction indices ($\Delta n = n(\lambda, T, c, gas) - n(\lambda, T, c, air)$) and (b) difference of reflectances ($\Delta\rho = \rho(\lambda, T, c, gas) - \rho(\lambda, T, c, air)$) for P-doped 6H-SiC in combustion gases.

The above data above clearly indicate that the reflectance of doped SiC can be changed by changing the electron density in different energy levels. The dependence of reflectance on the

electron density is very complicated and often all the required data are not available to calculate this dependence theoretically. However, the variation of reflectance with electron density can be estimated for some representative data using Equations (3-21) and (3-22) [76]:

$$n^2 + \kappa^2 = \frac{\varepsilon_r}{2}[1 + (bn_e)^2]^{\frac{1}{2}}, \qquad (7\text{-}8)$$

where e_r is the dielectric constant of the semiconductor and n_e is the electron density. $b = \frac{\lambda q \mu_e^*}{2\pi c \varepsilon_0 \varepsilon_r}$, where l, q and μ_e^* are the wavelength of the He-Ne laser (probe beam) in vacuum, electronic change and the electron mobility, respectively. c and e_0 are the speed of light in vacuum and the permittivity of free space, respectively.

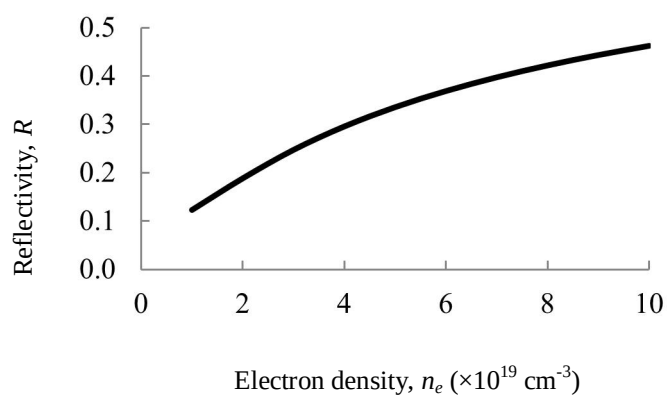

Figure 7-12: Variation of reflectivity as a function of electron density in a typical crystalline SiC semiconductor material, showing that the reflectivity changes fairly rapidly for $n_e = 10^{19} - 5\times10^{19}$ cm^{-3} and, therefore, the detector is expected to be sensitive in this range of n_e.

The absorption index of SiC, κ, has been found [153] to be very small (~10^{-4}) compared to the refraction index, n, at the He-Ne laser wavelength of 632.8 nm. The dielectric constant and electron mobility of SiC are typically 6.7 and 900 $cm^2/V\cdot s$, respectively. Using these values in Equation (3-19), the refraction index is calculated as a function of the electron density, which enables determining the reflectivity, R, using Equations (3-20) and (3-21). The reflectivity is plotted as a function of n_e in Figure 9, which shows that n_e affects the reflectivity significantly. The detector is expected to be sensitive over a certain range of n_e (10^{19} – 5×10^{19} cm^{-3}) since R varies fairly rapidly in this range. Using the refraction indices data, n_s, $s = u$ and d, in Figures 7-8 to 7-11, the reflectance due to multiple reflections of the He-Ne beam inside the SiC samples were calculated for the four doped samples with the corresponded gas species as shown in above figures. The changes in the reflectance, $\Delta\rho_s = \rho_s - \overline{\rho_s}$, are showing that the doped SiC can change the reflectance of the detector significantly compared to that of the undoped sample.

7.5 Conclusions

A method to fabricate wireless chemical sensors is presented. The sensor is based on the semiconductor optics principle, i.e., an energy gap is created in a semiconductor by doping it with an appropriate dopant to ensure that the energy gap matches with an emission spectral line of the gas of interest. Specifically four sensors have been fabricated by laser doping four quadrants of a 6H-SiC substrate with Ga, Al, Sc and P atoms to detect CO_2, NO, CO and NO_2 gases respectively. The photons, which are emitted by the gas, excite the electrons in the doped

sample and consequently change the electron density in various energy states. This phenomenon affects the refraction index of the semiconductor and, therefore, the reflectivity of the semiconductor is altered by the gas. The optical response of this semiconductor sensor is the reflected power of a probe beam, which is a He-Ne laser beam in this study. The CO_2, NO, CO and NO_2 gases change the refraction indices of Ga-, Al-, Sc- and Al-doped 6H-SiC, respectively, more prominently than the other gases tested in this study. So these doped 6H-SiC samples can be used as CO_2, NO, CO and NO_2 gas sensors respectively.

CHAPTER 8: SUMMARY

8.1 Conclusions

This dissertation consists of largely three parts which include fabrication of the optical infrared detector by using laser doing technique, performance characterization of the doped detector material and its application for gas detection capability. Through this research, it can be concluded that;

1. Laser Doping
    1) Gallium was incorporated into n-type 4H-SiC substrate using a CW Nd:YAG laser for different number of laser scans.
    2) The laser parameters were selected using a thermal model to incorporate dopants without melting the substrate, articularly solid-phase diffusion of Ga was achieved below the peritectic temperature of SiC.
    3) The surface *I-V* curves show that higher dopant concentrations reduce the resistance at the sample surface.
    4) From the SIMS data, the surface concentration and the diffusion length of Ga are 6.25×10^{20} cm^{-3} and 360 nm respectively.
    5) The activation energy, pre-exponential factor and diffusion coefficient were calculated by a method of parameter fitting based on a diffusion model involving temperature-dependent diffusion coefficient. The values of these diffusion parameters

are 1.84 eV, 1.05×10^{-2} cm^2/s and 5.53×10^{-7} cm^2/s, respectively, for the case of four laser passes.

6) The diffusion coefficient is five orders of magnitude higher than the typical diffusion coefficient of Ga in SiC, which indicates that the laser doping process enhances the dopant diffusion coefficient significantly. Comparison of experimental and calculated dopant concentration profiles shows that they exhibit similar trends along the depth of the substrate.

2. Performance Characterization of the Doped SiC as an Infrared Detector

1) Optical spectroscopy of the doped sample reveals absorption peaks at the MWIR wavelengths 4.21 and 4.63 μm. Ga atoms were incorporated into a 4H-SiC substrate by a laser doping technique to fabricate the MWIR detector because Ga creates an impurity energy level corresponding to the infrared wavelengths.

2) The detector produced optical signal due to radiations from a stainless steel surface, which was at room temperature (25°C), when two lenses were used as the MWIR radiation collection optics and the Si detector was operated at the sub-nanowatt resolution scale (0.631 nW) for measuring the change in the reflected He-Ne laser power. Significant changes in the reflectance and refraction index of the Ga-doped sample confirm that such samples can be used as MWIR detectors.

3) The experimental and theoretical detectivity were compared. The experimental detectivity of the SiC/Si detector system is 7.15×10^{9} $cm\cdot Hz^{1/2}/W$ for the MWIR wavelength 4.21 μm, while the theoretical value is 5.1×10^{11} $cm\cdot Hz^{1/2}/W$.

4) The NETD is found to be 1774 mK based on experimental data for the radiation source at 25°C, while it is 207 mK based on theoretical calculation.

5) The optical response of the sensor is almost constant over the thermal operating range of about -50°C to 30ºC. The free carriers degrade the sensor performance due to increased electronic noise with increasing temperature.

3. Gas Detection Application

1) The sensor is based on the semiconductor optics principle, i.e., an energy gap is created in a semiconductor by doping it with an appropriate dopants in SiC.

2) Four sensors have been fabricated by laser doping four quadrants of a 6H-SiC substrate with Ga, Al, Sc and P atoms to detect CO_2, NO, CO and NO_2 gases respectively.

3) The optical response of these sensors is the reflected power of a probe beam, which is a He-Ne laser beam. The CO_2, NO, CO and NO_2 gases change the refraction indices of Ga-, Al-, Sc- and Al-doped 6H-SiC, respectively, more prominently than the other gases tested. So these doped 6H-SiC samples can be used as CO_2, NO, CO and NO_2 gas sensors respectively.

8.2 Future Work

Here are some proposed future works based on this research. Since the He-Ne laser as a probe beam can detect one spot at a time, light emitting diode (LED) source and pin-hole on Fourier plane can be used to increase the detection area as shown in Figure 8-1. The Rayleigh-Rice method is one of the oldest and most popular scattering theories and it is

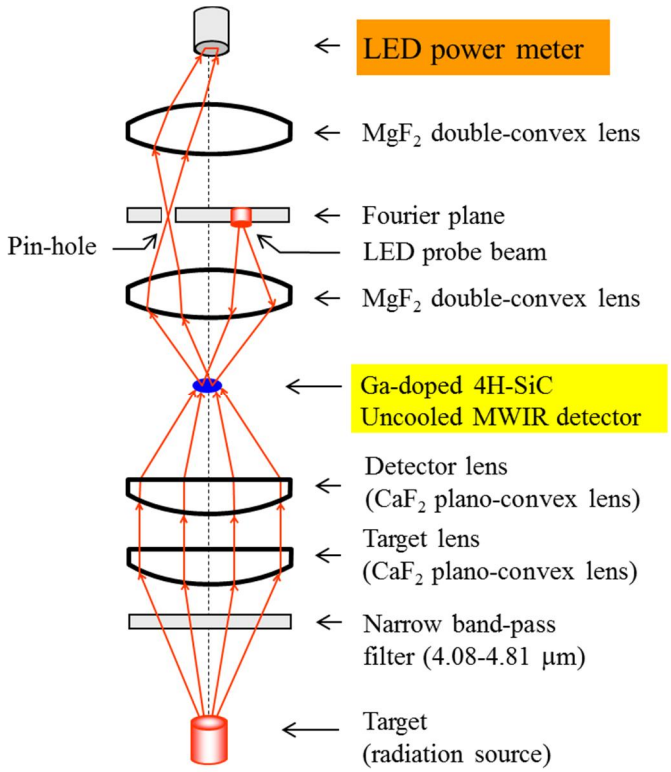

Figure 8-1: Optical setup for detector performance with LED as a probe beam.

There are advantages of using SiC for infrared detector than other semiconductor materials as compared in Table 8-1.

Table 8-1: Comparison of the optical infrared detector with a conventional infrared detector.

	Silicon carbide [1]			**GaN** [1]		**Si** [2,3]	**GaAs** [2,3]
	3C-SiC	**4H-SiC** a/c=0.3	**6H-SiC** a/c=0.2	**Hex.** a/c=0.6	**Cubic**		
Bandgap (eV)	**2.36** indirect	**3.23** indirect	**3.00** indirect	3.39 direct	3.20 direct	1.12 indirect	1.35 direct
Mobility (cm^2/Vs)							
Electron	**800**	**900**	**400**	1000	1000	1500	8500
Hole	**320**	**120**	**90**	200	350	450	400
Diffusion coeff. (cm^2/s)							
Electron	**20**	**22**	**10**	25	25	36	200
Hole	**8**	**3**	**2**	5	9	12	10
Junction temp. (°C)	**600-650°C**			600-650°C		100-150°C	100-150°C

The electrons and holes have low mobility and diffusion coefficient in SiC: The loss of signal due to the diffusion of electrons to the neighboring pixels is less. Such losses reduce the contrast in the image as illustrated in Figure 8-2. Focal plane arrays and other devices can be built on a Single SiC chip. GaN is available in polycrystalline thin films containing numerous defects that can act as thermal absorbers in the IR and MWIR ranges. Although SiC crystals tend to have micropipe and dislocation defects, the number of these defects per unit area has been reduced significantly by improving in the crystal growth process.

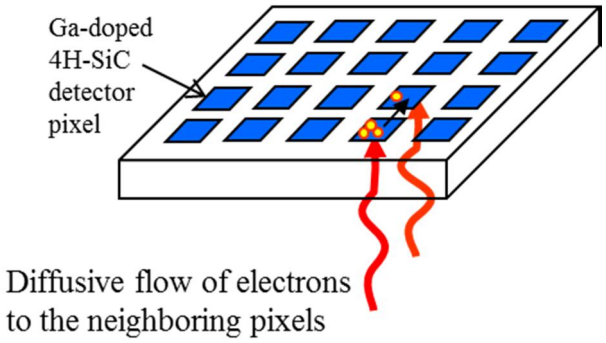

Figure 8-2: Focal plane array can be built on a single SiC chip which has less loss of signal due to the diffusion of electrons to the neighboring pixels than other semiconductor materials

APPENDIX A: DOPANT CONCENTRATION DISTRIBUTION

Defining the spatial and concentration variables as ξ and $\chi(\xi)$, respectively, by the following two expressions:

$$\xi = \int_0^z \frac{dz'}{\sqrt{D_T\left(T(z',\tau)\right)}} = L(z) \quad , \tag{A-1}$$

and

$$\chi(\xi) = \overline{C}(z,s)\left[D_T\left(T(z,\tau)\right)\right]^{1/4} . \tag{A-2}$$

Equation (2-18) can be simplified as

$$\frac{d^2\chi(\xi)}{d\xi^2} - \frac{s\chi(\xi)}{D_0} = g(\xi) , \tag{A-3}$$

where $g(\xi) = -\frac{C_i(z)}{D_0}\left(D_T\left(T(z,\tau)\right)\right)^{1/4} - \frac{1}{16}\left(D_T\left(T(z,\tau)\right)\right)^{-1}\left(D_T'\left(T(z,\tau)\right)\right)^2\chi(\xi) + \frac{1}{4}D_T''\left(T(z,\tau)\right)\chi(\xi)$.

The solution of the ordinary differential Equation (A-3) subject to the boundary conditions Equations (2-11) and (2-12) is given by

$$\begin{aligned}\overline{C}(z,s) = \left(D_T\left(T(z,\tau)\right)\right)^{-1/4}\Bigg[& C_0\left(D_T\left(T(0,\tau)\right)\right)^{1/4}\frac{e^{-\sqrt{s/D_0}L(z)}}{s} \\ & + \int_0^{L(\infty)} \frac{e^{-\sqrt{s/D_0}\left[L(z')+L(z)\right]}}{\sqrt{s}} F_1(z')dz' + \int_0^{L(\infty)} \frac{e^{-\sqrt{s/D_0}\left[L(z')+L(z)\right]}}{\sqrt{s}} F_2(z')\overline{C}(z',s)dz' \\ & - \int_{L(z)}^{L(\infty)} \frac{e^{-\sqrt{s/D_0}\left[L(z')-L(z)\right]}}{\sqrt{s}} F_1(z')dz' - \int_{L(z)}^{L(\infty)} \frac{e^{-\sqrt{s/D_0}\left[L(z')-L(z)\right]}}{\sqrt{s}} F_2(z')\overline{C}(z',s)dz' \\ & - \int_0^{L(z)} \frac{e^{-\sqrt{s/D_0}\left[L(z)-L(z')\right]}}{\sqrt{s}} F_1(z')dz' - \int_0^{L(z)} \frac{e^{-\sqrt{s/D_0}\left[L(z)-L(z')\right]}}{\sqrt{s}} F_2(z')\overline{C}(z',s)dz' \Bigg]\end{aligned} , \tag{A-4}$$

where

$$F_1(z') = -\frac{C_i(z')}{2\sqrt{D_0}\left(D_T'\left(T(z',\tau)\right)\right)^{1/4}}, \tag{A-5}$$

and

$$F_2(z') = \frac{\sqrt{D_0}}{2\left(D_T\left(T(z',\tau)\right)\right)^{1/4}}\left\{\frac{1}{4}D_T''\left(T(z',\tau)\right) - \frac{1}{16}\frac{\left(D_T'\left(T(z',\tau)\right)\right)^2}{D_T\left(T(z',\tau)\right)}\right\}. \tag{A-6}$$

Taking the inverse Laplace transform of Equation (A-4) and applying the convolution theorem [163] to the integral terms that contain $\overline{C}(z',s)$ as a factor, the dopant concentration distribution can be obtained as given by Equation (2-19).

APPENDIX B: PHOTOEXCITED FREE ELECTRON DENSITY

The rate of change of free electron density can be obtained by

$\begin{Bmatrix} Rate\ \ of\ \ change\ \ of \\ free\ \ electron\ \ density \end{Bmatrix} = \begin{Bmatrix} Rate\ \ of\ \ generation\ \ of \\ free\ \ electron\ \ density \end{Bmatrix} - \begin{Bmatrix} Rate\ \ of\ \ loss\ \ of \\ free\ \ electron\ \ density \end{Bmatrix}$. The photo-excited rate of free electrons within the doped SiC detector per unit volume depends on the absorbed irradiance I_a, the internal quantum efficiency $\eta_{i,SiC}$, the detector area A_{SiC}, and the photon energy $h\nu_M$, as $\frac{I_a \eta_{i,SiC} A_{SiC}}{h\nu_M V}$. The photo-generated electrons decay based on their recombination lifetime τ_r, and this decay is approximate as $\frac{\Delta N_e}{\tau_r}$. The other term of free electron loss is by diffusion. The free electrons are diffusing into the detector area A_{SiC} with the diffusivity D at diffusion rate as $DA_{SiC}\frac{\Delta N_e}{l_D}$, where the diffusion length (l_D) is expressed as $l_D \approx \sqrt{4D\tau_d}$ for 2-dimensional diffusion [164]. It keeps diffusing before recombining with characteristic diffusion time τ_d which is taken as MWIR irradiation time. The rate of free electron loss by diffusion per unit volume is written as $\frac{\Delta N_e A_{SiC}}{V}\sqrt{\frac{D}{4\tau_d}}$ which becomes $\frac{\Delta N_e}{d_d}\sqrt{\frac{D}{4\tau_d}}$ by considering the detector volume V as the product of the detector area and the thickness of the doped region (d_d).

APPENDIX C: NETD AND DETECTIVITY

Derivation of NETD and detectivity;

1) Derivation of NETD and detectivity for SiC detector

1-a) SiC detector from the noise due to photon shot noise from the radiation source, Johnson noise and generation-recombination (Equations (5-17) and (5-21)).

The internal quantum efficiency of SiC detector is can be written as $\eta_{i,SiC} = \frac{N_e}{P_{a,MWIR}} \frac{h\nu_M}{\tau_d}$.

Therefore, the absorbed MWIR radiation in SiC detector can be expressed as

$$P_{a,MWIR} = N_e \frac{h\nu_M}{\eta_{i,SiC}\tau_d}. \tag{C-1}$$

The noise equivalent power (NEP) which is the amount of radiant power collected on a detector that will produce an signal-to-noise ratio is equal to unity (S/N = 1) can be written as the root-mean-square (RMS) noise as

$$NEP_{SiC} = \left\langle \delta N_e^{\,2} \right\rangle^{1/2} \frac{h\nu_M}{\eta_{i,SiC}\tau_d}, \tag{C-2}$$

where $\left\langle \delta N_e^{\,2} \right\rangle^{1/2}$ is the total noise of free electron density that is given by $\left\langle \delta N_e^{\,2} \right\rangle^{1/2} = \left\langle \delta N_{e,Q}^{\,2} \right\rangle^{1/2} + \left\langle \delta N_{e,J}^{\,2} \right\rangle^{1/2} + \left\langle \delta N_{e,GR}^{\,2} \right\rangle^{1/2}$ from Equations (5-1)-(5-3). Rewrite Equation (C-2) as

$$\frac{\left\langle \delta N_e^{\,2} \right\rangle^{1/2}}{NEP_{SiC}} = \eta_{i,SiC} \frac{\tau_d}{h\nu_M}. \tag{C-3}$$

Noise equivalent power (NEP) is expressed in terms of detectivity as [85]

$$\frac{1}{NEP_{SiC}} = \frac{D^*_{SiC}}{\sqrt{A_{SiC}}\sqrt{\Delta f_{SiC}}} . \tag{C-4}$$

Equation (C-1) can be written in terms of N_e as

$$N_e = P_{a,MWIR}\eta_{i,SiC}\frac{\tau_d}{h\nu_M} . \tag{C-5}$$

Take derivative of Equation (C-5) with respect to T_s as

$$\frac{\Delta N_e}{\Delta T_s} = \eta_{i,SiC}\frac{\tau_d}{h\nu_M}\frac{\partial P_{a,MWIR}}{\partial T_s} , \tag{C-6}$$

where $P_{a,MWIR}$ is the absorbed power of MWIR from the radiation source through optics in SiC detector given by $P_{a,MWIR} = \alpha_{SiC}\varepsilon_s \frac{\tau_0}{4F^2} A_{SiC}\left(L_B\right)_{\lambda_{12}}$. Substituting $P_{a,MWIR}$ into Equation (C-6) becomes

$$\frac{\Delta N_e}{\Delta T_s} = \eta_{i,SiC}\frac{\tau_d}{h\nu_M}\alpha_{SiC}\varepsilon_s\frac{\tau_0}{4F^2}A_{SiC}\left(\frac{dL_B}{dT_s}\right)_{\lambda_{12}} . \tag{C-7}$$

Substituting Equation (C-3) into Equation (C-7) becomes

$$\frac{\Delta N_e}{\Delta T_s} = \frac{\left\langle \delta N_e{}^2 \right\rangle^{1/2}}{NEP_{SiC}}\alpha_{SiC}\varepsilon_s\frac{\tau_0}{4F^2}A_{SiC}\left(\frac{dL_B}{dT_s}\right)_{\lambda_{12}} . \tag{C-8}$$

Equation (C-8) can be rewritten in terms of signal-to-noise ratio (S/N) as

$$\frac{S}{N} = \frac{\Delta N_e}{\left\langle \delta N_e^{\,2} \right\rangle^{1/2}} = \frac{\Delta T_s}{NEP_{SiC}} \alpha_{SiC} \varepsilon_s \frac{\tau_0}{4F^2} A_{SiC} \left(\frac{dL_B}{dT_s} \right)_{\lambda_{12}}$$
$$= \frac{\Delta T_s D^*_{SiC}}{\sqrt{A_{SiC}} \sqrt{\Delta f_{SiC}}} \alpha_{SiC} \varepsilon_s \frac{\tau_0}{4F^2} A_{SiC} \left(\frac{dL_B}{dT_s} \right)_{\lambda_{12}} . \tag{C-9}$$

Since $\frac{\Delta T_s}{S/N} = NETD_{SiC}$ at $S/N = 1$, see Ref. [85], Equation (C-9) can be expressed as

$$NETD_{SiC} = \frac{4F^2 \sqrt{A_{SiC}} \sqrt{\Delta f_{SiC}}}{D^*_{SiC} \alpha_{SiC} \varepsilon_s \tau_0 A_{SiC} \left(\frac{dL_B}{dT_s} \right)_{\lambda_{12}}} . \tag{C-10}$$

Rewrite Equation (C-10) in terms of detectivity as

$$D^*_{SiC} = \frac{4F^2}{NETD_{SiC} \alpha_{SiC} \varepsilon_s \tau_0 \left(\frac{dL_B}{dT_s} \right)_{\lambda_{12}}} \sqrt{\frac{\Delta f_{SiC}}{A_{SiC}}} . \tag{C-11}$$

1-b) Detectivity derivation by using responsivity (Equation (5-21)).

The responsivity is a useful technical parameter that allows the prediction of the detector signal levels caused by an infrared radiation of the given power and wavelength or as a result of thermal radiation from an object at a given temperature and emissivity. In this study, the responsivity of SiC detector can be defined in terms of the absorbance response of the MWIR wavelength per absorbed power of infrared radiation. Therefore, the absorbance can be expressed as

$$\alpha_{SiC} = \Re_{SiC} P_{a,MWIR} \,, \tag{C-12}$$

where $\Re_{SiC}$ is the responsivity of SiC detector at MWIR wavelength given by $\Re_{SiC} = \frac{\eta_{i,SiC}\tau_d}{h\nu_M}$ and $P_{a,MWIR}$ is the absorbed power of MWIR from the radiation source through optics in SiC detector given by $P_{a,MWIR} = \alpha_{SiC}\varepsilon_s \frac{\tau_0}{4F^2} A_{SiC}\left(L_B\right)_{\lambda_{12}}$. From Equations (C-3), (C-4) and (C-12), $\Re_{SiC}$ is expressed in terms of noise equivalent power (*NEP*) as [85]

$$\Re_{SiC} = \frac{\left\langle \delta\alpha_{SiC}{}^2 \right\rangle^{1/2}}{NEP_{L,SiC}} = \frac{\left\langle \delta\alpha_{SiC}{}^2 \right\rangle^{1/2} D^*_{SiC}}{\sqrt{A_{SiC}}\sqrt{\Delta f_{SiC}}} \,. \tag{C-13}$$

Take derivative of Equation (C-12) with respect to T_s as

$$\frac{\Delta\alpha_{SiC}}{\Delta T_s} = \Re_{SiC}\frac{\partial P_{MWIR}}{\partial T_s} = \Re_{SiC}\alpha_{SiC}\varepsilon_s \frac{\tau_0}{4F^2} A_{SiC}\left(\frac{dL_B}{dT_s}\right)_{\lambda_{12}} \,. \tag{C-14}$$

Substituting Equation (C-13) into Equation (C-14) becomes

$$\frac{\Delta\alpha_{SiC}}{\Delta T_s} = \frac{\left\langle \delta\alpha_{SiC}{}^2 \right\rangle^{1/2} D^*_{SiC}}{\sqrt{A_{SiC}}\sqrt{\Delta f_{SiC}}}\alpha_{SiC}\varepsilon_s \frac{\tau_0}{4F^2} A_{SiC}\left(\frac{dL_B}{dT_s}\right)_{\lambda_{12}} \,. \tag{C-15}$$

Equation (C-15) can be rewritten in terms of signal-to-noise ratio (S/N) as

$$\frac{S}{N} = \frac{\Delta\alpha_{SiC}}{\left\langle \delta\alpha_{SiC}{}^2 \right\rangle^{1/2}} = \frac{\Delta T_s D^*_{SiC}}{\sqrt{A_{SiC}}\sqrt{\Delta f_{SiC}}}\alpha_{SiC}\varepsilon_s \frac{\tau_0}{4F^2} A_{SiC}\left(\frac{dL_B}{dT_s}\right)_{\lambda_{12}} \,. \tag{C-16}$$

The signal-to-noise ratio (S/N) can be expressed as $\frac{S}{N} = \frac{\Delta\alpha_{SiC}}{\left\langle \delta\alpha_{SiC}{}^2 \right\rangle^{1/2}} = \frac{\Delta N_e}{\left\langle \delta N_e{}^2 \right\rangle^{1/2}}$. Therefore, Equation (C-16) becomes

$$\frac{S}{N} = \frac{\Delta N_e}{\left\langle \delta N_e{}^2 \right\rangle^{1/2}} = \frac{\Delta T_s D^*_{SiC}}{\sqrt{A_{SiC}}\sqrt{\Delta f_{SiC}}} \alpha_{SiC}\varepsilon_s \frac{\tau_0}{4F^2} A_{SiC} \left(\frac{dL_B}{dT_s} \right)_{\lambda_{12}} . \tag{C-17}$$

Since $\frac{\Delta T_s}{S/N} = NETD_{SiC}$ at S/N = 1, see Ref. [85], $NETD_{SiC}$ from Equation (C-17) can be expressed as

$$NETD_{SiC} = \frac{\sqrt{\Delta f_{SiC}}}{D^*_{SiC}\alpha_{SiC}\varepsilon_s \frac{\tau_0}{4F^2}\sqrt{A_{SiC}} \left(\frac{dL_B}{dT_s} \right)_{\lambda_{12}}} . \tag{C-18}$$

Therefore, the detectivity can be obtained from Equation (C-18) as

$$D^*_{SiC} = \frac{4F^2}{NETD_{SiC}\alpha_{SiC}\varepsilon_s\tau_0 \left(\frac{dL_B}{dT_s} \right)_{\lambda_{12}}} \sqrt{\frac{\Delta f_{SiC}}{A_{SiC}}} . \tag{C-19}$$

2) He-Ne laser and SiC detector from the interferometric noise due to multiple reflection and interference (Equations (5-18) and (5-22)).

The signal-to-noise ratio (S/N) for He-Ne laser beam and doped SiC detector can be calculated by $\frac{S}{N} = \frac{\Delta P_{r,L}}{\left\langle \delta P_{r,L}{}^2 \right\rangle^{1/2}} \equiv \frac{\Delta \rho_{SiC,L}}{\left\langle \delta \rho_{SiC,L}{}^2 \right\rangle^{1/2}}$ ($P_{r,L} = P_{i,L} \Delta \rho_{SiC,L}$, where $P_{i,L}$ and $P_{r,L}$ are the incident and reflected power of He-Ne laser respectively), where $\left\langle \delta P_{r,L}{}^2 \right\rangle^{1/2}$ is the noise on the reflected power of He-Ne laser due to multiple reflection and interference. Since the noise of reflected laser power is the same as the interferometric noise ($\left\langle \delta P_{r,I}{}^2 \right\rangle^{1/2}$), it can be expressed as $\left\langle \delta P_{r,L}{}^2 \right\rangle^{1/2} = \left\langle \delta P_{r,I}{}^2 \right\rangle^{1/2}$.

Here $\left\langle \delta P_{r,I}{}^2 \right\rangle^{1/2} = P_{i,L} \sqrt{16\pi (1-\sqrt{R_{au}})^4 R_{au} \Delta \nu \left(R_{du}\tau_1 + (1-\sqrt{R_{du}})^4 R_{ad}\tau_2 \right)}$ from Equation (5-11).

The S/N is

$$\begin{aligned} \frac{S}{N} &= \frac{\Delta P_{r,L}}{P_{i,L}\sqrt{16\pi (1-\sqrt{R_{au}})^4 R_{au} \Delta \nu \left(R_{du}\tau_1 + (1-\sqrt{R_{du}})^4 R_{ad}\tau_2 \right)}} \\ &= \frac{\Delta \rho_{SiC,L}}{\sqrt{16\pi (1-\sqrt{R_{au}})^4 R_{au} \Delta \nu \left(R_{du}\tau_1 + (1-\sqrt{R_{du}})^4 R_{ad}\tau_2 \right)}} \end{aligned} , \qquad \text{(C-20)}$$

The reflectance of SiC detector ($\Delta \rho_{SiC,L}$) is dependent variable as a function of the SiC detector temperature (T_{SiC}) and the radiation source temperature (T_s) with two cases as

$$\Delta \rho_{SiC,L}(T_{SiC}, T_s) = \left. \frac{d\rho_{SiC,L}(T_{SiC}, T_s)}{dT_{SiC}} \right|_{T_{SiC1}} \Delta T_{SiC} \quad \text{with constant } T_s , \qquad \text{(C-21)}$$

$$\Delta\rho_{SiC,L}(T_{SiC},T_s) = \left.\frac{d\rho_{SiC,L}(T_{SiC},T_s)}{dT_s}\right|_{T_{s1}} \Delta T_s \quad \text{with constant } T_{SiC}. \tag{C-22}$$

With constant T_s ($\Delta\rho_{SiC,L}(T_{SiC})$), the S/N is

$$\begin{aligned}\frac{S}{N} &= \frac{\Delta\rho_{SiC,L}(T_{SiC})}{\sqrt{16\pi(1-\sqrt{R_{au}})^4 R_{au}\Delta\nu\left(R_{du}\tau_1 + (1-\sqrt{R_{du}})^4 R_{ad}\tau_2\right)}} \\ &= \frac{\left(\left.\frac{d\rho_{SiC,L}(T_{SiC})}{dT_{SiC}}\right|_{T_{SiC1}} \Delta T_{SiC}\right)}{\sqrt{16\pi(1-\sqrt{R_{au}})^4 R_{au}\Delta\nu\left(R_{du}\tau_1 + (1-\sqrt{R_{du}})^4 R_{ad}\tau_2\right)}},\end{aligned} \tag{C-23}$$

Since $\frac{\Delta T_{SiC}}{S/N} = NETD_{L,SiC}$ at $S/N = 1$, the $NETD_{L,SiC}$ is

$$NETD_{L,SiC} = \frac{\sqrt{16\pi(1-\sqrt{R_{au}})^4 R_{au}\Delta\nu\left(R_{du}\tau_1 + (1-\sqrt{R_{du}})^4 R_{ad}\tau_2\right)}}{\left.\frac{d\rho_{SiC,L}(T_{SiC})}{dT_{SiC}}\right|_{T_{SiC1}}}, \tag{C-24}$$

Recalling the definition of noise equivalent power (NEP) [85], the amount of radiant power collected on a detector that will produce an S/N of unity,

$$NEP_{L,SiC} = \frac{P_{a,L}}{S/N}, \tag{C-25}$$

where $P_{a,L}$ is the absorbed laser power in Si detector given by $P_{a,L} = \alpha_{Si} P_{r,L}$.

The detectivity is defined as [85]

$$D^*_{L,SiC} = \frac{\sqrt{A_{Si}}\sqrt{\Delta f_{Si}}}{NEP_{L,SiC}}. \tag{C-26}$$

Substitute Equation (C-25) into Equation (C-26) and the detectivity can be written as

$$\begin{aligned} D^*_{L,SiC} &= \frac{S}{N}\frac{\sqrt{A_{Si}}\sqrt{\Delta f_{Si}}}{P_{a,L}} \\ &= \frac{\Delta P_{r,L}(T_{SiC})\sqrt{A_{Si}}\sqrt{\Delta f_{Si}}}{\alpha_{Si}\rho_{SiC,L}P_{i,L}{}^2\sqrt{16\pi(1-\sqrt{R_{au}})^4 R_{au}\Delta\nu\left(R_{du}\tau_1 + (1-\sqrt{R_{du}})^4 R_{ad}\tau_2\right)}}. \\ &= \frac{\Delta\rho_{SiC,L}(T_{SiC})\sqrt{A_{Si}}\sqrt{\Delta f_{Si}}}{\alpha_{Si}\rho_{SiC,L}P_{i,L}\sqrt{16\pi(1-\sqrt{R_{au}})^4 R_{au}\Delta\nu\left(R_{du}\tau_1 + (1-\sqrt{R_{du}})^4 R_{ad}\tau_2\right)}} \end{aligned} \tag{C-27}$$

The detectivity is expressed in terms of $NETD_{L,SiC}$ as

$$\begin{aligned} D^*_{L,SiC} &= \frac{\sqrt{A_{Si}}\sqrt{\Delta f_{Si}}}{NETD_{L,SiC}\dfrac{dP_{a,L}}{dT_{SiC}}} \\ &= \frac{\sqrt{A_{Si}}\sqrt{\Delta f_{Si}}}{NETD_{L,SiC}\alpha_{Si}\rho_{SiC,L}P_{i,L}\dfrac{d\rho_{SiC,L}(T_{SiC})}{dT_{SiC}}} \end{aligned}. \tag{C-28}$$

3) He-Ne laser and Si detector from the power noise due to intensity and frequency fluctuations (Equations (5-19) and (5-23)).

The photo-generated current in Si detector can be expressed as

$$i_{Si} = \frac{q\eta_{i,Si}\alpha_{Si}\rho_{SiC,L}P_L}{h\nu_L}. \tag{C-29}$$

The noise equivalent power (NEP) of the incident He-Ne laser power in Si detector is written as

$$NEP_{L,Si} = \left\langle \delta i_{Si}{}^{2} \right\rangle^{1/2} \frac{h\nu_L}{q\eta_{i,Si}\alpha_{Si}\rho_{SiC,L}}. \tag{C-30}$$

The electric current in Si detector (i_{Si}) is a function of the reflected power of He-Ne laser beam ($P_{r,L}$), i.e., $i_{Si}(P_{r,L})$. Since $P_{r,L}$ depends on the incident power of He-Ne laser beam (P_L) and P_L depends on the temperature of He-Ne laser (T_L), i_{Si} can be written as a function of P_L for constant temperatures of the SiC detector (T_{SiC}) and the radiation source (T_s), i.e., $i_{Si}(P_{r,L}(P_L(T_L)))$. The He-Ne laser is produced by the plasma of Helium and Neon gas mixture in the ratio ranging from 5:1 to 14:1 by volume [165]. Random thermal motion of atoms within the He-Ne plasma broadens the spectral line of the He-Ne laser. Some of the photons, which do not exit the laser system as a He-Ne laser beam, deposits their energy in the surrounding medium such as the laser tube and mirrors. Therefore, the temperature of these materials of the laser cavity fluctuates undergoing thermal expansion. This expansion affects the frequency and intensity of the longitudinal cavity mode and, consequently, the laser output power changes. Typically the longer the laser cavity, the smaller is the fluctuation. For instance, a seven-inch-long laser cavity typically will have mode-sweeping fluctuations of 10%, while a fourteen-inch-long laser cavity will normally have less than 2% [166]. Therefore, Equation (C-29) can be rewritten as $i_{Si}(P_{r,L}(P_L(T_L))) = \dfrac{q\eta_{i,Si}\alpha_{Si}\rho_{SiC,L}P_L(T_L)}{h\nu_L}$.

The change in the electric current in the Si detector due to a variation in the He-Ne laser temperature $\Delta T_L = T_{L2} - T_{L1}$, where T_{L1} and T_{L2} are the nominal and drifted temperature of the laser cavity, respectively, can be written as

$$\begin{aligned}\Delta i_{Si}(P_{r,L}(P_L(T_L))) &= i_{Si}(P_{r,L}(P_L(T_{L2}))) - i_{Si}(P_{r,L}(P_L(T_{L1}))) \\ &= i_{Si}(P_{r,L}(P_L(T_{L1}+\Delta T_L))) - i_{Si}(P_{r,L}(P_L(T_{L1}))) \cdot\end{aligned} \tag{C-30}$$

By linear approximation, $i_{Si}(P_{r,L}(P_L(T_{L1}+\Delta T_L)))$ in Equation (C-31) can be written as

$$\begin{aligned}i_{Si}(P_{r,L}(P_L(T_{L1}+\Delta T_L))) &= i_{Si}(P_{r,L}(P_L(T_L)))\Big|_{T_{L1}} + \frac{di_{Si}(P_{r,L}(P_L(T_L)))}{dT_L}\Bigg|_{T_{L1}} \cdot \Delta T_L \\ &= i_{Si}(P_{r,L}(P_L(T_{L1}))) + \frac{di_{Si}(P_{r,L}(P_L(T_L)))}{dT_L}\Bigg|_{T_{L1}} \cdot \Delta T_L\end{aligned} \quad . \tag{C-31}$$

Applying Equation (C-32) to Equation (C-31), the current change can be expressed as

$$\Delta i_{Si}(P_{r,L}(P_L(T_L))) = \frac{di_{Si}(P_{r,L}(P_L(T_L)))}{dT_L}\Bigg|_{T_{L1}} \cdot \Delta T_L \, . \tag{C-32}$$

The current change in Si detector by applying Equation (C-29) into Equation (C-33) can be written as

$$\Delta i_{Si}(P_{r,L}(P_L(T_L))) = \frac{q\eta_{i,Si}\alpha_{Si}\rho_{SiC,L}}{h\nu_L}\frac{dP_L(T_L)}{dT_L}\Bigg|_{T_{L1}} \Delta T_L \quad \text{with constant } T_{SiC} \text{ and } T_s \, . \tag{C-33}$$

In Equation (C-34), Δi_{Si} is the signal to obtain the signal-to-noise ratio. The signal-to-noise (S/N) can be obtained from Equation (C-30) and Equation (C-34) as

$$\frac{\Delta i_{Si}}{\left\langle \delta i_{Si}{}^{2} \right\rangle^{1/2}} = \frac{\Delta T_L}{NEP_{L,Si}} \frac{dP_L}{dT_L}. \tag{C-34}$$

By assuming that all other noise contributions are negligible compared to the noise associated with the incident photon flux from the He-Ne laser (photon shot noise by power fluctuation), the current noise can be expressed as

$$\left\langle \delta i_{Si}{}^{2} \right\rangle^{1/2} \approx \left\langle \delta i_{Si,Q}{}^{2} \right\rangle^{1/2} = \frac{q\eta_{i,Si}\alpha_{Si}\rho_{SiC,L}}{h\nu_L}\left(\left\langle \delta P_{r,P}{}^{2} \right\rangle^{1/2} + \left\langle \delta P_{r,F}{}^{2} \right\rangle^{1/2} \right). \tag{C-35}$$

Since $\frac{\Delta T_L}{S/N} = NETD_{L,Si}$ at $S/N = 1$, the $NETD_{L,Si}$ from Equation (C-35) can be written as

$$NETD_{L,Si} = \frac{\left(\left\langle \delta P_{r,P}{}^{2} \right\rangle^{1/2} + \left\langle \delta P_{r,F}{}^{2} \right\rangle^{1/2} \right)}{\left(\frac{dP_L}{dT_L} \right)}, \tag{C-36}$$

where $\left\langle \delta P_{r,P}{}^{2} \right\rangle^{1/2}$ and $\left\langle \delta P_{r,F}{}^{2} \right\rangle^{1/2}$ are given by Equations (5-6) and (5-7) as $\left\langle \delta P_{L,P}{}^{2} \right\rangle^{1/2} = \sqrt{\frac{\pi\eta_{e,L}P_L h\nu_L}{t_p{}^2\omega_1}}$ and $\left\langle \delta P_{L,F}{}^{2} \right\rangle^{1/2} = \sqrt{\frac{\pi\eta_{e,L}P_L h\nu_L \alpha_{SiC,L}{}^2\tau^2\omega_1}{2t_p{}^2}}$.

Substitute $\left\langle \delta P_{r,P}{}^{2} \right\rangle^{1/2}$ and $\left\langle \delta P_{r,F}{}^{2} \right\rangle^{1/2}$ into Equation (C-37) as

$$NETD_{L,Si} = \frac{\left(\sqrt{\frac{\pi\eta_{e,L}P_L h\nu_L}{t_p{}^2\omega_1}} + \sqrt{\frac{\pi\eta_{e,L}P_L h\nu_L \alpha_{SiC,L}{}^2\tau^2\omega_1}{2t_p{}^2}} \right)}{\left(\frac{dP_L}{dT_L} \right)}, \tag{C-37}$$

Substitute Equation (C-30) into Equation (C-26) and rewrite the detectivity in terms of $NETD_{L,Si}$ as

$$D^*_{L,Si} = \frac{q\eta_{i,Si}\alpha_{Si}\rho_{SiC,L}\sqrt{A_{Si}\Delta f_{Si}}}{h\nu_L\left\langle \delta i_{Si}{}^2 \right\rangle^{1/2}} = \frac{\sqrt{A_{Si}\Delta f_{Si}}}{NETD_{L,Si}\dfrac{dP_L}{dT_L}} . \tag{C-38}$$

4) Si detector from the current noise due to photon shot noise from He-Ne laser, Johnson, shot and generation-recombination (Equations (5-20) and (5-24)).

Since the current in Si detector is varying depend on $P_{r,L}$ which is ultimately affected by T_{SiC} at constant temperature of the radiation source (T_s), Equation (C-29) can be rewritten as

$$i_{Si}(P_{r,L}(\rho_{SiC,L}(T_{SiC}))) = \frac{q\eta_{i,Si}\alpha_{Si}\rho_{SiC,L}P_{r,L}(\rho_{SiC,L}(T_{SiC}))}{h\nu_L} .$$

The change in electric current in the Si detector due to a variation of SiC detector temperature $\Delta T_{SiC} = T_{SiC2} - T_{SiC1}$, where T_{SiC1} and T_{SiC2} are the nominal and drifted temperature of SiC detector, respectively, can be written as

$$\begin{aligned}\Delta i_{Si}(P_{r,L}(\rho_{SiC,L}(T_{SiC}))) &= i_{Si}(P_{r,L}(\rho_{SiC,L}(T_{SiC2}))) - i_{Si}(P_{r,L}(\rho_{SiC,L}(T_{SiC1}))) \\ &= i_{Si}(P_{r,L}(\rho_{SiC,L}(T_{SiC1} + \Delta T_{SiC}))) - i_{Si}(P_{r,L}(\rho_{SiC,L}(T_{SiC1}))) .\end{aligned} \tag{C-39}$$

By linear approximation, $i_{Si}(P_{r,L}(\rho_{SiC,L}(T_{SiC1} + \Delta T_{SiC})))$ in Equation (C-40) can be written as

$$i_{Si}(P_{r,L}(\rho_{SiC,L}(T_{SiC1}+\Delta T_{SiC}))) = i_{Si}(P_{r,L}(\rho_{SiC,L}(T_{SiC})))\Big|_{T_{SiC1}} + \frac{di_{Si}(P_{r,L}(\rho_{SiC,L}(T_{SiC})))}{dT_{SiC}}\Bigg|_{T_{SiC1}} \cdot \Delta T_{SiC}$$
$$= i_{Si}(P_{r,L}(\rho_{SiC,L}(T_{SiC1}))) + \frac{di_{Si}(P_{r,L}(\rho_{SiC,L}(T_{SiC})))}{dT_{SiC}}\Bigg|_{T_{SiC1}} \cdot \Delta T_{SiC} \quad . \qquad \text{(C-40)}$$

Applying Equation (C-41) to Equation (C-40), the current change can be expressed as

$$\Delta i_{Si}(P_{r,L}(\rho_{SiC,L}(T_{SiC}))) = \frac{di_{Si}(P_{r,L}(\rho_{SiC,L}(T_{SiC})))}{dT_{SiC}}\Bigg|_{T_{SiC1}} \cdot \Delta T_{SiC} \, . \qquad \text{(C-41)}$$

The current change in Si detector by applying Equation (C-29) into Equation (C-42) can be written as

$$\Delta i_{Si}(P_{r,L}(\rho_{SiC,L}(T_{SiC}))) = \frac{q\eta_{i,Si}\alpha_{Si}\rho_{SiC,L}}{h\nu_L}\frac{dP_{r,L}(\rho_{SiC,L}(T_{SiC}))}{dT_{SiC}}\Bigg|_{T_{SiC1}} \Delta T_{SiC} \quad \text{with constant } T_s \, . \qquad \text{(C-42)}$$

In Equation (C-43), Δi_{Si} is the signal to obtain the signal-to-noise ratio. The current noise can be obtained by summation of the given noise mechanisms in above section 5.5 as

$$\left\langle \delta i_{Si}{}^2 \right\rangle^{1/2} = \left\langle \delta i_{Si,Q}{}^2 \right\rangle^{1/2} + \left\langle \delta i_{Si,J}{}^2 \right\rangle^{1/2} + \left\langle \delta i_{Si,S}{}^2 \right\rangle^{1/2} + \left\langle \delta i_{Si,GR}{}^2 \right\rangle^{1/2} . \qquad \text{(C-43)}$$

Expressions for these noise terms are obtained from Equations (5-12) to (5-15) as $\left\langle \delta i_{Si,Q}{}^2 \right\rangle^{1/2} = q\sqrt{\frac{\eta_{e,Si}P_L\rho_{d,L}\Delta f_{Si}}{h\nu_L}}$, $\left\langle \delta i_{Si,J}{}^2 \right\rangle^{1/2} = \sqrt{\frac{4k_BT_{Si}\Delta f_{Si}}{R_{e,Si}}}$, $\left\langle \delta i_{Si,S}{}^2 \right\rangle^{1/2} = \sqrt{2q\left\langle \delta i_{L,Q}{}^2 \right\rangle^{1/2}\Delta f_{Si}}$ and $\left\langle \delta i_{Si,GR}{}^2 \right\rangle^{1/2} = 2qG\sqrt{\eta_{e,Si}\frac{P_L\rho_{d,L}}{h\nu_L}\Delta f_{Si} + g_{th}A_{Si}\Delta f_{Si}l_t}$.

Therefore, from Equation (C-43) the S/N is expressed as

$$\frac{\Delta i_{Si}}{\left\langle \delta i_{Si}{}^{2} \right\rangle^{1/2}} = \frac{q\eta_{i,Si}\alpha_{Si}\rho_{SiC,L}\Delta T_{SiC}}{h\nu_L \left\langle \delta i_{Si}{}^{2} \right\rangle^{1/2}} \frac{dP_{r,L}}{dT_{SiC}} . \tag{C-44}$$

Since $\frac{\Delta T_{SiC}}{S/N} = NETD_{Si}$ at $S/N = 1$, the $NETD_{Si}$ from Equation (C-45) can be expressed as

$$NETD_{Si} = \frac{\frac{h\nu_L}{q\eta_{i,Si}\alpha_{Si}} \left(q\sqrt{\frac{\eta_{e,Si}P_L\rho_{d,L}\Delta f_{Si}}{h\nu_L}} + \sqrt{\frac{4k_B T_{Si}\Delta f_{Si}}{R_{e,Si}}} + \sqrt{2q\left\langle \delta i_{L,Q}{}^{2} \right\rangle^{1/2}\Delta f_{Si}} + 2qG\sqrt{\eta_{e,Si}\frac{P_L\rho_{d,L}}{h\nu_L}\Delta f_{Si} + g_{th}A_{Si}\Delta f_{Si}l_t} \right)}{\left(\frac{dP_{r,L}}{dT_{SiC}} \right)} . \tag{C-46}$$

Substitute Equation (C-30) into Equation (C-26) and rewrite the detectivity in terms of $NETD_{Si}$ as

$$D_{Si}^{*} = \frac{\sqrt{A_{Si}\Delta f_{Si}}}{NETD_{Si}\frac{dP_{r,L}}{dT_{SiC}}} = \frac{\sqrt{A_{Si}\Delta f_{Si}}}{NETD_{Si}\alpha_{Si}\rho_{SiC,L}P_L\frac{d\rho_{SiC,L}}{dT_{SiC}}} . \tag{C-47}$$

APPENDIX D: LIST OF PUBLICATIONS

Journal Papers

1. G. Lim and A. Kar, “Modeling of Thermal Barrier Coating Temperature due to Transmissive Radiative Heating,” J. Mater. Sci., vol. 44, pp. 3589-3599, 2009.

2. G. Lim and A. Kar, “Radiative Properties of Thermal Barrier Coatings at High Temperatures,” J. Phys. D: Appl. Phys., vol. 42, pp. 155412, 2009.
3. G. Lim, U. P. DeSilva, N. R. Quick and A. Kar, “Laser Optical Gas Sensor by Photoexcitation Effect on Refractive Index,” Appl. Optics, vol. 49, pp. 1563-1573, 2010.
4. G. Lim, T. Manzur and A. Kar, “Optical Response of Laser-doped Silicon Carbide for Uncooled Mid-wave Infrared Detector,” Appl. Optics, vol. 50, pp. 2640-2653, 2011.
5. G. Lim and A. Kar, “Effects of Laser Scans on the Diffusion Depth and Diffusivity of Gallium in n-type 4H-SiC During Laser Doping,” Mater. Sci. Eng. B, vol. 176, pp. 660-668, 2011.
6. G. Lim, T. Manzur and A. Kar, “Improved Optical Properties and Detectivity of Uncooled Silicon Carbide Mid-wave Infrared Optical Detector with Increased Dopant Concentration,” J. Optics, vol. 14, pp. 105601-1-13, 2012.
7. G. Lim, T. Manzur and A. Kar, “Noise Sources in Mid-wave Infrared Uncooled Silicon Carbide Optical Photodetector,” accepted in Applied Optics.

Conference Papers

1. G. Lim, U. P. DeSilva, N. R. Quick and A. Kar, “Optical Property-based Wireless Chemical Sensor Using Silicon Carbide,” The 2009 Spring PIWG Meeting held in conjunction with the ISA's 55th International Instrumentation Symposium, 3 – 5 June 2009, South Shore Harbour Resort & Conference Center, 2500 South Shore Blvd., League City, Texas 77573, USA.
2. G. Lim, T. Manzur and A. Kar, “Laser Fabrication of Silicon Carbide Detector for Gas Sensing and Focal Plane Array Imaging,” The SPIE (Society of Photo-optical Instrumentation Engineers) Europe Remote Sensing 2009, 31 August – 3 September 2009, Berliner Congress Centre, Alexanderplatz, 10178 Berlin, Germany.
3. G. Lim, N. R. Quick and A. Kar, “Laser Doping for Bandgap Engineering,” The 28th ICALEO (International Congress on Applications of Lasers & Electro-Optics) conference, 2 – 5 November 2009, Hilton in the Walt Disney World Resort, 1751 Hotel Plaza Blvd., Lake Buena Vista, Orlando, FL 32830, USA.
4. G. Lim and A. Kar, “Wireless Chemical Sensor for Combustion Species at High Temperatures Using 4H-SiC,” The 34th ICACC (International Conference on Advanced Ceramics and Composites) conference, 24 – 29 January 2010, Hilton Daytona Beach Resort & Ocean Center, 100 North Atlantic Ave., Daytona Beach, FL 32118, USA.
5. G. Lim, T. Manzur and A. Kar, “Wireless Chemical Sensor for Combustion Species at High Temperatures Using 4H-SiC,” The SPIE Security + Defence, 20 – 23 September 2010, Centre de Congres Pierre Baudis, Toulouse, France.

6. G. Lim, T. Manzur and A. Kar, “Development of Wireless Gas Detector by Laser Doping Technique in Silicon Carbide,” The SPIE Remote Sensing, 20 – 23 September 2010, Centre de Congres Pierre Baudis, Toulouse, France.
7. G. Lim, T. Manzur and A. Kar, “Effect of Laser Irradiation Passes for Fabricating Mid-wave Infrared Silicon Carbide Detectors”, The 29th ICALEO (International Congress on Applications of Lasers & Electro-Optics) conference, 26 – 30 September 2010, Anaheim Marriott, 700 West Convention Way, Anaheim, CA 92802, USA.
8. G. Lim, T. Manzur and A. Kar, “Laser-Doped SiC as Wireless Remote Gas Sensor based on Semiconductor Optics”, Materials Science Forum, vol. 717-720, pp. 1195-1198, 2012.
9. G. Lim, T. Manzur and A. Kar, “Novel SiC Detector Based on Optical Signal Instead of Electrical Signal”, Mater. Res. Soc. Symp. Proc., vol. 1693, 2014.
10. G. Lim, T. Manzur and A. Kar, “Silicon Carbide Novel Optical Sensor for Combustion Systems,” The SPIE Optics + Photonics, 17 – 21 August 2014, San Diego Convention Center, San Diego, CA, USA.

REFERENCES

[1] D. Klocke, A. Schmitz, H. Soltner, H. Bousack and H. Schmitz, "Infrared Receptors in Pyrophilous ("Fire Loving") Insects as Model for New Un-cooled Infrared Sensors," *Beilstein J. Nanotechnol.*, vol. 2, pp. 186-197, 2011.

[2] W. Gronenberg and H. Schmitz, "Afferent Projections of Infrared-sensitive Sensilla in the Beetle Melanophila Acuminata (Coleoptera: Buprestidae)," *Cell Tissue Res.*, vol. 297, pp. 311-318, 1999.

[3] H. Schmitz and A. Schmitz, "Australian Fire-beetles," *Landscope*, vol. 18, pp. 36-41, 2002.

[4] L. Kurten and U. Schmidt, "Thermoperception in the Common Vampire Bat (Desmodus Rotundus)," *J. Comp. Physiol.*, vol. 146, pp. 223-228, 1982.

[5] R. C. Goris, "Infrared Organs of Snakes: And Integral Part of Vision," *J. Herpetology*, vol. 45(1), pp. 2-14, 2011.

[6] A. B. Sichert, P. Friedel and J. L. van Hemmen, "Snake's Perspective on Heat: Reconstruction of Input Using an Imperfect Detection System," *Phys. Rev. Lett.*, vol 97(6), pp. 068105, 2006.

[7] N. K. Dhar, R. Dat and A. K. Sood, Advances in Infrared Detector Array Technology, Ch. 7 in Optoelectronics – Advanced Materials and Devices, edited by S. L. Pyshkin and J. M. Ballato, Open access: InTech, 2013.

[8] A. Rogalski, "Infrared Detectors: An Overview," *Infrared Phys. Techn.*, vol. 43, pp. 187-210, 2002.

[9] A. Rogalski, J. Antoszewski and L. Faraone, "Third-generation Infrared Photodetector Arrays," *J. Appl. Phys.*, vol. 105, pp. 091101, 2009.

[10] L. J. Kozlowski and W. F. Kosonocky, Infrared Detector Arrays, Ch. 33 in: Handbook of Optics, Volume II: Design, Fabrication and Testing; Sources and Detectors; Radiometry and Photometry, edited by M. Bass, C. M. DeCusatis, J. M. Enoch, V. Lakshminarayanan, G. Li, C. MacDonald, V. N. Mahajan and E. V. Stryland, 3rd ed., New York: McGraw-Hill, 2010.

[11] W. J. Choyke, H. Matsunami and G. Pensl, Silicon Carbide, New York: Springer, 2004.

[12] A. A. Lebedev, Deep-level Defects in SiC Materials and Devices, Ch. 4 in: Silicon Carbide: Materials, Processing, and Devices, Volume 20, edited by Z. C. Feng and J. H. Zhao, New York: Taylor and Francis, 2004.

[13] A. A. Lebedev, "Deep-level Centers in Silicon Carbide: A Review," *Semiconductors*, vol. 33, pp. 107-130, 1999.

[14] A. Rogalski, "Infrared Detectors: Status and Trends," *Prog. in Quant. Electron.*, vol. 27, pp. 59-210, 2003.

[15] A. Rogalski, "History of Infrared Detectors," *Opto-electron. Rev.*, vol. 20(3), pp. 279-308, 2012.

[16] A. Rogalski, Infrared Detectors, 2nd ed., New York: CRC Press, 2011.

[17] P. R. Norton, Photodetectors, Ch. 15 in: Handbook of Optics, Volume I: Fundamentals, Techniques and Design, edited by M. Bass, C. M. DeCusatis, J. M. Enoch, V. Lakshminarayanan, G. Li, C. MacDonald, V. N. Mahajan and E. V. Stryland, 2nd ed., New York: McGraw-Hill, 1995.

[18] S. Sundaram and E. Mazur, "Inducing and Probing Non-thermal Transitions in Semiconductors Using Femtosecond Laser Pulses," *Nat. Mater.*, vol. 1, pp. 217-224, 2002.

[19] M. D. Perry, B. C. Stuart, P. S. Banks, M. D. Feit, V. Yanovsky and A. M. Rubenchik, "Ultrashort-pulse Laser Machining of Dielectric Materials," *J. Appl. Phys.*, vol. 85, pp. 6803-6810, 1999.

[20] R. M. Wood, Laser Damage in Optical Materials, Boston: Hilger, 1986.

[21] J. M. Fairfield and G. H. Schwuttke, "Silicon Diodes Made by Laser Irradiation," *Solid State Electronics*, vol. 11 (12), pp. 1175-1176, 1968.

[22] A. Garulli, M. Servidori and I. Vecchi, "In-depth Oxygen Contamination Produced in Silicon by Pulsed Laser Irradiation," *J. Phys. D: Appl. Phys.*, vol. 13, pp. L199, 1980.

[23] S. R. Wenham, "Laser Grooved Silicon Solar Cells," Ph.D thesis, UNSW, 1986.

[24] P. G. Carey, B. J. Woratschek, F. Bachmann, "Progress Toward Excimer Laser Metal Planarization and Via Hole Filling Using In-situ Monitoring," *Microelectron. Eng.*, vol. 20, pp. 89-106, 1993.

[25] E. Landi, P. G. Carey and T. W. Sigmon, "Numerical Simulation of the Gas Immersion Laser Doping (GILD) Process in Silicon," *IEEE Trans. Computer-aided Design Integr. Circuits Syst.*, vol. 7(2), pp. 205-214, 2006.

[26] E. Fogarassy, R. Stuck, J. C. Muller, A. Grob, J. J. Grob and P. Siffert, "Effects of Laser Irradiation on Phosphorus Diffused Layers in Silicon," *J. Electron. Mater.*, vol 9(1), pp. 197-209, 1980.

[27] G. L. Harris, Properties of Silicon Carbide, London, INSPEC, 1995.

[28] P. Friedrichs, T. Kimoto and L. Ley, Silicon Carbide: Volume 1: Growth, Defects, and Novel Applications, Weinheim: Wiley-VCH, 2011.

[29] J. A. Powell, J. B. Petit, J. H. Edgar, I. G. Jenkins, L. G. Matus, J. W. Yang, P. Pirouz, W. J. Choyke, L. Clemen, M. Yoganathan, J. W. Yang and P. Pirouz, "Application of Oxidation to the Streuctural Characterization of SiC Epitaxial Films," *Appl. Phys. Lett.*, vol. 59(2), pp. 183-185, 1991.

[30] J. A. Powell, J. B. Petit, J. H. Edgar, I. G. Jenkins, L. G. Matus, W. J. Choyke, L. Clemen and M. Yoganathan, "Controlled Growth of 3C-SiC and 6H-SiC Films on Low-tilt-angle Vicinal (0001) 6H-SiC Wafers," *Appl. Phys. Lett.*, vol. 59(3), pp. 333-335, 1991.

[31] S. J. Pearton, Processing of Wide Bandgap Semiconductors, New York: William Andrew, 2000.

[32] W. Wondrak, R. Hel, E. Niemann and U. Schmid, "SiC Devices for Advanced Power and High-temperature Applications," *IEEE Trans. Electron Devices*, vol. 48, pp. 307-308, 2001.

[33] E. Monroy; F. Omnes and F. Calle, "Wide-bandgap Semiconductor Ultraviolet Photodetectors," *Semicond. Sci. Technol.*, vol. 18, pp. R33-R51, 2003.

[34] G. Bertuccio and R. Casiraghi, "Study of Silicon Carbide for X-ray Detection and Spectroscopy," *IEEE Trans. Nucl. Sci.*, vol. 50, pp. 175-186, 2003.

[35] S. Lloyd, S. Savage, Advances in SiC Field Effect Gas Sensors, in: Silicon Carbide, edited by W.J. Choyke, H. Matsunami, G. Pensl, Springer, New York, 2004.

[36] T. Kimoto and H. Matsunami, Epitaxial Growth of High-Quality Silicon Carbide: Fundamentals and Recent Progress, in: Optoelectronic Properties of Semiconductors and Superlattices, edited by Z. C. Feng and J. H. Zhao, Taylor & Francis, New York, 2004.

[37] M. S. Janson, M. K. Linnarsson, A. Hallen, B. G. Svensson, N. Nordell and H. Bleichner, "Transient Enhanced Diffusion of Implanted Boron in 4H-Silicon Carbide," *Appl. Phys.*

Lett., vol. 76, pp. 1434-1436, 2000.

[38] G. J. Phelps, E. G. Chester, C. M. Johnson and N. G. Wright, "Field Enhanced Diffusion of Nitrogen and Boron in 4H-Silicon Carbide," *J. Appl. Phys.*, vol. 94, pp. 4285-4290, 2003.

[39] M. K. Linnarsson, M. S. Janson, A. Schoner and B. G. Svensson, "Aluminum and Boron Diffusion in 4H-SiC," Mat. Res. Soc. Symp. Proc., vol. 742, pp. K6.1-11, 2003.

[40] I. O. Usov, A. A. Suvorova, V. V. Sokolov, Y. A. Kudryavtsev and A. V. Suvorov, "Transient Enhanced Diffusion of Aluminum in SiC During High Temperature Ion Implantation," *J. Appl. Phys.*, vol. 86, pp. 6039-6042, 1999.

[41] A. Pokhmurska, O. Bonchik, S. Kiyak, G. Savitski and A. Gloskovsky, "Laser Doping in Si, InP and GaAs," *Appl. Surf. Sci.*, vol. 154, pp. 712-715, 2000.

[42] T. Akane, T. Nii and S. Matsumoto, "Two-Step Doping Using Excimer Laser in Boron Doping of Silicon," *Jpn. J. Appl. Phys.*, vol. 31, pp. 4437-4440, 1992.

[43] S. Matsumoto, S. Yoshioka, J. Wada, S. Inui and K. Uwasawa, "Boron Doping of Silicon by ArF Excimer Laser Irradiation in B_2H_6," *J. Appl. Phys.*, vol. 67, pp. 7204-7210, 1990.

[44] E. Fogarassy and J. Venturini, Long Pulse Excimer Laser Doping of Silicon and Silicon Carbide for High Precision Junction Fabrication, in: Recent Advances in Laser Processing of Materials, edited by J. Perriere, E. Millon and E. Fogarassy, Oxford: Elsevier, 2005.

[45] W. L. Brown, Laser Processing of Semiconductor, in: Laser Materials Processing, edited by M. Bass, New York: North-Holland Publishing Company, 1983.

[46] S. Kato, T. Nagahori and S. Matsumoto, "ArF Excimer Laser Doping of Boron into Silicon," *J. Appl. Phys.*, vol. 62(9), pp. 3656-3659, 1987.

[47] S. Ahmed, C. J. Barbero and T. W. Sigmon, "Activation of Ion Implanted Dopants in α-SiC," *Appl. Phys. Lett.*, vol. 66, pp. 712-714, 1995.

[48] S. Y. Chou, Y. Chang, K. H. Weiner, T. W. Sigmon and J. D. Parsons, "Annealing of Implantation Damage and Redistribution of Impurities in SiC using a Pulsed Excimer Laser," *Appl. Phys. Lett.*, vol. 56, pp. 530-532, 1990.

[49] T. Mizunami and N. Toyama, "ArF-Excimer-Laser Annealing of 3C-SiC Films," *Jpn. J. Appl. Phys.*, vol. 37, pp. 94-95, 1998.

[50] Y. Hishida, M. Watanabe, K. Sekine, K. Sugino and J. Kudo, "Suppression of Implantation-Induced Damage in 6H-SiC by Simultaneous Excimer Laser Irradiation

During Ion Implantation," *Appl. Phys. Lett.*, vol. 76, pp. 3867-3869, 2000.

[51] T. F. Deutsch, J. C. Fan, G. W. Turner, R. L. Chapman, D. J. Ehrlich and R. M. Osgood, "Efficient Si Solar Cells by Laser Photochemical Doping," *Appl. Phys. Lett.*, vol. 38, pp. 144-146, 1981.

[52] D. J. Ehrlich, R. M. Osgood, Jr. and T. F. Deutsch, "Direct Writing of Regions of High Doping on Semiconductors by UV-laser Phtodeposition," *Appl. Phys. Lett.*, vol. 36, pp. 916-918, 1980.

[53] T. Sameshima, S. Usui and M. Sekiya, "Laser-Induced Melting of Predeposited Impurity Doping Technique used to Fabricate Shallow Junctions," *J. Appl. Phys.*, vol. 62, pp. 711-713, 1987.

[54] J. Pezoldt, A. A. Kalnin, D. R. Moskwina and W. D. Savelyey, "Polytype Transitions in Ion Implanted Silicon Carbide," *Nucl. Instrum. Methods Phys. Res. B*, vol. 80, pp. 943-948, 1993.

[55] A. G. Grigoryants, Basics of Laser Material Processing, Boca Ranton: CRC, 1994.

[56] Y. Tajima, K. Kijima and W. D. Kingery, "Diffusion of Ion Implanted Aluminum in Silicon Carbide," *J. Chem. Phys.*, vol. 77(5), pp. 2592-2598, 1982.

[57] Z. Tian, I. A. Salama, N. R. Quick and A. Kar, "Effects of Different Laser Sources and Doping Methods Used to Dope Silicon Carbide," *Acta Mater.*, vol. 53, pp. 2835-2844, 2005.

[58] Z. Tian, N. R. Quick and A. Kar, "Laser-Enhanced Diffusion of Nitrogen and Aluminum Dopants in Silicon Carbide," *Acta Mater.*, vol. 54, pp. 4273-4283, 2006.

[59] S. Bet, N. R. Quick and A. Kar, "Effect of Laser Field and Thermal Stress on Diffusion in Laser Doping of SiC," *Acta Mater.*, vol. 55, pp. 6816-6824, 2007.

[60] S. Bet, N. R. Quick and A. Kar, "Laser Doping of Chromium as a Double Acceptor in Silicon Carbide with Reduced Crystalline Damage and Nearly All Dopants in Activated State," *Acta Mater.*, vol. 56, pp. 1857-1867, 2008.

[61] S. Bet, N. R. Quick and A. Kar, "Laser-Doping of Silicon Carbide for p-n Junction and LED Fabrication," *Physica Status Solidi (a)*, vol. 204 (4), pp. 1147-1157, 2007.

[62] C. Zhang, I. A. Salama, N. R. Quick and A. Kar, "One-Dimensional Transient Analysis of Volumetric Heating for Laser Drilling," *J. Appl. Phys.*, vol. 99, pp. 113530-1-10, (2006).

[63] M. N. Ozisik, Heat Conduction, 2nd ed., New York: John Wiley & Sons, 1993.

[64] M. E. Glicksman, Diffusion in Solids: Field Theory, Solid-State Principles and Applications, New York: John Wiley & Sons, 2000.

[65] Y. Gao, S. I. Soloviev and T. S. Sudarshan, "Investigation of Boron Diffusion in 6H-SiC," *Appl. Phys. Lett.*, vol. 83, pp. 905-907, 2003.

[66] J. Tersoff, "Enhanced Solubility of Impurities and Enhanced Diffusion Near Crystal Surfaces," *Phys. Rev. Lett.*, vol. 74, 5080-5083, 1995.

[67] H. Bracht, N. A. Stolwijk, M. Laube and G. Pensl, "Diffusion of Boron in Silicon Carbide: Evidence for the Kick-out Mechanism," *Appl. Phys. Lett.*, vol. 77, 3188-3190, 2000.

[68] W. Z. Shen and A. G. U. Perera, "Application of Free Carrier Absorption for Far-infrared Detection," *Int. J. Infrared Millimeter Waves*, vol. 21, pp. 1579-1587, 2000.

[69] Y. Yang, H. C. Liu, W. Z. Shen, N. Li, W. Lu, Z. R. Wasilewski and M. Buchanan, "Optimal Doping Density for Quantum-well Infrared Photodetector Performance," *IEEE J. Quantum Electron.*, vol. 45, pp. 623-628, 2009.

[70] R. Siegel and J. Howell, Thermal Radiation Heat Transfer, New York: Taylor & Francis, 1994.

[71] F. P. Incropera and D. P. DeWitt, Introduction to Heat Transfer, New York: John Wiley & Sons, 1985.

[72] E. Hecht, Optics, Singapore: Pearson Education, 2002.

[73] M. Rubin, "Solar Optical Properties of Windows," Energy Research, vol. 6, pp. 123-133, 1982.

[74] Born M and Wolf E 1983 Principles of Optics (New York: Pergamon Press) pp. 660-664.

[75] P. W. Kruse, L. D. McGlauchlin and R. B. McQuistan, Elements of Infrared Technology: Generation, Transmission, and Detection, New York: John Wiley & Sons, 1963.

[76] J. Mazumder and A. Kar, Theory and Application of Laser Chemical Vapor Deposition, New York: Plenum Press, 1995.

[77] V. Dhar, Quantum Efficiency, in: Encyclopedia of Optical Engineering, edited by R. G. Driggers, Volume 3, New York: Marcel Dekker, 2003.

[78] J. A. Jamieson, R. H. McFee, G. N. Plass, R. H. Grube and R. G. Richards, Infrared Physics and Engineering, New York: McGraw-Hill, 1963.

[79] W. J. Choke, "Silicon carbide," *Mater. Res. Bull.*, vol. 4 pp. S141-S152, 1969.

[80] A. Galeckas, J. Linnros, M. Frischholz, K. Rottner, N. Nordell, S. Karlsson and V. Grivickas, Investigation of Surface Recombination and Carrier Lifetime in 4H/6H-SiC, *Mater. Sci. Eng. B*, vol. 61-62, pp. 239-243, 1999.

[81] N. S. Kopeika, A System Engineering Approach to Imaging, Washington: SPIE - The International Society for Optical Engineering, 1998.

[82] D. Grbovic, N. V. Lavrik, S. Rajic, S. R. Hunter and P. G. Datskos, Nano-mechanical infrared detectors, In: Encyclopedia of Nanoscience and Nanotechnology, edited by H. S. Nalwa, American Scientific Publishers (in press), 2011.

[83] J. Matovic and Z. Jaksic, "Micromechanical Sensors Based on Lateral and Longitudinal Displacement of a Cantilever Sensing Element: A Comparative Performance Study," *Proc. of SPIE*, vol. 7362, pp. 73621E-1-10, 2009.

[84] J. M. Lloyd, Thermal Imaging Systems, New York: Plenum Press, 1975.

[85] E. L. Dereniak and G. D. Boreman, Infrared Detectors and Systems, New York: John Wiley & Sons, 1996.

[86] J. Piotrowski and A. Rogalski, "Uncooled Long Wavelength Infrared Photon Detectors," *Infrared Phys. Technol.*, vol. 104, pp. 115-131, 2004.

[87] J. L. Gimlett and N. K. Cheung, "Effects of Phase-to-intensity Noise Conversion by Multiple Reflections on Gigabit-per-second DFB Laser Transmission Systems," *J. Lightwave Technol.*, vol. 7, pp. 888-895, 1989.

[88] K. Petermann, Laser Diode Modulation and Noise, Boston: Kluwer Acacemic Publishers, 1988.

[89] A. Yariv, Quantum Electronics, New York: Wiley, 1989.

[90] D. Scribner, J. Schuler, P. Warren, J. Howard and M. Kruer, "Image Preprocessing for the Infrared," in Infrared Detectors and Focal Plane Arrays VI, *Proc. of SPIE*, vol. 4028, edited by E. L. Dereniak and R. E. Sampson, pp. 222-233, (SPIE, Orlando, Florida, 2000).

[91] M. Reine, "Review of HgCdTe Photodiodes for IR Detection," in Infrared Detectors and Focal Plane Arrays VI, *Proc. of SPIE*, vol. 4028, edited by E. L. Dereniak and R. E.

Sampson,), pp. 320-330, (SPIE, Orlando, Florida, 2000).

[92] M. Schlessinger, Infrared Technology Fundamentals, New York: Marcel Dekker, 1995.

[93] J. A. Jamieson, R. H. McFee, G. N. Plass, R. H. Grube and R. G. Richards, Infrared Physics and Engineering, New York: McGraw-Hill, 1963.

[94] J. L. Miller, Principles of Infrared Technology, New York: Van Nostrand Reinhold, 1994.

[95] A. Rogalski, "HgCdTe Infrared Detector Material: History, Status and Outlook," *Rep. Prog. Phys.*, vol. 68, pp. 2267-2336, 2005.

[96] P. Norton, "HgCdTe Infrared Detectors," *Opto-Electron. Rev.*, vol. 10, pp. 159-174, 2002.

[97] A. Rogalski, Infrared Photon Detectors, Bellingham, Washington: SPIE Optical Engineering Press, 1995.

[98] S. J. Lee, Y. H. Lee, S. H. Suh, Y. J. Oh, T. Y. Kim, M. H. Oh, C. J. Kim, and B. K. Ju, "Uncooled Thermopile Infrared Detector with Chromium Oxide Absorption Layer," *Sens. Actuat. A*, vol. 95, pp. 24-28, 2001.

[99] P. Muralt, "Micromachined Infrared Detectors Based on Pyroelectric Thin Films," *Rep. Prog. Phys.*, vol. 64, pp. 1339-1388, 2001.

[100] M. Noda, K. Hashimoto, R. Kubo, H. Tanaka, T. Mukaigawa, H. Xu and M. Okuyama, "A New Type of Dielectric Bolometer Mode of Detector Pixel using Ferroelectric Thin Film Capacitors for Infrared Image Sensor," *Sens. Actuat. A*, vol. 77, pp. 39-44, 1999.

[101] F. Niklaus, C. Vieider and H. Jakobsen, "MEMS-based Uncooled Infrared Bolometer Arrays – A Review," in MEMS/MOEMS Technologies and Applications III, *Proc. of SPIE* vol. 6836, edited by J. Chiao, X. Chen, Z. Zhou and X. Li, pp. 68360D1-15, (SPIE, Beijing, China, 2007).

[102] F. Dong, Q. Zhang, D. Chen, L. Pan, Z. Guo, W. Wang, Z. Duan and X. Wu, "An Uncooled Optically Readable Infrared Imaging Detector," *Sens. Actuat. A*, vol. 133, pp. 236-242, 2007.

[103] G. N. Violina, E. V. Kalinina, G. F. Kholujanov, V. G. Kossov, R. R. Yafaev, A. Hallen and A. O. Konstantinov, "Silicon Carbide Detectors of High-energy Particles," *Semiconductors*, vol. 36, pp. 710-713, 2002.

[104] E. Vittone, N. Skukan, Z. Pastuovic, P. Olivero and M. Jaksic, "Charge Collection Efficiency Mapping of Interdigitated 4H-SiC Detectors," *Nucl. Instrum. Methods Phys.*

Res. Sect. B, vol. 267, pp. 2197-2202, 2009.

[105] F. Nava, G. Bertuccio, A. Cavallini and E. Vittone, "Silicon Carbide and its Use as a Radiation Detector Material," *Meas. Sci. Technol.*, vol. 19, pp. 102001, 2008.

[106] J. E. Greivenkamp, Field Guide to Geometrical Optics, Bellingham, Washington: SPIE Press, 2004.

[107] C. A. Bennett, Principles of Physical Optics, New York: John Wiley & Sons, 2008.

[108] E. L. Dereniak and D. G. Crowe, Optical Radiation Detectors, New York: John Wiley & Sons, 1984.

[109] Y. Li, D. Pan, C. Yang and Y. Luo, "NETD Test of High-sensitivity Infrared Camera," in 3rd International Symposium on Advanced Optical Manufacturing and Testing Technologies: Optical Test and Measurement Technology and Equipment, *Proc. of SPIE*, vol. 6723, edited by J. Pan, J. C. Wyant and H. Wang, pp. 67233Q1-5, (SPIE, Beijing, China, 2007).

[110] P. J. Picone, Advanced Infrared Photodetectors, Materials Review, Surveillance Research Laboratory Research Report, pp. 13-20, 1993.

[111] M. C. Gupta and J. Ballato, The Handbook of Photonics, Boca Raton, Florida: CRC Press, 2006.

[112] S. Sheng, M. G. Spencer, X. Tang, P. Zhou, K. Wongchotigul, C. Taylor and G. L. Harris, "An Investigation of 3C-SiC Photoconductive Power Switching Devices," *Mater. Sci. Eng. B*, vol. 46, pp. 147-151, 1997.

[113] S. Dogan, A. Teke, D. Huang, H. Morkoc, C. B. Roberts, J. Parish, B. Ganguly, M. Smith, R. E. Myers and S. E. Saddow, "4H-SiC Photoconductive Switching Devices for Use in High-power Applications," *Appl. Phys. Lett.*, vol. 82, pp. 3107-3109, 2003.

[114] F. Zhao, M. M. Islam, P. Muzykov, A. Bolotnikov and T. S. Sudarshan, "Optically Activated 4H-SiC p-i-n diodes for High-power Applications," *IEEE Electr. Device L.*, vol. 30, pp. 1182-1184, 2009.

[115] P. S. Cho, J. Goldhar, C. H. Lee, S. E. Saddow and P. Neudeck, "Photoconductive and Photovoltaic Response of High-dark-resistivity 6H-SiC Devices," *J. Appl. Phys.*, vol. 77 pp. 1591-1599, 1995.

[116] J. S. Sullivan and J. R. Stanly, "6H-SiC Photoconductive Switches Triggered at Below Bandgap Wavelengths," *IEEE Trans. Dielectrics and Electrical Insulation*, vol. 14, pp.

980-985, 2007.

[117] T. J. Phillips, "High Performance Thermal Imaging Technology," *III-Vs Review*, vol. 15, pp. 32-34, 2002.

[118] X. Bai, X. Guo, D. C. McIntosh, H.-D. Liu and J. C. Campbell, "High Detection Sesitiivty of Ultraviolet 4H-SiC Avalanche Photodiodes," *IEEE J. Quantum Electron.*, vol. 43, pp. 1159-1162, 2007.

[119] F. Qian, R. Schnupp, C. Q. Chen, R. Helbig and H. Ryssel, "Indirect-coupling Ultraviolet-sensitive Photodetector with High Electrical Gain, Fast Response, and Low Noise," *Sensor. Actuator.*, vol. 86, pp. 66-72, 2000.

[120] A. Samman, S. Gebremariam, L. Rimai, X. Zhang, J. Hangas and G. W. Auner, "Silicon-Carbide MOS Capacitors with Laser-ablated Pt Gate as Combustible Gas Sensors," *Sens. Actuat. B*, vol. 63, pp. 91-102, 2000.

[121] C. K. Kim, J. H. Lee, Y. H. Lee, N. I. Cho and D. J. Kim, "A Study on a Platinum-silicon Carbide Schottky Diode as a Hydrogen Gas Sensor," *Sens. Actuat. B*, vol. 66, pp. 116-118, 2000.

[122] K. Nakashima, Y. Okuyama, S. Ando, O. Eryu, K. Abe, H. Yokoi and T. Oshima, "A New Type of SiC Gas Sensor with a Pn-junction Structure," *Mater. Sci. Forum*, vol. 389-393, pp. 1427-1430, 2002.

[123] N. G. Wright and A. B. Horsfall, "SiC Sensors: A Review," *J. Phys. D: Appl. Phys.*, vol. 40, pp. 6345-6354, 2007.

[124] K. Matocha, V. Tilak, P. Sandvik and J. Tucker, "High-temperature SiC MOSFET Gas Sensors," *Mater. Res. Soc. Symp. Proc.*, vol. 828, pp. A7.9.1-6, 2005.

[125] P. Tobias, B. Golding and R. Ghosh, "Interface States in High Temperature Gas Sensors Based on SiC," *IEEE Sens. J.*, vol. 3, pp. 543-547, 2003.

[126] P. Tobias, H. Hui, M. Koochesfahani and R. N. Ghosh, "Millisecond Response Time Measurements of High Temperature Gas Sensors," *Proc. IEEE Sensors*, (Vienna, Austria, 24-27 Oct. 2004).

[127] A. L. Spetz, P. Tobias, L. Uneus, H. Svenningstorp, L. Ekedahl and I. Lundstrom, "High Temperature Catalytic Metal Field Effect Transistors for Industrial Applications," *Sens. Actuat. B*, vol. 70, pp. 67-76, 2000.

[128] A. L. Spetz, L. Uneus, H. Svennningstorp, P. Tobias, L. G. Ekedahl, O. Larsson, A. Goras, S. Savage, C. Harris, P. Martensson, R. Wigren, P. Salomonsson, B. Haggendahl, P. Ljung,

M. Mattsson and I. Lundstrom, "SiC Based Field Effect Gas Sensors for Industrial Applications," *Phys. Stat. Sol. A*, vol. 185, pp. 15-25, 2001.

[129] R. N. Ghosh, R. Loloee, T. Isaacs-Smith and J. R. Williams, "High Temperature Reliability of SiC n-MOS Devices up to 630°C," *Mater. Sci. Forum*, vol. 527-529, pp. 1039-1042, 2006.

[130] T. J. Fawcett, J. T.Wolan, R. L.Myers, J. Walker and S. E. Saddow, "Wide-range (0.33%-100%) 3C-SiC Resistive Hydrogen Gas Sensor Development," *Appl. Phys. Lett.*, vol. 85, pp. 416-418, 2004.

[131] T. J. Fawcett, J. T.Wolan, A. L. Spetz, R. L.Myers and S. E. Saddow, "Thermal Detection Mechanism of SiC Based Hydrogen Resistive Gas Sensors," *Appl. Phys. Lett.*, vol. 89, pp. 182102, 2006.

[132] V. B. Shields, M. A. Ryan, R. M. Williams, M. G. Spencer, D. M. Collins and D. Zhang, "A Variable Potential Porous Silicon Carbide Hydrocarbon Gas Sensor," (Document ID: 20060037241, File Series: NASA Technical Reports), 1995.

[133] F. Solzbacher, C. Imawan, H. Steffes, E. Obermeier and M. Eickhoff, "A Highly Stable SiC Based Microhotplate NO_2 Gas-sensor," *Sens. Actuat. B*, , vol. 78, pp. 216-220, 2001.

[134] H. Konta, "A Silicon Carbide Based Gas Sensor," (State University of New York at Buffalo, Project Reports), 2001.

[135] N. G. Wright and A. B. Horsfall, "SiC Sensors: A Review," *J. Phys. D: Appl. Phys.*, vol. 40, pp. 6345-6354, 2007.

[136] S. Nakagomi, P. Tobias, A. Baranzahi, I. Lundstrom, P.Martensson and A. L. Spetz, "Influence of Carbon Monoxide, Water and Oxygen on High Temperature Catalytic Metal-oxide-silicon Carbide Structures," *Sens. Actuat. B*, vol. 45, pp. 183-191, 1997.

[137] R. Loloee, B. Chorpening, S. Beer and R. N. Ghosh, "Hydrogen Monitoring for Power Plant Applications Using SiC Sensors," *Sens. Actuat. B*, vol. 129, pp. 200-210, 2008.

[138] A. L. Spetz, A. Baranzahi, P. Tobias and I. Lundstrom, "High Temperature Sensors Based on Metal-insulator-silicon Carbide Devices," *Phys. Stat. Sol. A*, vol. 162, pp. 493-511, 1997.

[139] P. Tobias, B. Golding and R. N. Ghosh, "Interface States in High-temperature Gas Sensors Based on Silicon Carbide," *IEEE Sens. J.*, vol. 2, pp. 543-547, 2003.

[140] J. Schalwig, P., Kreisl, S. Ahlers and G. Muller, "Response Mechanism of SiC-based MOS

Field-effect Gas Sensors," *IEEE Sens. J.*, vol. 2, pp. 394-402, 2002.

[141] A. Vasiliev, W. Moritz, V.Fillipov, L. Bartholomaus, A. Terentjev and T. Gabusjan, "High Temperature Semiconductor Sensor for the Detection of Fluorine," *Sens. Actuat. B*, vol. 49, pp. 133-138, 1998.

[142] P. Tobias, A. Baranzahi, A. L. Spetz, O. Kordina, E. Janzen and I. Lundstrom, "Fast Chemical Sensing with Metal-insulator Silicon Carbide Structures," *IEEE Electron. Device Lett.*, vol. 18, pp. 287-289, 1997.

[143] A. L. Spetz, P. Tobias, A. Baranzahi, P. Martensson and I. Lundstrom, "Current Status of Silicon Carbide Based High-temperature Gas Sensors," *IEEE Trans. Electron. Devices*, vol. 46, pp. 561-566, 1999.

[144] H. Svenningstorp, P. Tobias, I. Lundstrom, P. Salomonsson, P. Martensson, L. Ekedahl and A. L. Spetz, "Influence of Catalytic Reactivity on the Response of Metal-oxide-silicon Carbide Sensor to Exhaust Gases," *Sens. Actuat. B*, vol. 57, pp. 159-165, 1999.

[145] S. Kandasamy, A. Trinchi, W. Wlodarski, E. Comini and G. Sberveglieri, "Hydrogen and Hydrocarbon Gas Sensing Performance of Pt/WO_3/SiC MROSiC Devices," *Sens. Actuat. B*, vol. 111-112, pp. 111-116, 2005.

[146] A. Baranzahi, A. L. Spetz and I. Lundstrom, "Reversible Hydrogen Annealing of Metal-oxide-silicon Carbide Devices at High Temperatures," *Appl. Phys. Lett.*, vol. 67, pp. 3203-3205, 1995.

[147] L. Chen, G. W. Hunter, P. G. Neudeck and D. Knight, "Surface and Interface Properties of PdCr/SiC Schottky Diode Gas Sensor Annealed at 425°C," *Solid-State Electron.*, vol. 42, pp. 2209-2214, 1998.

[148] C. I. Muntele, D. Ila, E. K. Williams, D. B. Poker, D. K. Hensley, D. J. Larkin, I. Muntele, "Fabrication of SiC Hydrogen Sensor by Pd-implantation," *Mater. Sci. Forum*, vol. 338-342, pp. 1443-1446, 2000.

[149] W. Gao, L.Shi, S. A. Khan, Y. Hasegawa and T. Katsube, "High Temperature and High Sensitive NO_x Gas Sensor with Hetero-junction Structure Using Laser Ablation Method," (The 13th International Conference on Solid-State Sensors, Actuators and Microsystems, Seoul, Korea), June 2005.

[150] M. Ali, V. Cimalla, V. Lebedev, T. Stauden, G. Ecke, V. Tilak, P. Sandvik and O. Ambacher, "SiC-based FET for Detection of NO_x and O_2 Using $InSnO_x$ as a Gate Material," *Sens. Actuat. B*, vol. 122, pp. 182-186, 2007.

[151] H. Wingbrant, H. Svenningstorp, P. Salomonsson, D. Kubinski, J. H. Visser, M. Lofdahl and A. L. Spetz, "Using a MISiC-FET Sensor for Detecting NH_3 in SCR Systems," *IEEE Sens. J.*, vol. 5, pp. 10991105, 2005.

[152] S. Kandasamy, W. Wlodarski, A. Holland, S. Nakagomi and Y. Kokubun, "Electrical Characterization and Hydrogen Gas Sensing Properties of a n-ZnO/p-SiC Pt-gate Metal Semiconductor Field Effect Transistor," *Appl. Phys. Lett.*, vol. 90, pp. 064103, 2007.

[153] G. Lim, U. P. DeSilva, N. R. Quick and A. Kar, "Optical Property-based Wireless Sensors for CO_2 and NO Gases Using Silicon Carbide," (Spring PIWG Meeting: The ISA's 55th International Instrumentation Symposium, League City, Texas), June 2009.

[154] S. Dakshinamurthy, N. R. Quick and A. Kar, "Temperature-dependent Optical Properties of Silicon Carbide for Wireless Temperature Sensors," *J. Phys. D: Appl. Phys.*, vol. 40, pp. 353-360, 2007.

[155] S. Dakshinamurthy, N. R. Quick and A. Kar, "SiC-based Optical Interferometry at High Pressure and Temperature for Pressure and Chemical Sensing," *J. App. Phys.*, vol. 99, pp. 094902, 2006.

[156] A. Chakravarty, N. R. Quick and A. Kar, "Decoupling of Silicon Carbide Optical Sensor Response for Temperature and Pressure Measurements," *J. Appl. Phys.*, vol. 102, pp. 073111, 2007.

[157] A. J. de Castro, J. Meneses, S. Briz and F. Lopez, "Nondispersive Infrared Monitoring of NO Emissions in Exhaust Gases of Vehicles," *Rev. Sci. Instrum.*, vol. 70, pp. 3156-3159, 1999.

[158] U. Willer, M. Saraji, A. Khorsandi, P. Geiser and W. Schade, "Near- and Mid-infrared Laser Monitoring of Industrial Processes, Environment and Security Applications," *Opt. Lasers Eng.*, vol. 44, pp. 699-710, 2006.

[159] H. Herbin, N. Picque, G. Guelachvili, E. Sorokin and I. Sorokina, "N_2O Weak Lines Observed between 3900 and 4050 cm^{-1} from Long Path Absorption Spectra," *J. Molecular Spect.*, vol. 238, pp. 256-259, 2006.

[160] T. Troffer, G. Pensl, A. Schoner, A. Henry, C. Hallin, O. Kordina and E. Janzen, "Electrical Characterization of Gallium Acceptor in 6H SiC," *Mater. Sci. Forum*, vol. 557, pp. 264-268, 1998.

[161] A. Schöner, N. Nordell, K. Rottner, R. Helbig and G. Pensl, "Dependence of the Aluminum Ionization Energy on Doping Concentration and Compensation in 6H–SiC," *Inst. Phys. Conf. Ser.*, vol. 142, pp. 493–496, 1996.

[162] Z. Li and R. C. Bradt, “Thermal Expansion and Elastic Anisotropies of SiC as Related to Polytype Structure,” (Proc. Silicon Carbide 1987 Symposium, Volume of Ceramic Trans., Columbus, OH), August 1987.

[163] A. D. Polyanin and A. V. Manzhirov, Handbook of Mathematics for Engineers and Scientists, New York: Chapman & Hall/CRC, 2007.

[164] D. B. Dusenbery, Living at Micro Scale: The Unexpected Physics of Being Small, Cambridge, USA: Harvard University Press, 2009.

[165] W. T. Silfvast, Laser Fundamentals - 2nd edition, UK: Cambridge University Press Harvard University Press, 2004.

[166] A. D. White and L. Tsufura, Helium-Neon Lasers, in Handbook of Laser Technology and Applications; volume II: Laser Design and Laser Systems, edited by C. Webb and J. Jones, Philadelphia: IOP Publishing, 2004.